

The Dissertation Committee for Sushil Naresh Dhoot certifies that this is the approved version of the following dissertation:

**SORPTION AND TRANSPORT OF GASES AND ORGANIC
VAPORS IN POLY(ETHYLENE TEREPHTHALATE)**

Committee:

Benny D. Freeman, Supervisor

Donald R. Paul

Isaac C. Sanchez

R. Bruce Eldridge

Mark E. Stewart

**SORPTION AND TRANSPORT OF GASES AND ORGANIC
VAPORS IN POLY(ETHYLENE TEREPHTHALATE)**

by

Sushil Naresh Dhoot, B.S., M.S.

Dissertation

Presented to the Faculty of the Graduate School of

The University of Texas at Austin

In Partial Fulfillment

Of the Requirements

For the Degree of

Doctor of Philosophy

The University of Texas at Austin

May 2004

DEDICATION

This dissertation is dedicated to my parents, Sudha and Naresh Dhoot, and to the rest of my family for their constant love, encouragement, and support.

ACKNOWLEDGMENTS

I wish to thank my advisor, Dr. Benny Freeman, my industrial mentor at Eastman Chemicals, Dr. Mark Stewart, and the other committee members: Dr. Donald Paul, Dr. Isaac Sanchez, and Dr. Bruce Eldridge, for assistance over the course of my graduate studies at North Carolina State University and The University of Texas at Austin.

In addition, I would like to thank the Eastman Chemical Analytical Laboratories for performing some characterization experiments, and in particular, Dr. Craig Sass and Rick McGill, for their assistance with the wide angle X-ray diffraction measurements. I would also like to thank Dr. Anita Hill at CSIRO in Australia for performing the positron annihilation lifetime spectroscopy experiments reported in this dissertation.

The past and present graduate students of the Freeman Polymer Research Group are also thanked for their technical assistance, support, and patience: Rajeev Prabhakar, Haiqing Lin, George Serad, Dr. Timothy Merkel, Sabrina Dixon-Garrett, Nikunj Patel, Conor Braman, Scott Kelman, Scott Matteuci, Roy Raharjo; and the group's post-doctoral researchers: Dr. Kazukiyo Nagai, Dr. Hyuck Jai Lee and Dr. Teruhiko Kai. I am especially thankful to three colleagues and friends, who were always available as a supportive ear during the highs and lows of research and ready to engage in endless discussions about anything on our minds: Dr. Lora Toy, Dr. Michelle Arnold, and Anna Iwasinska.

Finally, I would like to thank my family for their love, support, and understanding during my graduate studies.

SORPTION AND TRANSPORT OF GASES AND ORGANIC VAPORS IN POLY(ETHYLENE TEREPHTHALATE)

Publication No. _____

Sushil Naresh Dhoot, Ph.D.
The University of Texas at Austin, 2004

Supervisor: Benny D. Freeman

Poly(ethylene terephthalate) (PET) is one of the most widely used barrier polymers for food and beverage packaging. The sorption and transport of organic molecules in PET are important considerations in flavor scalping, carryover, contamination, and therefore, container shelf life. However, literature data on transport properties of large flavor and aroma compounds in PET are limited due to their extremely low vapor pressures and long experimental timescales. The goal of this research project is to develop a systematic database of sorption and transport properties of large organic compounds in PET by overcoming these technical challenges.

Ultra-thin (0.9 μm thick) biaxially oriented PET films were used to overcome the drawback of long experimental timescales. Several model flavor compounds (*i.e.*, low molecular weight analogs of common flavor compounds) were selected from various classes of non-polar and polar organic compounds to study the effect of penetrant size, shape, and thermodynamic properties on solubility and diffusivity in PET. For example,

n-butane, *i*-butane, *n*-pentane, and *i*-pentane were selected to study the effect of chain length and branching in non-polar alkane hydrocarbons; acetone, methyl ethyl ketone (MEK), methyl *n*-propyl ketone (MnPK), and methyl *i*-propyl ketone (MiPK) from the family of ketones, and methyl acetate and ethyl acetate from the family of esters, were also studied to provide a similar series of data for polar organic model flavor compounds.

To overcome the drawback of extremely low vapor pressures of large organic compounds, a new experimental sorption technique was developed. It is estimated that penetrants with vapor pressures as low as 10^{-7} mmHg might be studied using this technique. It could be useful in industrial applications involving polymer membrane-based gas/vapor separations and food packaging. The solubility and diffusion coefficients of toluene vapor in PET were obtained using this technique.

Interestingly, the solubility difference between *n*-pentane and *i*-pentane is 10 times larger in glassy PET than in rubbery low-density polyethylene. Among the ketones and esters studied, both solubility and diffusivity decrease in the following order, acetone > MEK > MnPK > MiPK and methyl acetate > ethyl acetate. The diffusion coefficients of MiPK and *i*-pentane are among the lowest ever reported for PET. Surprisingly, diffusion coefficients of acetone and methyl acetate, and MEK and ethyl acetate are quite similar despite the esters being somewhat larger than ketones. For all penetrants studied, solubility and diffusion coefficients correlate well with penetrant critical temperature and critical volume, respectively. By extending these correlations, it might be possible to predict the sorption and transport properties of large flavor compounds in PET with reasonable accuracy.

TABLE OF CONTENTS

	Page
LIST OF TABLES	xii
LIST OF FIGURES	xv
CHAPTER 1 INTRODUCTION	1
1.1 Glassy Poly(ethylene terephthalate).....	2
1.2 Overview of Sorption and Transport of Small Molecules in Polymers.....	4
1.2.1 Solubility.....	4
1.2.2 Effect of Penetrant Partial Pressure on Solubility.....	5
1.2.3 Diffusivity.....	7
1.3 Overview of Fickian and non-Fickian Kinetics.....	9
1.4 Goals and Organization of This Research.....	10
CHAPTER 2 BARRIER POLYMERS	22
2.1 Summary.....	23
2.2 Introduction.....	24
2.3 Fundamentals of Permeation in Polymers.....	25
2.4 Mechanism of Penetrant Transport in Dense Polymers.....	29
2.5 Factors Affecting Permeability, Diffusivity, and Solubility.....	32
2.5.1 Free Volume.....	32
2.5.2 Temperature.....	35
2.5.3 Chemical Structure.....	37
2.5.4 Crystallinity.....	39
2.5.5 Chain Orientation.....	42
2.5.6 Penetrant Concentration (or Partial Pressure).....	44
2.5.7 Humidity.....	45

	Page
2.6	Techniques for Measuring Transport Properties.....46
2.6.1	Oxygen and Carbon Dioxide Permeation.....48
2.6.2	Water Vapor Permeation.....49
2.6.3	Flavor and Aroma Compounds.....50
2.7	Techniques for Predicting Transport Properties.....52
2.7.1	Modeling Transport Properties of Gases and Condensable Vapors in Polymers.....52
2.7.2	‘Migration Modeling’ of Polymer Additives into Packaged Foods and Beverages.....59
2.8	Chemical Structures and Properties of Barrier Polymers..... 62
2.8.1	High Barrier Polymers..... 62
2.8.2	Moderate Barrier Polymers..... 73
2.9	Improving Barrier Properties of Polymers..... 82
2.9.1	Barrier Structures..... 82
2.9.2	Oxygen-Scavenging Systems.....92
2.10	Conclusions.....95
 CHAPTER 3 EXPERIMENTAL TECHNIQUES AND SAMPLE CHARACTERIZATION RESULTS.....143	
3.1	Materials.....144
3.2	Gravimetric Sorption.....144
3.3	Dual Volume Pressure Decay Sorption..... 146
3.4	Polymer Characterization Techniques..... 147
3.4.1	Nuclear Magnetic Resonance Spectroscopy..... 147
3.4.2	Inherent Viscosity..... 147
3.4.3	Thermal and Physical Characterization.....147
3.4.4	Positron Annihilation Lifetime Spectroscopy..... 148
3.4.5	Profilometry.....149

	Page
3.5 Polymer Characterization Results and Discussion.....	150
3.5.1 Inherent Viscosity, Nuclear Magnetic Resonance, and Profilometry.....	150
3.5.2 Sample Morphology.....	150
 CHAPTER 4 NOVEL EXPERIMENTAL TECHNIQUE FOR KINETIC GRAVIMETRIC SORPTION OF LOW VOLATILITY GASES AND ORGANIC VAPORS IN POLYMERS.....	165
4.1 Summary.....	166
4.2 Introduction.....	166
4.3 Principle of Operation.....	169
4.4 Experimental Results.....	172
4.5 Discussion.....	179
4.6 Acknowledgments.....	180
 CHAPTER 5 SORPTION AND TRANSPORT OF LINEAR ALKANE HYDROCARBONS IN BIAXIALLY ORIENTED POLY(ETHYLENE TEREPHTHALATE).....	189
5.1 Summary.....	190
5.2 Experimental.....	190
5.2.1 Materials.....	190
5.2.2 Gravimetric Sorption.....	191
5.3 Results and Discussion.....	191
5.3.1 Equilibrium <i>n</i> -Butane and <i>n</i> -Pentane Uptake.....	191
5.3.2 <i>n</i> -Butane and <i>n</i> -Pentane Sorption Kinetics.....	196
5.4 Conclusions.....	202

	Page
CHAPTER 6	
SORPTION AND TRANSPORT OF LINEAR AND BRANCHED KETONES IN BIAXIALLY ORIENTED POLY(ETHYLENE TEREPHTHALATE).....	214
6.1 Summary.....	215
6.2 Experimental.....	215
6.2.1 Materials.....	215
6.2.2 Gravimetric Sorption.....	216
6.3 Results and Discussion.....	216
6.3.1 Equilibrium Uptake of Ketones in PET.....	216
6.3.2 Sorption Kinetics of Ketones in PET.....	221
6.4 Conclusions.....	227
 CHAPTER 7	
SORPTION AND TRANSPORT OF LINEAR ESTERS AND BRANCHED ALKANES IN BIAXIALLY ORIENTED POLY(ETHYLENE TEREPHTHALATE).....	245
7.1 Summary.....	246
7.2 Experimental.....	247
7.2.1 Materials.....	247
7.2.2 Gravimetric Sorption.....	247
7.3 Results and Discussion.....	248
7.3.1 Equilibrium Uptake of Alkanes in PET.....	248
7.3.2 Equilibrium Uptake of Esters in PET.....	252
7.3.3 Sorption Kinetics of Alkanes and Esters in PET.....	256
7.4 Conclusions.....	261
Appendix 7A.....	263

	Page
CHAPTER 8	
SORPTION AND DIFFUSION OF TOLUENE AND	
CO₂ IN BIAXIALLY ORIENTED POLY(ETHYLENE	
TEREPHTHALATE).....	283
8.1 Summary.....	284
8.2 Introduction.....	284
8.3 Experimental.....	286
8.3.1 Materials.....	286
8.3.2 Gravimetric Sorption.....	287
8.3.3 Dual Volume Pressure Decay Sorption.....	287
8.4 Results and Discussion.....	287
8.4.1 Equilibrium Uptake and Sorption Kinetics of Toluene	
in PET.....	287
8.4.2 Equilibrium Uptake and Sorption Kinetics of CO ₂ in PET....	290
8.5 Conclusions.....	297
8.6 Acknowledgments.....	298
CHAPTER 9	
CONCLUSIONS AND RECOMMENDATIONS.....	311
9.1 Summary of Conclusions.....	312
9.2 Recommendations for Future Work.....	316
9.2.1 Solubility and Diffusivity Correlations.....	316
9.2.2 New Gravimetric Sorption Technique for Low Volatility	
Organic Vapors.....	317
9.2.3 Solvent-Induced Crystallization of Amorphous PET.....	318
9.2.4 Effect of Processing Conditions on Sorption and	
Transport Properties of PET.....	319
BIBLIOGRAPHY.....	322
VITA.....	345

LIST OF TABLES

Page

CHAPTER 1

Table 1.1	List of some common flavor and aroma compounds.....	16
-----------	---	----

CHAPTER 2

Table 2.1	Table of common gas permeability units with conversion factors.....	97
-----------	---	----

Table 2.2	Table of common water vapor transmission rate (WVTR) units with conversion factors.....	99
-----------	---	----

Table 2.3	Effect of orientation on oxygen permeability characteristics of semicrystalline and amorphous barrier resins.....	100
-----------	---	-----

Table 2.4	Physical, mechanical, optical, and chemical properties of some commonly used barrier polymers.....	102
-----------	--	-----

Table 2.5	Oxygen and carbon dioxide permeabilities of various high and moderate barrier polymers.....	103
-----------	---	-----

Table 2.6	Water vapor transmission rates of various high and moderate barrier polymers.....	105
-----------	---	-----

Table 2.7	Permeability, diffusivity, and solubility coefficients of flavor and aroma compounds in various high and moderate barrier polymers at 25°C and 0% RH.....	106
-----------	---	-----

Table 2.8	Compositions of commercial, high barrier nitrile copolymers.....	109
-----------	--	-----

Table 2.9	Comparison of properties of biaxially oriented LCP and PET films.....	110
-----------	---	-----

Table 2.10	Gas permeabilities of LCP-PET blends.....	111
------------	---	-----

CHAPTER 3

Table 3.1	Positron annihilation lifetime spectroscopy (PALS) parameters for biaxially oriented PET (BPET) and amorphous PET (APET) samples.....	159
-----------	---	-----

	Page
CHAPTER 4	
Table 4.1	Gas chromatograph settings.....181
Table 4.2	Mass flow rates, total pressures, and corresponding toluene vapor mole fractions in mixtures with nitrogen at 25°C.....182
CHAPTER 5	
Table 5.1	Positron annihilation lifetime spectroscopy (PALS) parameters for BPET and APET samples.....203
Table 5.2	Dual-mode model parameters for <i>n</i> -butane and <i>n</i> -pentane sorption in BPET and <i>n</i> -butane sorption in APET at 35°C.....204
CHAPTER 6	
Table 6.1	Chemical structures, critical properties, solubility parameters, and saturation vapor pressures at 35°C of acetone, MEK, MiPK, and MnPK.....228
Table 6.2	Dual-mode model parameters for acetone, MEK, MnPK, and MiPK sorption in BPET and acetone sorption in solvent-cast PET (SPET) at 35°C.....229
Table 6.3	D_{∞} and ω values for acetone, MEK, MnPK, and MiPK at 35°C.....230
CHAPTER 7	
Table 7.1	Chemical structure, critical properties, solubility parameters, and saturation vapor pressures at 35°C of linear and branched alkane hydrocarbons and esters.....265
Table 7.2	Dual-mode and Flory-Huggins model parameters for linear and branched alkane hydrocarbons and esters in BPET at 35°C. The model parameters for <i>n</i> -butane and <i>n</i> -pentane were obtained from the literature.....266
Table 7.3	Hansen solubility parameters, critical volumes, and dipole moments of acetone, methyl ethyl ketone, methyl acetate, and ethyl acetate.....267

	Page
Table 7.4	268

D_{∞} and ω values for linear and branched alkane hydrocarbons and esters at 35°C. The values for *n*-butane and *n*-pentane were obtained from the literature.....

CHAPTER 8

Table 8.1	299
-----------	-----

Dual-mode sorption model parameters for toluene and CO₂ in PET.....

Table 8.2	300
-----------	-----

Comparison of estimated amorphous phase CO₂ permeability (P_a) and Henry's Law mode diffusion coefficients ($D_{D,a}$) at 25°C in a thin BPET film from this study with literature data for much thicker films.....

LIST OF FIGURES

	Page
CHAPTER 1	
Figure 1.1	Timescale for sorption experiments based on Fickian diffusion. Diffusion coefficients are expressed in cm^2/s17
Figure 1.2	Effect of penetrant partial pressure on the concentration of penetrant dissolved in polymer matrix.....18
Figure 1.3	Effect of penetrant partial pressure on penetrant concentration in the two modes of sorption postulated by the dual-mode model for glassy polymers.....19
Figure 1.4	An example of Fickian sorption kinetics.....20
Figure 1.5	Two examples of non-Fickian sorption and desorption kinetics.21
CHAPTER 2	
Figure 2.1	Cartoon depicting mechanism of penetrant transport in polymers.....112
Figure 2.2	Cartoon depicting polymer chain position before, during, and after a diffusion step by a penetrant molecule.....113
Figure 2.3	Crankshaft Motion – An example of local segmental dynamics in polyolefins. Each ball represents, for example, a methylene (<i>i.e.</i> , CH_2) unit in polyethylene and the solid lines represent the covalent chemical bonds between neighboring CH_2 groups. Such molecular motions are believed to be important in providing pathways for diffusion of small molecules in polymers. The crankshaft motion requires the simultaneous rotation of several contiguous methylene units about bonds 1 and 7 or 1 and 5.....114
Figure 2.4	Computer simulation of the displacement of an oxygen molecule in poly(2,6-dimethyl-1,4-phenylene oxide) as a function of time.....115

	Page
Figure 2.5	Computer simulation of the displacement of a nitrogen molecule in poly(2,6-dimethyl-1,4-phenylene oxide) as a function of time.....116
Figure 2.6	Correlation of gas diffusion coefficients with inverse of polymer fractional free volume in a series of substituted polysulfones.....117
Figure 2.7	Correlation of oxygen permeability with inverse of polymer fractional free volume for several families of amorphous, glassy polymers and liquid crystalline polymers. (■) Polystyrene (35°C), (Δ) Polycarbonates (35°C), (●) Polyesters (30°C), (□) Polyamides (25°C), (◆) Liquid Crystalline Polymers (35°C).....118
Figure 2.8	Effect of temperature on oxygen permeability at 75% relative humidity. PET is poly(ethylene terephthalate), AN is an acrylonitrile-styrene copolymer, PVDC is vinylidene chloride-vinyl chloride copolymer (coextrusion resin grade), and EVOH 27 is ethylene vinyl alcohol copolymer containing 27 mol% ethylene.....119
Figure 2.9	Correlation of D_0 with E_D/RT for glassy polymers. (O) Poly(ethylene terephthalate), (●) Bisphenol-A Polycarbonate (PC), (□) Tetramethyl Bisphenol-A PC (TMPC).....120
Figure 2.10	Effect of cohesive energy density (CED) on oxygen permeability for six barrier polymers: Polyethylene (PE), Polystyrene (PS), Poly(vinyl acetate) (PVA), Poly(vinyl chloride) (PVC), Polyacrylonitrile (PAN), Poly(vinyl alcohol) (PVOH).....121
Figure 2.11	Effect of crystalline content on gas permeability in polyethylene at 25°C.....122
Figure 2.12	Typical permeability-pressure dependence in rubbery and glassy polymers. (A) Hydrogen in polyethylene (PE) at 30°C, (B) Carbon dioxide in polycarbonate (PC) at 35°C, (C) Propane in polyethylene at 20°C, (D) Acetone in ethyl cellulose (EC) at 40°C. The permeability values have units of ($\text{cm}^3 \text{ mil} / (100 \text{ in}^2 \text{ day atm})$).....123

	Page
Figure 2.13	Effect of relative humidity on oxygen permeability of hydrophilic barrier polymers. AmNY is amorphous nylon (Selar [®]), BON is biaxially oriented nylon 6, MXD-6 is oriented poly(metaxylylenediamine-adipic acid), EVOH 44 and 32 are ethylene vinyl alcohol copolymers containing 32 and 44 mol% ethylene.....124
Figure 2.14	(A) Mass of permeating penetrant per unit film area (q) as a function of time (providing a measure of time lag, t_L) (B) Normalized penetrant flux (N_A) as a function of time (providing a measure of half time, $t_{1/2}$). t_{SS} is time required to achieve steady state.....125
Figure 2.15	A schematic of a permeation cell in the Ox-Tran [®] (MOCON, Inc.) oxygen transmission rate measurement system.....126
Figure 2.16	A schematic of the McBain spring balance apparatus for measuring sorption and desorption of organic vapors in barrier polymers.....127
Figure 2.17	Correlation of infinite dilution penetrant solubility with penetrant critical temperature in poly(ethylene terephthalate) (PET). (●) non-polar penetrants, (○) polar and quadrupolar penetrants, (◆) aromatic penetrants. The slope, $M = 0.019 \pm 0.001 \text{ K}^{-1}$ and intercept, $N = -9.6 \pm 0.4$128
Figure 2.18	Effect of penetrant size on infinite dilution, amorphous phase diffusion coefficients in poly(ethylene terephthalate) at 25°C. The best-fit parameters of Equation 2.31 are: $\tau = 5.7 \pm 1.2 \times 10^8 \text{ (cm}^2/\text{s) (cm}^3/\text{mol)}^{9.1}$, $\eta = 9.1 \pm 0.9$129
Figure 2.19	Effect of ethylene content on oxygen permeability and water vapor transmission rates (WVTR) of ethylene vinyl alcohol copolymer (EVOH). The figure also shows data for poly(vinyl alcohol) (PVOH) and high density polyethylene (HDPE) for comparison.....130
Figure 2.20	A comparison of oxygen and water vapor barrier properties of various high and moderate barrier polymers at 23°C.....131

	Page
Figure 2.21	Typical effect of density on various properties of polyethylene. LTI is low temperature impact strength and ESCR is environmental stress crack resistance.....132
Figure 2.22	Diffusion coefficients in unplasticized and plasticized poly(vinyl chloride) (PVC) as a function of penetrant molecular diameter.....133
Figure 2.23	Effect of thickness of barrier layer on permeability of a hypothetical two-layer barrier composite structure.....134
Figure 2.24	A comparison of processing temperatures of various commercially used barrier polymers.....135
Figure 2.25	An example of a typical symmetrical nine-layer coextruded barrier composite structure.....136
Figure 2.26	Effect of plasma-deposited silica coating thickness on steady state oxygen transmission rates of poly(ethylene terephthalate) films that have an uncoated thickness of 13 μm137
Figure 2.27	Influence of ORMOCER [®] coatings on oxygen transmission rates (OTR) of SiO _x -coated oriented polypropylene (OPP) (OTR measured at 23°C and 70% RH).....138
Figure 2.28	A comparison of oxygen and water vapor transmission rates of various barrier polymer composite structures. BOPP (met) is biaxially oriented, metallized polypropylene, PET (met.) is metallized poly(ethylene terephthalate), PEN (met) is metallized poly(ethylene naphthalate), Al composites are aluminum composites.....139
Figure 2.29	Typical examples of heterogeneous, immiscible blends. (A) Random spheres in a dispersed phase, (B) Aggregated spheres in a dispersed phase, (C) Oriented platelets in a dispersed phase, (D) Oriented rods in a dispersed phase.....140
Figure 2.30	Effect of EVOH content on oxygen permeability of PE-EVOH blends that exhibit (a) discontinuous morphology and (b) co-continuous lamellar morphology.....141

	Page
Figure 2.31	142

Reduction in oxygen transmission rates due to oxygen scavenging in blends of PET and nylon MXD-6. The measurements were made at 23°C and 50% RH. (A): 4 wt.% MXD-6 and 50 ppm cobalt (as metal), (B): 4 wt.% MXD-6 and 200 ppm cobalt (as metal).....

CHAPTER 3

Figure 3.1	160
Figure 3.2	161
Figure 3.3	162
Figure 3.4a	163
Figure 3.4b	164

Schematic of McBain quartz spring balance for gravimetric sorption.....

Schematic of a dual volume pressure decay sorption system.....

Wide angle X-ray diffraction spectrum of biaxially oriented PET (BPET).....

Variation of *o*Ps intensity (normalized to an amorphous basis) in PET with degree of crystallinity.....

Variation of *o*Ps lifetime (normalized to an amorphous basis) in PET with degree of crystallinity.....

CHAPTER 4

Figure 4.1	183
Figure 4.2	184
Figure 4.3	185
Figure 4.4a	186

Vapor pressures of linear alkanes at 25°C as a function of number of carbon atoms.....

Schematic diagram of modified spring balance system.....

Sorption isotherms of toluene in poly(dimethyl siloxane) at 25°C determined from pure and mixed vapor sorption experiments. The saturation vapor pressure of toluene at 25°C is 2.9 cmHg. The experimental data were fit using the Flory-Huggins sorption model ($\chi = 1.14 \pm 0.05$).....

Comparison of kinetic sorption data from pure and mixed vapor sorption experiments at 25°C and vapor activity increasing from 0 to 0.5 (● pure vapor: $M_\infty = 7.3 \pm 0.1$ g toluene/100g PDMS and $\bar{D} = 1.3 \pm 0.1 \times 10^{-6}$ cm²/s; ◇ mixed vapor: $M_\infty = 7.1 \pm 0.2$ g toluene/100g PDMS and $\bar{D} = 1.1 \pm 0.1 \times 10^{-6}$ cm²/s).....

	Page
Figure 4.4b	Comparison of kinetic sorption data from mixed vapor sorption experiments at 25°C using nitrogen and helium carrier gases and vapor activity increasing from 0 to 0.35 (● helium: $M_\infty = 4.1 \pm 0.1$ g toluene/100g PDMS and $\bar{D} = 1.9 \pm 0.3 \times 10^{-6}$ cm ² /s; ◇ nitrogen: $M_\infty = 4.1 \pm 0.1$ g toluene/100g PDMS and $\bar{D} = 1.2 \pm 0.2 \times 10^{-6}$ cm ² /s).....187
Figure 4.5	Comparison of diffusion coefficients of toluene in poly(dimethyl siloxane) at 25°C from pure and mixed vapor sorption experiments.....188
CHAPTER 5	
Figure 5.1a	Sorption isotherm of <i>n</i> -butane in BPET at 35°C. The saturation vapor pressure of <i>n</i> -butane at 35°C is 245.8 cmHg.....205
Figure 5.1b	Sorption isotherm of <i>n</i> -pentane in BPET at 35°C. The saturation vapor pressure of <i>n</i> -pentane at 35°C is 72.7 cmHg.....206
Figure 5.2	Correlation of infinite dilution, amorphous phase solubility coefficients in PET with critical temperature. The slope, M of the least squares line is 0.019 ± 0.001 K ⁻¹ and the intercept, N is -9.6 ± 0.4207
Figure 5.3a	Fickian sorption of <i>n</i> -butane in BPET at 35°C. $P_{\text{sat}} = 245.8$ cmHg, $p_i = 36.8$ cmHg, $p_f = 67.5$ cmHg, $M_\infty = 0.15 \pm 0.006$ g/100g, $\bar{D} = 1.5 \pm 0.5 \times 10^{-12}$ cm ² /s.....208
Figure 5.3b	Non-Fickian sorption of <i>n</i> -butane in BPET at 35°C. $P_{\text{sat}} = 245.8$ cmHg, $p_i = 11.5$ cmHg, $p_f = 59.6$ cmHg, $M_\infty = 0.43 \pm 0.04$ g/100g, $\bar{D} = 1.3 \pm 0.4 \times 10^{-12}$ cm ² /s, $\alpha_R = 0.32 \pm 0.04$, $\tau_R = 115 \pm 5$ min., $\tau_F = 115 \pm 41$ min., $t_D = 74 \pm 9$ min.....209
Figure 5.3c	Fickian sorption of <i>n</i> -pentane in BPET at 35°C. $P_{\text{sat}} = 72.7$ cmHg, $p_i = 0$ cmHg, $p_f = 14.5$ cmHg, $M_\infty = 0.41 \pm 0.007$ g/100g, $\bar{D} = 4.8 \pm 0.8 \times 10^{-14}$ cm ² /s.....210

	Page
Figure 5.3d	Non-Fickian desorption of <i>n</i> -pentane in BPET at 35°C. $P_{\text{sat}} = 72.7 \text{ cmHg}$, $p_i = 10.4 \text{ cmHg}$, $p_f = 2.7 \text{ cmHg}$, $M_{\infty} = 0.22 \pm 0.006 \text{ g/100g}$, $\bar{D} = 5 \pm 3 \times 10^{-13} \text{ cm}^2/\text{s}$, $\alpha_R = 0.47 \pm 0.06$, $\tau_R = 389 \pm 13 \text{ min.}$, $\tau_F = 330 \pm 220 \text{ min.}$, $t_D = 145 \pm 16 \text{ min.}$211
Figure 5.4	Effect of concentration on <i>n</i> -butane and <i>n</i> -pentane diffusion coefficients in BPET at 35°C.....212
Figure 5.5	Effect of penetrant size on estimated infinite dilution, amorphous phase diffusion coefficients in PET at 25°C. The best-fit parameters of Equation 5.15 are: $\eta = 9.1 \pm 0.9$, $\tau = 5.7 \pm 1.2 \times 10^8 \text{ (cm}^2/\text{s (cm}^3/\text{mol)}^{9.1})$213
 CHAPTER 6	
Figure 6.1	Sorption isotherms of acetone (■), MEK (●), MnPK (□), and MiPK (○) in biaxially oriented PET (BPET) at 35°C as a function of pressure.....231
Figure 6.2	Sorption isotherms of acetone in biaxially oriented PET (BPET) and solvent-cast PET (SPET) at 35°C as a function of relative pressure.....232
Figure 6.3	Correlation of infinite dilution, estimated amorphous phase solubility coefficients in PET with penetrant critical temperature. For most penetrants, the data have been extrapolated to infinite dilution. For MEK, MiPK, and MnPK, the data are reported at a relative pressure of 0.1.....233
Figure 6.4	Sorption isotherms of acetone (■), MEK (●), MnPK (□), and MiPK (○) in BPET at 35°C as a function of relative pressure.....234
Figure 6.5a	Sorption isotherms of MEK and <i>n</i> -butane in BPET at 35°C as a function of relative pressure.....235
Figure 6.5b	Sorption isotherms of MnPK and <i>n</i> -pentane in BPET at 35°C as a function of relative pressure.....236

	Page
Figure 6.6a	Non-Fickian sorption kinetics of acetone in BPET at 35°C. $p_i = 0$ cmHg, $p_f = 0.9$ cmHg, $M_\infty = 0.31 \pm 0.02$ g/100g, $\overline{D} = 1.1 \pm 0.2 \times 10^{-12}$ cm ² /s, $\alpha_R = 0.21 \pm 0.04$, $\tau_R = 340 \pm 20$ min., $\tau_F = 140 \pm 30$ min, $t_D = 0$ min.....237
Figure 6.6b	Fickian sorption kinetics of MEK in BPET at 35°C. $p_i = 0$ cmHg, $p_f = 2.3$ cmHg, $M_\infty = 0.94 \pm 0.003$ g/100g, $\overline{D} = 4.4 \pm 1.8 \times 10^{-13}$ cm ² /s.....238
Figure 6.6c	Fickian sorption kinetics of MnPK in BPET at 35°C. $p_i = 0$ cmHg, $p_f = 0.3$ cmHg, $M_\infty = 0.61 \pm 0.001$ g/100g, $\overline{D} = 5.1 \pm 0.7 \times 10^{-14}$ cm ² /s.....239
Figure 6.7a	Non-Fickian desorption kinetics of MEK from BPET at 35°C. $p_i = 1.6$ cmHg, $p_f = 0$ cmHg, $M_\infty = 0.98 \pm 0.03$ g/100g, $\overline{D} = 2.3 \pm 0.4 \times 10^{-13}$ cm ² /s, $\alpha_R = 0.24 \pm 0.01$, $\tau_R = 1075 \pm 70$ min., $\tau_F = 650 \pm 160$ min., $t_D = 0$ min240
Figure 6.7b	Non-Fickian desorption kinetics of MiPK from BPET at 35°C. $p_i = 3.3$ cmHg, $p_f = 0.3$ cmHg, $M_\infty = 0.8 \pm 0.04$ g/100g, $\overline{D} = 2.5 \pm 0.4 \times 10^{-14}$ cm ² /s, $\alpha_R = 0.29 \pm 0.01$, $\tau_R = 5360 \pm 380$ min., $\tau_F = 6020 \pm 1360$ min., $t_D = 0$ min.....241
Figure 6.7c	Non-Fickian desorption kinetics of MnPK from BPET at 35°C. $p_i = 1.7$ cmHg, $p_f = 0.4$ cmHg, $M_\infty = 0.49 \pm 0.01$ g/100g, $\overline{D} = 1.9 \pm 0.3 \times 10^{-13}$ cm ² /s, $\alpha_R = 0.43 \pm 0.003$, $\tau_R = 3900 \pm 70$ min., $\tau_F = 790 \pm 330$ min., $t_D = 0$ min.....242
Figure 6.8	Effects of average concentration on apparent diffusion coefficients of acetone, MEK, MnPK, and MiPK in BPET at 35°C.....243
Figure 6.9	Effect of penetrant size on infinite dilution, estimated amorphous phase diffusion coefficients in PET at 25°C.....244

	Page
CHAPTER 7	
Figure 7.1a	Sorption isotherms of <i>n</i> -butane and <i>i</i> -butane in biaxially oriented PET (BPET) at 35°C as a function of penetrant pressure.....269
Figure 7.1b	Sorption isotherms of <i>n</i> -pentane and <i>i</i> -pentane in BPET at 35°C as a function of penetrant pressure.....270
Figure 7.2	Sorption isotherms of <i>n</i> -butane, <i>i</i> -butane, <i>n</i> -pentane, and <i>i</i> -pentane in low density polyethylene (LDPE) at 25°C.....271
Figure 7.3	Sorption isotherms of methyl acetate and ethyl acetate in BPET at 35°C as a function of penetrant pressure.....272
Figure 7.4	Correlation of infinite dilution, estimated amorphous phase solubility coefficients in PET with penetrant critical temperature. The data for methyl acetate and ethyl acetate from this study and for methyl ethyl ketone (MEK), methyl <i>i</i> -propyl ketone (MiPK), and methyl <i>n</i> -propyl ketone (MnPK) from an earlier study are reported at a relative pressure of 0.1.....273
Figure 7.5	Sorption isotherms of methyl acetate (■), ethyl acetate (●), <i>n</i> -butane (▲), <i>n</i> -pentane (◇), <i>i</i> -butane (△), and <i>i</i> -pentane (◆) in BPET at 35°C as a function of relative pressure.....274
Figure 7.6a	Sorption isotherms of methyl acetate and acetone in BPET at 35°C as a function of relative pressure. The saturation vapor pressures of methyl acetate and acetone at 35°C are 32.9 and 34.7 cmHg, respectively.....275
Figure 7.6b	Sorption isotherms of ethyl acetate and methyl ethyl ketone (MEK) in BPET at 35°C as a function of relative pressure. The saturation vapor pressures of ethyl acetate and MEK at 35°C are 14.9 and 14.2 cmHg, respectively.....276
Figure 7.7a	Fickian sorption kinetics of <i>i</i> -butane in BPET at 35°C. $p_i = 0$ cmHg, $p_f = 31.1$ cmHg, $M_\infty = 0.16 \pm 0.01$ g/100g, $\bar{D} = 1.0 \pm 0.2 \times 10^{-14}$ cm ² /s.....277

	Page	
Figure 7.7b	Non-Fickian sorption kinetics of methyl acetate in BPET at 35°C. $p_i = 2.5 \text{ cmHg}$, $p_f = 5.0 \text{ cmHg}$, $M_\infty = 0.32 \pm 0.02 \text{ g/100g}$, $\bar{D} = 6.0 \pm 1.0 \times 10^{-12} \text{ cm}^2/\text{s}$, $\alpha_R = 0.53 \pm 0.06$, $\tau_R = 240 \pm 20 \text{ min.}$, $\tau_F = 25 \pm 6 \text{ min.}$, $t_D = 32 \pm 3 \text{ min.}$	278
Figure 7.8	Effect of average concentration on apparent diffusion coefficients of linear and branched alkane hydrocarbons in BPET at 35°C.....	279
Figure 7.9	Infinite-dilution, estimated amorphous phase diffusion coefficients of linear and branched alkane hydrocarbons in PET as a function of carbon number.....	280
Figure 7.10	Effect of average concentration on apparent diffusion coefficients of methyl acetate (■) and ethyl acetate (○) in BPET at 35°C. The literature data for acetone (Δ) and MEK (▼) are included for comparison.....	281
Figure 7.11	Effect of penetrant size on infinite-dilution, estimated amorphous phase diffusion coefficients in PET at 35°C. The best-fit parameters of Equation 7.11 are $\eta = 8.4 \pm 1.0$, $\tau = 4.4 \pm 1.2 \times 10^7 \text{ (cm}^2/\text{s (cm}^3/\text{mol)}^{8.4})$	282
 CHAPTER 8		
Figure 8.1	Sorption isotherm of toluene in PET at 35°C.....	301
Figure 8.2	Correlation of infinite-dilution, estimated amorphous phase solubility coefficients in PET with penetrant critical temperature. The solubility coefficient of toluene (highlighted) is reported at an activity of 0.1.....	302
Figure 8.3a	Fickian sorption kinetics of toluene in BPET at 35°C. $p_i = 0 \text{ cmHg}$, $p_f = 0.8 \text{ cmHg}$, $M_\infty = 1.7 \pm 0.02 \text{ g/100g}$, $\bar{D} = 1.3 \pm 0.2 \times 10^{-13} \text{ cm}^2/\text{s}$	303
Figure 8.3b	Non-Fickian sorption kinetics of toluene in BPET at 35°C. $p_i = 0 \text{ cmHg}$, $p_f = 0.07 \text{ cmHg}$, $M_\infty = 0.52 \pm 0.04 \text{ g/100g}$, $\bar{D} = 4.8 \pm 0.8 \times 10^{-14} \text{ cm}^2/\text{s}$, $\alpha_R = 0.18 \pm 0.01$, $\tau_R = 775 \pm 33 \text{ min.}$, $t_D = 980 \pm 42 \text{ min.}$	304

	Page
Figure 8.4	Diffusion coefficients of toluene in PET at 35°C as a function of average penetrant concentration.....305
Figure 8.5	Correlation of infinite-dilution, estimated amorphous phase diffusion coefficients in PET with penetrant critical volume.....306
Figure 8.6	Sorption isotherm of CO ₂ in PET at 25°C.....307
Figure 8.7	Comparison of CO ₂ sorption isotherms in PET at 25°C. (●) This study (dual volume pressure decay sorption experiments), (○) This study (gravimetric sorption experiments).....308
Figure 8.8	Comparison of CO ₂ sorption isotherms on an amorphous basis in PET at 25°C. (●) This study (dual volume pressure decay sorption experiments), (○) This study (gravimetric sorption experiments).....309
Figure 8.9	Average diffusion coefficients of CO ₂ in BPET at 25°C as a function of CO ₂ pressure at the end of the experiment. The curve-fit is based on the dual mobility model (Equation 8.8).....310

CHAPTER 9

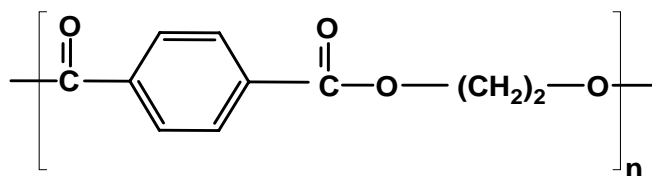
Figure 9.1	Differential Scanning Calorimetry thermograms of amorphous and solvent-crystallized PET films.....320
Figure 9.2	Wide Angle X-ray Diffraction spectra of amorphous and solvent-crystallized PET films.....321

CHAPTER 1

Introduction

1.1 Glassy Poly(ethylene terephthalate)

Poly(ethylene terephthalate) (PET) is a barrier polyester, which is widely used in food and beverage packaging applications [1-4]. It is a linear, thermoplastic glassy polymer made from terephthalic acid and ethylene glycol or dimethyl terephthalate and ethylene glycol [4]:



PET has a very useful property profile. At ambient conditions, it is strong, stiff, ductile, and tough [1]. It is used in rigid food and beverage containers due to a good balance of physical and mechanical properties, barrier properties, processibility and formability, ecological and toxicological characteristics, and economics [1]. It can be oriented by stretching during molding and extrusion, which further increases its strength, stiffness, and barrier properties [1].

Organic molecules, often of complex structure and large size, are present in foods and beverages as flavors and aromas. Natural and artificial flavor systems contain a vast number of compounds, which contribute to the overall aroma and taste of a particular food. For example, chocolate and peanut flavors each contain well over 200 flavor compounds [5]. Their concentrations are usually measurable in parts per million to parts per thousand. These compounds dissolve and diffuse in polymers, such as PET, to varying degrees. Flavor and aroma compounds are believed to follow the same principles of solution and diffusion as do gases and liquids in polymers. But they are much more

likely than light gases (*e.g.*, O₂, N₂) to interact strongly with polymers and, hence, their solubility and diffusivity can depend strongly on activity or concentration. Some important issues in flavor and aroma migration in packaging materials are [6]: (1) the capacity of the package material to sorb flavor compounds, (2) the kinetics of flavor sorption, and (3) the total loss of flavor components during the expected shelf life of the product. Sorption capacity is determined by the equilibrium solubility coefficient, whereas the rate of sorption and total loss depend on both the solubility and diffusion coefficient.

Much of the design of barrier packaging involves controlling the exchange of gaseous components (*e.g.*, O₂, CO₂) between the external environment and the internal package contents. However, flavor scalping (*i.e.*, the sorption of flavor components *into* the package walls) is also important [7,8]. Literature data on transport properties of flavor and aroma compounds in PET are extremely limited and not as extensive as the data for moisture and other light gases [8,9]. The very low diffusion coefficients of large organic flavor molecules in PET contribute to the lack of data. Low diffusion coefficients, which may be of the order of 10⁻¹⁵ cm²/s or less, coupled with typical film thicknesses (of the order of several tens of micrometers), result in experimentally inaccessible timescales to attain sorption equilibrium. If Fickian diffusion controls penetrant uptake in a polymer film of uniform thickness (whose length and width are substantially larger than the thickness), the time, t_{eq} , required to reach sorption equilibrium is [8]:

$$t_{eq} \approx \frac{\ell^2}{D} \quad (1.1)$$

where ℓ is film thickness, and D is the penetrant diffusion coefficient. Figure 1.1 shows the timescale for sorption experiments as a function of film thickness for various diffusion coefficient values. As an example, for a diffusion coefficient of 10^{-14} cm²/s and a 10 μ m thick PET film, this timescale would be approximately 3 years! To address this inherent limitation, very thin films (less than 1 μ m thick) have been used in this study.

1.2 Overview of Sorption and Transport of Small Molecules in Polymers

1.2.1 Solubility

Penetrant solubility, S , in a polymer matrix is defined as:

$$S = \frac{C}{p} \quad (1.2)$$

where C is the equilibrium concentration of penetrant dissolved in the polymer, and p is the partial pressure of penetrant in the phase contiguous to the polymer. For condensable organic vapors or liquid penetrants, partial pressure is often replaced by penetrant activity or relative pressure, p/p_{sat} , where p_{sat} is the penetrant saturation vapor pressure.

PET is a glassy polymer that typically contains significant levels of crystallinity, and the amount of crystallinity depends sensitively on the thermal processing history. Crystalline regions of most polymers preclude penetrant sorption, and the effect of crystallinity on solubility is often described using the following simple two-phase model [10]:

$$S = S_a \phi_a \quad (1.3)$$

where S_a is the amorphous phase penetrant solubility, and ϕ_a is the amorphous phase volume fraction of the polymer. Although it is widely used, this relation should be regarded as a first approximation [11]. Being a non-equilibrium glassy polymer, properties of PET, such as amorphous phase density, depend on the processing history of the polymer [12,13]. The above equation does not account for changes in the amorphous phase solubility that might accompany changes in the amorphous phase density for samples with varying levels of crystallinity. It also does not account for the trapping of amorphous regions in the crystalline regions of the polymer.

1.2.2 Effect of Penetrant Partial Pressure or Activity on Solubility

The effect of penetrant partial pressure on the penetrant concentration dissolved in the polymer matrix is qualitatively presented in Figure 1.2. The sorption of light gases in rubbery polymers is similar to the sorption of gases in low molecular weight liquids, and gas concentration in the polymer, C , often obeys Henry's law [14]:

$$C = k_D p \quad (1.4)$$

where k_D is the Henry's law constant, and p is the gas pressure in contact with the polymer.

For highly sorbing penetrants, such as organic vapors, or gases at high pressures, penetrant concentration in the polymer may deviate from Henry's law (BET III). Under these conditions, penetrant concentration in the polymer can often be satisfactorily represented by the Flory-Huggins equation [15]:

$$\ln a = \ln \phi + (1 - \phi) + \chi(1 - \phi)^2 \quad (1.5)$$

where a is penetrant activity, ϕ is the volume fraction of penetrant dissolved in the polymer, and χ is the Flory-Huggins interaction parameter.

Differences between sorption and transport properties of rubbery and glassy polymers can arise from the non-equilibrium nature of glassy polymers [16]. Unlike rubbers, which are equilibrium materials, the physical properties, including sorption and transport properties, of glassy polymers drift over time towards a seemingly unattainable equilibrium. This phenomenon is closely related to the existence of non-equilibrium excess volume in glassy polymers [16,17]. This excess volume results from the inability of the polymer chains to undergo conformation rearrangement sufficiently rapidly to attain equilibrium below the glass transition temperature.

Sorption isotherms for gases in glassy polymers are typically concave to the pressure axis at low pressure and linear at high pressures [8,9]. Such isotherms are often modeled successfully by the dual-mode model (*cf.* Figure 1.2) [17]. In this model, penetrant molecules are viewed as being partitioned between the dense equilibrium structure of the polymer (dissolved mode) and the non-equilibrium excess volume of the glassy polymer (so-called hole filling or Langmuir mode). The model is given by [18]:

$$C = C_D + C_H \quad (1.6)$$

where C is the total concentration of penetrant in the polymer, C_D is the dissolved mode penetrant concentration, and C_H is the penetrant concentration in the Langmuir mode. As shown in Figure 1.3, C_D is a linear function of pressure, and C_H is expressed as a Langmuir isotherm to give [18]:

$$C = k_D p + \frac{C_H' b p}{1 + b p} \quad (1.7)$$

where C_H' is the Langmuir sorption capacity, and b is the Langmuir affinity parameter.

Sorption isotherms of organic vapors in glassy polymers over a wide activity range may be sigmoidal in shape, exhibiting dual-mode behavior at low activities, and Flory-Huggins behavior at high activities (BET II) [19]. An inflection marks the transition from glassy to rubbery behavior. The position of the inflection is determined by the glass transition temperature of the polymer and the plasticizing effectiveness of the penetrant [19].

1.2.3 Diffusivity

Crystallites typically act as impenetrable barriers to penetrant diffusion in polymers. Michaels *et al.* described the effect of crystallinity on diffusivity as [20]:

$$D = \frac{D_a}{\tau \beta} \quad (1.8)$$

where D_a is the amorphous phase diffusion coefficient, τ is a geometric impedance factor, and β is a chain immobilization factor. Crystallites force penetrants to follow a tortuous path through amorphous regions. The geometric impedance factor, which is the ratio of the average distance traveled by a penetrant molecule in traversing a sample to the sample thickness, accounts for this effect. Crystallites can also restrict segmental mobility by acting as physical crosslinks. The chain immobilization factor accounts for this effect.

The reduction in amorphous phase chain mobility due to crystallites can be pronounced in flexible rubbery polymers such as polyethylene [21]. In glassy polymers, such as PET, the inherent rigidity of the chain backbone can impose more impedance to chain mobility than the crystallites, and β is often taken to be approximately one [20], whereas for rubbery polymers, β is greater than one. The geometric impedance factor may be a complex function of crystallite amount, shape, size, and orientation [22]. A simple empirical model describing the effect of crystallinity on impedance factor in PET is given as [20]:

$$\tau = \frac{1}{\phi_a} \quad (1.9)$$

With this result, Equation 1.8 becomes:

$$D = D_a \phi_a \quad (1.10)$$

Thus, based on this simple model, penetrant diffusivity, like solubility, is directly proportional to the polymer amorphous phase volume fraction.

In oriented glassy polymers like PET, diffusivity is also affected by orientation [23]. Hence, the effective diffusivity of an oriented, semicrystalline polymer would usually be lower than that estimated based on Equation 1.10, if D_a were taken to be the amorphous phase diffusivity of unoriented polymer. For example, oxygen permeability in PET is reduced by a factor of approximately two when an initially unoriented film is subject to 4×4 biaxial orientation [24]. The effect of orientation on sorption and

diffusion of larger molecules (*e.g.*, flavor components) in PET has not been systematically investigated.

1.3 Overview of Fickian and non-Fickian Kinetics

Penetrant diffusion through rubbery polymers is typically well described by the Fickian transport model [25]. This behavior is also observed in glassy polymers at low penetrant activity. The signature of Fickian diffusion in a thin, non-porous polymer film contacted with a penetrant is a weight increase in the polymer, due to penetrant absorption, which initially increases with square root of the contact time before approaching a fixed equilibrium value [25], as shown in Figure 1.4.

In glassy polymers, deviations from this ideal Fickian behavior are often observed. These deviations are generally believed to arise as a consequence of the finite rate of polymer structure reorganization in response to penetrant-induced swelling during the sorption-diffusion process [26]. The penetrant may sorb in the polymer in two stages, an initial Fickian-like stage followed by a protracted drift towards a final equilibrium value [27]. In another departure from Fickian sorption kinetics, the penetrant weight uptake may be a linear function of contact time until equilibrium is reached [28]. This behavior is called as ‘Case II’ sorption to distinguish it from Fickian or ‘Case I’ sorption [25,29,30]. When penetrant sorption is accompanied by significant swelling of the polymer, any time dependent resistance to changes in the volume of the polymer can lead to non-Fickian sorption kinetics. It is commonly observed when organic vapors sorb into glassy polymers [29]. As the penetrant swells the polymer, local stresses are built up

when the chains disentangle from each other. These stresses can be quite high, and can, in fact, cause mechanical failure in the polymer [31]. Two examples of non-Fickian sorption kinetics are shown in Figure 1.5.

If the polymer chains do not deform significantly upon penetrant sorption or if the chains reorganize very quickly relative to the rate of penetrant diffusion, Fickian behavior is observed [32]. Between the bounds of no response and infinitely fast response by the polymer chains to the presence of penetrant molecules, there is a regime where the rates of polymer deformation and swelling to accommodate the penetrant molecules and rate of penetrant diffusion occur over similar timescales. Non-Fickian behavior is commonly understood to occur in this regime.

1.4 Goals and Organization of This Research

As discussed earlier, sorption and transport properties of flavor molecules in PET are important considerations in flavor scalping, carryover, and contamination. Several examples of common flavor and aroma compounds are provided in Table 1.1. The major roadblock to obtaining this information is the extremely long experimental timescales with conventional polymer samples. These considerations lead to the following question:

Based on experimental data for lower molecular weight “model” flavor molecules, is it possible to estimate sorption and transport properties of large flavor molecules in PET?

There is some indication that it may be possible to develop systematic correlations for solubility and diffusivity in PET. For example, the logarithm of infinite dilution, amorphous phase solubility in rubbery and glassy polymers increases approximately

linearly with critical temperature, as demonstrated in the literature for PET [9]. The infinite dilution, amorphous phase diffusion coefficients decrease strongly with increasing penetrant size, as characterized by penetrant critical volume. In this case, a simple empirical power law model was used to describe the data for PET [9]. These experimental results suggest that sorption and transport properties of large flavor molecules in PET can be estimated, albeit crudely, based on their critical properties. However, the penetrants included in the solubility and diffusivity correlation plots based on available literature data [9] do not include even low molecular weight analogs of many classes of flavor and aroma compounds.

There is a need to develop a more systematic database of sorption and transport properties of organic molecules in PET to better understand effects of penetrant size, shape, and polarity on solubility and diffusion coefficients of such molecules. Apart from filling a significant void in the literature, these results would provide a valuable database for quantifying the effects of penetrant backbone length, branching, and chemical structure on transport properties of large flavor molecules in PET.

This research project focused on an experimental study of sorption and transport of large organic molecules (model flavor molecules) in PET. The difficulty of very long experimental timescales has been addressed by using extremely thin (less than 1 μm thick) biaxially-oriented PET (henceforth referred to as BPET) films. The use of such thin, uniform films permits the study of sorption and transport of large penetrants over experimentally-accessible timescales.

Current experimental techniques in our laboratory are limited to the sorption study of gases and volatile (or high vapor pressure) organic liquids in polymers. The vapor pressures of several classes of flavor compounds are extremely low. For example, vapor pressures of *d*-limonene, benzyl alcohol, and benzaldehyde at 25°C are 1.5, 0.1, and 1.3 mmHg, respectively [33]. Hence, there is a need to develop experimental tools for measuring solubility and diffusivity of low volatility organic liquids in polymers over a wide range of activity. The latter part of this research project focused on developing an experimental technique for this purpose, and it represents one of the very few techniques [34-37] of its kind for studying sorption and transport properties of low volatility organic liquids at low activity in a barrier polymer like PET.

This dissertation comprises nine chapters, including this introductory chapter, which provides background information, underlying motivation, and overall goals of this research. Chapter 2 provides a broad overview of various types of barrier polymers and structures, their permeability characteristics (including the underlying principles involved), measurement techniques, methods to predict and improve barrier properties, and current as well as potential future applications for barrier polymers. This chapter is adapted from a review paper published in the Encyclopedia of Polymer Science and Technology.

Chapter 3 describes the biaxially oriented polyester films used in this research project. The films were characterized using differential scanning calorimetry, wide-angle X-ray diffraction, positron annihilation lifetime spectroscopy, and other techniques. The experimental procedures and characterization results are described in this chapter. This

chapter also describes the low-pressure gravimetric sorption technique and high-pressure dual volume pressure decay sorption technique used for collecting the data presented in Chapters 5, 6, 7, and 8 of this dissertation.

Chapter 4 describes a new experimental technique for kinetic gravimetric sorption of low volatility (or highly condensable) gases and organic vapors in polymers over a wide range of activity. Sorption and transport data for toluene vapor in poly(dimethyl siloxane) at 25°C are provided to illustrate the method. Penetrants with vapor pressures as low as 10^{-7} mmHg might be studied using this new technique, as compared with traditional gravimetric sorption methods (such as the one described in Chapter 3) that have only been used for studying penetrants with vapor pressures as low as 0.1 mmHg.

Chapter 5 describes results from a kinetic gravimetric sorption study of linear alkane hydrocarbons in BPET films at 35°C. The solubility and diffusivity data for *n*-butane and *n*-pentane in 0.9 μm BPET films are presented. *n*-Pentane has higher solubility and lower diffusivity than *n*-butane, consistent with critical temperatures and critical volumes of these penetrants. The infinite dilution, amorphous phase solubility of *n*-butane in semicrystalline BPET is approximately two times higher than that in microtomed, amorphous PET (APET) [9] primarily due to the presence of higher non-equilibrium excess volume in BPET.

Chapter 6 presents results from a kinetic gravimetric sorption study of four linear and branched ketones, namely acetone, methyl ethyl ketone (MEK), methyl *n*-propyl ketone (MnPK), and methyl *i*-propyl ketone (MiPK), in BPET films at 35°C. The

diffusion coefficients and equilibrium solubility at fixed relative pressure decrease in the following order:

acetone > MEK > MnPK > MiPK.

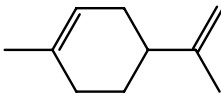
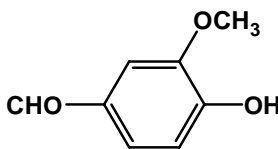
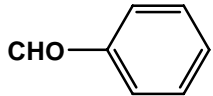
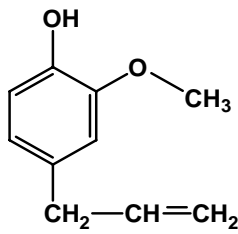
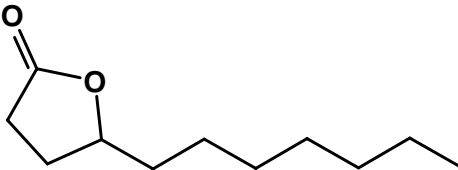
Solubility of polar ketones in BPET is approximately two times higher than that of non-polar alkanes having the same number of carbon atoms and a similar carbon skeleton.

Chapter 7 presents results from a kinetic gravimetric sorption study of two branched alkane hydrocarbons, *i*-butane and *i*-pentane, and two linear esters, methyl acetate and ethyl acetate, in BPET films at 35°C. The equilibrium solubility of *i*-butane and *i*-pentane is lower than that of the corresponding linear alkanes (presented in Chapter 5), most likely due to restricted access of the branched penetrants to the non-equilibrium excess volume of PET. Interestingly, the solubility difference between *n*-pentane and *i*-pentane is approximately 10 times higher in PET than in low density polyethylene (LDPE). At constant relative pressure, the solubility of methyl acetate is higher than that of ethyl acetate, consistent with solubility trends of esters in other polymers and polar liquids, and the solubility of esters in PET is higher than that of ketones having the same number of carbon atoms. Surprisingly, the diffusion coefficients of esters (methyl acetate and ethyl acetate) are quite similar to those of ketones (acetone and methyl ethyl ketone) with the same number of carbon atoms despite the esters being somewhat larger than the ketones. This result suggests that penetrant diffusion coefficients in PET, which are primarily dependent on penetrant size and shape, are influenced by polarity effects as well.

Chapter 8 presents equilibrium solubility and diffusivity values of toluene vapor in BPET films at 35°C using the new experimental technique described in Chapter 4. This chapter also presents a comparison of CO₂ sorption in BPET films at 25°C and pressures up to approximately 10 atm with literature data for thicker PET films. Diffusion coefficients of CO₂ in BPET obtained from low-pressure (less than 1 atm) gravimetric sorption experiments have also been presented. The so-called dual mobility model was used to estimate CO₂ permeability coefficients in BPET. On an amorphous basis, the estimated CO₂ solubility and permeability coefficients in the 0.9 μm BPET films are in good agreement with some literature values for much thicker films.

The solubility and diffusivity correlation plots, previously reported by Serad *et al.* [9], appear in chapters 5, 6, 7, and 8, with the data from each chapter being progressively added to these plots. Finally, chapter 9 summarizes the results from this research and provides recommendations for future work in this area.

Table 1.1 List of some common flavor and aroma compounds

Flavor/Aroma	Chemical Structure
<i>d</i> -Limonene	
Vanillin	
Benzaldehyde	
Eugenol	
Undelactone	
Methyl Octanoate	$\text{CH}_3(\text{CH}_2)_6-\overset{\text{O}}{\parallel}{\text{C}}-\text{OCH}_3$
Linalool	$\text{CH}_3-\overset{\text{CH}_3}{\underset{ }{\text{C}}}=\text{CH}-\text{CH}_2-\text{CH}_2-\overset{\text{CH}_3}{\underset{\text{OH}}{ }{\text{C}}}-\text{CH}=\text{CH}_2$

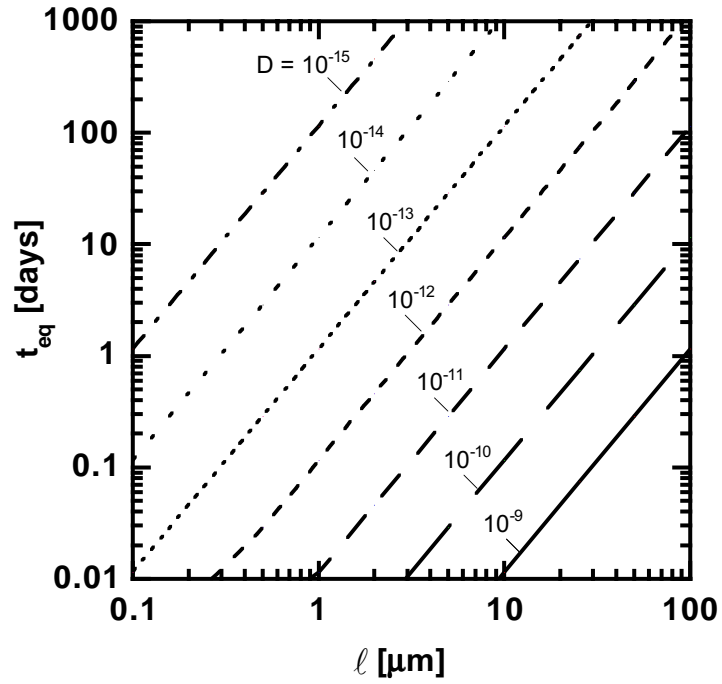


Figure 1.1 Timescale for sorption experiments based on Fickian diffusion. Diffusion coefficients are expressed in cm^2/s .

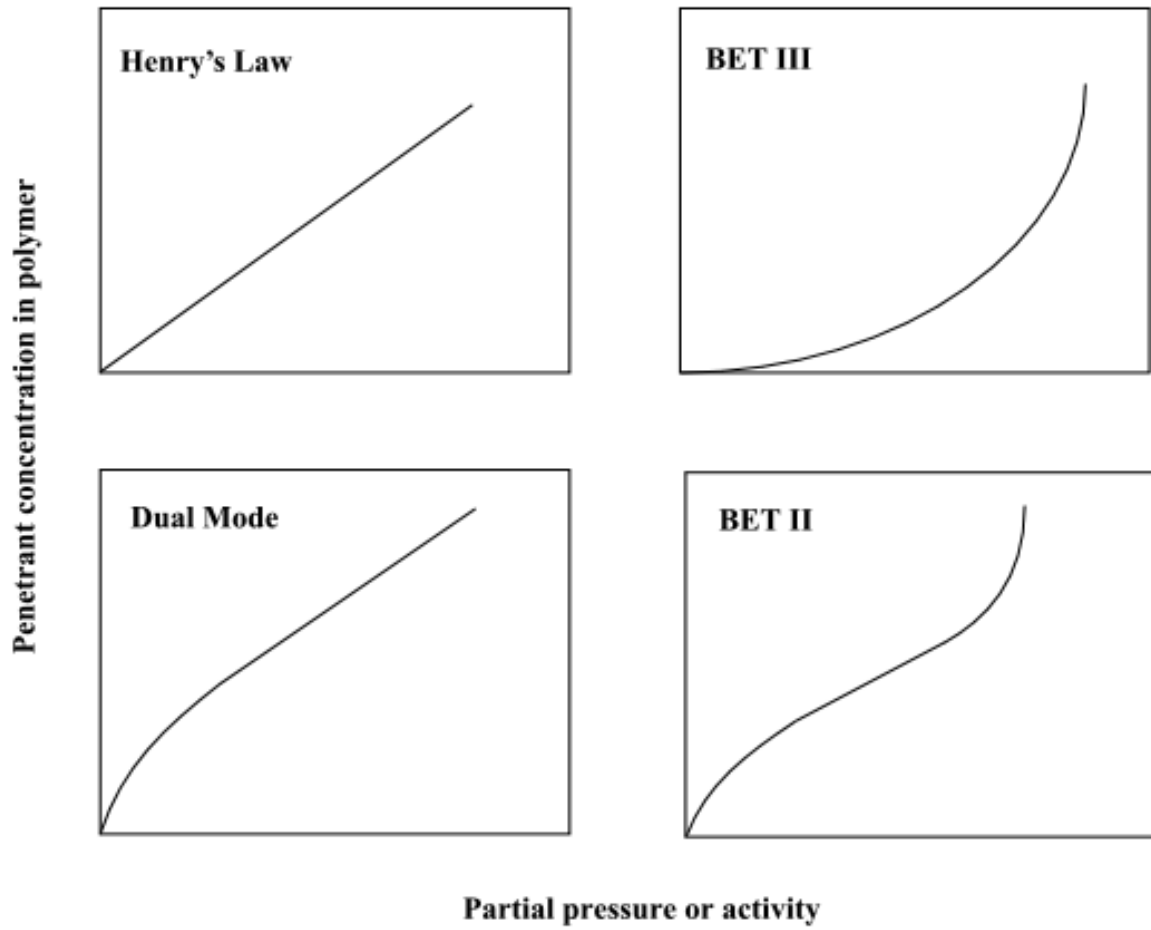


Figure 1.2 Effect of penetrant partial pressure on the concentration of penetrant dissolved in polymer matrix [14].

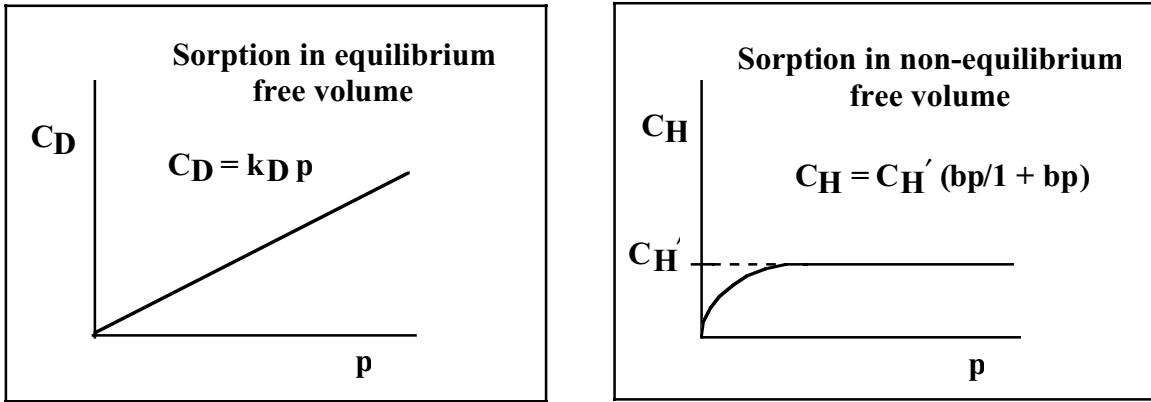


Figure 1.3 Effect of penetrant partial pressure on penetrant concentration in the two modes of sorption postulated by the dual-mode model for glassy polymers [17].

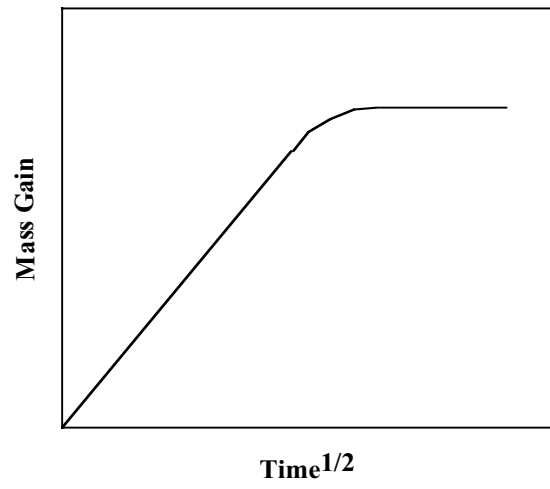


Figure 1.4 An example of Fickian sorption kinetics [25].

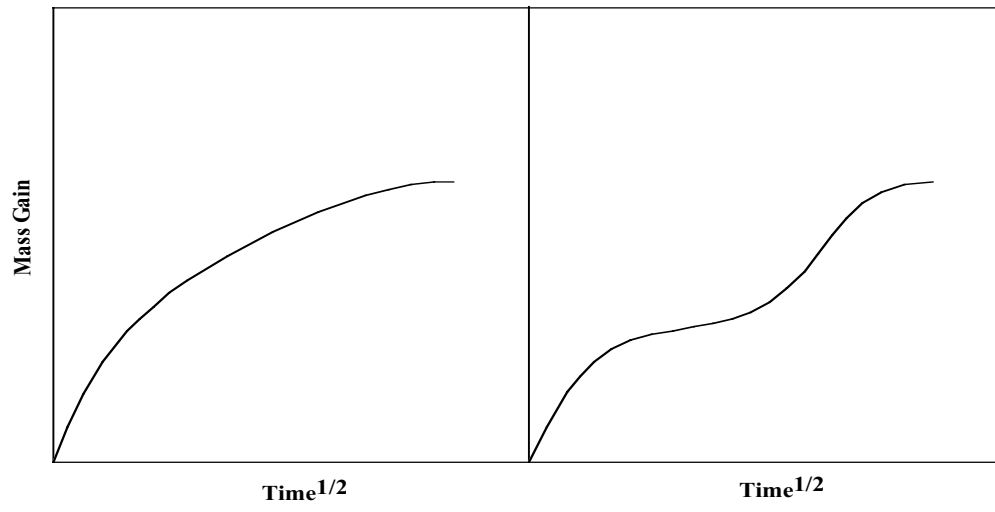


Figure 1.5 Two examples of non-Fickian sorption and desorption kinetics.

CHAPTER 2

Barrier Polymers

This chapter has been adapted with permission from a review article published under the same title in *Encyclopedia of Polymer Science and Technology*, 3rd ed., v.5, pp. 198-263, 2003. Copyright© 2003 John Wiley & Sons.

2.1 Summary

Although broadly defined as a macromolecule having the ability to restrict the passage of gases, vapors, and liquids, the definition of a barrier polymer varies from application to application and a material that provides sufficient barrier for a particular end use can be considered to be a barrier polymer. They are widely used in food, beverage, and other packaging industries. Some of the advantages that they offer over traditional packaging materials like glass, paper, and metals are flexibility, light weight, toughness, versatility, and printability. However, unlike glass and metals, no polymer offers an infinite gas barrier. Combinations of different polymers, or polymers with inorganic materials, in the form of multilayer structures or blends, can provide sufficient barrier for the intended shelf life of most products. Inorganic materials such as silicon & aluminum oxides and nanoclays can significantly enhance barrier and other mechanical properties of polymers. Other approaches for improving barrier properties such as oxygen-scavenging systems have also received considerable attention in recent years. This chapter discusses various types of barrier polymers and structures, their permeability characteristics (including the underlying principles involved), measurement techniques, ways to predict and improve barrier properties, and current as well as potential future applications for barrier polymers.

2.2 Introduction

Barrier polymers can be broadly defined as macromolecules having the ability to significantly restrict the passage of gases, vapors, and liquids. Since all polymers restrict the transport of penetrants to some degree and the barrier performance of polymers to different penetrants depends on a variety of factors, it is difficult to provide a concise, objective definition. In a practical sense, however, the definition of a barrier polymer depends upon the end use requirements, and a material that provides sufficient barrier for a particular application can be considered to be a barrier polymer for that purpose. In the present discussion, polymers that have resistance to transport of gases, vapors, and liquids as one of their key attributes will be considered to be barrier polymers.

Polymers have found wide acceptance as alternatives to traditional materials like glass, paper, and metals, in food, beverage, and other packaging industries. A key characteristic of glass and metals as packaging materials is their total barrier to transport of gases and vapors. While polymers can provide an attractive balance of properties such as flexibility, toughness, light weight, formability, and printability, they do allow the transport of gases and vapors to some extent. Unfortunately, an inexpensive, recyclable polymeric material possessing high barrier properties to every gas or vapor in addition to good mechanical, thermal, and optical properties is not available. For this reason, the selection of a barrier polymer for a particular application typically involves tradeoffs between permeation, mechanical, and aesthetic properties as well as economic and recycling considerations. Additionally, there is an ongoing interest in optimizing property

sets of barrier polymers to provide an efficient and economical method for packaging and for extending the shelf life of packaged foods and beverages.

This chapter discusses various types of barrier polymers and structures, their permeability characteristics and the underlying phenomena involved, measurement techniques, ways to predict and improve barrier properties, and current as well as potential future applications for barrier polymers.

2.3 Fundamentals of Permeation in Polymers

The permeability coefficient, or simply permeability, characterizes the steady state rate of mass transport of penetrant molecules through polymers. In a dense polymer film, the permeability, P , is defined as the molar flux of penetrant through the polymer relative to a fixed coordinate system, N_A , normalized by the film thickness, L , and the difference between the upstream (p_2) and downstream (p_1) partial pressures [14]:

$$P = \frac{N_A L}{(p_2 - p_1)} \quad (2.1)$$

Accordingly, permeability has dimensions of quantity of penetrant (either mass or moles) times thickness divided by area, time, and pressure. Several units have been used to report permeability of gases and water vapor in the literature. In the US, a commonly used unit for permeability of gases in barrier polymers is $\text{cm}^3(\text{STP}) \text{ mil}/(100 \text{ in}^2 \text{ day atm})$. Table 2.1 provides conversion factors for several permeability units, including the SI unit $\text{mol m}/(\text{m}^2 \text{ s Pa})$, which is typically preferred in technical encyclopedias.

The steady-state transport properties of water vapor in barrier polymers are characterized by water vapor transmission rate (WVTR). The dimensions of WVTR are quantity of water transmitted through a film times thickness divided by area and time, and a common unit for WVTR is gm mil/(100 in² day). Table 2.2 provides conversion factors for some WVTR units, including the SI unit mol m/(m² s). WVTR can be converted to water vapor permeability by dividing by the water partial pressure difference (which can be calculated from the specified relative humidity and temperature).

Penetrant transport through polymers is described by the so-called solution-diffusion model [14]. According to this model, permeation through a flat sheet or film occurs in three steps: penetrant dissolves into the upstream (*i.e.*, the high partial pressure or high thermodynamic activity) side of the film, diffuses through the film, and desorbs from the downstream (*i.e.*, the low partial pressure or low thermodynamic activity) side of the film. The rate-limiting step in this process is diffusion through the film. In one dimension, penetrant diffusion through a polymer typically follows Fick's law:

$$N_A = -D \frac{dC}{dx} \quad (2.2)$$

where D is the effective diffusion coefficient for the penetrant in the polymer and dC/dx is the local concentration gradient of the penetrant.

When the downstream side penetrant partial pressure and concentration are negligible relative to those on the upstream face of the film, using the Fick's law of diffusion (Equation 2.2), permeability can be expressed as product of the effective diffusion coefficient, D, and the solubility coefficient, S, which is the ratio of the

equilibrium penetrant concentration in the polymer at the upstream side of the film divided by the penetrant partial pressure or activity in the contiguous phase [14]:

$$P = D \times S \quad (2.3)$$

According to Equation 2.2, the diffusion coefficient is a kinetic term characterizing the mass flux of penetrant through a polymer film in response to a concentration gradient [14]. Diffusion coefficients have units of (length)²/time, and are often expressed in cm²/s. The solubility or partition coefficient is a thermodynamic factor that links the equilibrium penetrant concentration in the polymer, C , with the penetrant partial pressure contiguous to the polymer surface, p [14]:

$$C = S \times p \quad (2.4)$$

When the penetrants of interest are vapors, liquids, or solids, the partial pressure is often replaced by penetrant activity. For an ideal gas, penetrant activity is equal to the ratio of penetrant partial pressure to its saturation vapor pressure [14]. For non-ideal systems thermodynamic models must be used to estimate penetrant activity [38].

The diffusion process of penetrants in polymers can be broadly classified into two categories, Fickian (which obeys the Fick's law of diffusion), and non-Fickian. Penetrants in rubbery polymers and at low activities in glassy polymers typically exhibit Fickian behavior [39]. The signature of Fickian diffusion in a thin polymer film contacted on both faces with a constant partial pressure (or activity) of penetrant is a weight increase due to penetrant absorption that is initially a linear function of the square root of the contact time and then asymptotically approaches a fixed equilibrium value [39]. For Fickian diffusion-controlled kinetics of penetrant transport in a plane film whose

thickness (ℓ) is much smaller than its width or length, the time required to reach steady state in a permeation experiment, t_{ss} , is given by [39]:

$$t_{ss} = \frac{\ell^2}{D} \quad (2.5)$$

The diffusion coefficients of large penetrants (*e.g.*, flavor and aroma compounds) in barrier polymers, which can be of the order of 10^{-14} cm²/s or less, coupled with a typical film thickness of 10 μ m result in extremely large timescales (over 3 years) to reach steady state transport. Hence, over the shelf life of packaged products (typically of the order of several months), flavor and aroma compounds may never achieve equilibrium or steady state conditions. In such cases, the steady-state permeability does not provide sufficient information to predict package shelf life. As discussed later, more detailed knowledge of penetrant solubility and diffusivity is required to accurately predict migration of such compounds.

In glassy polymers, deviations from Fickian behavior can occur. These deviations are generally believed to arise as a consequence of the finite rate of polymer structure reorganization in response to penetrant-induced swelling during the sorption-diffusion process [26]. An example of so-called non-Fickian diffusion behavior is the penetrant sorbing into the polymer in two stages, an initial Fickian-like stage followed by a protracted, slow drift towards the final equilibrium sorption value [27]. In such cases, the time required to achieve steady state transport may be much higher than that predicted based on Equation 2.5. This type of diffusion behavior is often observed when organic vapors at relatively high activity sorb into amorphous glassy polymers [29]. For example,

toluene vapors exhibit Fickian diffusion behavior in amorphous poly(vinyl chloride) (PVC) films at activities up to 0.4 and show increasingly non-Fickian behavior at higher activities [40].

2.4 Mechanism of Penetrant Transport in Dense Polymers

The rate limiting step for penetrant diffusion is the creation of transient “gaps” in the polymer matrix *via* local scale polymer segmental dynamics involving several polymer chains [41]. Penetrant molecules vibrate inside local cavities in the polymer matrix at frequencies much higher than the frequency of polymer chain motion required to open a gap of sufficient size to accommodate the penetrant. These steps are shown schematically in Figure 2.1. In Figure 2.1a, a penetrant molecule is shown dissolved in a polymer matrix. The penetrant vibrates inside a gap or molecular scale cavity in the polymer matrix at very high frequency (*ca.* 10^{12} vibrations/sec or 1 vibration per picosecond) [41]. The polymer molecules do not occupy the entire volume of the polymer sample. Due to packing inefficiencies and polymer chain molecular motion, some of the volume in the polymer matrix is empty or “free” and this so-called free volume is redistributed continuously as a result of the random, thermally stimulated molecular motion of the polymer segments [14].

In Figure 2.1b, local polymer segmental motion has opened a connecting channel between two free volume elements in the polymer matrix and the penetrant molecule can, as a result of its own Brownian motion, explore the entire corridor between the initial free volume element which it occupied and the second free volume element which is

connected to it *via* the opening of a transient gap in the polymer matrix. Eventually, local segmental motion of the polymer segments closes the connection between the two free volume elements and if the penetrant happens to be away from its original position, as shown in Figure 2.1c, when the gap in the polymer matrix is closed, the penetrant will be trapped in another free volume element in the polymer matrix and will have executed a diffusion step. The process shown in Figure 2.1 has been called the “Red Sea” mechanism of penetrant transport in polymers [41].

Figure 2.2 shows a cartoon of two polymer chains undergoing coordinated local segmental motion as a result of random, thermally-stimulated movements of the polymer chains to open a gap between the polymer chains of sufficient size to permit passage of a penetrant molecule from one free volume element to another [42]. This cartoon emphasizes that the polymer segmental motion is the rate-controlling step in penetrant diffusion.

Figure 2.3 provides a very simplistic cartoon of the molecular processes involved in the local segmental motions of polymers that contribute to the formation of transient gaps in the polymer matrix important for penetrant diffusion. This figure shows what is believed to be a typical example of intramolecular cooperative local segmental motion of the polymer backbone of a polyethylene chain. This so-called crankshaft motion requires the cooperation of several adjacent ethylene units and can act to create gaps in the polymer matrix of sufficient size to accommodate small penetrant molecules. It should be emphasized that the detailed understanding of the molecular level motions in polymers that contribute to diffusion is evolving rapidly as a result of more detailed atomistic

simulation of penetrant transport in polymers. As a result, more realistic descriptions of the important molecular processes for penetrant diffusion in polymers should be expected in the near future.

The motion of polymer segments to produce a gap of sufficient size to accommodate a penetrant molecule is much slower than the vibration of the penetrant in a gap in the polymer matrix. For example, Hofman's computer simulations of oxygen diffusion in a polyimide reveal that the oxygen molecules execute a diffusion step approximately once every nanosecond ($1000\text{ps}=1\text{ns}$) [43]. The rate of production of gaps of sufficient size to accommodate penetrant molecules decreases with increasing size of the penetrant. That is, there are fewer gaps produced per unit time in a polymer matrix of sufficient size to accommodate methane (kinetic diameter= 3.8\AA), for example, than there are for hydrogen (kinetic diameter= 2.89\AA).

Fried *et al.* report computer simulation results of diffusion in poly(2,6-dimethyl-1,4-phenylene oxide) (PPO). Figures 2.4 and 2.5 present their results of the displacement of an oxygen molecule and a nitrogen molecule, respectively, as a function of time. There is about 1 diffusion jump for oxygen (kinetic diameter= 3.46\AA) every 300-350 picoseconds but only 1 diffusion step for nitrogen (kinetic diameter= 3.64\AA) over the entire 1000 picosecond duration of the computer simulation [44]. The oxygen molecule spends most of its time rattling within a small cage (or free volume element) with average displacements of the order of 2\AA or so. The diffusion jumps occurring approximately every 300-350 ps involve displacements of the oxygen atom of the order of $4\text{-}5\text{\AA}$. As shown in Figure 2.5, the diffusion jump length for nitrogen is longer (approximately

10Å) and the jumps occur less frequently. However, these results are obtained for very short periods of time due to computational limitations, and very long simulations would be required to generate precise estimates of jump lengths and jump frequencies. Due to the extremely demanding computational resources required for such molecular-level simulations, they are only now becoming possible for small molecule migration in relatively permeable polymers. As yet, computers are not fast enough to provide realistic simulations of phenomena such as migration of large flavor molecules in high barrier polymers.

2.5 Factors Affecting Permeability, Diffusivity, and Solubility

2.5.1 Free Volume

The dependence of penetrant transport properties on chain packing in polymers is often described using correlations involving the fractional free volume (FFV) of polymers. FFV is the fraction of volume in a polymer that is available to assist in penetrant transport. FFV does not include volume occupied by polymer molecules and volume in the polymer matrix that is otherwise unavailable for penetrant transport. FFV is often estimated using group contribution methods. One popular method for estimating FFV is based on the following expression [14]:

$$FFV = \frac{V - V_o}{V} \quad (2.6)$$

where V is the polymer specific molar volume, and V_o is the so-called occupied volume that is not available to assist in penetrant transport. The occupied volume is usually estimated by Bondi's method as follows [45]:

$$V_0 = 1.3 V_w \quad (2.7)$$

where V_w is van der Waals volume of the molecule. A good estimate of V_w can be obtained from bond radii, van der Waals radii of constituent atoms, and geometric factors. Bond radii are nearly constant from one molecule to another since the same chemical bond will always have the same radius. The most complete list of V_w values is available in the compilation by van Krevelen [46]. The dependence of diffusion coefficients on FFV can be expressed as [47]:

$$D = A \exp\left(\frac{-B}{FFV}\right) \quad (2.8)$$

where A and B are empirical constants. The higher the FFV, the larger the diffusion coefficient. Figure 2.6 shows the effect of free volume on gas diffusion coefficients in a series of substituted polysulfones [48].

The dependence of solubility on FFV is usually weaker than that of diffusivity especially in amorphous polymers [22]. Therefore, permeability often follows a similar dependence on free volume as penetrant diffusivity. Attempts have been made to correlate FFV of polymers with gas permeability [49,50]. As shown in Figure 2.7 [49], a nearly linear correlation was found to exist between the logarithm of oxygen permeability coefficients and the inverse of FFV in several families of amorphous, glassy polymers and high barrier liquid crystalline polymers. Many barrier polymers are glassy materials, since their use temperature is below their glass transition temperature. In glassy polymers, which are non-equilibrium materials, free volume can be altered to some extent by the processing history of the sample [51]. For instance, higher rates of cooling create

higher free volume in the glassy state, and *vice versa*. A more effective way to alter free volume is to vary the chemical structure by, for example, adding or removing pendant groups on the polymer backbone [51]. The presence of polar groups with low specific volumes can reduce the free volume (and hence, penetrant diffusion coefficients) by facilitating more efficient packing of the polymer chains due to stronger interactions between them [51]. For example, barrier polymers like polyacrylonitrile (PAN) and poly(vinyl alcohol) (PVOH) have polar pendant groups, which lead to strong energetic interactions between the polymer chains, efficient polymer chain packing, low free volume and, in turn, low permeability coefficients.

Free volume in polymers can be measured using probes such as electrochromic, photochromic, and fluorescent probes, as well as xenon nuclear magnetic resonance, small angle X-ray scattering, density measurements, and positron annihilation lifetime spectroscopy (PALS) [52]. Each method has its strengths and limitations, and a simple, direct measure of FFV is not available. The PALS technique has, however, emerged in the past several years as a valuable non-destructive probe of free volume in polymers [52,53]. PALS uses orthoPositronium (oPs) as a probe of free volume in the polymer matrix. oPs resides in regions of reduced electron density, such as free volume elements, that typically range in radius from 0.2 to 0.4 nm. This range of cavity radii compares well with non-bonded interatomic distances in polymers and molecular radii of diffusing penetrants [52]. PALS permits an estimate of both the size and concentration of free volume elements in the polymer matrix. Transport properties of barrier polymers,

copolymers, and polymer blends have been well correlated with FFV as measured by PALS [52-58].

2.5.2 Temperature

The temperature dependence of permeability and diffusivity are usually modeled using Arrhenius equations of the following forms [14]:

$$P = P_o \exp\left(\frac{-E_p}{RT}\right) \quad (2.9)$$

$$D = D_o \exp\left(\frac{-E_D}{RT}\right) \quad (2.10)$$

where E_p and E_D are activation energies for permeation and diffusion, and P_o and D_o are pre-exponential factors. The effect of temperature on solubility is usually expressed by a van't Hoff relationship [14]:

$$S = S_o \exp\left(\frac{-\Delta H_s}{RT}\right) \quad (2.11)$$

where S_o is a pre-exponential factor, and ΔH_s is the heat of sorption of penetrant in the polymer. Since steady-state permeability is the product of diffusivity and solubility, the activation energy of permeation can be defined as the sum of activation energy of diffusion and the heat of sorption [14]:

$$E_p = E_d + \Delta H_s \quad (2.12)$$

E_d is always positive, and ΔH_s can be positive or negative for light gases (such as H_2 , O_2 , N_2 *etc.*) as well as larger, more soluble penetrants (such as C_3H_8 , C_4H_{10} *etc.*). For polymers like low density polyethylene (LDPE) and poly(vinyl chloride) (PVC), E_p is

always positive [14]. Therefore, permeability increases with increasing temperature. To illustrate this behavior, Figure 2.8 shows the effect of temperature on oxygen permeability of four widely used barrier polymers [6].

As noted above, penetrant diffusion through polymers is an activated process. At temperatures far from the transition temperatures (*e.g.*, glass transition temperature, melting point, *etc.*) the Arrhenius relationship (Equation 2.10) is obeyed, and with a known activation energy of diffusion, E_D , the diffusion coefficient of a penetrant in a polymer can be estimated at any temperature. In cases where E_D is not reported, it can be estimated using a known correlation, reported by Barrer [59] and van Amerongen [60], between D_0 and E_D :

$$\ln D_0 = a \frac{E_D}{RT} - b \quad (2.13)$$

where a and b are independent of penetrant type. The parameter a is independent of polymer type and has a universal value of 0.64 [61]. b has a value of 9.2 ($-\ln(10^{-4} \text{ cm}^2/\text{s})$) for rubbery polymers (*i.e.*, polymers above their T_g) and 11.5 ($-\ln(10^{-5} \text{ cm}^2/\text{s})$) for glassy polymers (*i.e.*, polymers below their T_g) [46]. Equation 2.13 is often referred to as a "linear free energy" relation. Similar relations between D_0 and E_D are observed for viscosity of organic liquids, molten salts, and metals [62] and for first order chemical reaction kinetics [63], which are also activated processes described by the Arrhenius equation. Additionally, common barrier polymers such as poly(ethylene terephthalate) (PET) and polycarbonate (PC) are known to follow this relation both above and below the glass transition temperature, as shown in Figure 2.9 [7]. Combining Equations 2.10 and 2.13 gives:

$$D = \exp\left[-b - (1-a)\frac{E_D}{RT}\right] \quad (2.14)$$

Based on a single value of the diffusion coefficient at one temperature, E_D can be estimated from Equation 2.14. This equation can then be used to estimate the diffusion coefficient at other temperatures, provided that the two temperatures do not traverse thermal transitions (such as glass transition) and the polymer morphology is otherwise unchanged.

2.5.3 Chemical Structure

The presence of polar groups on or in polymer chains often increases chain rigidity, which can increase glass transition temperature and improve mechanical properties, and increases packing density [14]. Conventional barrier polymers like PAN have very low gas permeability as a result, in part, of restricted chain mobility due to the presence of polar groups. Polymer chain interactions can be quantified in terms of cohesive energy density (CED), and CED has a strong influence on penetrant diffusion. CED of a polymer is the square of its solubility parameter and characterizes the strength of attraction (or interactions) between the polymer chains. It can be estimated using group contribution techniques [46]. In a simple model of penetrant diffusion in polymers, due to Meares, the activation energy for diffusion is directly proportional to the CED of a polymer [64]. Based on this model and the linear free energy relation [65], the logarithm of penetrant diffusion coefficients should decrease linearly with increasing CED. Solubility of relatively non-polar penetrants usually has a weaker dependence on CED

than diffusivity, and hence, the logarithm of permeability should decrease linearly with increasing CED. As shown in Figure 2.10, a nearly linear correlation was found between oxygen permeability and CED of barrier polymers with permeability values ranging over 5 orders of magnitude [66,67].

Penetrant diffusivity, and hence permeability, can also be decreased by adding substituents to the polymer chain that reduce chain flexibility. Bulky side groups or rigid linkages such as aromatic groups decrease chain flexibility and hence, reduce penetrant diffusion coefficients. Flexible linkages, such as ether or methylene groups, produce the opposite effect [14]. Several methods are used to characterize chain flexibility [14]. The glass transition temperature is a measure of long range or bulk molecular motion, and high T_g materials are usually rigid and inflexible. Sub- T_g relaxations are another indication of molecular motion and correlations of O_2 and CO_2 permeability with sub- T_g relaxations have been observed within a family of amorphous polyesters and copolyesters [68]. However, the exact nature of molecular motions which control penetrant diffusion are complex and unclear, and hence T_g and sub- T_g relaxations do not, in general, provide predictive correlations with penetrant diffusivity [14].

Changes in molecular structure of the polymer often affect more than one factor influencing permeability and the net effect can be difficult to anticipate. For example, addition of bulky side groups can stiffen the polymer chains, which is expected to reduce the diffusion coefficients. However, the same modification could also decrease chain packing in the amorphous phase and reduce the level of crystallinity in the polymer,

which are expected to increase the diffusion coefficients [20]. The net result of these competing effects can be difficult to predict *a priori*.

2.5.4 Crystallinity

Increasing crystallinity in a polymer generally decreases gas permeability [22]. Crystallinity influences both solubility and diffusion coefficients. For most polymers and penetrants of interest, crystalline regions, which are much more dense and well-ordered than amorphous regions, preclude penetrant sorption, thereby reducing penetrant solubility. Additionally, the presence of impermeable crystallites in a polymer matrix act as barriers to diffusion, increasing the path length for diffusion and, in some cases, increasing chain rigidity, which also reduces diffusion coefficients [22]. Whereas crystallite size, shape, and orientation do not usually influence solubility in polymers significantly, these factors can be important in penetrant diffusion. Michaels *et al.* expressed the effect of crystallinity on penetrant diffusion using the following model [20]:

$$D = \frac{D_a}{\tau\beta} \quad (2.15)$$

where D_a is the penetrant diffusion coefficient in the amorphous polymer, τ is a geometric impedance (*i.e.*, tortuosity) factor, and β is a chain immobilization factor. Impermeable crystalline regions force penetrants to follow a tortuous pathway through the permeable amorphous regions. This effect is captured by the factor τ , which is the

ratio of the average distance traveled by a penetrant molecule to the thickness of the sample [20]. τ can be a complex function of crystalline content as well as crystallite size, shape, and orientation [22,69]. Crystallites can also restrict segmental mobility by acting as physical crosslinks. This effect is taken into account by the factor β and is generally more pronounced in flexible rubbery polymers such as PE. In glassy polymers such as PET, the inherent rigidity of the chain backbone imposes more impedance to chain mobility than the crystallites and hence, β is one [22].

A two-phase model is often used to describe penetrant solubility in a semicrystalline polymer [10]:

$$S = S_a \phi_a \quad (2.16)$$

where S_a is solubility coefficient in the amorphous regions of the polymer, and ϕ_a is amorphous phase volume fraction. This model assumes that the solubility of the crystalline regions is zero, and that the presence of crystallites does not change the amorphous phase solubility coefficient. For polymers used in barrier packaging applications, the assumption of zero solubility in the crystalline regions is generally accurate [70]. The second assumption that the amorphous phase solubility is independent of crystalline content is not necessarily obeyed, particularly in glassy polymers, whose state of amorphous phase structural organization may be influenced significantly by common processing protocols (*e.g.*, orientation, stretching, annealing, contact with crystallization-inducing agents, *etc.*) [9,71-73]. Nevertheless, the simplest and most

commonly used model for the effect of crystallinity on steady-state permeability is based on these assumptions and is expressed by the following relationship:

$$P = (S_a \phi_a) \left(\frac{D_a}{\tau \beta} \right) \quad (2.17)$$

Figure 2.11 shows the effect of crystallinity on gas permeability in polyethylene at 25°C. Permeability decreases with increasing crystallinity primarily due to decreasing diffusion coefficients. The effect of crystallinity is more pronounced on the tortuosity factor, τ than the chain immobilization factor, β [74]. In glassy polymers, the most widely used approximations for τ and β are $\tau = \phi_a^{-1}$ and $\beta = 1$. Introducing these values into the above equation yields, $P = P_a \phi_a^2$, where P_a is the amorphous phase permeability.

In certain polymers, the simple assumptions of the two-phase model do not hold. For example, poly(4-methyl-1-pentene) (PMP), which is a highly permeable polymer, has a very low density crystal structure and hence, penetrant molecules can sorb into its crystalline phase [70]. In PET, Michaels *et al.* observed that the presence of crystalline regions increased the concentration of sorption sites in the amorphous regions remaining in the polymer after crystallization [10]. Others have recently examined this phenomenon in PET in more detail [75,76]. Serad *et al.* [9] reported that exposing amorphous PET to a strongly sorbing penetrant at high activity results in penetrant-induced crystallization. This process affects the amorphous phase penetrant solubility of PET resulting in a marked increase in overall solubility with increasing crystallinity. For example, acetaldehyde solubility in PET increased by more than 300% as a result of penetrant-

induced crystallinity of about 36 wt% [9]. This effect was attributed to the creation of microvoids in the polymer as a by-product of penetrant-induced crystallization [9]. Evidence for microvoid formation in PET due to exposure to strongly sorbing penetrants has been presented in studies investigating solvent treatments to improve the dyeability of PET yarns [71], and in studies investigating the effect of crystallizing liquids on the morphology of PET [72,73]. For example, Weigmann *et al.* reported that dye uptake in PET fibers exposed to dimethylformamide (DMF) was four to five times higher than the unexposed fibers [71]. The dye diffusion coefficient was also more than two orders of magnitude higher in the DMF-exposed samples than in the unexposed samples [77].

2.5.5 Chain Orientation

Stretching or drawing of polymer films can improve mechanical properties, and under certain conditions, barrier properties. The degree of chain orientation achieved is dependent on the draw ratio and other process conditions [22]. Orientation is usually characterized by birefringence and quantified by the Herman's orientation function, f [78]:

$$f = \frac{1}{2}(3\cos^2\theta - 1) \quad (2.18)$$

where θ is the average angle between the polymer chain axis and the draw direction.

Depending on the mode of deformation and the physical processes that occur during orientation, permeability may either increase or decrease with increasing orientation [22]. Impermeable polymer crystallites may become oriented into plate-like

structures during deformation, and this process generally decreases penetrant diffusivity by increasing tortuosity [22]. In addition, drawing of semicrystalline polymers can improve barrier properties through stress-induced crystallization and orientation of the remaining amorphous phase. Hence, the reduction in permeability caused by orientation of crystallizable polymers can be greater than that in non-crystallizable polymers [22]. The dramatic effect of orientation is supported by oxygen permeability data for PET in the literature. A 4X biaxial orientation (*i.e.*, draw ratio = 4 in each axis) decreased the permeability of oxygen in PET by a factor of about two [24]. For other systems, however, increases in permeability upon biaxial orientation have also been reported. A vinylidene chloride/vinyl chloride (VDC) copolymer, for example, showed an increase in oxygen permeability from 0.2 cm³ mil / (100 in² day atm) to 0.3 cm³ mil / (100 in² day atm) upon 2.5X biaxial orientation [79]. The permeability increase was attributed to microvoid development during orientation of the polymer chains after crystallinity was fully developed. Table 2.3 shows the effect of orientation on oxygen permeability of semicrystalline and amorphous barrier polymers [79]. In semicrystalline VDC copolymer and nylon MXD-6 polymers, under the conditions studied, the orientation process results in a slight increase in oxygen permeability with chain orientation, whereas the reverse is true for amorphous Selar[®] 3426 and polyacrylic-imide barrier polymers.

2.5.6 Penetrant Concentration (or Partial Pressure)

The influence of penetrant concentration on solubility, diffusivity and, in turn permeability varies depending on the penetrant-polymer system. Rubbery and glassy polymers typically show little or no concentration dependence for solubility, diffusivity, and permeability of light gases such as H₂, N₂, O₂, *etc.* Consistent with this notion, Figure 2.12a shows essentially no influence of pressure on H₂ permeability in PE [51]. Gases such as CO₂, which are more soluble than light gases, typically have a permeability-pressure response in glassy polymers similar to that shown in Figure 2.12b. Permeability decreases monotonically with increasing pressure as predicted by the dual-mode sorption model [18]. The magnitude of the permeability decrease depends upon the amount of so-called non-equilibrium excess volume in the polymer, which can increase with increasing T_g, the affinity of the penetrant for the non-equilibrium excess volume, and the mobility of the penetrant in the non-equilibrium excess volume relative to its mobility in the equilibrium free volume [14]. The permeability of a rubbery polymer to an organic vapor often exhibits the behavior shown in Figure 2.12c. The monotonic increase in permeability is often due to increases in penetrant solubility with increasing pressure coupled with increases in diffusivity with increasing pressure [14]. The response shown in Figure 2.12d is typical for strongly interacting penetrants (*e.g.*, organic vapors) in glassy polymers at sufficiently high penetrant partial pressures. It can be viewed as a superposition of the behaviors in Figures 2.12b and 2.12c [14]. The sharp increase in permeability begins as the penetrant plasticizes the polymer. Plasticization occurs when penetrant molecules dissolve in the polymer matrix at sufficient concentration to force

polymer chain segment separation, thereby increasing the free volume, and in turn, facilitating polymer segmental motion. This increase in segmental mobility, which may be observed by the depression in T_g , results in an increase in penetrant diffusion coefficients and, in turn, permeability [14].

2.5.7 Humidity

The absorption of water can increase, decrease, or have no effect on gas permeability of barrier polymers [6]. Increasing the relative humidity (RH) from 0 to 50% increases the oxygen permeability of cellophane (regenerated cellulose) by an order of magnitude, and exposure to 90% RH removes it from the class of high barriers by further increasing the permeability by more than an order of magnitude [6]. For packaging of foods that require protection against oxygen ingress, cellophane is coated or laminated with water barriers such as polyolefins [6]. Other hydrophilic barrier polymers, with the exception of certain amorphous polyamides, also lose their barrier properties with increasing RH as shown in Figure 2.13. This is because water acts as a plasticizer and increases the free volume of the polymer [80]. However, at low to moderate RH, amorphous polyamides and poly(ethylene terephthalate) show slightly improved barrier properties with increasing RH [6]. This behavior has been explained as the water molecules not swelling the polymer, but occupying some the polymer free volume sites instead, resulting in reduction in permeability of other gases [81]. Vinylidene chloride copolymers, acrylonitrile copolymers, and polyolefins show essentially no effect of RH on gas permeability [82].

2.6 Techniques for Measuring Transport Properties

The determination of permeability, solubility, and diffusivity requires direct or indirect measurement of mass transfer under controlled conditions. The permeability of barrier polymers can be determined directly by measuring the pressure change or other physical evidence of transfer or indirectly by using an indicator of permeation, such as chemical reaction of the transferring gas with another substance. The preferred methods of measurement differ for different classes of penetrants: light gases, water vapor, condensable vapors, and food flavor and aroma compounds.

There are two basic methods for measuring permeability: isostatic and quasi-isostatic [80]. Isostatic methods employ a continuous flow on both sides of the polymer film to provide constant penetrant concentrations. Quasi-isostatic methods use a continuous flow to maintain constant penetrant concentration only on the upstream side and allow penetrant accumulation on the downstream side of the film. However, this accumulation is limited to a very low concentration, and hence the penetrant partial pressure difference can be approximated as a constant [80]. Figure 2.14a typically shows the course of an isostatic permeability experiment for a barrier polymer film of uniform thickness exposed to constant penetrant partial pressure, p , on the upstream side and constant removal of penetrant that has permeated through the film to the downstream side. Using a specified initial condition (concentration in the film uniformly equal to zero) and boundary conditions (constant penetrant concentration, C , at the upstream side and zero penetrant concentration at the downstream side), this situation can be described by the following mathematical expression [83]:

$$q = \frac{DC}{L} \left[t - \frac{L^2}{6D} \right] - \frac{2LC}{\pi^2} \sum_{n=1}^{\infty} \frac{(-1)^n}{n^2} \exp\left(\frac{-Dn^2\pi^2 t}{L^2}\right) \quad (2.19)$$

where q is the total mass of penetrant permeating per unit film area in time t , D is the diffusion coefficient, L is film thickness, and C is penetrant concentration at the upstream side in equilibrium with the upstream penetrant partial pressure, p . When steady state is reached, t becomes large enough to make the exponential term negligibly small, and the above equation reduces to:

$$q = \frac{DC}{L} \left[t - \frac{L^2}{6D} \right] \quad (2.20)$$

A plot of q vs. t yields a straight line whose slope is the steady-state penetrant flux ($N_A = DC/L$), and whose x-axis intercept is called the time lag (t_L).

$$t_L = \frac{L^2}{6D} \quad (2.21)$$

The time lag can be related to the time required to achieve steady state ($t_{SS} \approx 2.7t_L$) [6].

The diffusion coefficient can be calculated by rearranging the above equation [83]:

$$D = \frac{L^2}{6t_L} \quad (2.22)$$

Permeability can be calculated from Equation 2.1 and the steady-state flux value ($P = N_A L/p = DC/p$). It should be noted that, for concentration-dependent diffusion coefficients, t_L will vary with the pressure difference across the polymer film and, as a result, this simple time lag analysis may yield significant errors in the diffusion coefficients estimated using Equation 2.22 [83]. More general expressions for the time lag have been developed by including the concentration dependence of D [84].

Alternatively, a ‘concentration-averaged’ diffusion coefficient can be obtained by plotting normalized penetrant flux (*i.e.*, flux at any time t divided by the steady-state flux) as a function of time (Figure 2.14b). The diffusion coefficient can be estimated using the following relationship [85]:

$$D = \frac{L^2}{7.2t_{1/2}} \quad (2.23)$$

where $t_{1/2}$ is the half time (*i.e.*, time required for the penetrant flux to reach half of its steady-state value). Thus, permeability, diffusivity, and hence solubility ($S = P/D$), can be determined from a single experiment. Given the ready availability of computing power, it is now possible to use any of a variety of numerical techniques to fit the entire response and extract the desired parameters and, when applicable, their concentration dependence.

2.6.1 Oxygen and Carbon Dioxide Permeation

The most widely used commercial instrument for measuring oxygen transmission rates of flat films and packages is the Ox-Tran[®] (Modern Controls Inc., Minneapolis, MN), and measurements are made in accordance with ASTM method D 3985 [86]. In this isostatic coulometric method, flat film samples are clamped into a diffusion cell, which is then purged of residual oxygen using an oxygen-free carrier gas such as N₂. The carrier gas is routed to the instrument sensor until a stable zero has been established. Pure oxygen is then introduced into the outside chamber of the diffusion cell (see Figure 2.15) [87]. Oxygen molecules diffusing through the film to the inside chamber are conveyed to the sensor by the carrier gas. The Ox-Tran[®] system uses a patented coulometric sensor

(Coulox[®]) to detect oxygen transmission through both flat films and packages. This sensor provides parts-per-billion sensitivity to oxygen even in the presence of water vapor. Digital pressure and flow controls allow for RH control. Alternative instruments for measuring oxygen transmission rates include Oxygen Permeation Analyzers from Illinois Instruments Inc. (Ingleside, IL).

Modern Controls, Inc. (MOCON) also makes instruments for measuring carbon dioxide permeation. Their Permatran-C[®] line of instruments use an infrared detector to detect carbon dioxide that permeates through the test film.

2.6.2 Water Vapor Permeation

Water vapor transmission rates (WVTR) can either be measured by the traditional gravimetric ‘cup’ method [2], or by newer electronic instruments. The newer method (*e.g.*, ASTM method F 1249 [88]) uses infrared detection to measure water vapor transmission through barrier films. One of the most widely used commercial WVTR systems is Permatran-W[®] (Modern Controls Inc., Minneapolis, MN). The newest model of this system (Permatran-W 3/31[®]) uses a patented modulated infrared sensor to detect water vapor transmission through flat films and packages. It provides sensitivity in the range of parts-per-million. Various models are available with different temperature and RH capabilities.

Lyssy AG (Zollikon, Switzerland) also manufactures automatic water vapor permeability testers designated as the L80 line of instruments. The L80-5000 is the newest member and the fifth generation in this series.

In the traditional method (ASTM method E 96) [6], a sample cell containing either a desiccant or distilled water is covered with the sample film and placed in a controlled atmosphere. Typical conditions for the desiccant method are 100°F (37.8°C) and an external RH of 90%, although the standard also allows for temperatures between 70 and 90°F (21 and 32°C) at 50 ± 2% RH. The cell assembly is weighed periodically until steady state is reached. WVTR can be calculated from the steady-state rate of change in the weight of the cell.

2.6.3 Flavor and Aroma Compounds

Measurement of transport rates of flavor and aroma vapors in plastics is more complicated than that of either water vapor or light gases. Elaborate equipment and sensitive analytical devices are required to obtain reliable results. Since the transport behavior of these compounds is often strongly concentration dependent, measurements must be made in the activity range in which the compounds are present in practice. Thus, some of the major complexities include providing precisely mixed quantities of the condensable vapor in an inert carrier like nitrogen or argon at very low concentrations, typically a few parts-per-million, and assuring that the concentration is maintained. Temperature must also be carefully controlled to prevent condensation on equipment surfaces [6].

As such, no single instrument has gained the widespread acceptance noted above for instruments for O₂, CO₂, and water vapor, though several methods have been used to measure transport properties of flavor and aroma compounds in barrier polymers. These

include isostatic permeation techniques and gravimetric techniques [89]. The permeation techniques directly yield permeability and diffusivity of flavors in barrier polymers. Solubility can then be calculated indirectly using the relation, $P = D \times S$. One example of a commercially available permeation system was the MAS 2000[®] Organic Vapor Permeation Test System (MAS Technologies Inc., Zumbrota, MN). Mass spectrometry and flame ionization detection have also been successfully used as vapor concentration detectors [89]. In contrast, gravimetric techniques permit direct and independent measurements of both solubility and diffusivity [90]. It is possible to measure sorption and desorption of organic flavors in barrier polymers using sensitive gravimetric sorption instruments such as the McBain spring balance and the Rubotherm magnetic suspension balance [28,37,91,92]. A schematic of a McBain spring balance assembly is shown in Figure 2.16. The polymer sample is suspended from a sensitive helical quartz spring inside the sorption chamber. After introducing the penetrant, the spring position relative to a fixed reference rod hanging inside the chamber is recorded using a CCD camera. From the kinetic uptake data, solubility and diffusivity values are estimated [8]. Acceptable levels of agreement have been reported for solubility coefficients of ethyl acetate in LDPE, linear LDPE (LLDPE), and ionomer films obtained from gravimetric and isostatic permeation techniques [89].

2.7 Techniques for Predicting Transport Properties

2.7.1 Modeling Transport Properties of Gases and Condensable Vapors in Polymers

The permeation of low molecular weight gases such as O₂, N₂, CO₂ as well as large flavor and aroma compounds is an essential consideration in the selection and design of food packages and containers. Predictive models for permeation would minimize the number of experiments required in package material selection and development. Perhaps, more importantly, they also provide an insight into the underlying factors controlling permeation in barrier polymers.

The permachor method has been used to predict permeabilities of low molecular weight penetrants in barrier polymers [93]. Although originally developed for O₂, N₂, and CO₂, this method can be extended to other gases and vapors, provided there is no specific interaction between the penetrant and the polymer. It has been successfully used for over 60 different polymers [93]. In this method, numerical values (*i.e.*, group contributions) are assigned to polymer segments. An average numerical value can then be obtained for the polymer, which is referred to as the permachor value of the polymer. A simple equation is used to relate gas permeability, P, to polymer permachor value, π :

$$P = Ae^{-s\pi} \quad (2.24)$$

where A and s are temperature-dependent constants. This method also takes into account the reduction in permeability caused due to orientation of crystalline polymers using the following expressions:

$$P = \left(\frac{A}{\tau_o} \right) e^{-s\pi} \quad (2.25)$$

$$\tau_o \approx \frac{1.13}{\sqrt{\phi_a}} \quad (2.26)$$

where τ_o is tortuosity related to crystallite orientation, and ϕ_a is the amorphous phase volume fraction. A good agreement has been reported between experimental and model predictions of O₂, N₂, and CO₂ permeability values in a variety of polymers [93]. This method has also been modified for predicting liquid permeation through polymers [2]. The permachor method works well for polymers and copolymers, but is not applicable to polymer blends [6]. As with any group contribution method, care should be exercised when attempting to perform predictions which are outside the data set used to generate the correlation.

Other methods for correlating gas permeability in barrier polymers with polymer molecular structure have been developed using free volume theory [49,50,94]. Group contribution techniques can be used to estimate polymer free volume from densities and intrinsic volumes of various polymer components. In the method proposed by Lee *et al.* [50], polymer specific free volume was used, which was defined as, $(V-V_0)/M$, where V is specific volume, V_0 is specific occupied volume, and M is polymer molecular weight. V_0 can be calculated according to Bondi's method from van der Waals volumes of the various groups in the polymer structure [50]. In this model, free volume was defined on a unit weight basis so that various molecular structures could be compared on the same weight basis. The model predicts a linear relationship between logarithm of gas

permeability and the reciprocal of polymer specific free volume. Other improvements to this model have been suggested [49,94]. Gas permeability has often been correlated with fractional free volume (FFV) (as defined in Equation 2.6) using the following relation [94]:

$$P = A \exp\left(\frac{-B}{FFV}\right) \quad (2.27)$$

where A and B are constants for a particular gas. It has been observed that when this model is limited to a specific family of polymers, *e.g.*, polyesters, polyamides, *etc.* [49], a reasonably good correlation can be obtained. However, when the correlation is broadened to include a wider range of polymer types, there is considerable scatter in the data, particularly at low values of gas permeabilities. Even though these free volume-based models have some fundamental basis for correlating transport properties, they have the following limitations [50,94]: (i) the assumption of solubility being independent of free volume and polymer structure is clearly an approximation, (ii) the concept of free volume cannot capture all the factors affecting gas permeability (such as chain flexibility, CED, *etc.*), and (iii) there may be errors in values of van der Waals volumes available in the literature. Attempts have been made to refine these models by introducing more empirical parameters and making them more predictive, and these efforts have resulted in significant improvements in the accuracy of the correlations [94].

Larger and more condensable penetrants, *e.g.*, flavor and aroma compounds, can have extremely low diffusion coefficients in common barrier polymers resulting in extremely large timescales to achieve steady state. For example, *d*-limonene has diffusion

coefficients of the order of 10^{-14} cm²/s in PET [35]. When coupled with a typical film thickness of 10 μm, this leads to timescale to reach steady state of more than 3 years. Hence, as noted before, over the shelf life of the packaged product (typically of the order of several months), flavor and aroma compounds may never reach steady-state transport. Therefore, independent predictions of their diffusion and solubility coefficients become necessary. Several methods have been proposed for predicting solubility coefficients. A widely used method is based on a thermodynamic approach that relates penetrant sorption to solubility parameters of the penetrant and the polymer [95]. This dependence can be expressed as follows:

$$S = S_o \exp\left[\left(\Delta H_{vap} - \Delta H_{mix}\right) / RT\right] \quad (2.28)$$

$$\Delta H_{mix} = v_1 \phi_2 (\delta_1 - \delta_2)^2$$

where S_o is a constant for a particular polymer, v_1 is partial molar volume of the penetrant, ϕ_2 is volume fraction of polymer in the mixture, δ_1 and δ_2 are solubility parameters of penetrant and polymer respectively, and ΔH_{mix} is enthalpy change on mixing of penetrant molecules with polymer segments. The values of v_1 , δ_1 , and δ_2 can be obtained from the literature [66]. The enthalpy change on vaporization of the penetrant (ΔH_{vap}) can be calculated from the penetrant boiling point using available correlations [38]. Reasonably good agreements have been reported between model-predicted and experimentally observed solubility coefficients of several penetrants in vinylidene chloride/vinyl chloride copolymers and LDPE at 85°C and 30°C, respectively [96].

For penetrants that interact with the polymer matrix primarily *via* dispersion (*i.e.*, van der Waals) forces, penetrant solubility scales with measures of penetrant condensability such as penetrant boiling point, critical temperature, or the force constant in the Lennard-Jones potential model [9]. The following relation between penetrant critical temperature and penetrant solubility has been derived using a classical thermodynamics model [46,97]:

$$\ln S_a = N + MT_c \quad (2.29)$$

In this expression, N is a parameter that depends primarily on polymer-penetrant interactions and polymer free volume. T_c is the penetrant critical temperature, which is widely tabulated for many penetrants of interest [38]. M is constant and has a value of approximately 0.016 K^{-1} for gas dissolution in liquids and in rubbery and glassy polymers [46]. While N varies from polymer to polymer, van Krevelen recommends average values of -9.7 and -8.7 for rubbery and glassy polymers at 35°C , respectively, when solubility is expressed in $\text{cm}^3(\text{STP})/(\text{cm}^3 \text{ cmHg})$ [46]. Penetrants with strong dipole or quadrupole moments may be more soluble in a polar polymer matrix, such as PET, than predicted based on Equation 2.29 [8]. Although Equation 2.29 is strictly valid for penetrant sorption in equilibrium matrices, such as liquids or rubbery polymers, it also provides an excellent description of equilibrium solubility in glassy polymers [8]. Figure 2.17 shows the correlation of penetrant solubility in PET with penetrant critical temperature [8]. Non-polar penetrants show excellent agreement with the model presented in Equation 2.29 and polar or quadrupolar penetrants exhibit significant scatter around the correlation line.

Over wider ranges of critical temperature, Stern has suggested that penetrant solubility coefficients may be better correlated with the square of reciprocal reduced temperature, $(T_c/T)^2$ [98]:

$$\ln S_a = n + m \left(\frac{T_c}{T} \right)^2 \quad (2.30)$$

where T is the temperature of the experiment, and m and n are the slope and intercept of the correlation line, respectively. This equation may also be derived from fundamental thermodynamic considerations [9]. Other semi-empirical methods, *e.g.*, UNIFAC group contribution model, have also been proposed for predicting penetrant solubility in polymers [99,100].

Several predictive and correlative methods have been developed for diffusion coefficients of penetrants in polymers. An empirical relationship has been developed for correlating diffusion coefficients with penetrant critical volume [101]:

$$D_a = \frac{\tau}{V_c^\eta} \quad (2.31)$$

where D_a is amorphous phase diffusion coefficient, V_c is penetrant critical volume, and τ , η are adjustable constants. This equation has been proposed based on analogy with correlations of diffusion coefficients with critical volume of small molecules in liquids. For larger penetrants (*e.g.*, long chain hydrocarbons), diffusion steps may occur *via* motion of only part of the molecule, and critical volume is not expected to capture the effective size of a penetrant unit participating in a diffusion step [9]. In such cases, diffusion coefficients would be less sensitive to penetrant size than indicated in the above

equation. Also, critical volume fails to capture the effect of penetrant shape on diffusion coefficients [8]. Figure 2.18 shows a plot of D vs. V_c for PET at 25°C. Diffusion coefficients of penetrants (up to molecular weights of 100 Daltons) in PVC, PS, and PMMA have been correlated empirically with other measures of penetrant size, such as molecular diameter [102].

A theoretical model based on polymer free volume, temperature, and penetrant size and shape has been developed [103]. According to this model, diffusion coefficients of large penetrants in amorphous rubbery polymers are given by:

$$D = \frac{V_f^2}{6} \left(\frac{eRT}{M} \right)^{1/2} \left(\frac{1}{\ell_1 A c_1^2} + \frac{1}{\ell_2 A c_2^2} + \frac{1}{\ell_3 A c_3^2} \right) \exp\left(\frac{-E_D}{RT} \right) \quad (2.32)$$

where V_f is average free volume per polymer chain segment, e is the base of natural logarithm, M is penetrant molecular weight, ℓ_i is length of penetrant molecule along a given direction i (taken as the principal axis of inertia), $A c_i$ is effective penetrant molecular cross-sectional area perpendicular to the direction i , and E_D is the activation energy of diffusion. V_f can be calculated from the following equation [103]:

$$V_f = V \left[0.025 + \alpha_f (T - T_{g2} + k w_1) \right] \quad (2.33)$$

where V is the total volume per mole of the polymer repeat unit, α_f is temperature coefficient of free volume expansion, T_{g2} is glass transition temperature of the polymer, k is plasticizing efficiency of the penetrant for the polymer, and w_1 is weight fraction of the penetrant in the polymer. Equation 2.32 is strictly valid for large penetrants satisfying the size criterion, $V_s \gg V_f$, where V_s is effective steric volume of the penetrant [103]. The penetrant molecular shape dependence is represented by the three-termed expression

within the parenthesis of Equation 2.32. The equation can be applied to penetrants of a wide variety of molecular shapes [103]. This model has been tested using data for diffusion of plasticizers in PVC [103].

2.7.2 ‘Migration Modeling’ of Polymer Additives into Packaged Foods and Beverages

One of the key applications of barrier polymers is food and beverage packaging. Several low molecular weight components, *e.g.*, monomers and oligomers, as well as additives such as lubricants, stabilizers, and plasticizers, which are necessary for processing and stability, can be present in polymers used for packaging. Hence, there exists a potential for permeation (or migration) of these additives into the food or beverage with subsequent contamination [104-106]. To ensure the safety of packaged food components, the US Food and Drug Administration (FDA) established a ‘Threshold of Regulation’ approach which sets upper limits on the additive concentrations in the food [104]. Since traditional migration testing methods are time-consuming, expensive, and the analysis can be difficult (especially at low penetrant concentrations), the FDA has developed models for predicting the additive concentration in the food simulant and rate of transport of additives [104]:

$$q = 2C_o\rho\sqrt{\frac{D_p t}{\pi}} \quad (2.34)$$

where q is total mass of permeating species per unit surface area, C_o is initial additive concentration in the polymer, ρ is polymer density, D_p is additive diffusion coefficient,

and t is the package shelf life. This equation assumes that [104]: (i) permeation is diffusion-controlled and follows Fick's law, (ii) no solubility-limited partitioning occurs between the polymer and the food, and (iii) other external phase mass transfer resistances (*e.g.*, mixing, reaction with food) are negligible. The following empirical equation has been developed for predicting diffusion coefficients [104]:

$$D_p = 10^4 \times \exp\left(A_p - a \times MW - b\left(\frac{1}{T}\right)\right) \quad (2.35)$$

where D_p is additive diffusion coefficient (cm^2/s), A_p is constant for a particular polymer, MW is additive molecular weight (g/mol), and a , b are correlation constants with values of 0.01 mol/g and 10,450 K, respectively. The A_p values are 9 for LDPE, -3 for PET, and 5 for HDPE and PP [104]. A semi-empirical model for predicting diffusion coefficients has also been developed [107]:

$$\ln D_p = \ln A + \alpha(MW)^{1/2} - \frac{K(MW)^{1/3}}{T} \quad (2.36)$$

where A , α , and K are constants determined from experimental data. The diffusion coefficients follow Arrhenius type behavior and are taken to be independent of penetrant concentration [104]. These models do not explicitly account for the effect of polymer crystallinity or orientation on additive diffusion coefficients.

The approach of the European Commission (EC), on the other hand, has been to assign 'specific migration limits' to different substances with adverse toxicological properties [106]. A Fickian diffusion-based model, called the Piringer migration model,

which uses the ‘Migratest Lite’ program, has been used [105,106], and its mathematical form is given below:

$$M_t = C_o \rho L \left(\frac{\alpha}{1 + \alpha} \right) \left[1 - \sum_{n=1}^{\infty} 2\alpha(1 + \alpha)(1 + \alpha + \alpha^2 q_n^2) \exp\left(\frac{-D_p t q_n^2}{L^2} \right) \right] \quad (2.37)$$

$$\alpha = \frac{1}{K} \frac{V_F}{V_p}, \quad \tan q_n = -\alpha q_n$$

where L is film thickness, K is partition coefficient, and V_F & V_p are the volumes of food and polymer, respectively. The diffusion coefficient can be estimated from Equation 2.35.

The sorption and transport of flavor and aroma compounds from the food simulant into the packaging walls can affect the migration of additives from the walls into the food simulant. Neither approach (FDA or EC) takes this effect into account. In general, these migration models provide conservative estimates (from a safety viewpoint) of additive concentrations in the food simulant and their diffusion coefficients. However, there are certain cases when they can fail [104] (*e.g.*, in cases where the flavor and aroma compounds from the food simulant plasticize the polymer, or if the additive reacts either with the polymer or with the food simulant to produce a species that is not detectable), and attempts are being made to improve them.

2.8 Chemical Structures and Properties of Barrier Polymers

Barrier polymers can be broadly classified as high barrier, and moderate to low barrier polymers, depending on the degree to which they restrict the passage of gases like O₂ or CO₂ and water vapor. The boundaries between these classifications, while somewhat arbitrary, are based on the effect of the barrier properties of the polymer on the shelf life of the packaged products. In this section, we will discuss various properties of different classes of barrier polymers. The selection of a barrier polymer for a particular packaging application depends not only on its barrier properties but also on other physical properties and a comparison of physical, mechanical, and optical properties of some commonly used barrier polymers is, therefore, presented in Table 2.4 [108]. Permeabilities of light gases (O₂ and CO₂) and water vapor are presented in Tables 2.5 and 2.6, respectively [6], and Table 2.7 presents permeability, diffusivity, and solubility of flavor and aroma compounds in various high and moderate barrier polymers [2]. Permeability data of light gases and water vapor in barrier polymers [109-113] are more widely available than those of flavor and aroma compounds [114-116]. Proper care should be exercised when using or comparing data from different sources since, as discussed in the previous sections, polymer permeability values depend on a wide variety of factors.

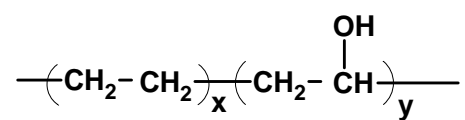
2.8.1 High Barrier Polymers

High barrier polymers are generally understood to be those polymers which offer a high resistance to gas transmission. There are no specific limits for the gas transmission

rates, but this category comprises polymers with gas permeabilities low enough to significantly prolong the shelf life of packaged products.

Ethylene-Vinyl Alcohol Copolymers

The general structure of ethylene-vinyl alcohol (EVOH) resins is as follows [117]:

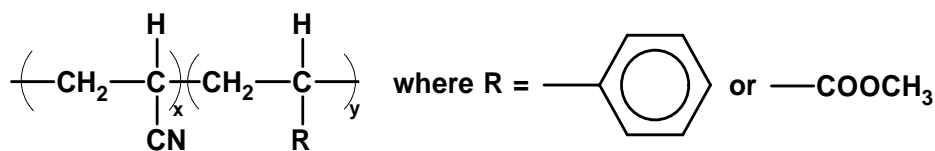


EVOH resins are random copolymers of ethylene and vinyl alcohol made by the hydrolysis of ethylene vinyl acetate copolymers [117]. The leading manufacturers are Kurray (EVALCA[®]) and Nippon Gohsei [82]. In commercial grades of EVOH used in packaging, ethylene concentration ranges from 29 to 44 mol % (EVAL Co., USA). No additives are required in their processing as the presence of ethylene units renders the otherwise intractable vinyl alcohol melt processable in conventional molding and extrusion equipments. A high concentration of ethylene is also recommended for thermoforming [118]. At low to moderate RH, EVOH copolymers provide an excellent barrier to gases. The hydroxyl units (or OH groups) contribute strongly to increasing chain cohesive energy density and improving barrier properties, so the greater the fraction of OH groups, the lower the permeability [119]. Figure 2.19 shows the effect of ethylene concentration on oxygen and water vapor permeability of EVOH [6]. This figure also presents permeation properties of poly(vinyl alcohol) (PVOH) (*i.e.*, fully hydrolyzed poly(vinyl acetate)) and HDPE (which has no OH groups) for comparison with the

EVOH series. As RH increases, the barrier properties of EVOH copolymers decrease (*cf.* Figure 2.13). The OH groups are also responsible for the hydrophilic nature of the polymer. Hence, the greater the percentage of vinyl alcohol units, the greater the influence of humidity on gas barrier properties of EVOH copolymers [6]. Conversely, high proportions of ethylene units improve resistance to moisture (as shown in Figure 2.13) and decrease the water vapor transmission rate, as shown in Figure 2.19. Moisture sensitivity can also be decreased somewhat by biaxial orientation [82]. EVOH also offers very high barrier to flavor and aroma compounds and these barrier properties are not as sensitive to moisture as its oxygen barrier [82]. In the majority of commercial applications, EVOH is used in a multilayer structure with moisture barrier and/or structural layers on each side, a typical example being multilayer bottles with polypropylene for ketchup [82]. EVOH has also been used as a flavor barrier on the inside of PE-coated paperboard containers, a typical application being packaging of orange juice, where it minimizes the loss of limonene from the juice into the PE layer [82]. EVOH is used as a barrier layer in many other rigid and flexible packaging applications.

Nitrile Polymers

The general structure of nitrile copolymers is shown below [117]:

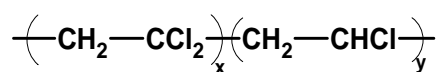


Application of polyacrylonitrile (PAN) in packaging started in the 1960s. Despite processing difficulties, PAN was used due to its excellent barrier properties. A group of copolymers were developed in the 1970s employing methyl acrylate or styrene as comonomers at concentrations up to 20 mol% [119]. They are efficient oxygen barriers and have high grease and oil resistance, strength, and stiffness. Lopac[®] (Monsanto Co.), Barex[®] (Sohio), and Cycopac[®] (Borg-Warner Chemicals) are three commercial nitrile copolymers used in packaging applications. Their compositions are shown in Table 2.8. Barex[®] and Cycopac[®] are rubber-modified for improved mechanical properties, and the barrier properties of these copolymers are relatively insensitive to moisture. Concerns about the possible migration of acrylonitrile monomer, a toxic compound [82], have limited the use of nitrile polymers in food contact applications.

Vinylidene Chloride Copolymers

Copolymers of vinylidene chloride (VDC) with vinyl chloride and acrylonitrile were among the first high barrier polymers to be widely used. During their commercial appearance in the late 1930s, they had the lowest permeabilities among plastics to gases and water vapor [119]. Poly(vinylidene chloride) (PVDC) homopolymer is soluble only in hot dichlorobenzene (among common solvents) and has a melting point only a few degrees below its decomposition temperature [119]. These characteristics make it difficult to fabricate by melt processing techniques. Copolymers were synthesized to overcome these drawbacks. Acrylates were found to be among the most useful comonomers, along with vinyl chloride and acrylonitrile [119]. By adding comonomers,

the melting point can be decreased to a range of 140-175°C (as compared to 198-205°C for PVDC), thus making melt processing feasible [120]. These copolymers are semicrystalline and soluble in only a limited range of solvents. The most notable attributes of VDC copolymers are their chemical resistance and extremely low permeabilities to gases and water vapor (*cf.*, Tables 2.5 and 2.6). The structure of the most widely used vinylidene chloride-vinyl chloride copolymer is shown below:

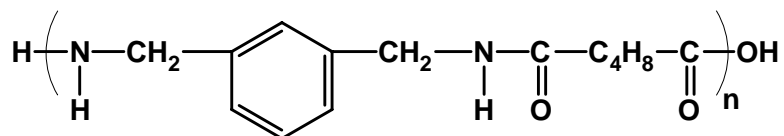


where x is 85 to 90 mol% [119]. Vinylidene chloride copolymers are commercially available under a variety of trade names such as Saran[®] (The Dow Chemical Co.), Daran[®] (W.R.Grace), Amsco Res[®] (Union Oil), and Serfene[®] (Morton Chemical) within the United States; Haloflex[®] (Imperial Chemical Ind.), Diofan[®] (BASF), Ixan[®] (Solvay and Cie SA), and Polyidene[®] (Scott-Bader) in Europe. Copolymers are available in the following forms [119]: (i) lattices of approx. 1000-1500 Å^o which can be applied as coatings to paper and plastic films to improve their barrier properties, (ii) resins for coating plastic films (especially cellophane) to improve their barrier properties, (iii) melt-processable resins for extrusion, coextrusion, and molding, and (iv) clear, transparent films for commercial packaging applications. Small amounts of processing aids and heat stabilizers are added to extrusion and molding resins.

Polyamides

The standard semicrystalline polyamides (PA) (nylon 6, nylon 66, *etc.*) used in packaging have medium gas barrier properties, and their barrier properties are affected by humidity [117]. However, specialty grades of polyamides with higher gas barrier properties are available. Commercial grades of Selar[®] amorphous polyamides (AmPA) (E.I. du Pont de Nemours & Co., DE), for example, exhibit good O₂ barrier and reduced dependence of gas barrier properties on RH. In fact, their gas barrier properties improve with increasing RH (*cf.* Figure 2.13). At a RH of 80% or more, their O₂ barrier is similar to that of PAN [118]. Moreover, at 95-100% RH, the O₂ barrier is equivalent to that of EVOH at similar conditions, and substantially better than that of nylon 6. The amorphous nature of Selar[®] results in a much broader range of processing conditions than those of semicrystalline nylon 6 [121]. The mechanical and barrier properties of AmPA can be improved by orientation.

Another high barrier polyamide is MXD-6 resin (Mitsubishi Co., Japan), which was developed in the 1970s. It is made from the reaction of meta-xylylenediamine and adipic acid [82]:



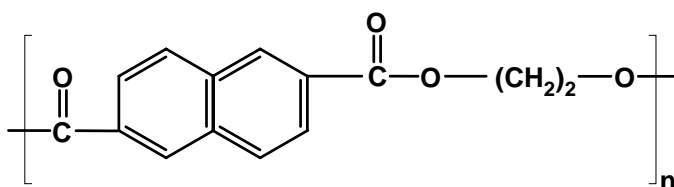
It provides improved clarity, mechanical, thermal, and barrier properties relative to standard nylons. It has better gas barrier properties than nylon 6 and poly(ethylene terephthalate) at all humidities, and is better than EVOH at 100% RH. The barrier properties of MXD-6 are relatively unaffected by moisture up to a RH of 70% [82].

Because of its cost and the lack of a domestic source, MXD-6 has found limited applications in the United States. It has a much wider market in Japan, appearing in commercial applications such as non-pasteurized plastic beer bottles and carbonated soft drink bottles [82].

Polyesters

The most widely used member of the polyester family for food and beverage packaging applications is poly(ethylene terephthalate) (PET). However, PET offers a moderate barrier to gases and water vapor. Poly(ethylene naphthalate) (PEN) offers a much higher barrier to gases and water vapor than PET and can be classified as a high barrier polyester.

PEN is a homopolymer of dimethyl-2,6-naphthalene dicarboxylate (NDC) and ethylene glycol [122]:

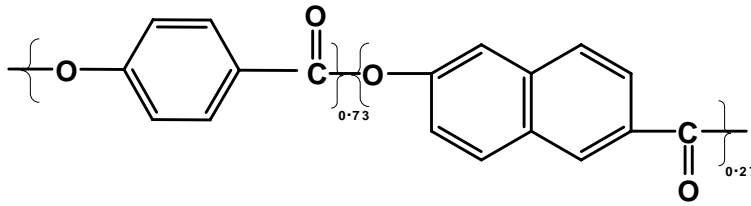


The rigid double-ring structure in the polymer backbone results in increased mechanical strength, heat stability, and barrier properties as compared to PET. As with PET, orientation produces a substantial reduction in gas permeability, and the oxygen permeability of oriented PEN is a factor of 5 lower than that of oriented PET [82]. Teijin (Japan) and ICI (UK) have been the leaders in manufacturing PEN films. Teijin manufactures both resin and films, the latter under the tradename Teonex[®]. Since 1990,

Dupont and Teijin have had a worldwide joint venture in polyester films, including PEN. Dupont has also acquired ICI's Melinex[®] PET film and Kaladex[®] PEN film operations. The main disadvantages of PEN currently are its high cost, and unsettled sources of monomer technology and supply [82]. One of the leading manufacturers of NDC, Amoco Chemical Co. (Decatur, Ala.), has developed a technology that uses o-xylene rather than naphthalene as the feedstock, which could reduce the manufacturing cost of PEN resin [82]. Other newer NDC technologies from Kobe Steel (Japan) and Mobil Chemicals could also lead to lower cost for PEN. Another way of addressing the price issue is by using blends or copolymers of PEN with PET. Gas and vapor permeability has been found to decrease continually as PEN is added to PET [123,124].

Liquid Crystalline Polymers

Liquid crystalline polymers (LCPs) offer excellent thermal and chemical resistance, and exhibit very high barrier properties that are almost unmatched by existing barrier polymers [22,125,126]. They also offer adequate mechanical properties for certain packaging applications [127]. LCPs are very efficiently packed, highly oriented, and often semicrystalline materials. Commercially available LCPs such as Vectra[®] (Hoechst-Celanese Corp.), Zenite[®] (E.I. du Pont de Nemours & Co., DE), and Xydar[®] (Amoco Performance Products) are aromatic copolyesters that have a significantly higher degree of chain orientation than typical polyesters such as PET [127].



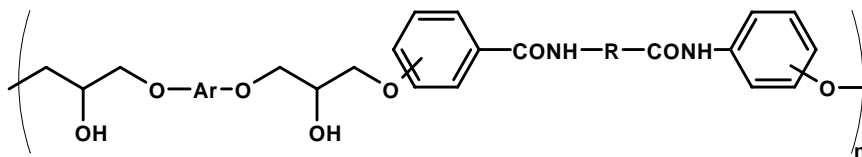
Structure of Vectra®

LCPs of this kind were first introduced to the market in the 1980s. Table 2.9 shows a comparison of properties of biaxially oriented LCP films with those of PET films [128]. Figure 2.20 compares barrier properties of LCPs with other barrier polymers. LCPs offer the best combination of water vapor and O₂ barrier properties among all known classes of polymers. They also offer excellent barrier to CO₂, N₂, and other gases and vapors [127]. However, commercial applications of LCPs have been limited primarily because of their high cost, lack of transparency, and processing characteristics [127]. One key to unlocking the potential of LCPs in barrier packaging is to be able to process thin uniform layers in coextruded multilayer structures. Recently, three-layered structures (PET-tie layer-LCP) have been coextruded (Superex Polymer, Inc. Waltham, MA) with a total thickness of 25-50 μm and 10-30% LCP layer thickness. This multilayer film is claimed to offer a high performance-cost ratio [127].

Poly(hydroxy amino ethers)

Poly(hydroxy amino ethers) (PHAE) are a new family of high barrier epoxy-based thermoplastics. The general chemical structure of amide-containing PHAE, which

are formed by the reaction of amide-containing bisphenols with aromatic diglycidyl ethers [129], is shown below:



where R can be $-(\text{CH}_2)_n-$ ($n=1,2,3\dots$) or an aromatic group, and Ar designates an aromatic moiety.

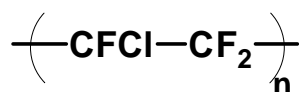
These polymers are amorphous with T_g values ranging from 90-133°C. They incorporate both amide and hydroxyl moieties on the chain backbone. In order to prevent crosslinking, the hydroxyl groups are generated during the polymerization of preferred amide-containing monomers [129]. The presence of aromatic groups between the amide groups in the polymer backbone can result in high T_g and good barrier properties. It has also been observed that the presence of *m*-phenylene units instead of *p*-phenylene units can reduce O_2 permeabilities (as much as 30-40%) by increasing the chain packing efficiency of the polymer [129]. This phenomenon is, in fact, rather general among aromatic polymers. Often, meta-linked aromatic rings in polymer backbones have lower permeability coefficients than their para-linked analogs [130,131]. Lower O_2 permeabilities can also be obtained when hydrogen bonding interactions in the polymer backbone are increased by either reducing the number of non-polar methylene units, or increasing the population density of polar amide groups [129]. Unlike other hydroxyl-containing polymers like EVOH, the barrier properties of amide-containing PHAE improve with increasing RH [51,129]. For example, a decrease in O_2 permeability from

1.4 cm³ mil/(100 in² day atm) at 5% RH, to 0.8 cm³ mil/(100 in² day atm) at 75-80 % RH has been reported. Based on preliminary work involving density and positron annihilation lifetime spectroscopy studies, it has been postulated that water molecules not only occupy free volume elements in these materials but also enhance interchain cohesion, thus inhibiting the transport of other non-polar gases [132].

A series of polymers from the PHAE family has recently been commercialized by Dow Chemical Co. (Midland, MI) under the tradename BLOXTM Adhesive and Barrier Resins [133,134]. They offer high gas barrier properties, excellent adhesion to a variety of substrates, high optical clarity, and good mechanical properties. For example, BLOXTM 4000 series resins exhibit an oxygen transmission rate of 0.1 cm³ mil/ (100 in² day atm) at 23°C and 60% RH [133]. The BLOXTM resins have found some commercial applications in barrier packaging, starch-based foam packaging, and powder coatings [134].

Polychlorotrifluoroethylene

Polychlorotrifluoroethylene (PCTFE) is a flexible thermoplastic made from fluorinated-chlorinated resins. It was first discovered in the 1950s and has been commercially produced since the 1960s [135]. Its chemical structure is as shown:



The key characteristics of this polymer are its high optical clarity and excellent moisture barrier properties [135]. In commercial Aclar[®] resins (AlliedSignal Corp., Morristown,

NJ), the polymer is generally modified by copolymerization, resulting in a semicrystalline material with T_g of about 45°C, and melting point of about 190°C [120]. It shows excellent thermal and chemical stability, and high water vapor and O₂ barrier properties [136] (*cf.*, Tables 2.5 and 2.6). For example, Aclar[®] films typically have water vapor transmission rates less than 0.04 gm mil/(100 in² day) (23°C) and oxygen transmission rates less than 14 cm³ mil/ (100 in² day) (25°C) [136]. PCTFE is most widely used for producing blister packs in pharmaceutical applications [135]. The moisture barrier properties can be tailored by varying the PCTFE layer thickness in coextruded multilayer structures, thereby adjusting the performance-to-cost ratio. An example of a commercial coextruded structure is Aclar[®] NT AE-1 (AlliedSignal Corp., Morristown, NJ), which is 33 μm thick, and contains about 8.4 μm of PCTFE [135]. PCTFE can also be laminated with PP, PAN, PET, HDPE, LDPE, and PVC and then formed into blister packs. Other applications of the same technology include electronic component packaging where lower moisture barrier may be acceptable resulting in more favorable economics [135].

2.8.2 Moderate Barrier Polymers

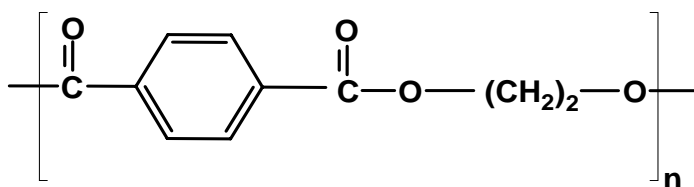
Polymers in this category include polyesters, polyolefins, polyvinyl chloride (PVC), polystyrene (PS), and certain semicrystalline polyamides. The polymers included in this section are typically more widely available, have more manufacturers, and are less expensive than the specialty barrier resins described in the previous section.

Polyesters

Polyesters represent a class of versatile barrier plastics. Poly(ethylene terephthalate) (PET) is by far, the most important member in this family from a commercial viewpoint. It is extensively used in the food and beverage packaging industries and is especially known for its widespread use in bottles for carbonated beverages [137]. The other members in this category are poly(trimethylene terephthalate) (PTT) and Polylactide (PLA).

Poly(ethylene terephthalate)

PET is a linear thermoplastic made from ethylene glycol and terephthalic acid, or ethylene glycol and dimethyl terephthalate [117]. The structure of PET is shown below:



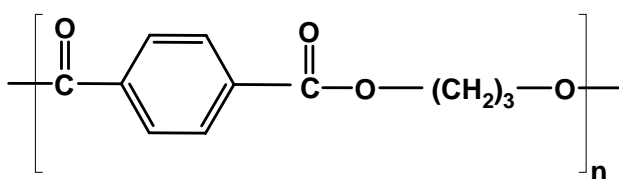
PET is used in many rigid food and beverage containers due to a good balance of physical and mechanical properties, barrier properties, processibility and formability, ecological and toxicological characteristics, and economics [138]. As a result, PET bottles have virtually replaced glass packages for carbonated soft drinks in the US. In the glassy state, it is strong, stiff, ductile, and tough. It can be oriented by stretching during molding and extrusion, which further increases its strength, stiffness, and barrier properties. One of the early drawbacks of PET was its low heat distortion temperature of 60°C (140°F), which prevented it from being used in applications requiring filling at

elevated temperatures [138]. However, careful heat-treatment increases the heat distortion temperature of crystalline PET containers and recently commercialized processes claim resistance to temperatures of up to 90-92°C (194 to 196°F) [138]. It has moderate barrier properties for light gases, but is a good barrier for flavors and aroma compounds. Its barrier properties can be improved by increasing crystallinity and orientation [138]. A 4X biaxial orientation of amorphous PET at temperatures near 100°C produces significant strain-induced crystallization and decreases the permeability of O₂ and CO₂ by a factor of about two [8].

Oriented and heat-set PET films have also found use in a broad range of flexible packaging applications due to their high strength, good barrier, high clarity, heat resistance, and good metalizability. There are more than 50 specific application areas for PET films [139]. Manufacturers have met the product requirements of each of the diverse end-use markets by tailoring formulations and process conditions. For example, in the food and beverage packaging industries, many types of PET films have been developed, including metallized PET films for packaging of coffee, wine, and meats, poly(vinylidene chloride)-coated PET films for meat and cheese packaging, and coextruded multilayer PET films for heat-sealable packaging [139]. Commercial manufacturers of PET films include DuPont Teijin Films (Mylar[®], Melinex[®], Tetoron[®]) and Mitsubishi Polyester Film, LLC. (Diafoil[®], Hostaphan[®]).

Poly(trimethylene terephthalate)

PTT is made from the polycondensation reaction of trimethylene glycol (also called 3G) with either terephthalic acid or dimethyl terephthalate [82]. Although this polymer was first synthesized in 1941, it was not commercialized due to lack of an economical source of 3G. In the early 1990s, Shell Chemical Co. announced a catalyst breakthrough to make 3G economically by hydroformylation of ethylene oxide [82].



PTT is an engineering resin and has been targeted mainly towards injection molding applications. However, there have been claims around its barrier properties [82], and it is therefore included in this chapter for completeness.

Due to the presence of an odd number of methylene units in the chain backbone, PTT has physical properties different from PET [82]. Its O₂ permeability is about 6 cm³ mil/(100 in² day atm) at 0% RH, and moisture absorption rate is typically 0.03 % after 24 hr. and 0.15 % after 14 days [82]. Typical properties of PTT are as follows: it has a melting point of 228°C, a T_g of 45-65°C, and can be produced with crystallinity values up to 45 % (w/w).

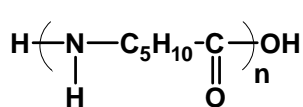
Poly lactide

Poly lactide (PLA) is a semicrystalline, linear thermoplastic made from lactic acid, especially as derived from corn (maize). Poly lactide is new to the commercial market

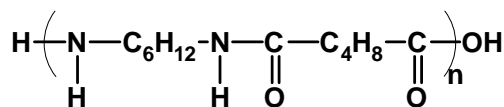
[140]. Its applications are still being explored. However, its barrier is adequate for some food packaging uses, especially for management of food and aroma profiles. It can be heat-sealed and thermoformed. It has a glass transition temperature of 55-65°C. The principal manufacturer of PLA is Cargill Dow, LLC (NatureWorks®).

Polyamides

This category of moderate barrier polymers includes nylon 6 and nylon 6,6. Nylon 6 is made by the polymerization of caprolactum, and nylon 6,6 is made by the reaction of hexamethylene diamine and adipic acid [117]. Their chemical structures are shown below:



Nylon 6



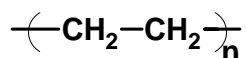
Nylon 6,6

In general, nylons have good gas and aroma barrier properties, but poor moisture barrier properties [82] (*cf.* Tables 2.5 and 2.6). Absorbed water has a plasticizing effect that leads to a reduction in tensile strength and increase in impact strength. Uniaxial and biaxial orientation can improve their flex-crack resistance, mechanical, and barrier properties [117]. Biaxially oriented nylons offer better gas barrier properties, softness, and puncture resistance, compared to oriented PET, which offers better rigidity and moisture barrier properties [117]. Nylons are less widely used in the packaging industry than polyolefins or PET, with the majority of the applications being blow molded bottles (coextrusion and blending of nylon 6 with PE), for industrial and household chemical markets [82].

Polyolefins

Polyethylene (PE) and polypropylene (PP) are two of the most widely used polymers in the food and beverage packaging industry. These polymers find use as films, moldings, coatings, adhesives, and closures [141]. They are available in a wide variety of types and grades. While they have much higher permeabilities to gases than many other barrier polymers, they are very good moisture barriers (*cf.*, Tables 2.5 and 2.6).

PE, whose structure is shown below, was one of the first olefinic polymers to be used commercially in the packaging industry:

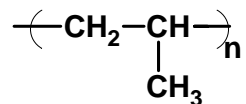


It is classified on the basis of density. Figure 2.21 shows the effect of density on various properties of PE [141]. A branched structure for low density PE (LDPE) results from exceptionally high temperature and pressure during its manufacture. It is tough, flexible, can be easily melt-processed, and has good moisture barrier properties. It is a semicrystalline polymer with crystallinity typically in the range of 40%. Medium density PE (MDPE) is stronger, stiffer, and has better barrier properties than LDPE. High density PE (HDPE) is essentially unbranched and is the strongest and most rigid polymer in this family. It offers barrier properties to moisture and gases that are superior to those of LDPE and MDPE.

If unsaturated comonomers such as butene, hexene, or octene are added to the HDPE polymerization process in the presence of a stereo-specific catalyst, it results in the formation of a linear polymer with short branch-like pendant groups [120]. Its density is in the same range as LDPE, but the degree of branching is greatly reduced. This polymer

is called linear LDPE (LLDPE) and its density depends on the amount of comonomer added. The larger the amount of the comonomer, the lower the density of the copolymer [120]. LLDPE combines the clarity and excellent heat-seal properties of LDPE with the strength and toughness of HDPE. It is often blended with LDPE in order to optimize the benefit obtained from both materials [120].

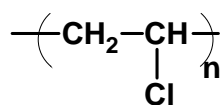
PP, whose chemical structure is shown below, can be made by the catalytic polymerization of propylene at high temperature and pressure [141]:



Isotactic PP (with all methyl groups on same side of the polymer chain) is the commercially desired form for packaging applications [141]. The concentration of atactic PP (with irregular arrangement of methyl groups) is kept low by suitable catalysts and polymerization conditions [141]. PP offers high resistance to water vapor permeation and is widely used in rigid as well as flexible food packaging applications. PP films can be oriented, which improves their barrier properties, mechanical strength, and optical properties. For example, oriented PP has about three times higher resistance to water vapor transmission than unoriented PP [6]. These properties can be varied over a wide range by the choice of the manufacturing process.

Poly(vinyl chloride)

Poly(vinyl chloride), also known as vinyl or PVC, is made by low-pressure free radical polymerization of vinyl chloride at temperatures in the 100-160°F range [117]. Its chemical structure is shown below:



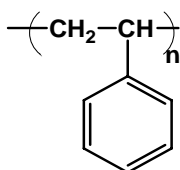
PVC is a versatile polymer that can be formulated to meet the requirements of many applications in packaging and other industries [108]. Its properties can be tuned over a very wide range by incorporating comonomers, plasticizers, and other additives. When used as a rigid sheet or bottle, little modification is required, but PVC requires the addition of plasticizers to make it useful as a barrier film for flexible packaging [108]. The plasticizers increase chain flexibility and reduce the processing temperature of PVC. For example, addition of 40 vol.% dioctyl phthalate plasticizer reduces the T_g of PVC from 100°C to about 5°C [142]. The increase in chain flexibility of plasticized PVC also results in a reduction in its gas barrier properties primarily as a result of higher diffusion coefficients in plasticized films. Figure 2.22 presents a comparison of diffusion coefficients of several penetrants in plasticized and unplasticized PVC films [143].

PVC has some drawbacks as a food-packaging material [108]: Vinyl chloride monomer is an animal carcinogen and causes liver cancer in humans. Thus the amount of monomer in the finished polymer should be brought down to 1 ppm or less. There is concern about the toxicity of plasticizers and other additives used in PVC. Moreover, there have also been concerns that incineration of chlorine-containing plastics can

possibly lead to the formation of dioxin, a chlorinated toxic molecule. Finally, the release of plasticizers over long periods of time can lead to gradual embrittlement of PVC films. However, none of these drawbacks significantly affect the functionality of PVC and it is used to make flexible films, rigid sheets and bottles for a variety of food (*e.g.*, fresh fruits, vegetables, and poultry packaging in the US) and non-food packaging applications [120].

Polystyrene

Polystyrene (PS) is made by the peroxide-catalyzed bulk or suspension polymerization of styrene [117]. The polymerization reaction takes place at low pressure and temperature in the range of 250-400°F, and the polymer chemical structure is given by:



Polymer molecular weight, which affects the processing characteristics of the resin, is often in the range of 40,000 to 220,000; variations in molecular weight can be obtained by changing the catalysts and polymerization conditions. PS is an amorphous, clear, hard, brittle, low-strength material with poor impact resistance [117]. It has low to moderate moisture and gas barrier properties [108]. Copolymerization with butadiene or other rubbers increases its impact strength and decreases stiffness [108]. This copolymer is commonly referred to as high impact polystyrene (HIPS). Comonomers such as alpha

methyl styrene can improve the heat resistance of PS by increasing the heat distortion temperature to 100°C or higher [108]. PS can be foamed by adding foaming agents such as hexane to the reaction mixture during the suspension polymerization. This so-called expanded polystyrene (EPS) is a very low density, yet highly rigid material that is used for making egg cartons, and trays for meat, poultry and other products [108]. However, EPS has poor gas barrier properties.

2.9 Improving Barrier Properties of Polymers

2.9.1 Barrier Structures

As mentioned in the previous sections, the principal application of barrier polymers is in the food and beverage packaging industries. Combining two or more polymers, or other materials, can achieve performance advantages not available in any of the materials taken alone. In many cases, to achieve better barrier performance, it is more efficient and economical to use a thin layer of an expensive high barrier polymer (*e.g.*, EVOH) sandwiched between layers of less expensive, moderate barrier, structural polymers (*e.g.*, PP, PET) than to increase the monolayer thickness of the moderate barrier polymer. Multilayer structures can be obtained by coextrusion, lamination, and coating. Barrier polymers may also be combined to form miscible and immiscible blends.

Multilayer Structures

Steady-state barrier properties of multilayer films can be described by their permeability, which can be calculated by treating the individual layers as resistances in series [2]:

$$\frac{1}{P'} = \frac{L_t}{P_t} = \frac{L_1}{P_1} + \frac{L_2}{P_2} + \dots + \frac{L_n}{P_n} \quad (2.38)$$

where P_t , L_t and P' are permeability, thickness, and permeance of the composite structure, and P_1, P_2, \dots, P_n and L_1, L_2, \dots, L_n are the permeabilities and thicknesses of the individual layers. The permeability P_t (or permeance P') can be used to evaluate the performance of the composite structure for packaging applications. Figure 2.23 illustrates the effect of barrier layer thickness on permeability of a hypothetical two-layer sheet, the permeability of the barrier layer being $0.1 \text{ cm}^3 \text{ mil}/(100 \text{ in}^2 \text{ day atm})$ and that of the non-barrier layer being $100 \text{ cm}^3 \text{ mil}/(100 \text{ in}^2 \text{ day atm})$. For moisture-sensitive polymers (*e.g.*, EVOH or nylon), it is important to use the permeability that corresponds to the effective RH that the layer will experience in the composite structure.

Coextrusion is one of the most cost-effective techniques for producing multilayer barrier polymer films [144]. Although coextruded films typically have three to seven layers, as many as eleven layers can be extruded simultaneously [145]. This technique allows for the thinnest possible layers of the individual polymer resins within the structure. Resins that do not bond well can be bonded together with an adhesive 'tie' layer [145]. The materials must be compatible in terms of their melt temperatures and viscosities in order to undergo simultaneous coextrusion. Figure 2.24 presents a

comparison of processing temperatures of various commonly used barrier polymers [146]. Figure 2.25 shows a cartoon of a typical nine-layer coextruded structure. A coextrusion line will have several different extruders, each extruder responsible for supplying individual polymer resins [144].

Coating and lamination are two additional processes for producing multilayer structures and are especially useful in applications where a non-polymeric material is part of the structure. Coatings can be melt extrusions of a polymer onto a base film or can be made by applying solutions or dispersions of polymers to the base film [145]. Barrier polymers that resist water vapor and provide gas barrier are often laminated to paper and paperboard. Cellophane, a flexible transparent gas barrier polymer, can also be made ‘moisture-proof’ by coating or laminating with other polymer films [6]. A commercial application of solvent coating with barrier polymers is vinylidene chloride resin dissolved in a polar solvent and coated onto cellophane or PET [2]. Water-based emulsion coatings of vinylidene chloride are used for plastic PET beer bottles, primarily in the United Kingdom. They can typically lower O₂ permeability of PET bottles by nearly 60% [82]. Several companies produce PVDC emulsions for coating films such as nylon, PE, PP, and PET to improve their O₂ and moisture barrier properties [82]. In the mid-1990s, PPG Industries, Inc. introduced BairocadeTM external epoxy-amine organic coatings for improving barrier properties of PET bottles [147,148]. It is claimed that these coatings can reduce O₂ permeability of PET bottles by a factor of 6 or more with the level of barrier improvement depending on the thickness and formulation used, and that coated

bottles extend the shelf life of carbonated beverages by a factor of 3, and beer by a factor of 20 relative to uncoated bottles [148].

Another way of improving barrier properties of polymers is by coating them with thin inorganic layers [82,149,150]. This can typically improve barrier properties by a factor of 100, whereas the thickness of the barrier coating applied is less than 0.5% of the base film [82]. Laminations and coatings of aluminum foil or aluminum oxide on barrier polymers can provide significant improvements in gas barrier properties [82]. These metallized films contain an extremely thin layer of aluminum, which not only enhances the barrier properties of the base film, but also provides a shiny metallic appearance. Because the layer is very thin, it does not appreciably affect the strength and flexibility of the base film [151]. The barrier properties of metallized films can approach those of pure aluminum foil. However, unlike aluminum foil, metallized films are not subject to flex-cracking and hence, are better at maintaining their barrier properties [151]. Barrier polymers that have been successfully metallized include PP, nylons, PET, and unplasticized PVC. As an example, 99% decrease in oxygen permeability and 98.5% decrease in water vapor permeability have been reported for metallized PET films as compared to unmetallized PET films [152]. Metallized films are widely used in the flexible packaging industry, an example being potato chip packages consisting of multilayer structures of oriented PP, PE, and metallized PP [153].

However, one of the main disadvantages of metallized structures is that they may not be transparent – a desirable feature for many packaging applications. In part to address this shortcoming, several alternative high barrier coating technologies, typically

producing amorphous carbon or glass-like layers, are being investigated. These newer coatings have achieved limited market penetration to date, with most of the commercial activity in Europe and Japan. It is still unclear what their eventual importance will be, but these technologies are being actively pursued. Among the various glass and ceramic materials used as barrier coatings, silicon dioxide (silica) has been the most widely used [82,150]. These barrier composite structures are clear, microwaveable, and recyclable. Electron beam treatment and plasma-enhanced chemical vapor deposition (PECVD) are two of the most widely used techniques for depositing thin silica layers on barrier polymers [82,154]. In the electron beam treatment, a high-energy electron beam source is used to vaporize silica, which then precipitates onto the polymer film, forming a continuous coating as the film passes through a vacuum chamber. The resulting coatings are uniform and can be as thin as 0.04 microns. PECVD has the advantage of being able to control coating density and thickness, by changing the process variables [154]. Figure 2.26 presents the effect of coating thickness on oxygen permeability of a PECVD silica-coated PET film [154]. Barrier properties of silica-coated polymers can be superior to those of high barrier polymers like PVDC and EVOH. Moreover, they are not influenced by moisture and temperature [82]. However, due to poor adhesion and mechanical properties, for all practical applications silica-coated films have to be laminated.

Recently, inorganic-organic hybrid polymers have been developed which can be used as laminating agents and in conjunction with silica to enhance barrier properties of polymers [155,156]. An example is ORMOCER[®] or organically modified ceramic (Fraunhofer Gesellschaft, Germany). Such materials can be used as coatings as well as

high-barrier laminating agents in multilayer structures. The use of ORMOCER[®] as a top layer on silica-coated PP can significantly improve its oxygen barrier properties as shown in Figure 2.27. The composite structure also offers good water vapor barrier properties. Similar improvements in barrier properties of PET have been reported [155]. Figure 2.28 shows a comparison of O₂ and water vapor barrier properties of different barrier polymer composite structures [157].

Another potential candidate as an effective barrier coating is diamond-like carbon (DLC) [149]. DLC refers to a group of amorphous, hard, and chemically inert materials consisting of carbon, bonded partially as diamond (sp³) and partially as graphite (sp²) and containing 0-40% hydrogen atoms. These coatings are transparent, flexible, extremely impermeable, biocompatible, and adhere well to a wide range of polymers.

Among the most recent commercial applications of barrier polymeric containers coated with thin inorganic layers is plastic beer packaging. Glaskin[™] (Tetra Pak, Geneva, Switzerland) is a proprietary technology that utilizes a vacuum deposition process for coating clear, extremely thin layers of silicon oxide on the inside of blown plastic bottles [158]. It offers excellent barrier properties for O₂, CO₂, and flavor compounds, and it is completely recyclable. For beer packaging, a shelf life of six months has been claimed using this technology. BESTPET[™] (Barrier Enhanced Silica Coated PET) is another silica-based coating technology patented by the Coca-Cola Company. The exterior surface of PET bottles is coated with a thin silica layer and improvements in barrier properties of PET by a factor of at least 2 have been claimed, which results in a shelf life of over six months for packaged beer [159]. A carbon-based high-barrier bottle

coating technology is ACTIS™ (Sidel, France) (Amorphous Carbon Treatment on Internal Surface technology) [160]. In this process, the internal surface of plastic bottles is coated with a 0.15 μm thick layer of highly hydrogenated amorphous carbon obtained from a food-safe gas (*e.g.*, acetylene) in its plasma state. This technology has been claimed to improve O₂ barrier properties of PET bottles by a factor of 30, and CO₂ barrier properties by a factor of 7. Another carbon-based DLC coating technology (Kirin Brewery, Japan) claims to improve the barrier properties of PET for O₂, CO₂, and H₂O by factors of 20, 7, and 8, respectively [159].

Miscible and Immiscible Blends

Polymer blending offers an alternative, simple, unique, and economical approach for improving barrier properties for several applications. In general, the goal is to add small amounts of a high barrier polymer (generally more expensive) to a selected matrix polymer (generally low cost) [69]. High-cost polymers such as PEN and LCPs can be blended with lower cost polymers like PET to achieve a balance of barrier properties and cost. A common objective of blending is to attenuate the deficiencies, while maintaining as much as possible the desirable properties of each component. Occasionally, synergistic effects result in blend properties better than those of the individual components [69]. Reactive blending is also possible, for example, with the mixing of different polyester polymers (transesterification), or polyester and nylon (polyesteramide formation) [69].

In general, polymer blends can be broadly classified as homogenous or miscible blends and multiphase or immiscible blends. The permeability coefficient, *P*, of miscible

blends as well as copolymers often follows an empirical semi-logarithmic additivity rule [69]:

$$\ln P = \phi_1 \ln P_1 + \phi_2 \ln P_2 \quad (2.39)$$

where ϕ_i is volume fraction of the i^{th} component, and P_i is the component's permeability coefficient. This simple additivity rule is generally obeyed only if there are no interactions between the components. Deviations from this rule can either be positive or negative depending on the nature and magnitude of interactions [69]. For example, a miscible blend of styrene-acrylonitrile copolymers (SAN) containing 9% acrylonitrile (AN) and tetramethyl bisphenol A polycarbonate (TMPC) shows negative deviations from the linear additivity rule indicating strong polymer-polymer interactions. On the other hand, blends of SAN containing 13.5 and 28% AN, and polymethylmethacrylate (PMMA) show positive deviation from the linear additivity rule [69].

When immiscible polymers are blended, or when inorganic filler is added to a polymer matrix, it results in the formation of a dispersion of one component in a continuous matrix of the other. Figure 2.29 shows several schematic examples of such systems [161]. Immiscible polymer blends are far more common than miscible blends [69]. Barrier properties of an immiscible blend depend on the permeabilities of the individual components, their volume fractions, phase continuity, and the aspect ratio of the dispersed (or discontinuous) phase [69]. The aspect ratio, L/W , refers to the shape of the particles in the dispersed phase. Spheres and cubes have an aspect ratio of 1, whereas platelets and rods have higher aspect ratios.

The presence of an impermeable dispersed phase lowers the permeability by increasing tortuosity. The Maxwell model can be used to calculate the permeability of a polymer blend, P , with impermeable spherical particles dispersed in a continuous phase [69]:

$$P = \frac{P_m(1 - \phi_d)}{1 + \phi_d/2} \quad (2.40)$$

where P_m is permeability of the continuous polymer phase, and ϕ_d is volume fraction of the dispersed phase. Barrer reviewed different models for permeation in a heterogeneous media wherein the dispersed phase is impermeable and represented by different geometrical shapes [161]. Several modifications to the Maxwell model have been made to describe permeation behavior in platelets and ellipsoid-shaped particles dispersed in a more permeable continuous phase [69]. For example, oxygen barrier properties of blends of oriented PET and EVOH have been successfully modeled with one such modification (Fricke model) [162]. Robeson extended the Maxwell model by applying it to blends in which both the polymers contribute to the continuous phase [69]. This model considers the practical implications of attempts to increase the barrier performance of a moderate barrier polymer by adding small amounts of a high barrier polymer to it. According to this model, a multilayer structure provides the highest barrier followed by a blend in which the high barrier polymer is the continuous phase [69].

Figure 2.30 shows the improvement in O_2 barrier properties of PE-EVOH blends as a function of EVOH volume fraction. Blends of PET with MXD-6 nylon (Mitsubishi Gas Chemical Co.) have shown significant reduction in O_2 and CO_2 permeability

coefficients relative to those of PET and are being investigated for use in plastic containers [69]. PET-EVOH blends have been promoted (Kuraray Co.) for potential applications in the beverage industry [82]. The transport properties of PET-LCP blends have also been studied and Table 2.10 shows the reductions in permeabilities of O₂, N₂, and CO₂ that have been reported for blown films containing 2, 10, and 30 wt.% LCP [163].

Polymer Nanocomposites

Polymer nanocomposites are immiscible blends made by adding nanometer-size particles to barrier polymers. Since nanometer-size grains, fibers, and plates have dramatically increased surface area compared to conventional-size materials, the chemistry of nanosized materials is different from other conventional materials. Polymers filled with nanometer-size particles have significantly different properties than those filled with conventional inorganic materials [164]. Properties of nanocomposites such as high tensile strength can be achieved by using higher conventional filler loading, but other properties such as improved clarity cannot be duplicated by filled resins at any loading [165].

Polymer nanocomposites were developed in the late 1980s, and were first commercialized by Toyota, which used nanocomposite parts in one of its car models for several years [82]. Initial developments focussed on the use of nylon resins and very fine smectite clay particles, with surface area of about 750 m²/g, as fillers [82]. Ube Industries developed its first nylon nanocomposite in 1989 for an automotive timing belt cover.

They have also developed other nylon nanocomposites called nylon clay hybrids (NCH) [82]. More recently, novel nanocomposite nylon 6 resins developed by Honeywell Engineered Applications and Solutions (Morristown, NJ) have been claimed to improve O₂ and CO₂ barrier properties by a factor of three to four [166]. It has also been claimed that these nanocomposites double the heat resistance of nylon 6 and improve other mechanical properties by 30 to 50% [166]. Others such as Nanocor, Inc. [167] are also actively developing nanocomposites for enhanced barrier performance. Commercial products are available for PP and fluoropolymers. Some of the other potential candidate polymers for nanocomposites include polyesters, PS, and ethylene vinyl acetate copolymers [82]. Several polymer nanocomposites, including amorphous nylon and EVOH matrices, intended for high barrier applications are in various stages of development.

2.9.2 Oxygen-Scavenging Systems

Another strategy for improving the barrier properties of polymers is the introduction of reactive groups in the polymer. These groups can reduce the transmission of penetrants like oxygen and water vapor and the term “active barrier” is often used to describe this approach to distinguish it from “passive barrier” packages that rely on reduced permeability to decrease gas transmission. By using an oxygen-scavenger, which absorbs the residual oxygen after packaging, quality changes of oxygen-sensitive foods can be minimized [168-170]. Although oxygen-scavenging technology is rapidly evolving and encompasses a wide variety of chemistries, the majority of current

commercial oxygen-scavenger packages probably still employ sachets that remove oxygen from the headspace *via* iron oxidation. Ageless[®] (Mitsubishi Gas Chemical Co., Japan) oxygen absorbers are the most commonly used sachets that are placed inside the food package [82]. If the initial oxygen concentration and oxygen permeability of the packaging polymer is known, then an oxygen-scavenger can be chosen with a higher capacity than the theoretically needed capacity, and near total absence of oxygen can be maintained during the expected shelf life of the product [168]. Other iron-based oxygen-scavenger sachets are ATCO[®] (Standa Ind., France), Freshlizer[®] (Toppan Printing Co., Japan), Vitalon[®] (Toagosei Chem. Ind., Japan), Freshpax[®] (Multisorb Technologies Inc., USA), and Sanso-cut[®] (Finetec Co., Japan) [168].

An alternative to sachets is the incorporation of the oxygen-scavenger into the barrier polymer structure itself [168]. An example of this strategy is Oxbar[™] (Crown Cork And Seal, UK), which involves cobalt-catalyzed oxidation of nylon MXD-6 polymer used in multilayer PET bottles for packaging of beverages. Another example of a polymer-based absorber is Amosorb[®] (Amoco Chemicals, USA), which can reportedly be incorporated into various rigid and flexible packaging structures [168]. This is a rapidly evolving field and several other companies have also introduced or announced oxygen-scavenging resins. Among those active in this area are: EVAL Co., USA, Kuraray Co. Ltd., Japan, and Darex Co., USA with DarEval[®] [171], Owens-Illinois/Continental PET Technologies with CPTX-312, Honeywell International, Inc. with scavenging nylon resin [172], Cryovac with OS 1000, and Chevron Phillips Chemical Co. with their OSP scavengers [173]. While the speed and capacity of oxygen-

scavenging films are considerably lower than iron-based oxygen-scavenger sachets [168], oxygen ingress into the package can be reduced to very low levels with appropriately designed scavenger structures. Figure 2.31 presents an example of the reduction in oxygen transmission rate due to oxygen scavenging in blends of PET and nylon MXD-6 [174]. Scavengers can also be incorporated into the liner of bottle closures where they can significantly reduce the ingress of oxygen into the package through the closure liner [175].

A recent study by Cussler *et al.* [176] has shown that incorporation of inorganic fillers as well as reactive groups in barrier polymer films can significantly improve the shelf life of packages. According to their theory, the presence of immobile reactive groups dramatically increases the time lag (*i.e.*, the time required to achieve steady-state permeability), but do not affect steady-state transport of penetrants across barrier polymer films. For example, in LDPE and PVDC films containing 10% flakes of mica or clay and linolenic acid as the oxygen-scavenging species, the time lag for permeation of O₂ dramatically increased by about three orders of magnitude to 40 hours and 3 years, respectively [176].

2.10 Conclusions

Barrier polymers are widely used in food, beverage, and other packaging industries. Some of their advantages over traditional packaging materials like glass, paper, and metals are flexibility, light weight, toughness, versatility, and printability. The selection of a polymer for a particular packaging application depends on its barrier as well as other physical properties. A comparison of these properties and current as well as potential future applications for different types of barrier polymers has been presented. Additionally, important factors governing permeability (*e.g.*, penetrant size, polymer chemical structure, temperature, humidity, *etc.*) as well as ways to measure and predict permeability have also been discussed.

Unlike glass and metals, no polymer offers an infinite gas barrier. Despite this limitation, monolayer polymer structures in many instances satisfy the barrier requirements for a package. In other situations, combinations of different polymers, or polymers with inorganic materials, in the form of multilayer structures or blends, can provide cost-effective barrier for the intended shelf life of packaged products. As a result, plastic packaging is ubiquitous. Market pressures, however, drive the need for continual improvements in packaging materials. Hence, there is an ongoing interest in improving the barrier properties of polymers used in packaging, and the search for improved barrier polymers and structures is ongoing. Inorganic materials such as silicon & aluminum oxides and clays can be used to significantly enhance gas barrier and other mechanical properties of polymers. One area of recent activity is polymer nanocomposites, which involves dispersion of nanoscale barrier particles in a polymer matrix. A considerable

amount of research is also being focussed on techniques for developing thin layers of inorganic coatings on barrier polymer films and containers. In addition, work in the field of oxygen-scavenging technologies (so-called ‘active packaging systems’) has resulted in several developments. While advances in these newer barrier technologies have recently opened up several commercial applications, with plastic beer packaging being perhaps the most publicized, it is much too early to accurately predict their eventual success in the market place. Constructions with established “passive” barrier polymers currently dominate the barrier packaging market, and these materials are expected to be commercially important for many years to come.

Table 2.1 Table of common gas permeability units with conversion factors^a

To obtain → Given ↓	Barrer	$\frac{\text{cc cm}}{\text{cm}^2 \text{ s cmHg}}$	$\frac{\text{cc cm}}{\text{cm}^2 \text{ s atm}}$	$\frac{\text{cc cm}}{\text{cm}^2 \text{ s Pa}}$	$\frac{\text{mols cm}}{\text{cm}^2 \text{ s cmHg}}$	$\frac{\text{mols m}}{\text{m}^2 \text{ s Pa}}$	$\frac{\text{cc mil}}{100 \text{ in}^2 \text{ day atm}}$	$\frac{\text{cc } 20\mu\text{m}}{\text{m}^2 \text{ day atm}}$
Barrer	1	1.00×10^{-10}	7.60×10^{-9}	7.501×10^{-14}	4.461×10^{-15}	3.346×10^{-16}	1.668×10^2	3.283×10^3
$\frac{\text{cc cm}}{\text{cm}^2 \text{ s cmHg}}$	1.00×10^{10}	1	76	7.501×10^{-4}	4.461×10^{-5}	3.346×10^{-6}	1.668×10^{12}	3.283×10^{13}
$\frac{\text{cc cm}}{\text{cm}^2 \text{ s atm}}$	1.316×10^8	1.316×10^{-2}	1	9.869×10^{-6}	5.87×10^{-7}	4.403×10^{-8}	2.195×10^{10}	4.32×10^{11}
$\frac{\text{cc cm}}{\text{cm}^2 \text{ s Pa}}$	1.333×10^{13}	1.333×10^3	1.013×10^5	1	5.948×10^{-2}	4.461×10^{-3}	2.224×10^{15}	4.377×10^{16}
$\frac{\text{mols cm}}{\text{cm}^2 \text{ s cmHg}}$	2.241×10^{14}	2.241×10^4	1.703×10^6	16.81	1	7.501×10^{-2}	3.738×10^{16}	7.359×10^{17}
$\frac{\text{mols m}}{\text{m}^2 \text{ s Pa}}$	2.988×10^{15}	2.988×10^5	2.271×10^7	2.241×10^2	13.33	1	4.984×10^{17}	9.81×10^{18}
$\frac{\text{cc mil}}{100 \text{ in}^2 \text{ day atm}}$	5.996×10^{-3}	5.996×10^{-13}	4.557×10^{-11}	4.497×10^{-16}	2.675×10^{-17}	2.007×10^{-18}	1	19.68
$\frac{\text{cc } 20\mu\text{m}}{\text{m}^2 \text{ day atm}}$	3.046×10^{-4}	3.046×10^{-14}	2.315×10^{-12}	2.285×10^{-17}	1.359×10^{-18}	1.019×10^{-19}	5.08×10^{-2}	1

^a Given permeability in the units shown in one element of the first column, convert it to the units shown in one element of the first row by multiplying the original permeability by the factor at the intersection of the row and column of interest. For example, a value of 2 cc 20 μ m/(m² day atm) is equal to (2 \times 0.0508) or 0.1 cc mil/(100 in² day atm). In this table and throughout the chapter, cc (or cm³) has been used to denote cubic centimeters of gas as measured at standard temperature and pressure (STP) conditions, which are 0°C and 1 atmosphere.

Table 2.2 Table of common water vapor transmission rate (WVTR) units with conversion factors ^a

To obtain → Given ↓	$\frac{\text{mols m}}{\text{m}^2 \text{ s}}$	$\frac{\text{gm mil}}{100 \text{ in}^2 \text{ day}}$	$\frac{\text{gm cm}}{\text{m}^2 \text{ day}}$
$\frac{\text{mols m}}{\text{m}^2 \text{ s}}$	1	3.95×10^9	1.55×10^8
$\frac{\text{gm mil}}{100 \text{ in}^2 \text{ day}}$	2.53×10^{-10}	1	3.94×10^{-2}
$\frac{\text{gm cm}}{\text{m}^2 \text{ day}}$	6.45×10^{-9}	25.4	1

^a Given a WVTR value in units shown in one element of the first column, convert it to the units shown in one element of the first row by multiplying the original WVTR value by the factor at the intersection of the row and column of interest. For example, a value of 2 gm cm/(m² day) is equal to (2 × 25.4) or 50.8 gm mil/(100 in² day).

Table 2.3 Effect of orientation on oxygen permeability characteristics of semicrystalline and amorphous barrier resins [79]

Barrier polymer resins	Oxygen Permeability (23.5 °C, 65% RH) (cm ³ mil / (100 in ² day atm))
Semicrystalline resins	
<i>VDC copolymer</i> ^a	
Compression molded film	0.20 ± 0.02
Extrusion cast film	0.20 ± 0.01
Biaxially oriented – 2.5X	0.30 ± 0.01
<i>Aromatic Nylon MXD-6</i> ^b	
Extrusion cast	0.37 ± 0.09
Biaxially oriented – 2X	0.39
Amorphous resins	
<i>Amorphous Nylon Selar PA 3426</i> ^c	
Extrusion cast film	1.40 ± 0.31
Uniaxially oriented – 2.5X	1.14 ± 0.07
Biaxially oriented – 2.5X	1.01 ± 0.01
<i>Polyacrylic-imide XHTA-50A</i> ^d	
Extrusion cast	3.12 ± 0.17
Uniaxially oriented – 2X	2.95 ± 0.04
2.5X	2.84
Biaxially oriented – 2X	2.76 ± 0.03

- ^a The Dow Chemical Company's Vinylidene chloride/vinyl chloride copolymer (experimental grade XU 32009.02)
- ^b Trademark of Mitsubishi Gas Chemical Co., Japan
- ^c Trademark of E.I. du Pont de Nemours & Co.
- ^d Trademark of Rohm & Haas

Table 2.4 Physical, mechanical, optical, and chemical properties of some commonly used barrier polymers [108]

Property	HDPE	LDPE	PP	PET	PVC	PS	PVDC	Nylon 6	EVOH
Density (g/cm ³)	0.945-0.967	0.915-0.925	0.90	1.4	1.22-1.36	1.05	1.6-1.7	1.14	1.14-1.19
Glass transition temp. (°C)	-55	-25	-20	80	~80	100	-17	50	
Yield (m ² /kg) 1 mil	41.2	42.6	44	28.4	28	38	24	35	32.7-34.7
Tensile strength (kpsi)	2.5-6	1.5-5	20-30	25-33	4-8	8-12	8-16	25-37	1.2-1.7
Tensile modulus, 1% secant (kpsi)	125	20-40	350	700	350-600	400-475	50-150	250-300	300-385
Elongation at break (%)	200-600	200-600	50-275	70-130	100-400	2-30	50-100	70-120	120-280
Tear strength (lb/in)	-	100-500	1000-1500	1000-2000	100-300	300-1000	2	500-800	-
Chemical resistance	Inert	Inert	Inert	Inert	Inert	Inert (except oils, greases)		Inert, sorbs water	Inert
Haze (%)	3	5-10	3	2	1-2	1	1-5	1.5	1-2
Light transmission (%)	-	65	80	88	90	92	90	88	90
Heat-seal temp. range (°F)	275-310	250-350	200-300	275-350	280-340	250-350	250-300	250-350	350-400
Service temp. range (°F)	-40 to 250	-70 to 180	40 to 250	-100 to 300	-20 to 150	-80 to 175	0 to 275	-100 to 400	0 to 300

Table 2.5 Oxygen and carbon dioxide permeabilities of various high and moderate barrier polymers [6]

Barrier Polymer	Gas Permeability (cm ³ mil/(100 in ² day atm)) (75% RH and 23-25°C except as noted)	
	Oxygen	Carbon Dioxide
EVOH, 27 mol% ethylene	0.03 (20°C)	0.04 (20°C, 65% RH)
P(VDC-AN) barrier coating	0.04	0.1
Liquid crystalline polymer ^a	0.06 (100% RH)	
EVOH, 44 mol% ethylene	0.07 (20°C)	0.2 (20°C, 65% RH)
PVDC coextrusion resin	0.10	0.25
Nylon MXD-6 oriented film	0.17	
BLOX™ 4000 series PHAE resin ^b	0.2 (80% RH)	
Nitrile resin	0.65	1.6
Amorphous nylon	1.2	4.0 (30°C, 80% RH)
PEN polyester ^c	1.2	
Nylon 6, biaxially oriented	2.6	5.8 (dry)
PET, 25% crystalline (bottle wall)	4.8	24
PVC, rigid	5.0	20
Nylon 6, unoriented	6.6	10.2
Aclar™ 33C PCTFE film ^d	7.0 (0% RH)	16 (0% RH)
PP, biaxially oriented	150	548
HDPE, molded	185	580
MDPE, molded	250	1000
PS film, oriented	365	900
LDPE, molded	498	2500

- a Vectra[®] A950 LCP film (Hoechst AG) [177]
- b [133] BLOX[™] is a trademark of The Dow Chemical Co. (Midland, MI)
- c Ref [82]
- d [178] Aclar[™] is a trademark of Allied Signal Corp. (Morristown, NJ)

Table 2.6 Water vapor transmission rates of various high and moderate barrier polymers [6]

Barrier Polymer	Water Vapor Transmission Rate (gm mil/(100 in ² day)) (90% RH, 37.8°C)
P(VDC-AN) barrier coating	0.02
Aclar TM 33C PCTFE film ^a	0.025
PVDC coextrusion resin	0.09
Liquid crystalline polymer ^b	0.15 (100% RH)
PP, biaxially oriented	0.25
HDPE, molded	0.3
MDPE, molded	0.7
PVC, rigid	0.9
LDPE, molded	1.0
Nylon MXD-6 oriented film	1.2
EVOH, 44 mol% ethylene	1.4
PET, 25% crystalline (bottle wall)	1.8
Nitrile resin	4.0
EVOH, 27 mol% ethylene	5.7
PS film, oriented	7.1
Nylon 6, biaxially oriented	10
Amorphous nylon	10
Nylon 6, unoriented	15

^a [178] AclarTM is a trademark of Allied Signal Corp. (Morristown, NJ)

^b [177] Vectra[®] A950 LCP film (Hoechst AG)

Table 2.7 Permeability, diffusivity, and solubility coefficients of flavor and aroma compounds in various high and moderate barrier polymers [2] at 25°C and 0% RH

Flavor/aroma compound	Permeability (10^{-22} kg cm/(cm ² s Pa)) ^a	Diffusivity (cm ² /s)	Solubility (kg/cm ³ Pa)
<i>Ethylene Vinyl Alcohol Copolymer^b</i>			
ethyl hexanoate	0.41	3.2×10^{-14}	1.3×10^{-9}
ethyl 2-methylbutyrate	0.3	6.7×10^{-14}	4.7×10^{-10}
hexanol	1.2	2.6×10^{-13}	4.6×10^{-10}
trans-2-hexenal	110	6.4×10^{-13}	1.8×10^{-8}
d-limonene	0.5	1.1×10^{-13}	4.5×10^{-10}
3-octanone	0.2	1.0×10^{-14}	2.0×10^{-9}
propyl butyrate	1.2	2.7×10^{-13}	4.5×10^{-10}
<i>Vinylidene Chloride Copolymer^b</i>			
ethyl hexanoate	570	8.0×10^{-14}	7.1×10^{-7}
ethyl 2-methylbutyrate	3.2	1.9×10^{-13}	1.7×10^{-9}
hexanol	40	5.2×10^{-13}	7.7×10^{-9}
trans-2-hexenal	240	1.8×10^{-13}	1.4×10^{-7}
d-limonene	32	3.3×10^{-13}	9.7×10^{-9}
3-octanone	52	1.3×10^{-14}	4.0×10^{-7}
propyl butyrate	42	4.4×10^{-14}	9.4×10^{-8}
dipropyl disulfide	270	2.6×10^{-14}	1.0×10^{-6}

Table 2.7 (continued)

Flavor/aroma compound	Permeability (10^{-22} kg cm/(cm ² s Pa)) ^a	Diffusivity (cm ² /s)	Solubility (kg/cm ³ Pa)
<i>Low Density Polyethylene</i>			
ethyl hexanoate	4.1×10^6	5.2×10^{-9}	7.8×10^{-8}
ethyl 2-methylbutyrate	4.9×10^5	2.4×10^{-9}	2.3×10^{-8}
hexanol	9.7×10^5	4.6×10^{-9}	2.3×10^{-8}
trans-2-hexenal	8.1×10^5		
d-limonene	4.3×10^6		
3-octanone	6.8×10^6	5.6×10^{-9}	1.2×10^{-7}
propyl butyrate	1.5×10^6	5.0×10^{-9}	3.0×10^{-8}
dipropyl disulfide	6.8×10^6	7.3×10^{-10}	9.3×10^{-7}
<i>High Density Polyethylene</i>			
d-limonene	3.5×10^6	1.7×10^{-9}	2.5×10^{-7}
menthone	5.2×10^6	9.1×10^{-9}	4.7×10^{-7}
methyl salicylate	1.1×10^7	8.7×10^{-10}	1.6×10^{-6}
<i>Polypropylene</i>			
2-butanone	8.5×10^3	2.1×10^{-11}	4.0×10^{-8}
ethyl butyrate	9.5×10^3	1.8×10^{-11}	5.3×10^{-8}
ethyl hexanoate	8.7×10^4	3.1×10^{-11}	2.8×10^{-7}
d-limonene	1.6×10^4	7.4×10^{-12}	2.1×10^{-7}
<i>Poly(ethylene terephthalate)^c</i>			
d-limonene	1.5	6.0×10^{-13}	

- ^a To convert the permeability values to $\text{cm}^3 \text{ mil} / (100 \text{ in}^2 \text{ day atm})$, multiply the values provided in the table by $4.98 \times 10^{22} / \text{MW}$, where MW is penetrant molecular weight (g/mol).
- ^b Values have been extrapolated from higher temperatures
- ^c [179] 25°C; Values are not expected to show any significant variations with RH.

Table 2.8 Compositions of commercial, high barrier nitrile copolymers [2]

Polymer	Manufacturer	Chemical Composition ^a
Lopac TM	Monsanto Co.	70% acrylonitrile + 30% styrene
Barex TM	Sohio	74% acrylonitrile + 26% methyl methacrylate + 10% butadiene graft rubber
Cycopac TM	Borg-Warner Chemicals	74% acrylonitrile + 26% styrene + 10% butadiene graft rubber

^a Data from FDA regulations for corresponding materials

Table 2.9 Comparison of properties of biaxially oriented LCP and PET films [128]

Property	Biaxially oriented LCP film ^a	Biaxially oriented PET film ^b
Tensile strength (MPa)	240	170
Tensile modulus (GPa)	12.4	3.5
Oxygen permeability ^c (cm ³ mil/(100 in ² day atm))	0.05	4.8
Water vapor permeability ^d (gm mil/(100 in ² day atm))	0.02	1.7
Density (gm/cm ³)	1.4	1.4
Upper use temperature (°C)	> 250	120
Tear resistance (kN/m)		
Initiation	595	35
Propagation	175-525	9-53

^a Vectra[®] (Hoechst AG) isotropic LCP film (orientation angle = 45°)

^b Mylar[®] (Dupont) isotropic PET film (orientation angle = 45°)

^c Permeability value at 25°C (and unspecified RH)

^d Permeability value at 25°C and 90% RH

Table 2.10 Gas permeabilities of LCP-PET blends [69]

%LCP ^a in PET	CO ₂ permeability ^b	O ₂ permeability ^b	N ₂ permeability ^b
0	114.5	21.3	5.1
2	78.1	14.9	2.6
10	65.8	12.0	3.1
30	34.5	5.5	2.0

^a Rodrun[®] LC3000 LCP

^b Units are (cm³ mil/(100 in² day atm))

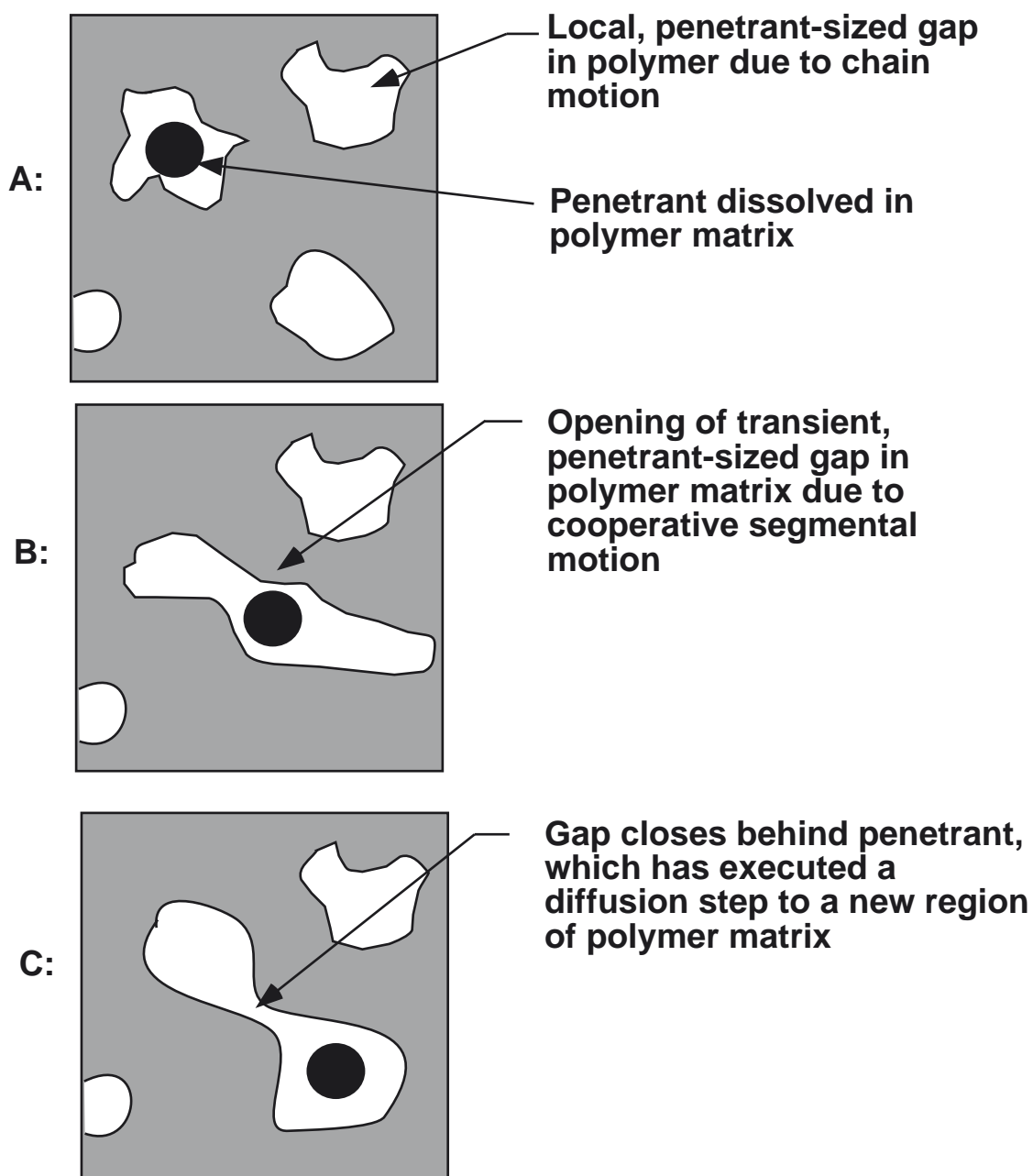


Figure 2.1 Cartoon depicting mechanism of penetrant transport in polymers [41].

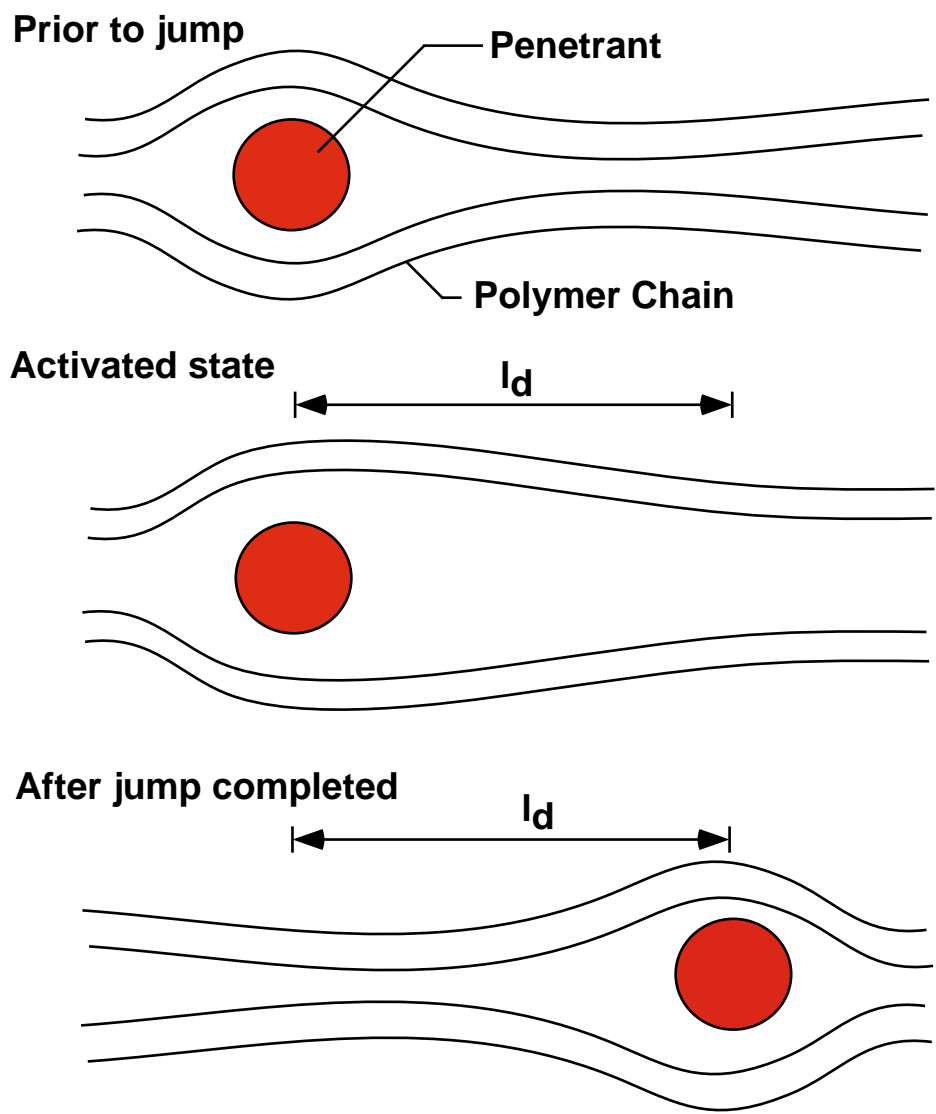


Figure 2.2 Cartoon depicting polymer chain position before, during, and after a diffusion step by a penetrant molecule [42].

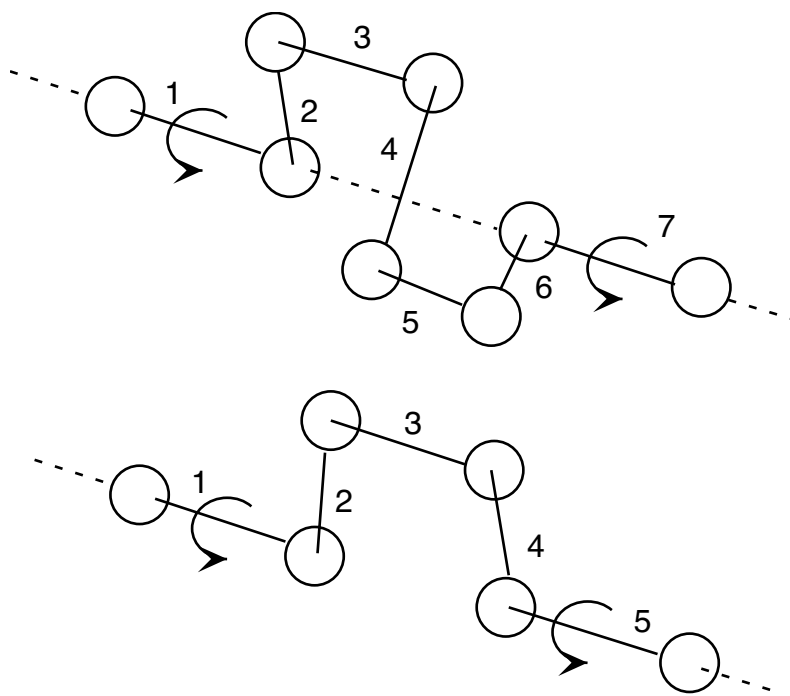


Figure 2.3 Crankshaft Motion – An example of local segmental dynamics in polyolefins. Each ball represents, for example, a methylene (*i.e.*, CH₂) unit in polyethylene and the solid lines represent the covalent chemical bonds between neighboring CH₂ groups. Such molecular motions are believed to be important in providing pathways for diffusion of small molecules in polymers. The crankshaft motion requires the simultaneous rotation of several contiguous methylene units about bonds 1 and 7 or 1 and 5 [42].

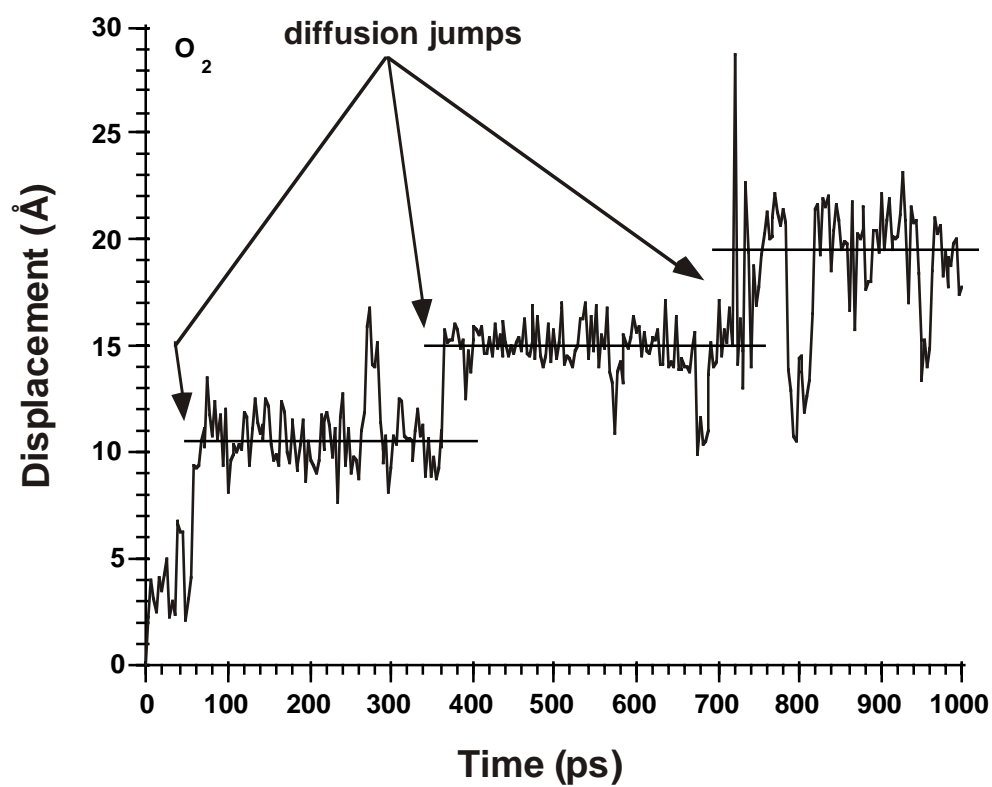


Figure 2.4 Computer simulation of the displacement of an oxygen molecule in poly(2,6-dimethyl-1,4-phenylene oxide) as a function of time [44].

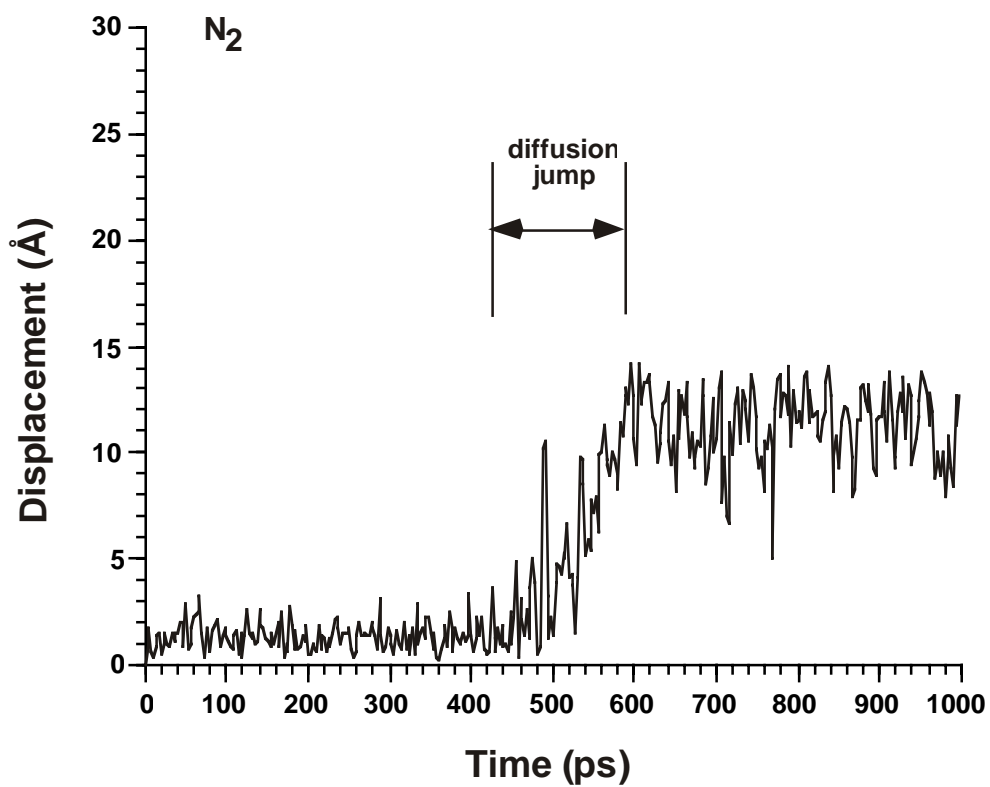


Figure 2.5 Computer simulation of the displacement of a nitrogen molecule in poly(2,6-dimethyl-1,4-phenylene oxide) as a function of time [44].

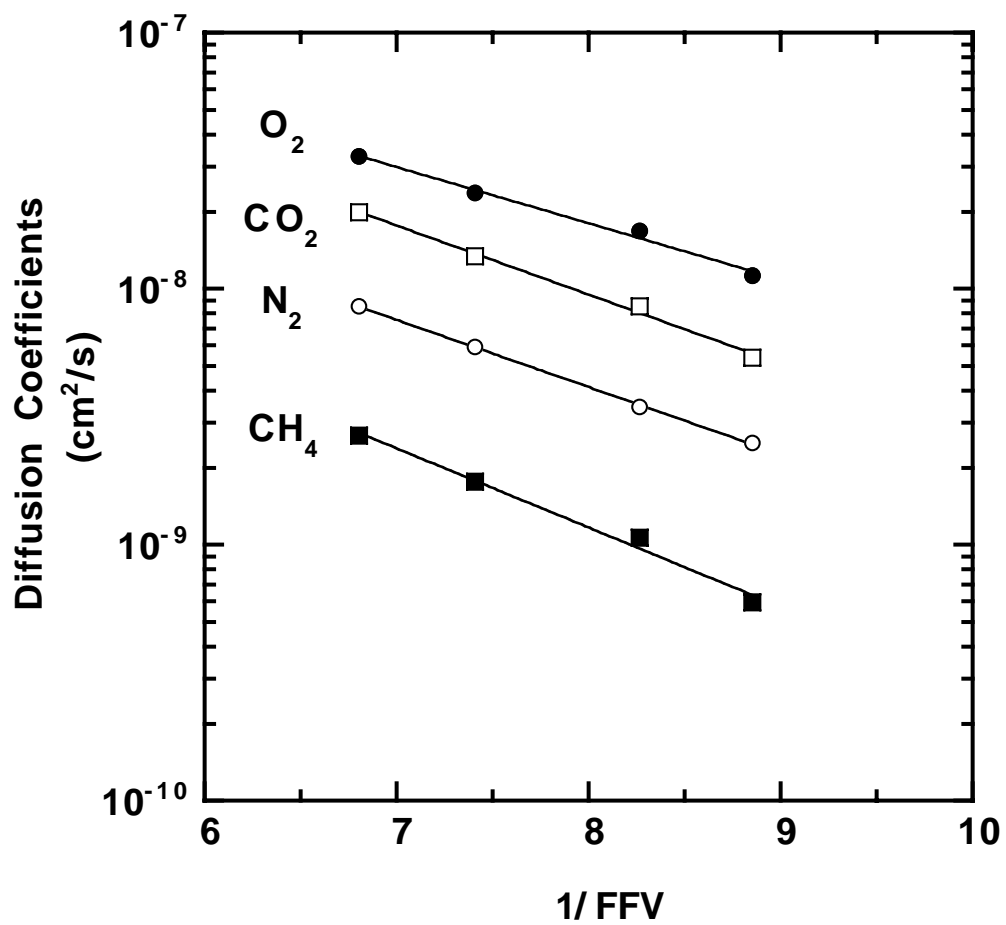


Figure 2.6 Correlation of gas diffusion coefficients with inverse of polymer fractional free volume in a series of substituted polysulfones [48].

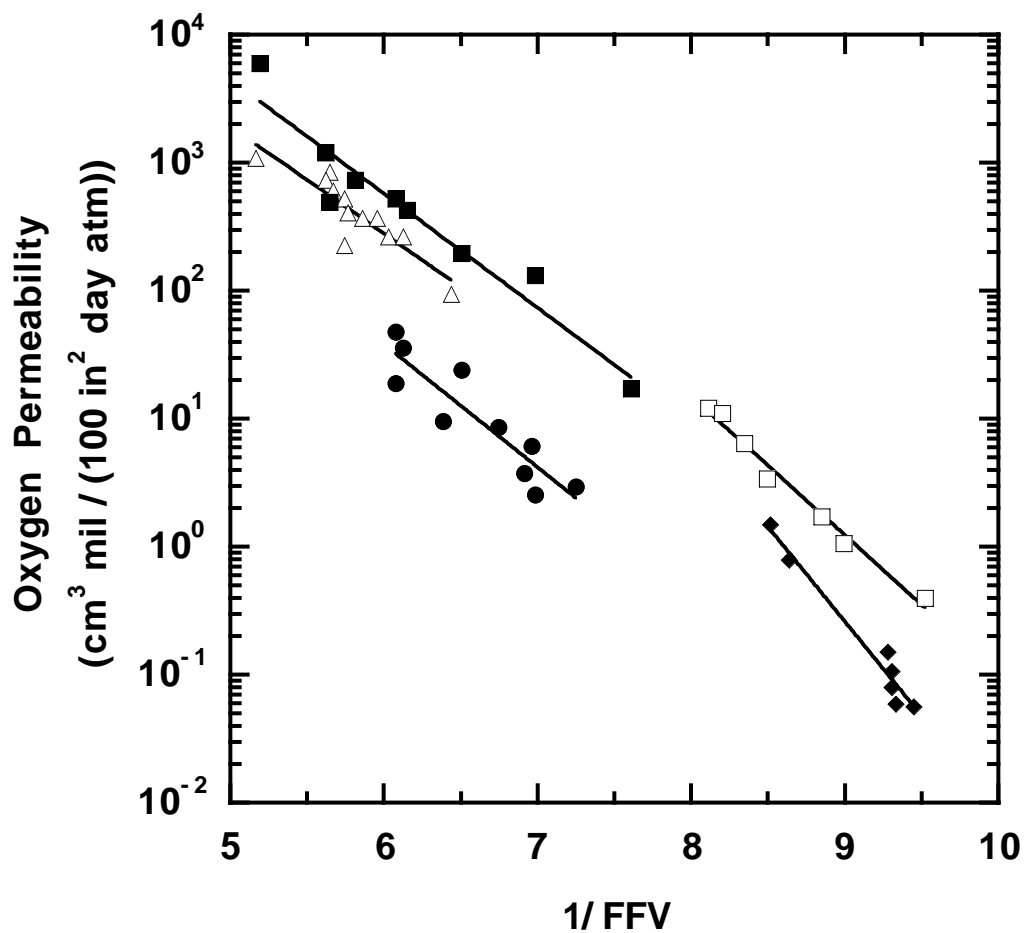


Figure 2.7 Correlation of oxygen permeability with inverse of polymer fractional free volume for several families of amorphous, glassy polymers and liquid crystalline polymers [49]. (■) Polystyrene (35°C), (Δ) Polycarbonates (35°C), (●) Polyesters (30°C), (□) Polyamides (25°C), (◆) Liquid Crystalline Polymers (35°C)

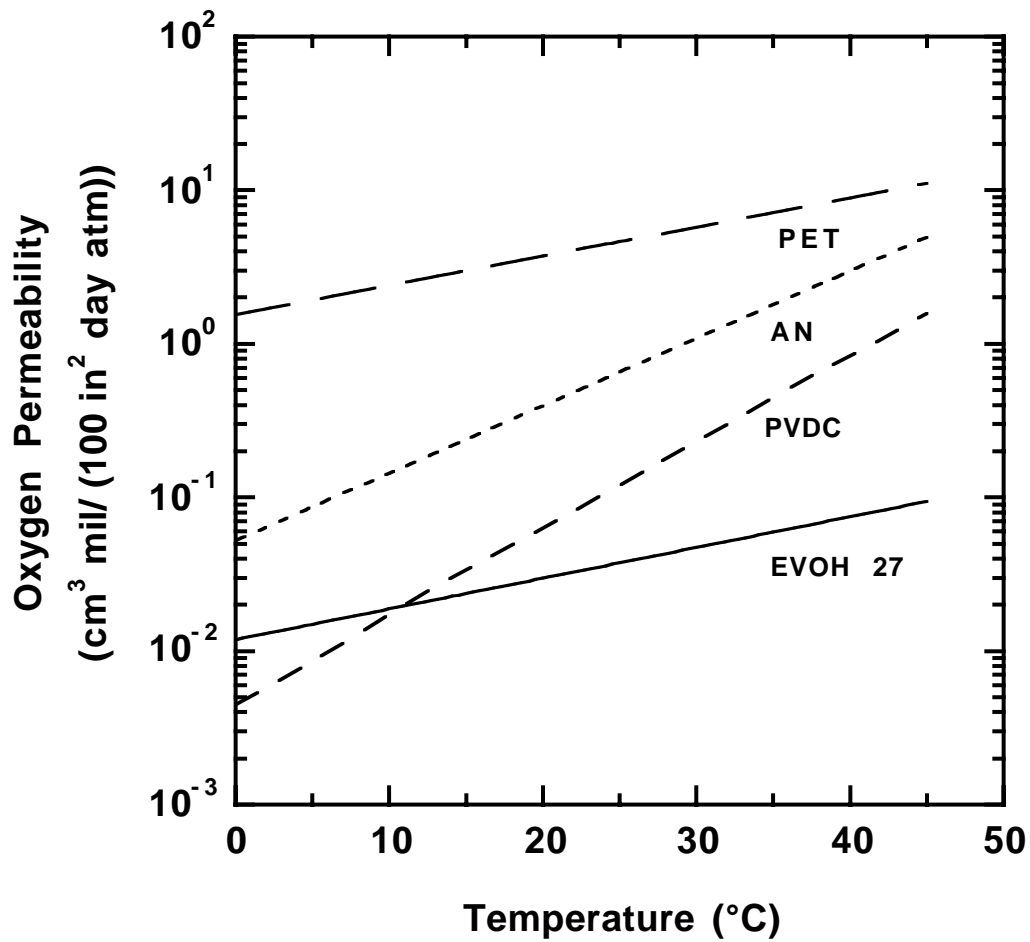


Figure 2.8 Effect of temperature on oxygen permeability at 75% relative humidity. PET is poly(ethylene terephthalate), AN is an acrylonitrile-styrene copolymer, PVDC is vinylidene chloride-vinyl chloride copolymer (coextrusion resin), and EVOH 27 is ethylene vinyl alcohol copolymer containing 27 mol% ethylene [6].

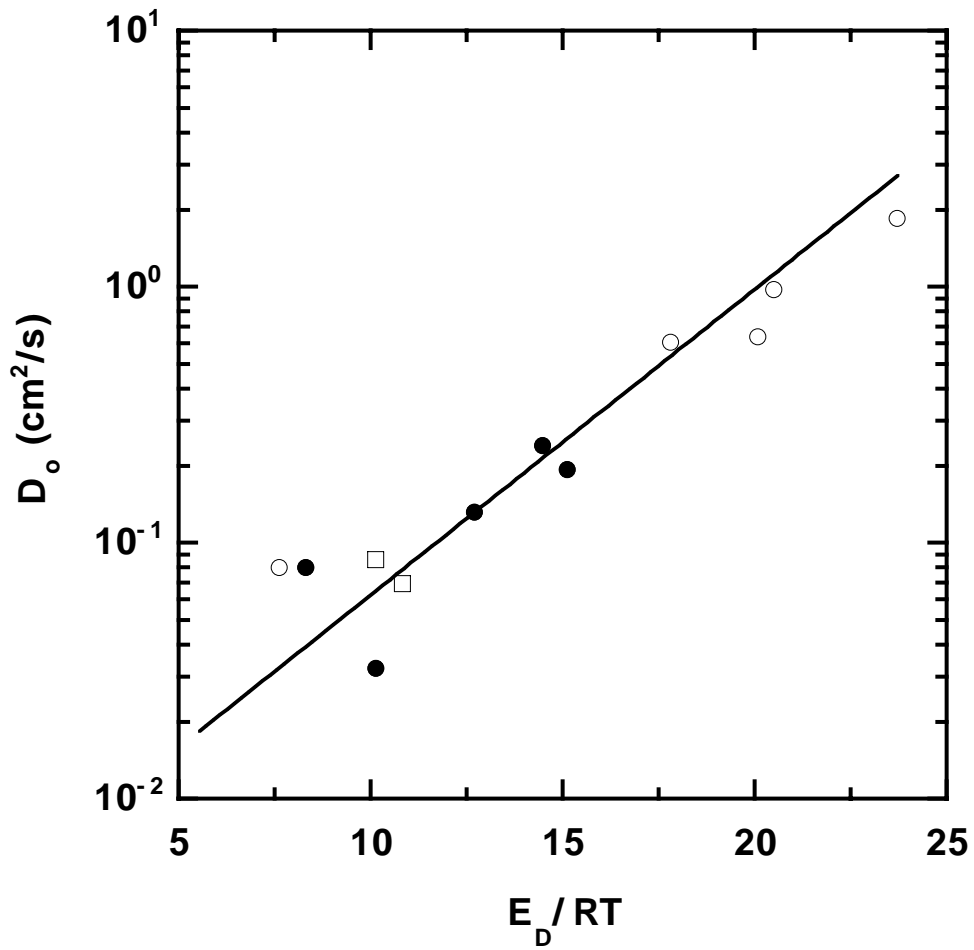


Figure 2.9 Correlation of D_o with E_D/RT for glassy polymers [7]. (○) Poly(ethylene terephthalate), (●) Bisphenol-A Polycarbonate (PC), (□) Tetramethyl Bisphenol-A PC (TMPC)

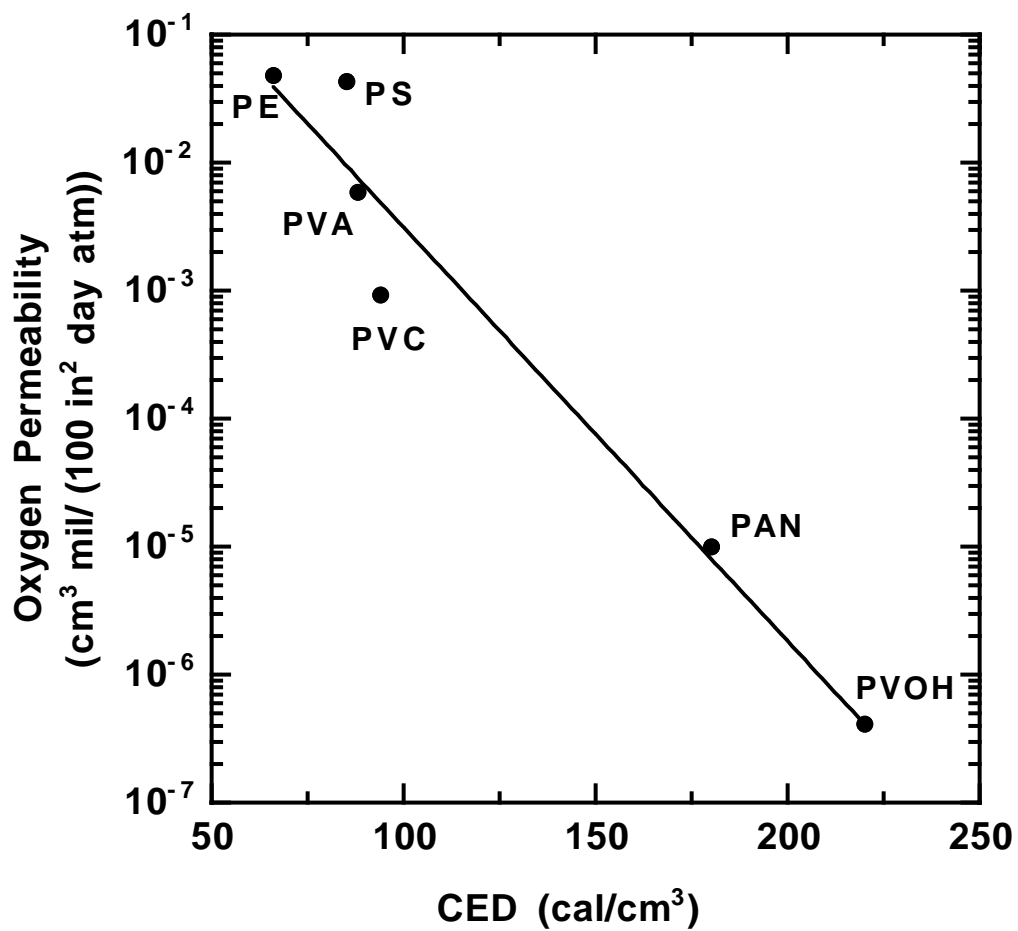


Figure 2.10 Effect of cohesive energy density (CED) on oxygen permeability for six barrier polymers: Polyethylene (PE), Polystyrene (PS), Poly(vinyl acetate) (PVA), Poly(vinyl chloride) (PVC), Polyacrylonitrile (PAN), Poly(vinyl alcohol) (PVOH) [66,67].

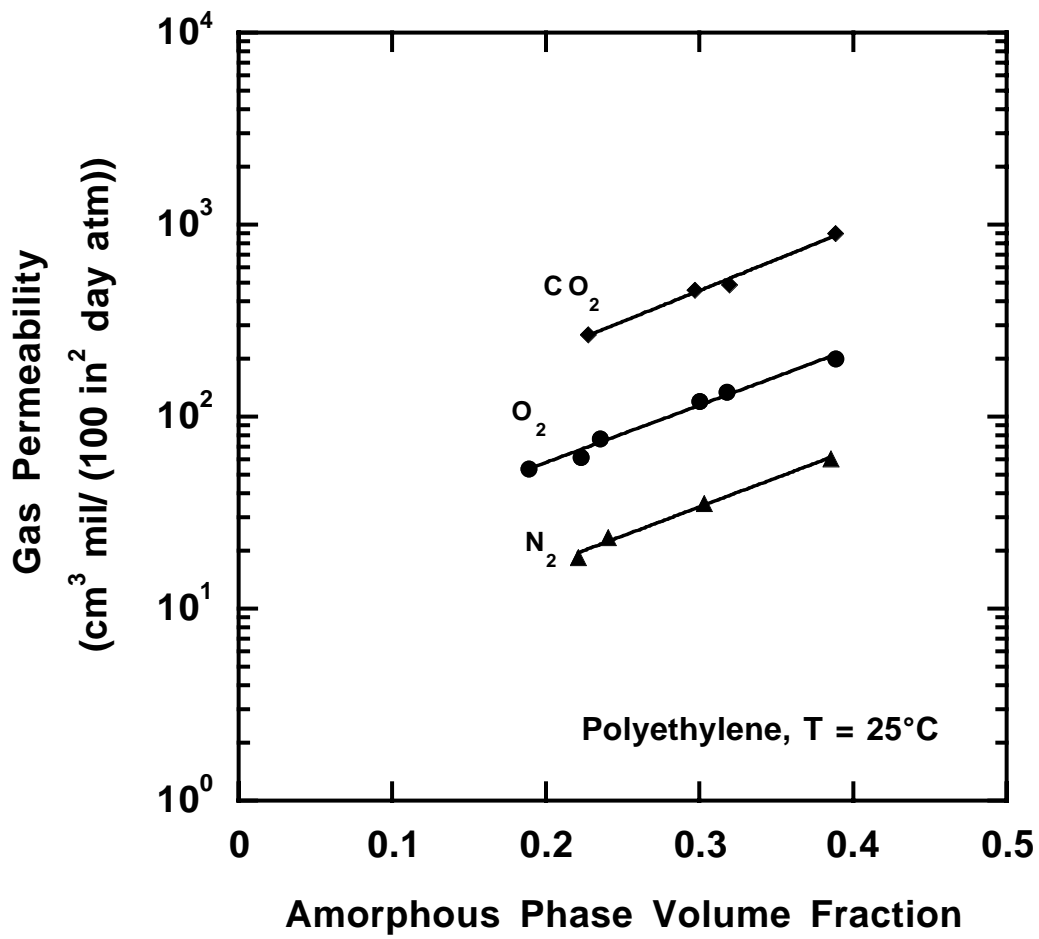


Figure 2.11 Effect of crystalline content on gas permeability in polyethylene at 25°C [74].

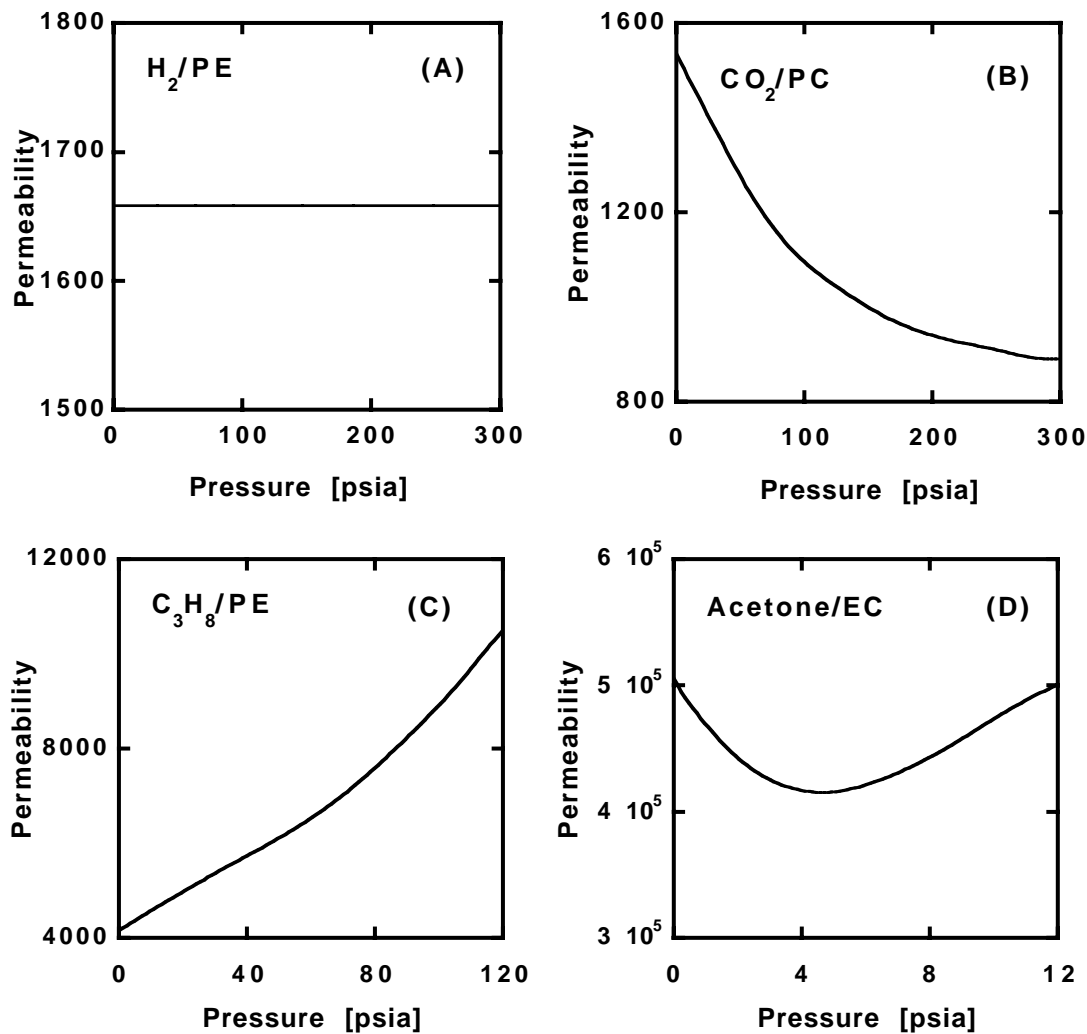


Figure 2.12 Typical permeability-pressure dependence in rubbery and glassy polymers. (A) Hydrogen in polyethylene (PE) at 30°C, (B) Carbon dioxide in polycarbonate (PC) at 35°C, (C) Propane in polyethylene at 20°C, (D) Acetone in ethyl cellulose (EC) at 40°C [51]. The permeability values have units of ($cm^3 \text{ mil} / (100 \text{ in}^2 \text{ day atm})$).

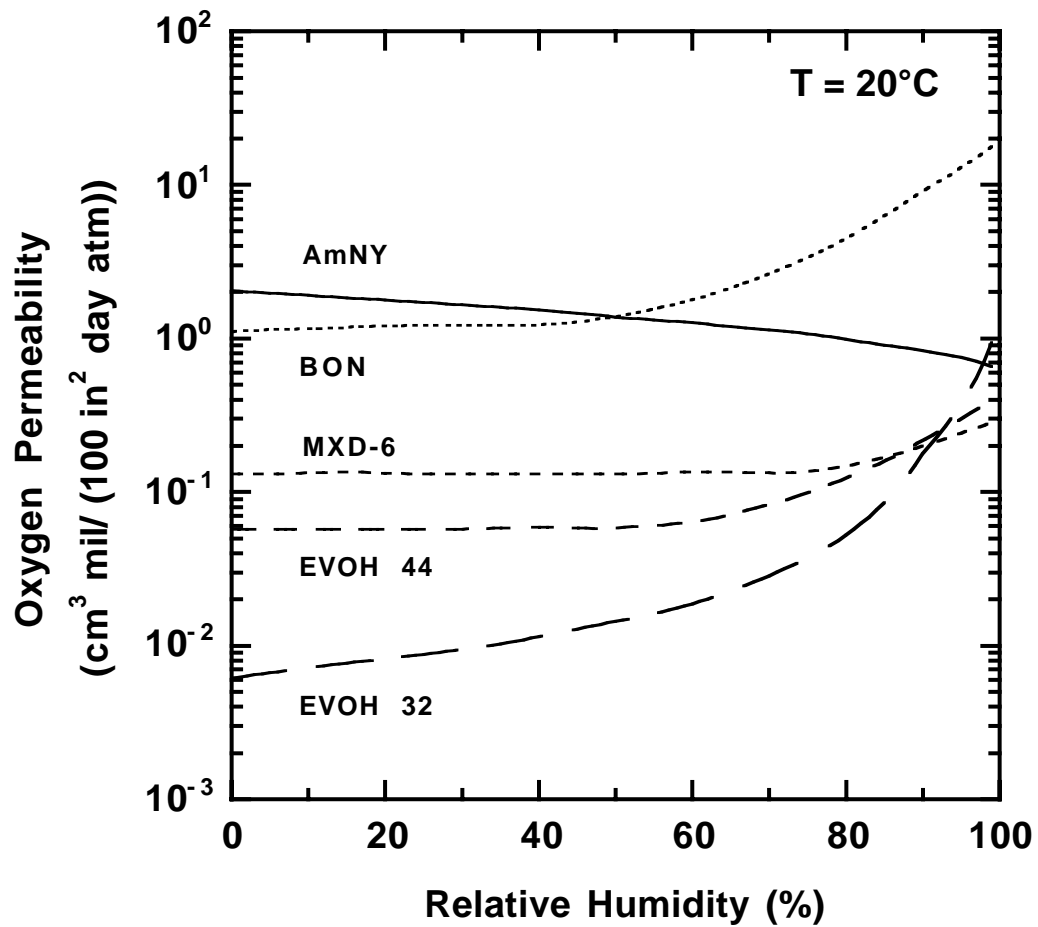


Figure 2.13 Effect of relative humidity on oxygen permeability of hydrophilic barrier polymers. AmNY is amorphous nylon (Selar[®]), BON is biaxially oriented nylon 6, MXD-6 is oriented poly(metaxylylenediamine-adipic acid), EVOH 44 and 32 are ethylene vinyl alcohol copolymers containing 32 and 44 mol% ethylene [6].

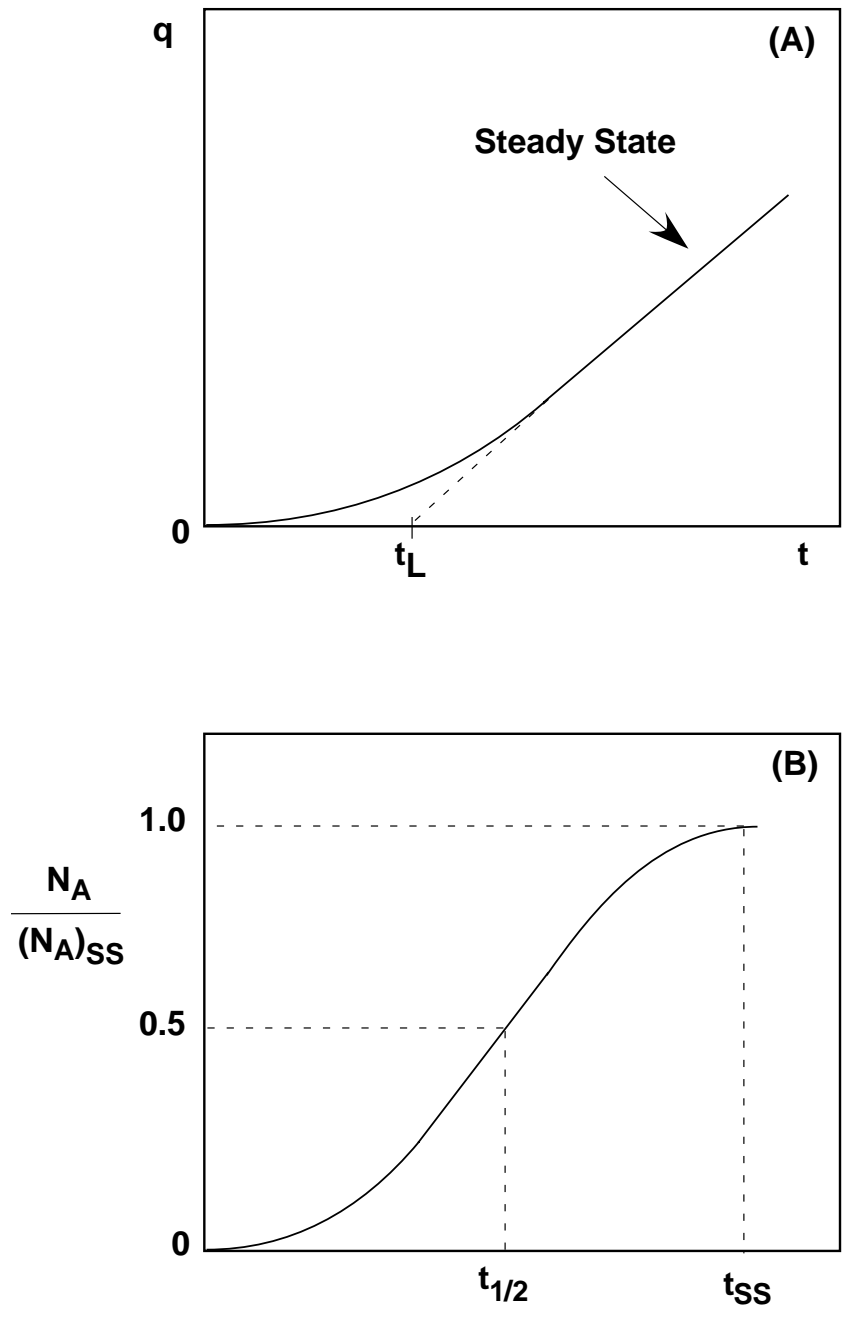


Figure 2.14 (A) Mass of permeating penetrant per unit film area (q) as a function of time (providing a measure of time lag, t_L).
 (B) Normalized penetrant flux (N_A) as a function of time (providing a measure of half time, $t_{1/2}$). t_{SS} is time required to achieve steady state.

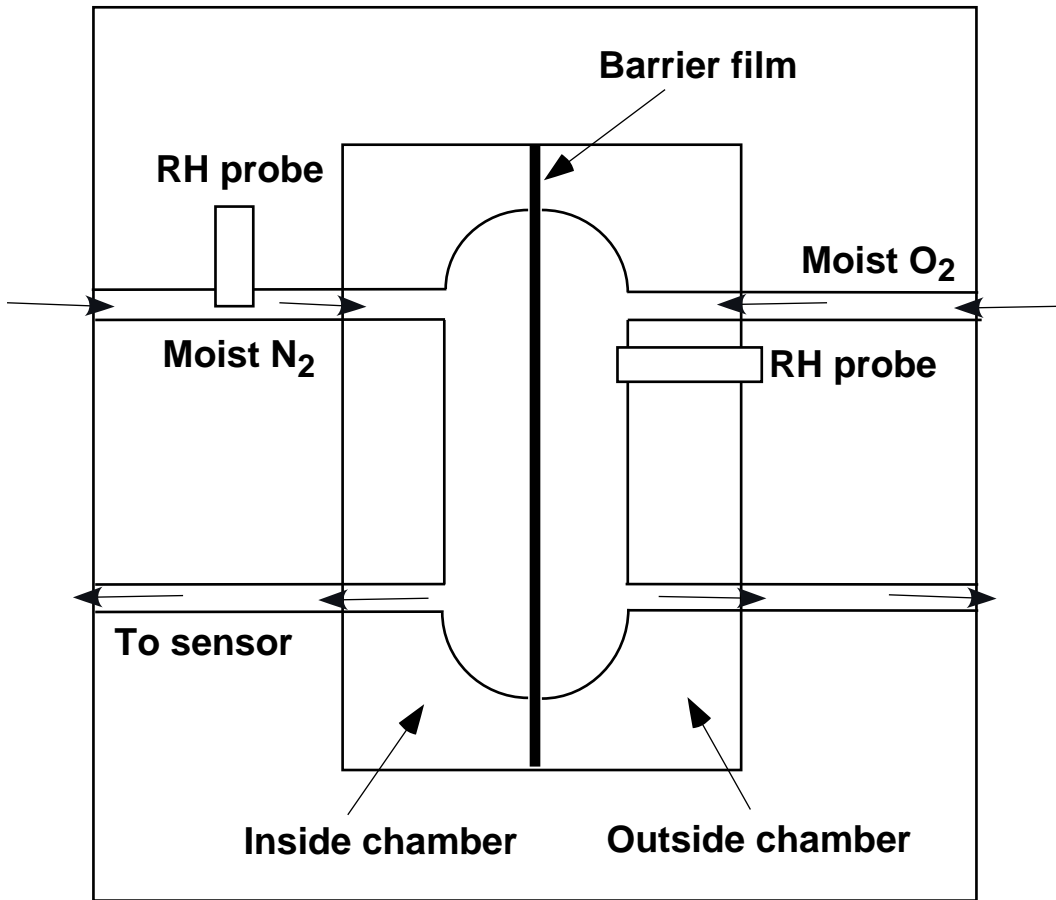


Figure 2.15 A schematic of a permeation cell in the Ox-Tran[®] (MOCON, Inc.) oxygen transmission rate measurement system [87].

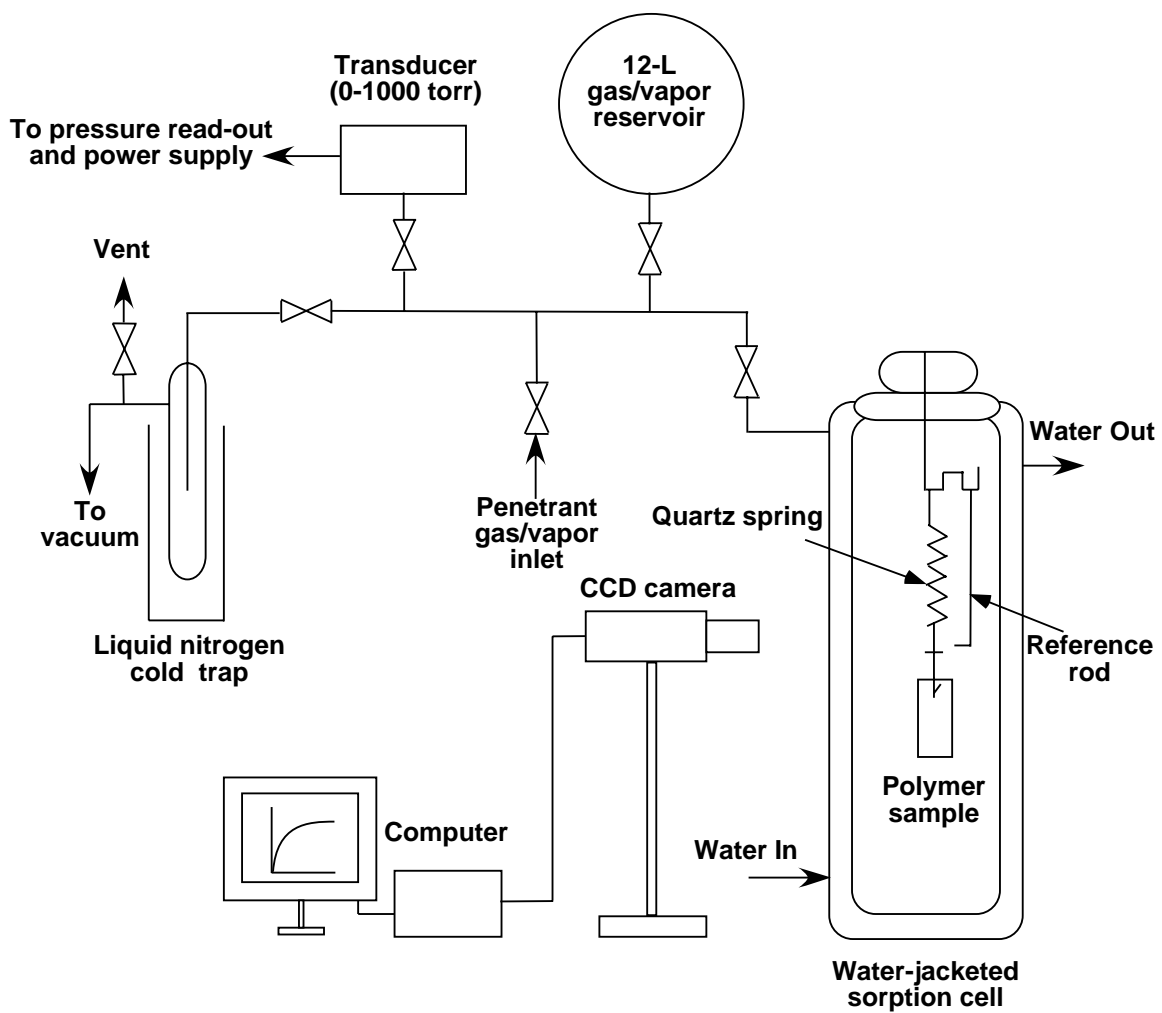


Figure 2.16 A schematic of the McBain spring balance apparatus for measuring sorption and desorption of organic vapors in barrier polymers [90].

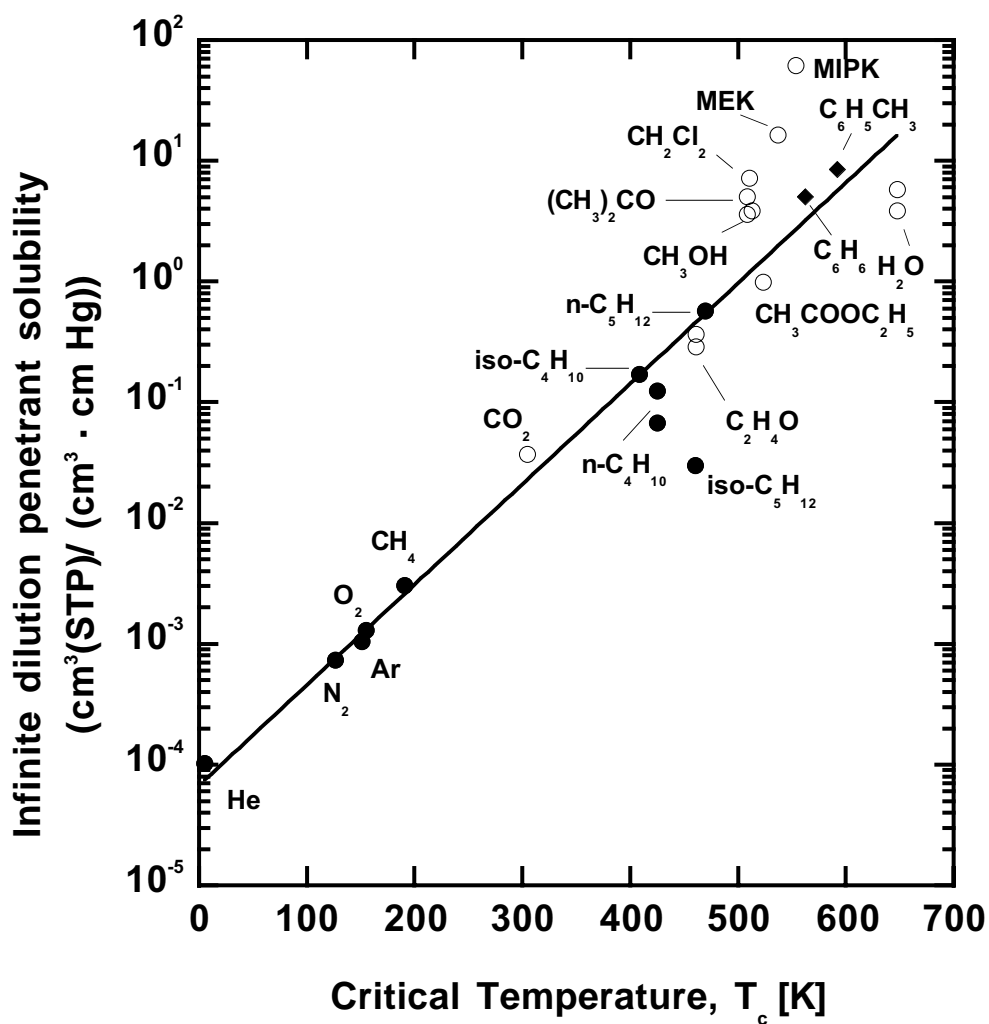


Figure 2.17 Correlation of infinite dilution penetrant solubility with penetrant critical temperature in poly(ethylene terephthalate) (PET) ([8] and unpublished data). (●) non-polar penetrants, (○) polar and quadrupolar penetrants, (◆) aromatic penetrants. The slope, $M = 0.019 \pm 0.001 \text{ K}^{-1}$ and intercept, $N = -9.6 \pm 0.4$.

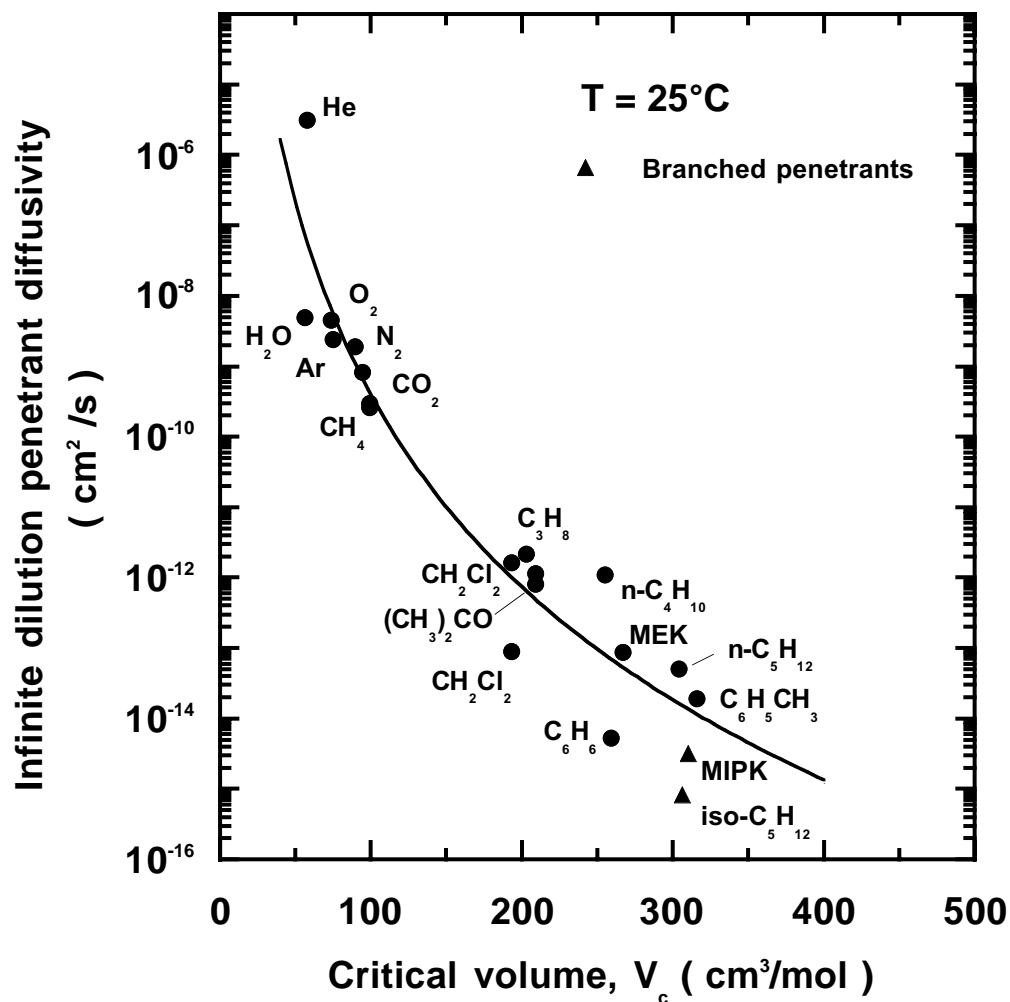


Figure 2.18 Effect of penetrant size on infinite dilution, amorphous phase diffusion coefficients in poly(ethylene terephthalate) at 25°C ([8] and unpublished data). The best-fit parameters of Equation 2.31 are: $\tau = 5.7 \pm 1.2 \times 10^8$ (cm^2/s) (cm^3/mol)^{9.1}, $\eta = 9.1 \pm 0.9$.

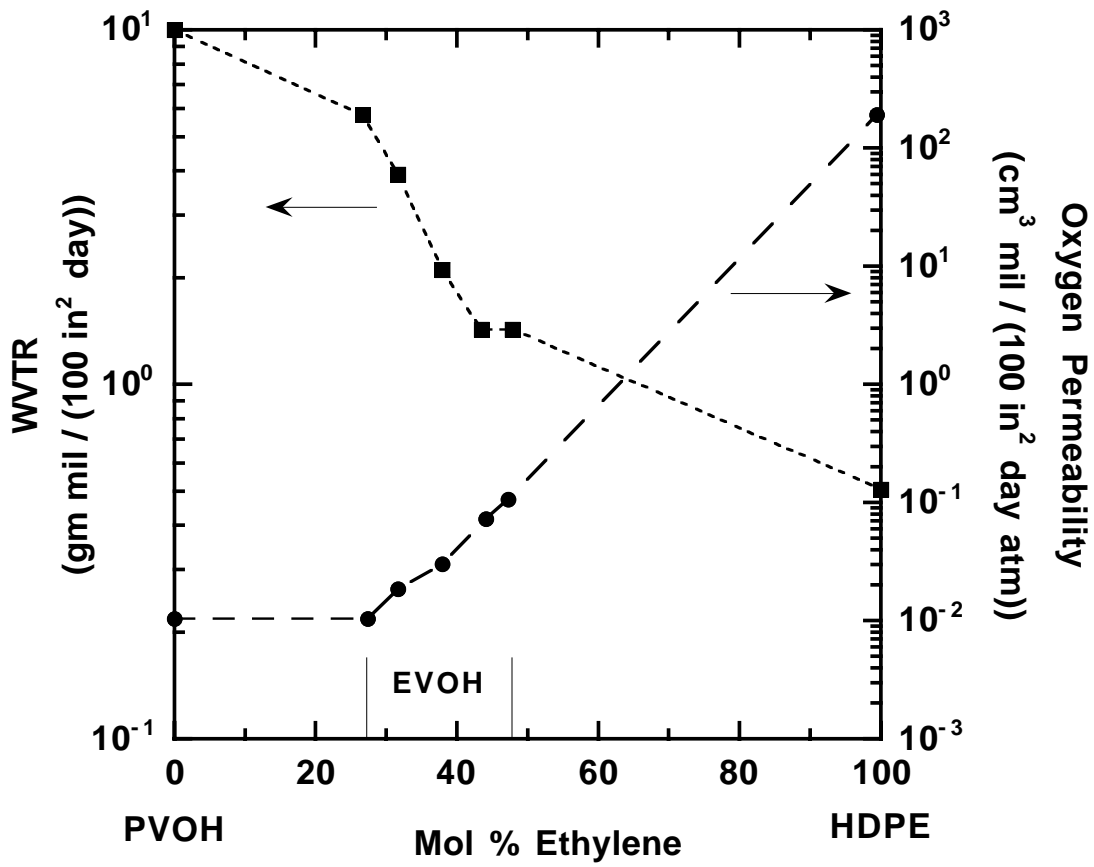


Figure 2.19 Effect of ethylene content on oxygen permeability and water vapor transmission rates (WVTR) of ethylene vinyl alcohol copolymer (EVOH). The figure also shows data for poly(vinyl alcohol) (PVOH) and high density polyethylene (HDPE) for comparison [6].

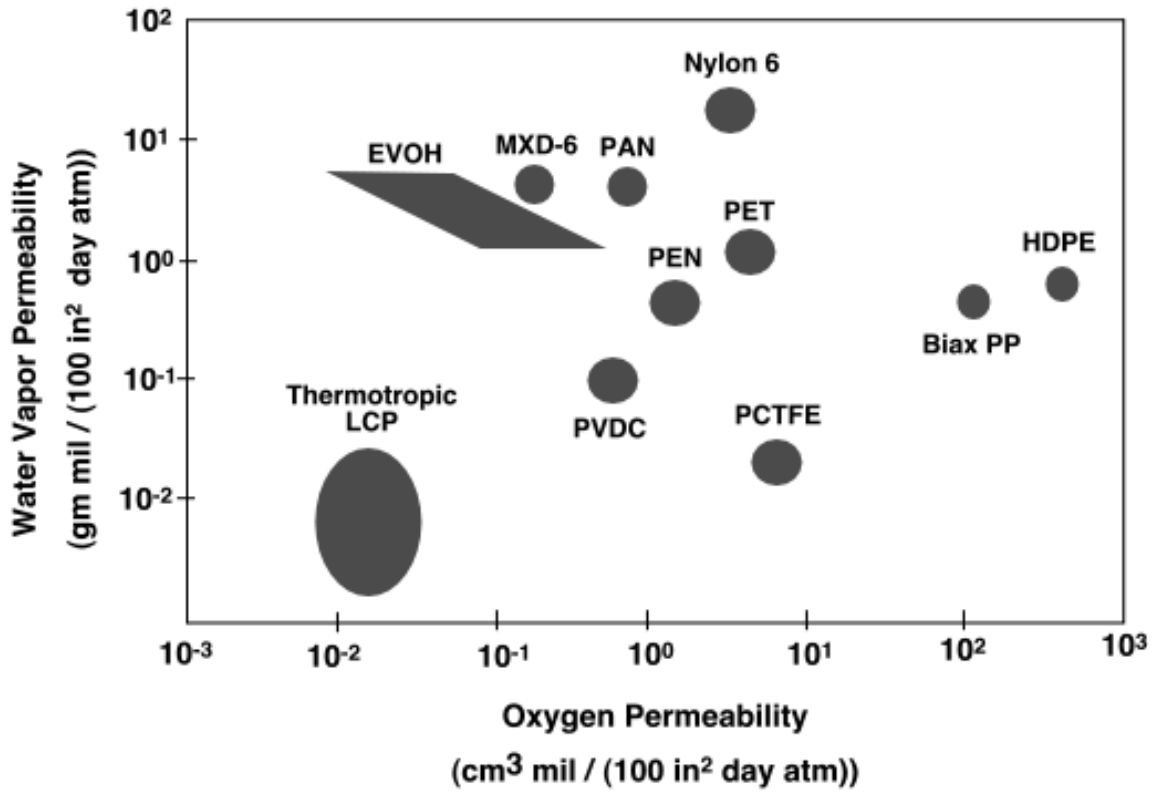


Figure 2.20 A comparison of oxygen and water vapor barrier properties of various high and moderate barrier polymers at 23°C [127].

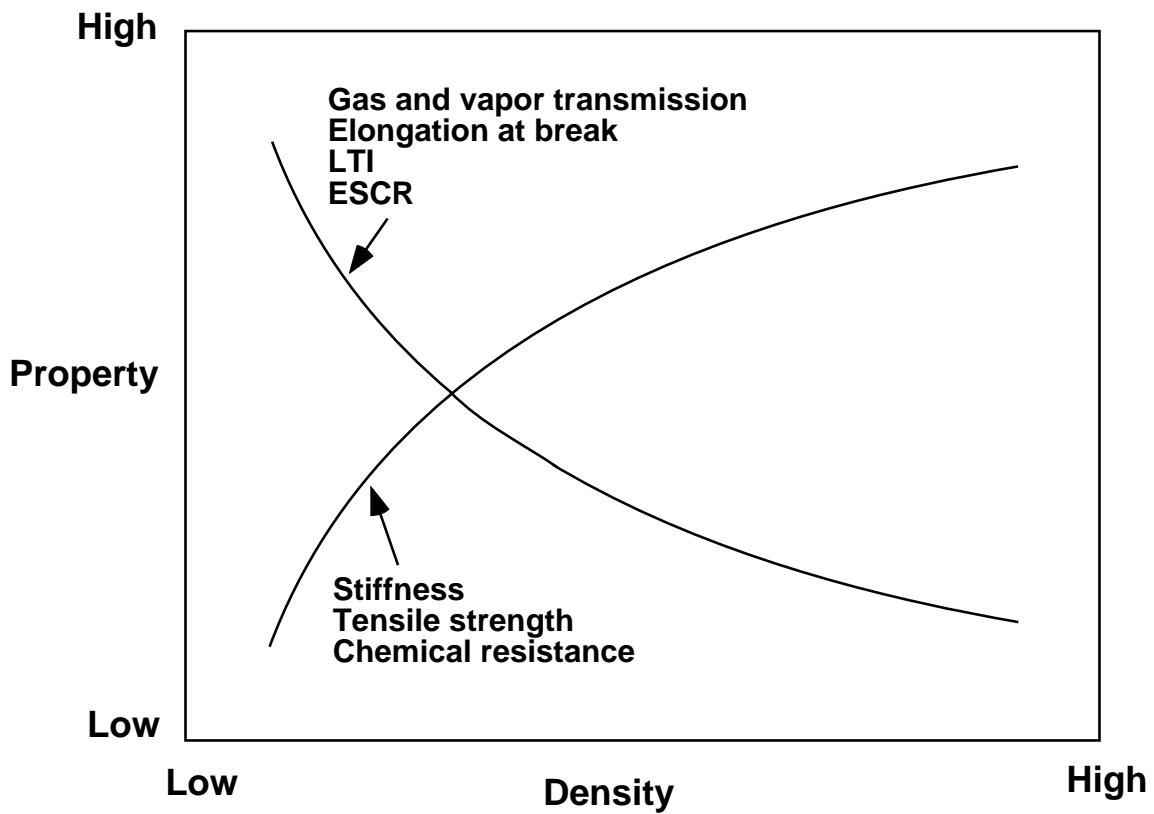


Figure 2.21 Typical effect of density on various properties of polyethylene. LTI is low temperature impact strength and ESCR is environmental stress crack resistance [141].

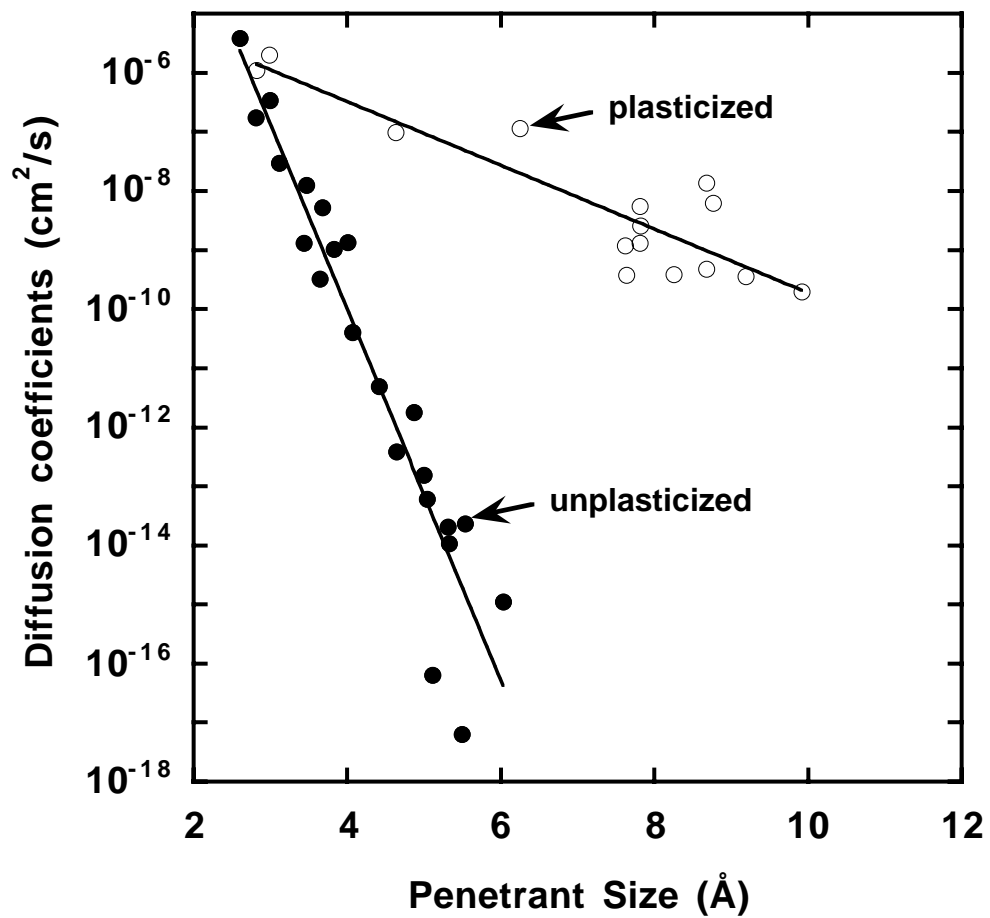


Figure 2.22 Diffusion coefficients in unplasticized and plasticized poly(vinyl chloride) (PVC) as a function of penetrant molecular diameter [143].

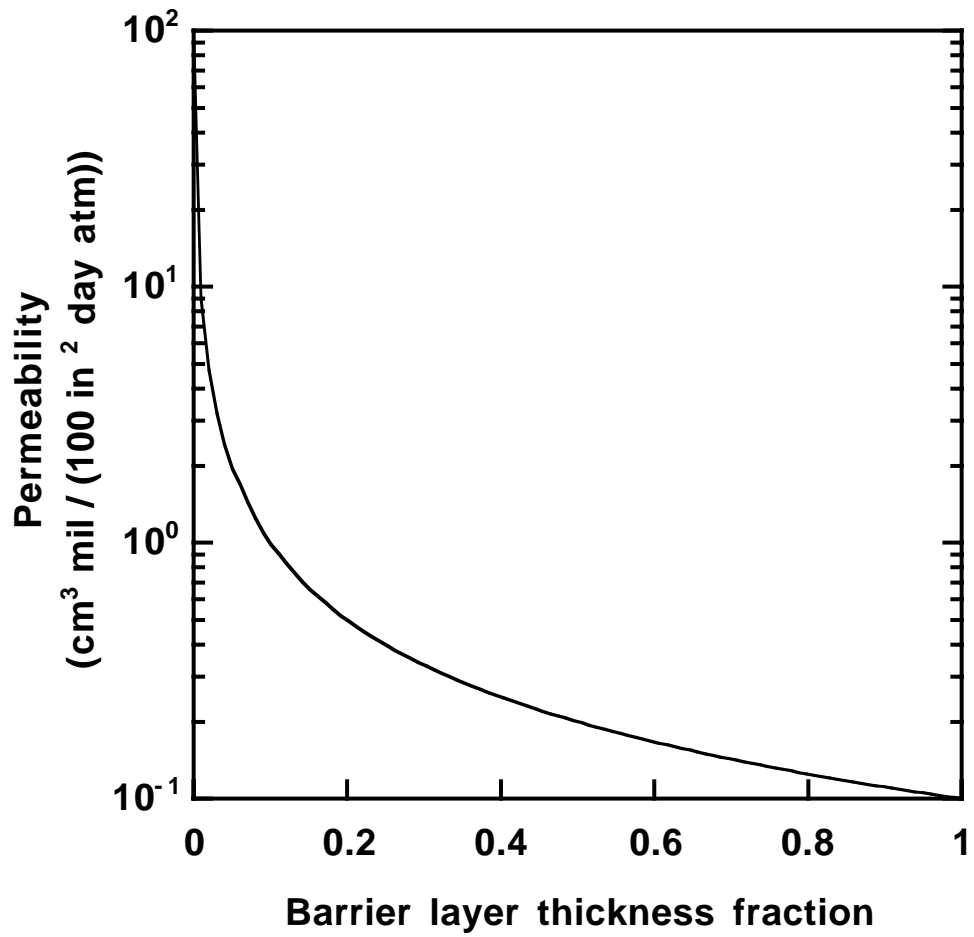


Figure 2.23 Effect of thickness of barrier layer on permeability of a hypothetical two-layer barrier composite structure.

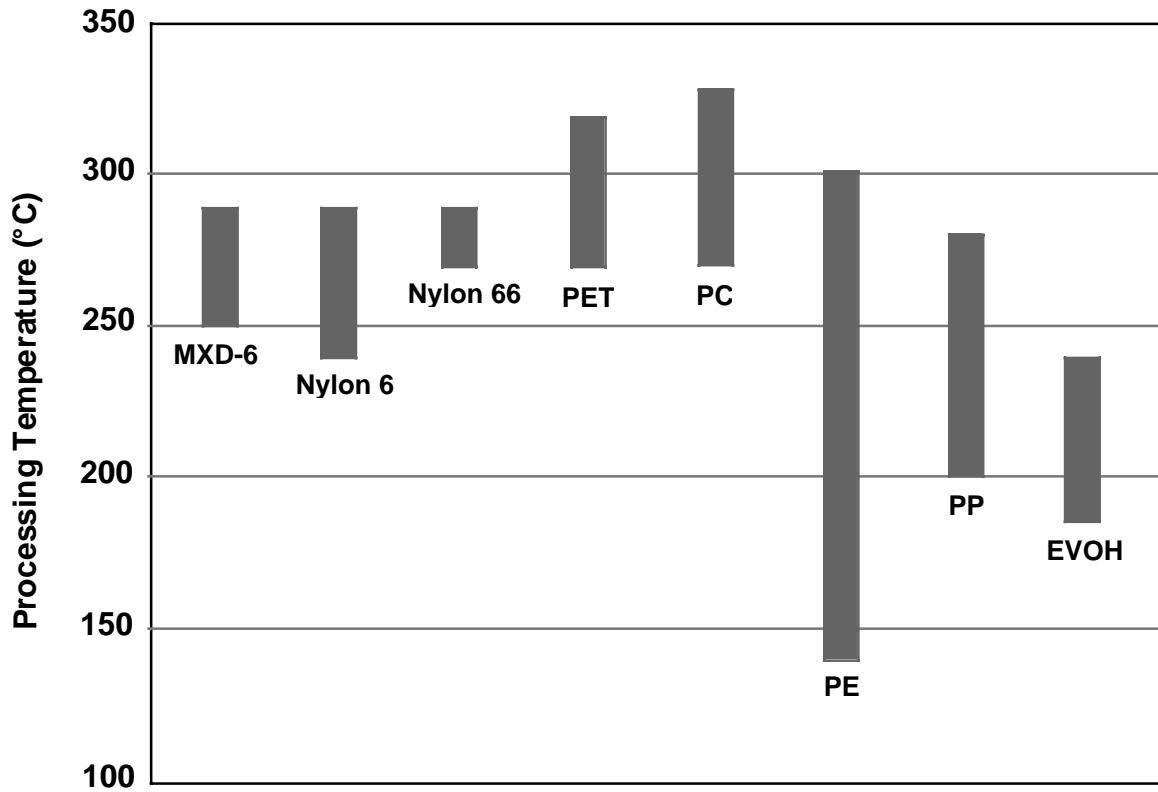


Figure 2.24 A comparison of processing temperatures of various commercially used barrier polymers [146].

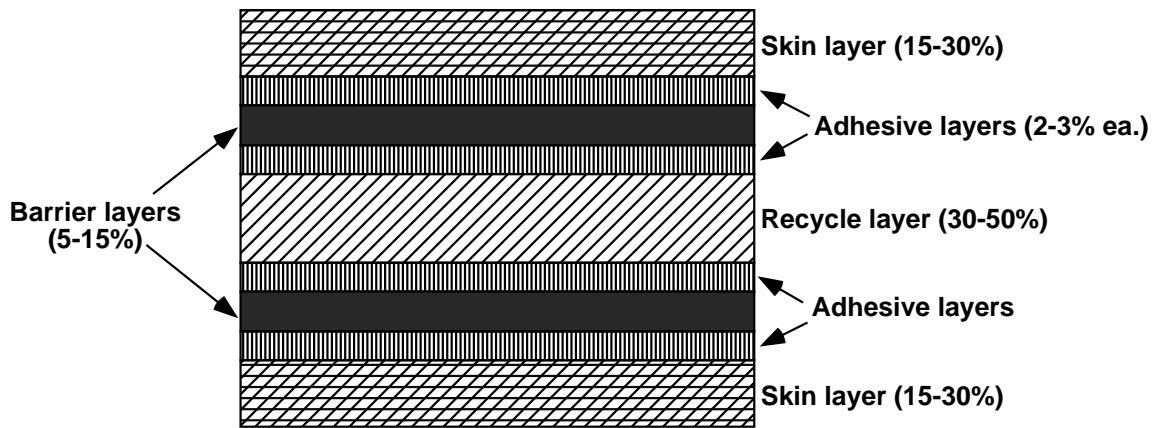


Figure 2.25 An example of a typical symmetrical nine-layer coextruded barrier composite structure [145].

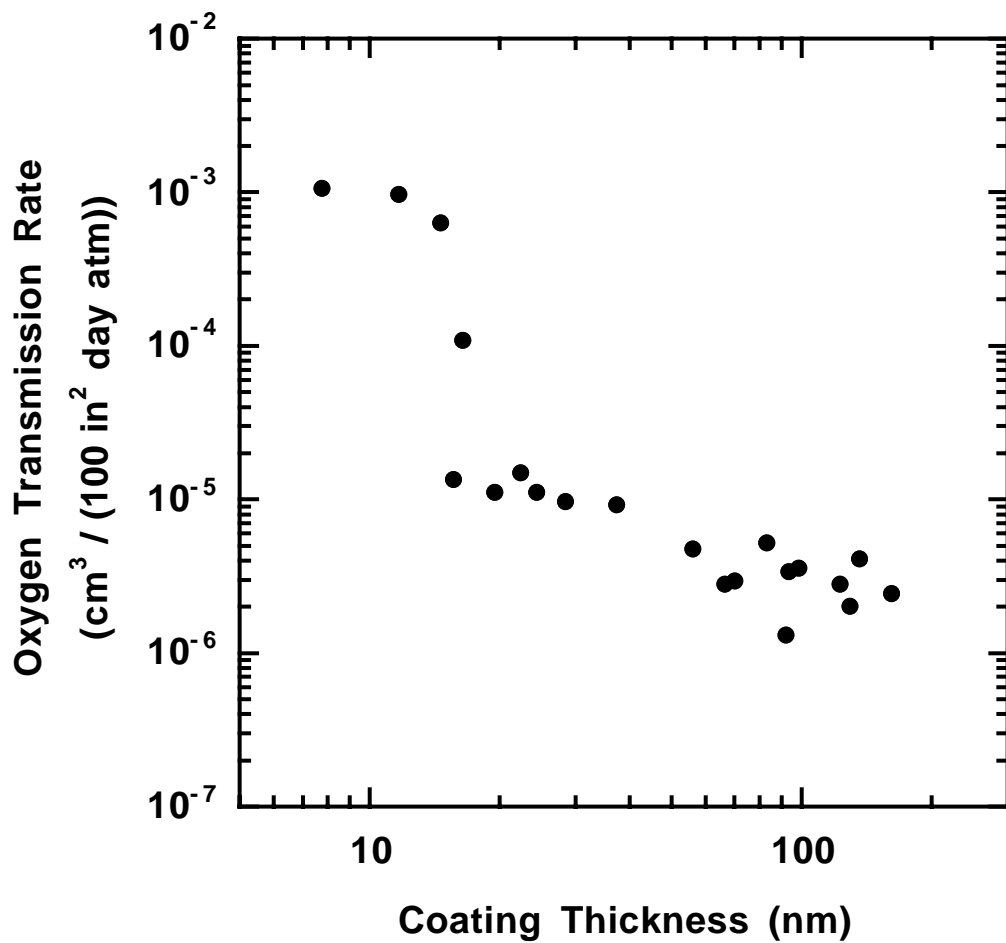


Figure 2.26 Effect of plasma-deposited silica coating thickness on steady state oxygen transmission rates of poly(ethylene terephthalate) films that have an uncoated thickness of 13 μm [154].

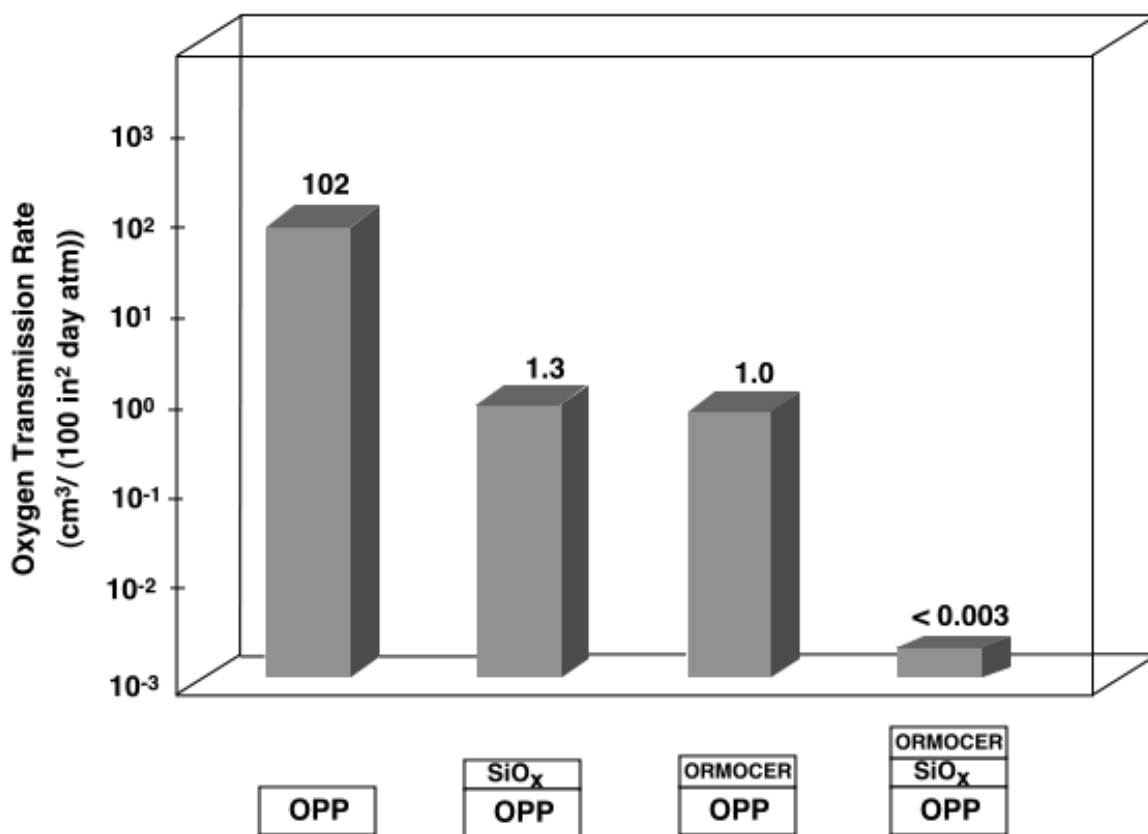


Figure 2.27 Influence of ORMOCER[®] coatings on oxygen transmission rates (OTR) of SiO_x-coated oriented polypropylene (OPP) (OTR measured at 23°C and 70% RH) [155].

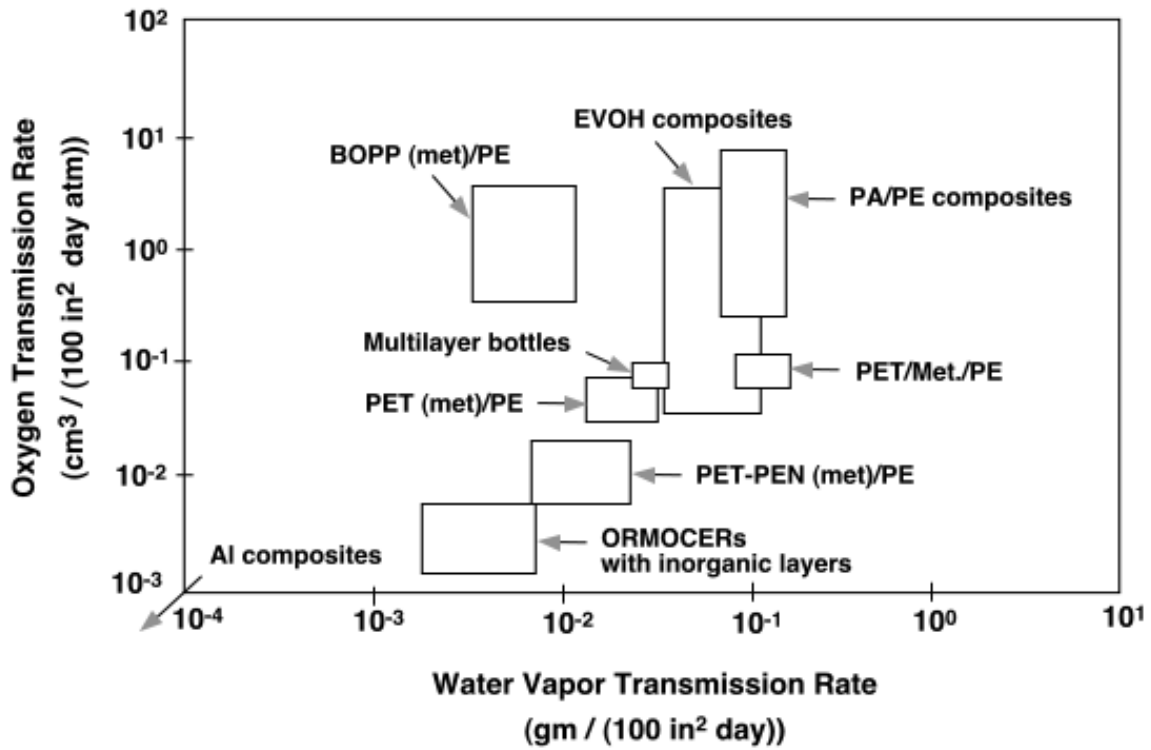


Figure 2.28 A comparison of oxygen and water vapor transmission rates of various barrier polymer composite structures [157]. BOPP (met) is biaxially oriented, metallized polypropylene, PET (met.) is metallized poly(ethylene terephthalate), PEN (met) is metallized poly(ethylene naphthalate), Al composites are aluminum composites.

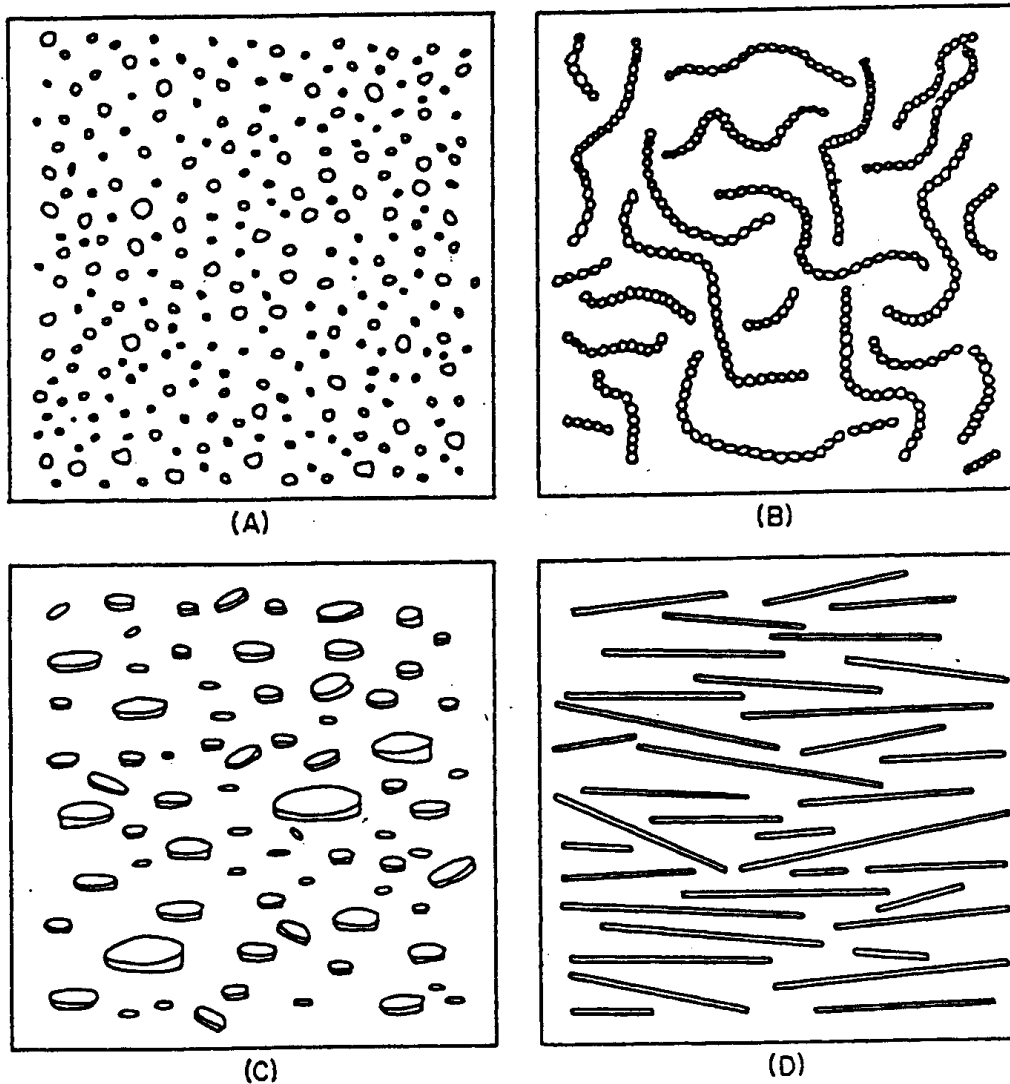


Figure 2.29 Typical examples of heterogeneous, immiscible blends. (A) Random spheres in a dispersed phase, (B) Aggregated spheres in a dispersed phase, (C) Oriented platelets in a dispersed phase, (D) Oriented rods in a dispersed phase [161].

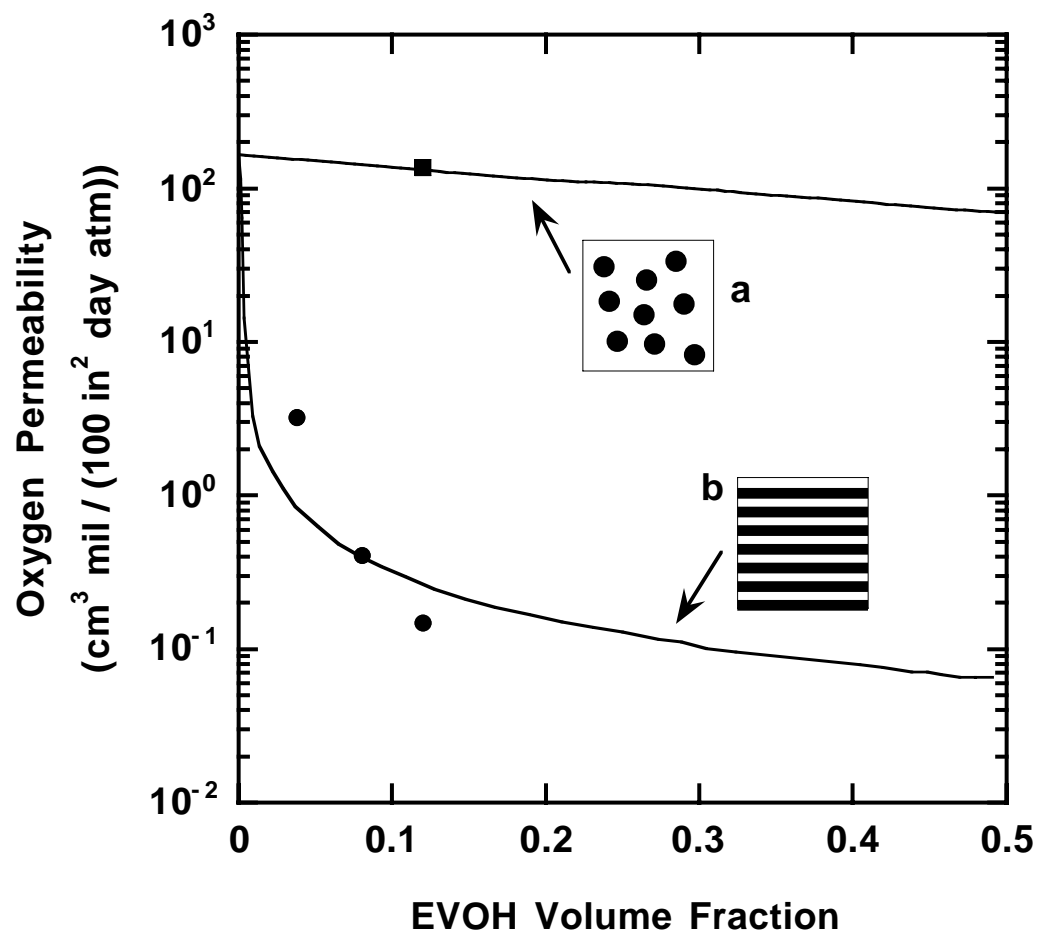


Figure 2.30 Effect of EVOH content on oxygen permeability of PE-EVOH blends that exhibit (a) discontinuous morphology and (b) co-continuous lamellar morphology [69].

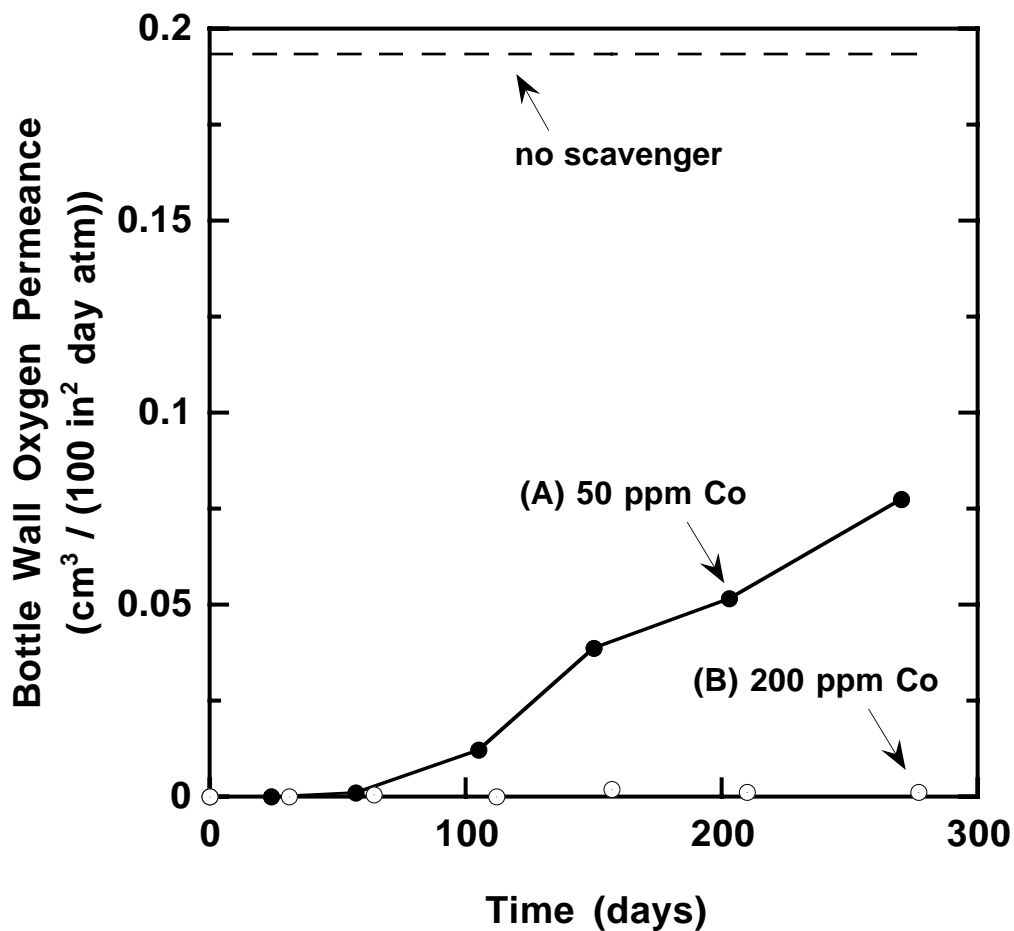


Figure 2.31 Reduction in oxygen transmission rates due to oxygen scavenging in blends of PET and nylon MXD-6 [174]. The measurements were made at 23°C and 50% RH. (A): 4 wt.% MXD-6 and 50 ppm cobalt (as metal); (B): 4 wt.% MXD-6 and 200 ppm cobalt (as metal). For comparison, the dotted line indicates oxygen permeance in the absence of cobalt catalyst (no scavenging).

CHAPTER 3

Experimental Techniques and Sample Characterization Results

3.1 Materials

Biaxially-oriented PET (BPET) films were purchased from the Goodfellow Company (Berwyn, PA). The films (product code: ES-301009) have a nominal thickness of 0.9 μm and the density, 1.395 g/cm^3 , was furnished by the supplier. These films were used as received for the gravimetric sorption and dual volume pressure decay sorption experiments described below.

3.2 Gravimetric Sorption

Kinetic gravimetric sorption experiments were performed using a McBain spring balance system [180]. A schematic diagram of this instrument is presented in Figure 3.1. Approximately 50 mg of polymer film sample is suspended from a calibrated quartz spring inside the sorption system. To minimize static-related problems, multiple layers of thin polymer films (such as the BPET films from this study) are typically used. Before starting the experiments, sorbed air gases and water vapor are removed from the polymer by exposing the sample to vacuum until there is no further spring displacement. Then the sample is exposed to penetrant gas or vapor at fixed pressures. In a typical sorption experiment, the penetrant pressure in contact with the polymer sample is increased in a series of steps, with the sample being allowed to equilibrate after each step. In this protocol (*i.e.*, an interval sorption experiment) the polymer sample is equilibrated in an environment where the penetrant pressure surrounding the sample is p_i prior to a step. Then, at $t = 0$, the penetrant pressure is increased to p_f , and the spring extension is monitored as a function of time. In this work, the spring position relative to a stationary

reference rod hanging in the sorption chamber is recorded using a Cohu (San Diego, CA) 4910 CCD camera, and Image, a software package from the National Institutes of Health (NIH), is used to process data from the camera on a computer. The spring position data are converted to mass uptake values, M_t , where M_t is the mass of penetrant sorbed by the polymer at time t per unit mass of penetrant-free polymer, and diffusion coefficients are extracted from the time dependence of M_t . A similar procedure also applies to kinetic desorption experiments, where the penetrant pressure is decreased from an initial value, p_i , to a final value, p_f , at $t = 0$, and the decrease in mass is monitored as a function of time.

Equilibrium mass uptake, M_∞ , values are determined from the sorption experiments. Equilibrium penetrant concentration in the polymer, C ($\text{cm}^3(\text{STP})/\text{cm}^3$ polymer), is calculated as follows:

$$C = \frac{M_\infty \times 22414 \times 100 \times \rho_{\text{polymer}}}{MW} \quad (3.1)$$

where M_∞ has units of g penetrant sorbed/100g polymer, ρ_{polymer} is polymer density (g/cm^3), and MW is penetrant molecular weight (g/mol). As mentioned in Chapter 1, equilibrium solubility, S ($\text{cm}^3(\text{STP})/\text{cm}^3 \text{ cmHg}$), is calculated from:

$$S = \frac{C}{p} \quad (3.2)$$

where p is the penetrant pressure in the gas phase contiguous to the polymer sample.

3.3 Dual Volume Pressure Decay Sorption

The gravimetric sorption technique described in the previous section can be used for solubility measurements up to pressures of 1 atm. In contrast, the dual volume pressure decay technique [181] can be used up to much higher pressure (30 atm) enabling the solubility measurement of light gases in low sorbing materials, such as barrier polymers. A schematic diagram of this apparatus is presented in Figure 3.2. To begin a sorption experiment, the system is first evacuated. Then, the charge chamber, C, is filled with the penetrant gas. The gas temperature, pressure, and volume of the chamber are known. Hence, the number of moles initially present in the charge chamber, n_1 , can be calculated with an appropriate equation of state. Then, a small amount of gas is expanded from the charge chamber to the polymer-containing sample chamber, S. After closing the valve between the two chambers, the pressure in the charge chamber is recorded, and the number of moles present after the expansion, n_2 , is calculated. The difference between the moles of gas initially present and the moles present after the expansion (*i.e.*, $n_1 - n_2$) equals the moles of gas transferred to the sample chamber, n_3 . The pressure in the sample chamber is continuously monitored using a computer and data acquisition software (LABTECH, Andover, MA) until no further change is observed, and the moles present in the gas phase at sorption equilibrium, n_4 , can be calculated. The moles of gas sorbed in the polymer sample is calculated as the difference between the moles of gas transferred to the sample chamber and the moles present in the gas phase at sorption equilibrium (*i.e.*, $n_3 - n_4$).

3.4 Polymer Characterization Techniques

3.4.1 Nuclear Magnetic Resonance Spectroscopy

Proton NMR spectroscopy was performed at Eastman Chemical Company (Kingsport, TN) to determine the polymer chemical composition. The NMR sample was prepared by dissolving 15 mg of the polymer sample in 0.6 ml of a mixture of 70% deuterated chloroform and 30% deuterated trifluoroacetic acid. The spectrum was recorded using a JEOL GX-400 instrument at room temperature with a pulse delay of 13.4 sec.

3.4.2 Inherent Viscosity

The inherent viscosity was also determined at Eastman Chemical Company (Kingsport, TN) at 25°C and atmospheric pressure by measuring the solution viscosity and using an established correlation to relate solution viscosity to inherent viscosity. A Schott AVS 500 viscometer (Yonkers, NY) was used to determine the solution viscosity. The solvent was a 60/40 (w/w) phenol/tetrachloroethane mixture. The polymer concentration was 0.5 wt. %.

3.4.3 Thermal and Physical Characterization

A Scintag PAD-V X-ray diffractometer (Cupertino, CA) equipped with a four-circle goniometer was used to record the wide angle X-ray diffraction (WAXD) spectrum of the polymer. This experiment was conducted at Eastman Chemical Company (Kingsport, TN). The following conditions were used: Radiation source: Cu K α ,

Accelerating potential: 45 kV, Emission current: 40 μ A, Scan mode: continuous, Step: 0.05°, Count time: 3s, Scan rate: 1°/min. For this study, samples were cut into 2 \times 2 inch squares and five films were stacked onto aluminum thin-film mounting plates for examination. To determine the Hermans crystalline orientation function, intensity as a function of scattering angle, ϕ , was recorded for the primary reflections of interest.

Thermal transitions were determined by differential scanning calorimetry (DSC). Samples were analyzed using a TA Instruments 2920 DSC (New Castle, DE) at Eastman Chemical Company (Kingsport, TN). First and second scan thermograms were recorded at a heating rate of 20°C per minute over a temperature range of 50 to 290°C. From the first scan thermogram, the areas under the cold crystallization and melting peaks were used to estimate the weight percent crystallinity [124]. The second scan thermogram was used to determine cold crystallization temperature, melting point temperature, and glass transition temperature.

3.4.4 Positron Annihilation Lifetime Spectroscopy

Positron annihilation lifetime spectroscopy (PALS) was used to characterize the amount of orthoPositronium-accessible free volume in the PET films. These experiments were performed at CSIRO (Melbourne, Australia). Measurements were made in air at room temperature (22.5 ± 1 °C) using an automated EG&G Ortec fast-fast coincidence system. The timing resolution of the system was 275 ps determined using the prompt curve from a ^{60}Co source with the energy windows set to ^{22}Na events. The polymer films

were stacked up to a total thickness of 1.5 mm on either side of the 30 μCi ^{22}Na -Ti foil source. Ten spectra were collected over a period of 10 hours, and the results reported are the mean values of these spectra. The spectra were modeled as a sum of three decaying exponentials using the computer program PFPOSFIT [182]. The shortest lifetime was fixed at 125 ps characteristic of paraPositronium self-annihilation. No source corrections were used in the analysis based on a fit for pure Al standards of 169 ± 2 ps, 99.3 ± 0.3 %; 820 ps, 0.7%. Only the orthoPositronium (*o*Ps) component (the longest lifetime, τ_3 and its intensity, I_3) is reported as it is this component that is most sensitive to penetrant accessible free volume in glassy polymers [53].

3.4.5 Profilometry

A Tencor Alpha-Step stylus surface profiler (San Jose, CA) was used to measure the thickness and surface uniformity of the samples. Samples were tested over a length of 1000-1700 μm at a speed of 20-50 $\mu\text{m}/\text{sec}$. The force applied to the stylus was 10 mg. Each reported measurement is the average of 3 scans. An average value of thickness was obtained from five measurements on different portions of the film sample used for the sorption experiments.

3.5 Polymer Characterization Results and Discussion

3.5.1 Inherent Viscosity, Nuclear Magnetic Resonance, and Profilometry

The inherent viscosity of the BPET polymer samples was 0.473 dL/g. The ^1H NMR spectrum indicated that the sample was PET containing 1.8 mole % diethylene glycol repeat units. The tencor profilometry study yielded an average thickness of $0.95 \pm 0.076 \mu\text{m}$. This thickness value was used for all subsequent calculations.

3.5.2 Sample Morphology

We used four independent techniques (DSC, density, WAXD and PALS) to characterize the morphology of the polymer film sample and extracted estimates of crystallinity from DSC, density and WAXD results. Using typical simplifying assumptions to characterize crystallinity *via* these three techniques, the apparent crystalline content from WAXD was much lower than the crystallinity values obtained from the other two methods. Therefore, it seemed appropriate to review the assumptions and basis for crystallinity estimates using these techniques. As will be discussed, we prefer the crystallinity estimate based on the DSC technique, when there is a discrepancy between the values obtained using different techniques [183].

Differential Scanning Calorimetry

The second scan DSC thermogram revealed a glass transition temperature, T_g , of 76.6°C (mid point of the endothermic shift observed in the temperature range of $70\text{--}80^\circ\text{C}$), cold crystallization temperature, T_c , of 130.3°C (maximum peak height of the exotherm at approximately 130°C), and melting point temperature, T_m , of 256.9°C

(minimum in the endotherm at approximately 257°C). The transition temperatures are in good agreement with those previously reported for highly amorphous, unoriented PET (APET) [9]: T_g (78°C), T_c (137°C) and T_m (249°C). The weight percent of crystallites, w_c , in BPET was estimated by subtracting the enthalpy of cold crystallization, ΔH_c , from the enthalpy of melting, ΔH_m , and dividing by the heat of fusion of PET [9]:

$$w_c = \left(\frac{\Delta H_m - \Delta H_c}{\Delta H_f^*} \right) \times 100 \quad (3.3)$$

ΔH_f^* is the reported heat of fusion of PET, 126.3 J/g [183]. The value of w_c was 42%.

Volume percent crystallinity, ϕ_c , was calculated from w_c using the following relationship [184]:

$$\phi_c = (\rho / \rho_c) \times w_c \quad (3.4)$$

where ρ is polymer density, and ρ_c is the reported crystal density of PET, 1.515 g/cm³ [12]. From Equation 3.4, ϕ_c was 39%.

PET cannot be prepared as a single crystal material, so estimates of ΔH_f^* are usually based on extrapolating enthalpy of fusion data for semicrystalline samples to the completely crystalline state. This procedure leads to some uncertainty in the value of the enthalpy of fusion [183]. The enthalpy of fusion is also typically assumed to be independent of sample processing history. In drawn PET, processing history has been reported to have a pronounced effect on crystallite density, but little effect on enthalpy of fusion [183]. Equation 3.3 neglects the effect of crystal size (*i.e.*, the contribution of the

surface energy to the overall enthalpy of fusion). This effect is believed to be of the order of a few J/g and is therefore, in the range of the typical uncertainty in ΔH_f^* [183]. During the DSC run of an oriented, drawn polymer, the sample undergoes shrinkage and disorientation. The influence of these processes on the measured heat of fusion of PET is not known. However, in polyethylene, only small effects have been reported. The difference between experimentally measured heats of fusion of polyethylene with free and restrained ends (*i.e.*, with and without shrinkage) was reported to be 2.5 to 6.3 J/g, which are almost similar, given that the uncertainty in the measurement was ± 2.0 J/g [185].

The phenomena discussed in the previous paragraph may influence the value of crystallinity estimated from DSC. However, for drawn PET, such phenomena are believed to make a minor contribution to the enthalpy of fusion [183]. The crystallinity estimate for our BPET samples, based on DSC, is in excellent agreement with the DSC estimate reported by Fischer *et al.* [186] (44 wt. %) for drawn PET having a density of 1.396 g/cm^3 , which is very close to the density of our sample (1.395 g/cm^3). Also, similar levels of crystallinity have been reported for other biaxially oriented PET films [187]. Based on these composite factors and the higher level of uncertainty associated with the procedures required to extract crystallinity values from other techniques (density and WAXD), we use the DSC crystallinity value in all sorption and diffusion calculations.

Wide Angle X-ray Diffraction

The WAXD spectrum is presented in Figure 3.3. The spectrum consists of a broad amorphous halo and peaks centered at $2\theta = 16.6, 22.5$ and 25.4° , which are associated with PET crystallites. The vertical lines in Figure 3.3 represent the peak locations expected for the $(0\bar{1}1)$, (010) , $(\bar{1}10)$ and (100) reflections in PET [27].

Based on the WAXD results, the Hermans orientation function, f_c , was determined from the following equation [78,188,189]:

$$f_c = \frac{1}{2}(3\langle \cos^2 \phi \rangle - 1) \quad (3.5)$$

where

$$\langle \cos^2 \phi \rangle = \frac{\int_0^{\pi/2} I(\phi) \sin \phi \cos^2 \phi d\phi}{\int_0^{\pi/2} I(\phi) \sin \phi d\phi} \quad (3.6)$$

where $I(\phi)$ is the WAXD intensity at scattering angle ϕ ($0 \leq \phi \leq \pi/2$). $\langle \cos^2 \phi \rangle$ is the mean-square cosine (averaged over all of the crystallites) of the angle between the crystal plane and the reference direction. A Hermans orientation function, f_c , of 1.0 indicates complete alignment of crystallites in the reference direction, zero indicates a completely random orientation of the crystallites, and $-1/2$ indicates crystallite alignment in the perpendicular direction. The crystalline Hermans orientation function for the BPET sample is 0.875, which indicates a high degree of orientation of the crystallites in the plane of the film.

Often, crystallinity is estimated from the WAXD spectrum using the following relation [184]:

$$w_c = \left(\frac{I_c}{I_c + K \times I_a} \right) \quad (3.7)$$

where I_c and I_a are the integrated areas under the sharp crystalline peaks and the broad amorphous halo, respectively. K is a calibration constant, which takes into account that the intensity associated with the crystalline peaks occurs at a different angular distribution than the amorphous halo. It is often assumed to be unity [190]. Based on the spectrum presented in Figure 3.3, the apparent weight percent crystallinity was 16.3%. This value was obtained by computing the areas under the amorphous halo and crystalline peaks after establishing a baseline for the spectrum. These areas were inserted into Equation 3.7, and K was set to unity, consistent with the approach often adopted in the literature. This value is lower than the crystallinity value obtained from DSC by more than a factor of two. Farrow and Ward [191] reported apparent crystallinity values of undrawn and drawn PET fibers based on WAXD (with $K = 1$), density and infrared techniques. They reported very similar crystallinities based on density and WAXD (36% and 35%, respectively) for undrawn PET fibers having a density of 1.378 g/cm^3 . In striking contrast, for drawn PET fibers having a density 1.361 g/cm^3 , the apparent crystallinity values were 22% (using density data and the two-phase model described below) and 2% (WAXD), which differ by more than one order of magnitude. Another study [184] reported that, for drawn PET, crystallinity estimated from WAXD (2 wt.%) was much lower than crystallinity estimate based on density (20 wt.%). However, for

undrawn PET, the WAXD-based crystallinity (29 wt.%) was much closer to that based on density (20 wt.%).

Assuming the value of K in Equation 3.7 to be unity, particularly for drawn samples, has been questioned. It has been suggested that K should be calculated from WAXD data for two different samples of known crystallinities [192]. Equation 3.7 presumes that all crystallites contribute to I_c and only chains in the amorphous regions contribute to I_a . However, this simple model cannot explain a sizeable fraction of the available experimental results, especially for highly oriented polymers [191]. Several studies propose a transition region of finite width between the amorphous and crystalline regions instead of a sharp jump in density [186,193]. The presence of this transition region would tend to lower the crystallinity estimate based on WAXD spectrum. The so-called ‘crystal defect model’ suggests that a portion of the X-ray scattering from crystalline domains (mainly due to crystal defects, folded chains and one- and two-dimensional ordering in drawn polymers) is diffuse and contributes to the apparent amorphous halo [194]. This effect lowers the crystallinity values estimated from WAXD studies.

Density

The film density value is 1.395 g/cm³. On the basis of the widely used two-phase model, volume percent crystallinity was estimated from [27,184]:

$$\phi_c = \left(\frac{\rho - \rho_a}{\rho_c - \rho_a} \right) \times 100 \quad (3.8)$$

where ρ , ρ_c and ρ_a are densities of the semicrystalline polymer sample, wholly crystalline PET and wholly amorphous PET, respectively. If we use the constant and widely reported amorphous and crystalline density values of 1.335 g/cm³ and 1.515 g/cm³ respectively [12,76,195], Equation 3.8 yields an apparent crystallinity of 36 wt. % or 33 vol. %. These values are similar to those estimated from the DSC results.

For undrawn PET, Equation 3.8 provides crystallinity estimates that are consistent with those obtained from WAXD and DSC results [9,27]. However, for drawn polymers, including PET, crystallinity estimates based on density often do not agree with the estimates based on other techniques [76,183,186,191,192]. The two-phase model (Equation 3.8) with constant crystalline and amorphous densities has been reported to fail for drawn PET [186,191]. Farrow and Ward [191] suggested that the amorphous PET density is not constant but rather, directly proportional to the draw ratio in oriented fiber samples. In other words, higher overall density is accompanied by higher amorphous phase density as well. In contrast, Sekelik *et al.* [76] report that amorphous PET density decreases with increasing overall density in oriented film samples. These composite and seemingly contradictory observations can be rationalized since, in drawn samples, the amorphous phase density is affected by two competing factors: it increases as a result of chain orientation and decreases due to the formation of microscopic voids during the orientation process [191].

In summary, our crystallinity results are in agreement with other reports of wide variations, depending on the measurement technique, particularly for drawn or highly oriented samples [184,191,192,196-198]. The literature suggests good agreement

between density, DSC, and WAXD estimates of crystallinity for undrawn PET [184,186,191]. For undrawn samples, thermal annealing results in almost perfect crystals, consistent with earlier reports for solvent-cast PET [27] and microtomed amorphous PET [9]. However, for drawn PET, there is often wide disagreement between crystallinity values estimated by these techniques when the typical simplifying assumptions described previously are used to interpret the results. In this regard, the assumptions required to obtain crystallinity estimates from DSC data appear to be less severe than those required to estimate crystallinity using the other techniques. Therefore, we use the DSC estimate of crystallinity of BPET for all sorption and diffusion calculations.

Positron Annihilation Lifetime Spectroscopy

Density provides a measure of static free volume related to chain packing, but not dynamic or sub- T_g mobility-related free volume. Both types of free volumes influence penetrant diffusion in polymers and can be characterized by PALS [199]. PALS probes dynamic and static free volume cavity size and the relative concentrations of free volume cavities accessible to ortho-Positronium (oPs). τ_3 , the average lifetime of oPs in the polymer matrix, is a measure of the mean size of the cavity in which oPs localizes in the polymer. I_3 , the relative number of oPs annihilations, is a measure of the relative concentration of the free volume cavities. Table 3.1 provides a list of PALS parameter values for our BPET sample along with those obtained by Serad *et al.* [9] for highly amorphous, unoriented PET (APET). Based on these results, the free volume elements in BPET are larger than in APET. However, the concentration of free volume elements,

characterized by I_3 , is lower in BPET. This indicates a difference in the free volume distribution of the two samples, presumably due to different processing histories. Other studies of the effects of biaxial orientation and crystallinity on PALS parameters of PET and a copolymer of PET and poly(cyclohexyldimethylene terephthalate) (PCT) also indicate that increasing degree of crystallinity *via* biaxial stretching increases τ_3 and decreases I_3 . It should also be noted from Table 3.1 that the estimated amorphous phase fractional free volume based on PALS ($\tau_3^3 I_3 / \phi_a$) is significantly higher for BPET than for APET.

The decrease in I_3 is consistent with the presence of fewer *o*Ps-accessible free volume sites due to the higher level of crystallinity in the BPET sample than in the APET material. However, I_3 does not decrease strictly due to volume filling (*i.e.*, replacement of *o*Ps-accessible amorphous regions with inaccessible crystalline ones), as shown in Figure 3.4a. Moreover, τ_3 increases with increasing crystallinity, as shown in Figure 3.4b. These results suggest that either the crystal-amorphous interphase region is poorly packed or that the crystals place a dilational constraint on the nearby amorphous regions, which influences the free volume distribution in the amorphous regions [24,200-202].

Table 3.1 Positron annihilation lifetime spectroscopy (PALS) parameters for biaxially oriented PET (BPET) and amorphous PET (APET) samples

Sample	$\tau_3 \pm 0.025$ (ns)	$I_3 \pm 0.3$ (%)	$\tau_3^3 I_3$	$\tau_3^3 I_3 / \phi_a$
0.9 μm BPET	1.691	17.9	86	141
APET [9]	1.645	22.1	98	104

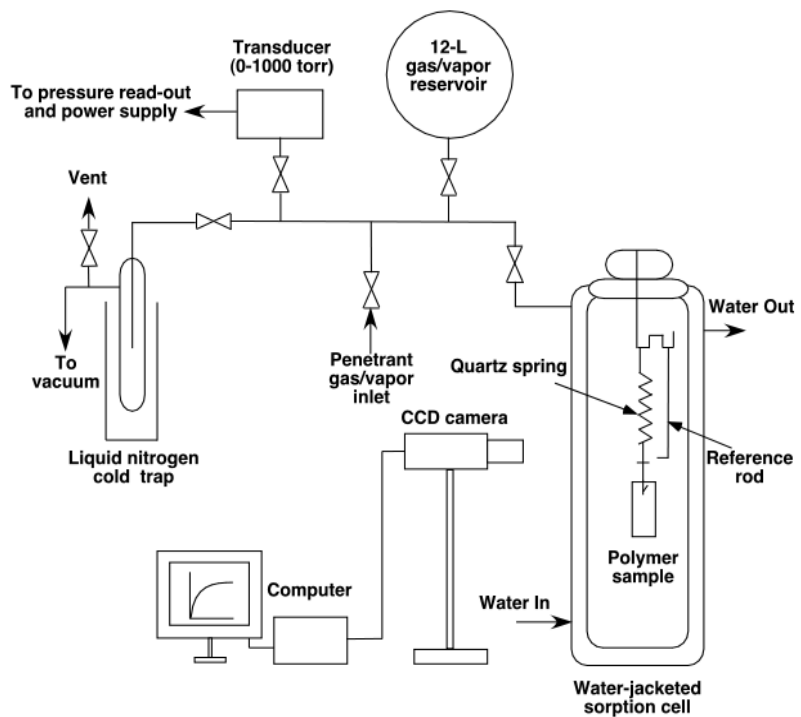


Figure 3.1 Schematic of McBain quartz spring balance for gravimetric sorption.

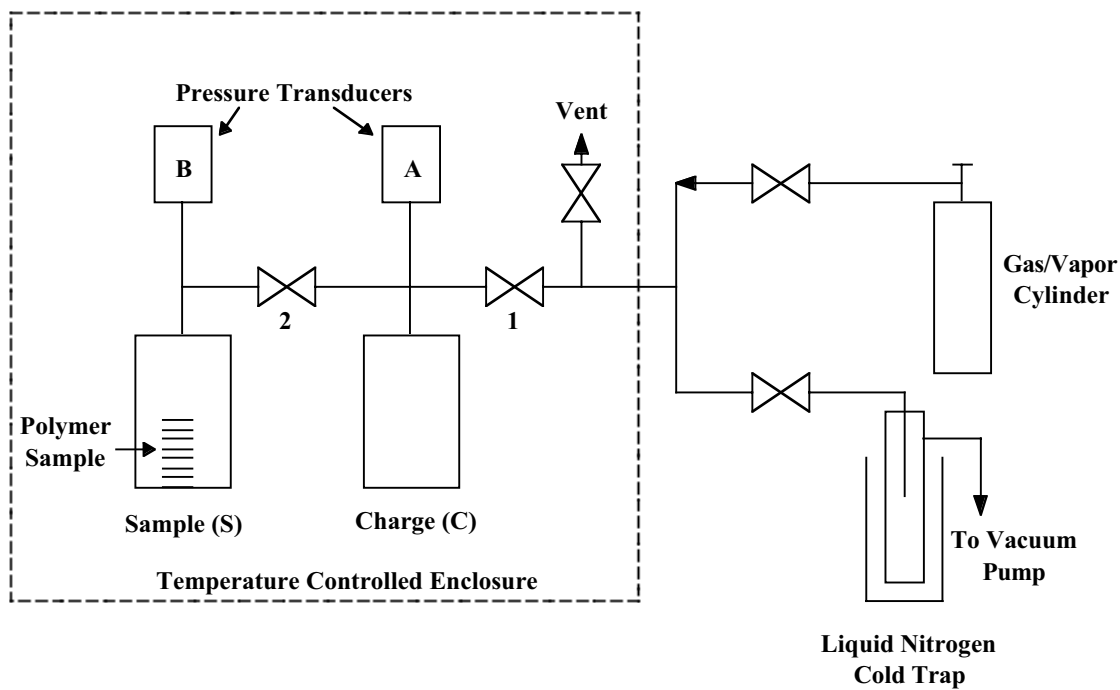


Figure 3.2 Schematic of a dual volume pressure decay sorption system.

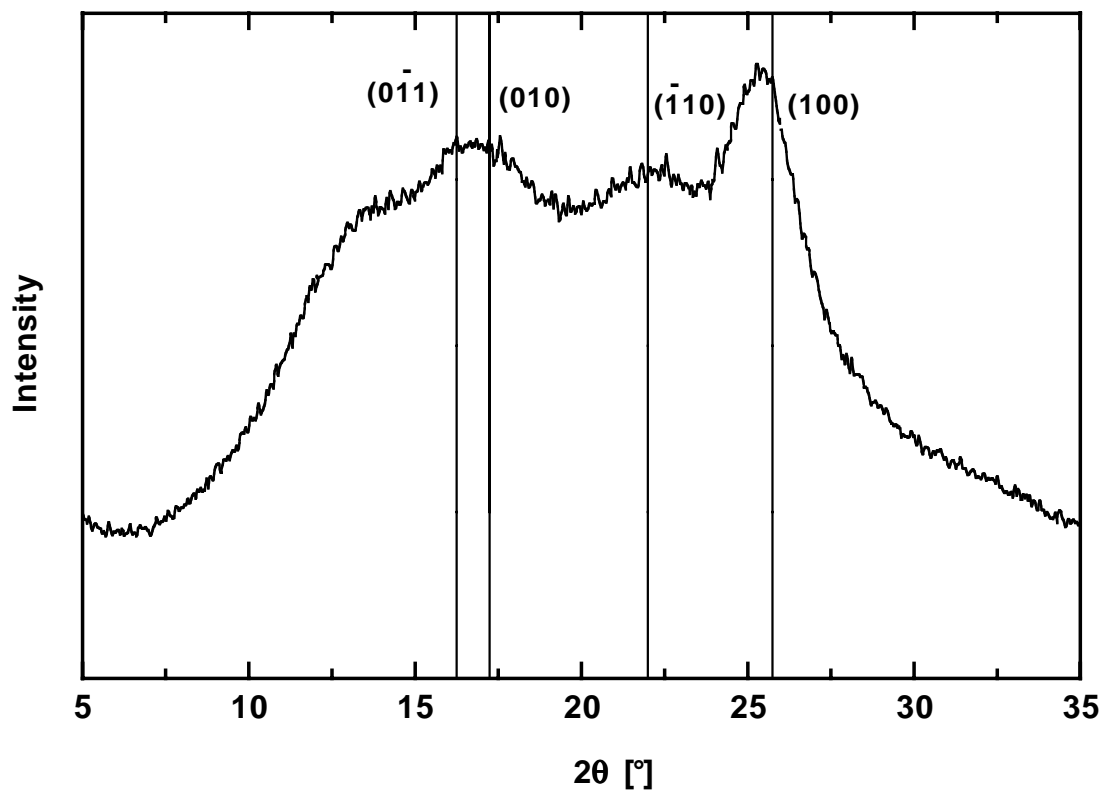


Figure 3.3 Wide angle X-ray diffraction spectrum of biaxially oriented PET (BPET).

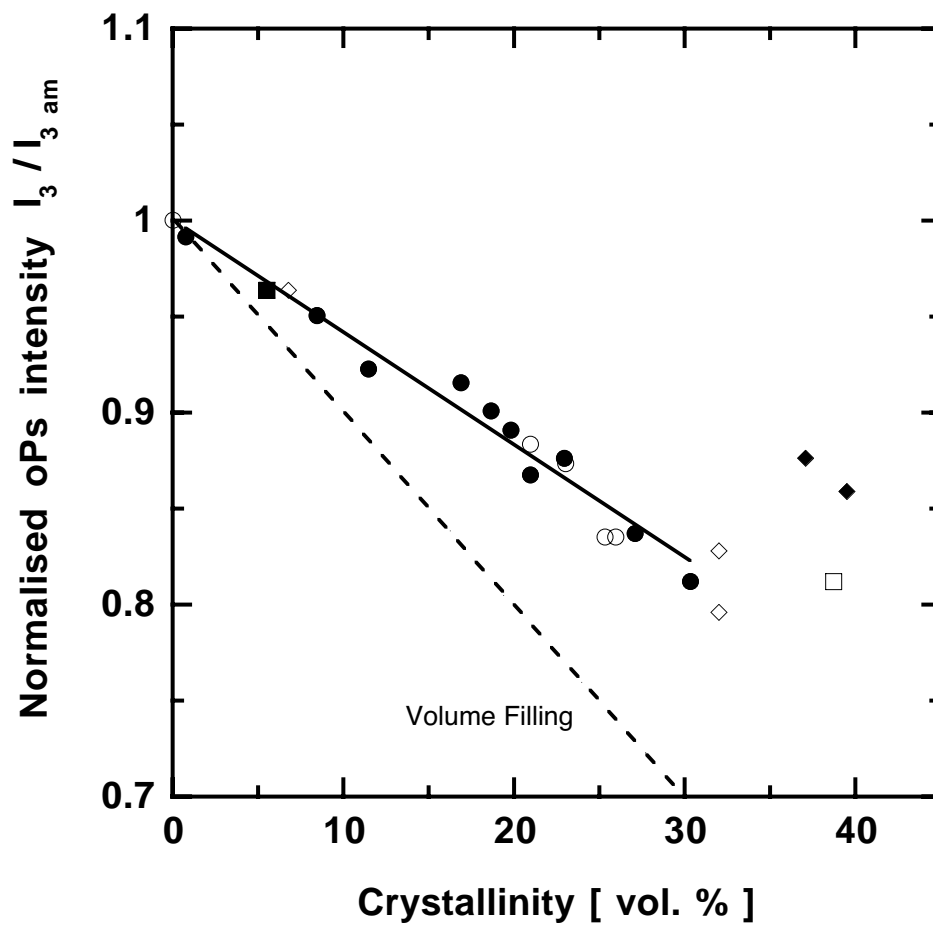


Figure 3.4a Variation of *oPs* intensity (normalized to an amorphous basis) in PET with degree of crystallinity. $I_{3 \text{ am}}$ is *oPs* intensity in a completely amorphous polymer sample. The dotted line was calculated based on simple volume filling (*i.e.*, replacement of the *oPs*-accessible amorphous regions with the inaccessible crystalline regions). (●) Xie *et al.* [201], (□) This study, (◆) Tant *et al.* [24], (■) Serad *et al.* [9], (○) Mohamed *et al.* [202], (◇) Tant *et al.* [24].

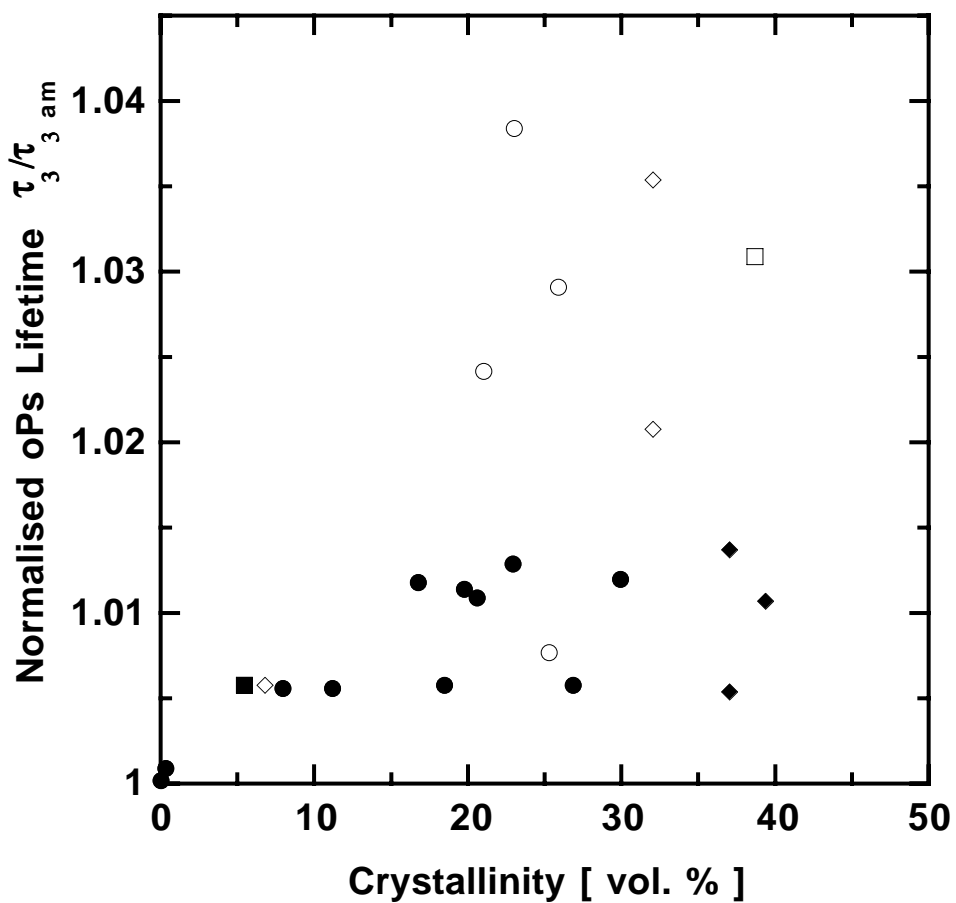


Figure 3.4b Variation of *oPs* lifetime (normalized to an amorphous basis) in PET with degree of crystallinity. $\tau_{3 \text{ am}}$ is *oPs* lifetime in a completely amorphous polymer sample. (●) Xie *et al.* [201], (□) This study, (◆) Tant *et al.* [24], (■) Serad *et al.* [9], (○) Mohamed *et al.* [202], (◇) Tant *et al.* [24].

CHAPTER 4

Novel Experimental Technique for Kinetic Gravimetric Sorption of Low Volatility Gases and Vapors in Polymers

This chapter has been adapted with permission from an article published in
Review of Scientific Instruments, 74 (12), pp. 5173-5178, 2003.

Copyright© 2003 American Institute of Physics.

4.1 Summary

A kinetic gravimetric sorption apparatus for measuring solubility and diffusivity of low vapor pressure gases and vapors in polymers and other sorbents is described. Sorption and transport data for toluene vapor in poly(dimethyl siloxane) at 25°C are provided to illustrate the method. These data were obtained by measuring the kinetic uptake of a mixture of carrier gas and toluene vapor and, for comparison, pure toluene vapor at the same thermodynamic activity. Excellent agreement was observed between toluene solubility and diffusivity values obtained from these two different experiments. In the mixture sorption experiments, the type of carrier gas (helium or nitrogen) had no effect on measured toluene solubility and diffusion coefficients.

4.2 Introduction

The sorption and transport of gases and organic vapors in polymeric materials are important in applications such as food packaging and membrane-based separations [4,14]. Several experimental techniques have been developed to characterize solubility and diffusivity of gases and vapors in polymers. The McBain spring balance is one of the most widely used methods to perform kinetic gravimetric sorption experiments in thin, uniform sheets of polymers [180]. This method provides independent measurements of penetrant solubility and diffusivity in a single experiment. It is often practiced as follows: A thin, uniform polymer film is suspended from a sensitive quartz spring and exposed to vacuum to remove all mobile and volatile species (*e.g.*, air gases). Then, the sample is contacted with a gas or vapor at fixed pressure. The time dependent spring extension

resulting from penetrant uptake in the polymer is monitored to determine mass uptake as a function of time. These data are readily deconvoluted to determine penetrant diffusion coefficients from the rate of uptake and solubility coefficients from the equilibrium uptake.

Due to the limited sensitivity of the pressure measuring devices commonly used in such systems, the sorption measurements are typically restricted to penetrants having substantial vapor pressures, especially at low penetrant activity (or relative pressure). To the best of our knowledge, 0.1 mmHg is the lowest vapor pressure penetrant for which gravimetric sorption experiments at low activity have been reported [203] using a highly sensitive pressure transducer.

The vapor pressures of gases and vapors typically decrease strongly with increasing size and condensability [204] (*cf.*, Figure 4.1). The sorption and transport of large, relatively low volatility penetrant molecules (*e.g.*, higher hydrocarbons, benzaldehyde, benzyl alcohol, benzophenone, benzyl acetate, *etc.*) in polymers are important considerations in food packaging applications [4,33]. However, due to the limitations mentioned earlier, kinetic gravimetric sorption experiments using such large and condensable penetrants at low thermodynamic activities (*i.e.*, low relative pressures) have been inconvenient. For this reason, data are often reported for such species based on experiments performed by exposing samples to saturated vapors or immersing them in liquid penetrant and weighing the samples at regular time intervals, effectively yielding sorption and transport measurements at very high activity [23]. Since penetrant solubility and diffusivity are often strongly dependent on concentration (or activity), these data may

not reflect practical conditions, where the penetrant solubility and diffusivity data at concentrations well below saturation are of interest [4].

For example, it has been proposed to reuse plastic packaging such as bottles by simply washing and then refilling them with a second product, possibly a beverage for human consumption. One concern with this approach is the possibility that low levels of organics sorbed in the package walls might be carried over from prior use of the package and potentially contaminate the second product by desorbing into it. In this regard, Miltz *et al.* reported sorption and transport data for liquid toluene and benzyl alcohol in poly(ethylene terephthalate) (PET) to characterize the migration of such contaminants into the polymer structure, and hence evaluate the migration of these components in post-consumer used PET [205]. Even though their study possibly represents the ‘worst-case’ contamination scenario, the sorption and transport data at much lower activities might be of more practical importance.

This chapter describes an experimental technique to extend the measurement capability of a McBain spring balance to perform kinetic gravimetric sorption studies of low volatility vapors over a wide range of activity. In this method, a carrier gas/vapor mixture is generated by bubbling an essentially non-sorbing carrier gas (*e.g.*, helium) through liquid penetrant and diluting the resulting gas/vapor mixture to the desired concentration using a second stream of pure carrier gas. The resulting vapor concentrations, which are accurately measured by a gas chromatograph, can be varied to cover the activity range of interest. Such a vapor generation/dilution scheme has previously been used for measuring mixed gas/vapor permeation properties of polymers

[206,207]. However, to the best of our knowledge, there are no reports of using such a system to control vapor activity for McBain spring balance experiments.

4.3 Principle of Operation

Figure 4.2 presents a schematic of the gravimetric sorption system. A constant vapor concentration is generated by bubbling a carrier gas (nitrogen or helium) through a standard washing bottle (labeled “organic liquid bubbler” in Figure 4.2) containing the organic liquid. The carrier gas is selected so that it sorbs to a negligible extent in the polymer sample at the pressure and temperature of interest. In this regard, gases such as nitrogen or helium, with low critical temperatures, are ideal for this purpose when used at ambient temperatures and low pressures (*e.g.*, at or below one atmosphere). The resulting gas/vapor mixture is mixed with another stream of carrier gas to produce the desired final concentration of the low volatility penetrant in the gas stream. The flow rates of these streams are controlled using mass flow controllers MFC 1 (0-1000 cm³/min.), and MFC 2 (0-100 cm³/min.), respectively. The mass flow controllers (Type 1259) and the mass flow readout unit (Type 247C) were from MKS Instruments (Andover, MA). Alphagaz 1 grade nitrogen and helium gases, obtained from Air Liquide (Houston, TX), are used as carrier gases. Check valves CV 1 and CV 2 (Model 53 series), obtained from Swagelok Co. (Solon, OH), prevent the organic vapors from contaminating the mass flow controllers. The gas bubbler is a 500 ml. washing bottle fitted with a coarse fritted disc-type gas dispersion tube purchased from Fisher Scientific International (Fair Lawn, NJ). A glass reservoir (12 liters) and glass manifold are used as penetrant reservoir. The entire

vapor generation/dilution apparatus and the penetrant reservoir are inside a temperature-controlled chamber. A sampling port for the gas chromatograph is provided on the glass manifold through valve B, and valve C connects the system to a vacuum pump used for sample degassing and system evacuation. Valve A connects the penetrant reservoir to a water-jacketed glass chamber. The polymer sample (typically 5-50 mg) is suspended from a sensitive quartz spring placed inside the chamber. The spring (Model 4501.3), supplied by Ruska Industries (Houston, TX), has a spring constant of 0.21 mg/mm. The water-jacketed glass chamber provides temperature control for the polymer sample environment by circulating water through the jacket and through an external circulation bath (not shown). The CCD camera and computer record spring extension as a function of time, as described in Chapter 3 [90].

Before beginning a sorption experiment, the sample is exposed to vacuum until there is no further spring displacement. This step removes previously sorbed air gases and water vapor from the polymer. The carrier gas/vapor mixture is initially routed through the purge valve for approximately 30 min. to produce a stream of gas containing a constant and reproducible vapor concentration. The mixture is then diverted through the inlet valve to fill the penetrant reservoir to the desired pressure. This mixture is then allowed to equilibrate inside the reservoir; the timescale for this step is a function of temperature and the dimensions and overall volume of the penetrant reservoir. A small injection volume (10-50 μL) is withdrawn from the system through the GC sampling port using a gas-tight syringe (Model #1705) supplied by Supelco Sigma Aldrich Co. (St. Louis, MO) and injected into an HP 5890 Series II gas chromatograph equipped with

flame ionization detector (FID). The operating parameters for the gas chromatograph are recorded in Table 4.1. The vapor concentration can be determined directly from standard calibration curves prepared prior to these measurements [208]. The polymer sample is then exposed to the penetrant vapor mixture by opening valve A, and the spring position is recorded as a function of time using the CCD camera and computer, as described previously [90]. The spring position data are converted to mass uptake data using the spring constant. Penetrant diffusion coefficients and equilibrium mass uptakes are extracted from these kinetic sorption data as described in the next section. Penetrant activity is calculated from the vapor phase concentration and total pressure using the following equation:

$$a = \frac{\left(\frac{c}{10^6} \right) \times P}{P_{sat}} \quad (4.1)$$

where a is penetrant activity, c is penetrant vapor concentration in parts per million (moles/moles), P is total pressure (mmHg), and P_{sat} is penetrant saturation vapor pressure (mmHg) at the temperature of the sorption experiment. This expression presumes that the vapor behaves as an ideal gas.

The following procedure is used for preparing the standard vapor calibration curve. A small but known amount of liquid penetrant is injected into a sealed container using a liquid syringe and the liquid/vapor system is allowed to reach equilibrium at a fixed temperature, T . A known volume of saturated vapor, v (cm^3), is withdrawn from the headspace of the container using a gas-tight syringe and injected into a glass vial of known volume, V (cm^3). The vapor phase concentration in the vial, c , in parts per million

(moles/moles) can be calculated from the vapor pressure of the liquid penetrant using the following equation:

$$c = \left(\frac{P_{sat,T} \times v}{760 \times V} \right) \times 10^6 \quad (4.2)$$

where $P_{sat,T}$ is vapor pressure of liquid penetrant (mmHg) at temperature T, which can be calculated using standard equations [204]. A series of samples of varying vapor concentration are prepared by repeating this procedure. Aliquots of these standard samples ranging from 5-50 μ L are injected into the gas chromatograph using a gas-tight syringe, and a calibration curve is prepared by plotting FID area response versus vapor concentration.

4.4 Experimental Results

The sorption and transport data for toluene in crosslinked poly(dimethyl siloxane) (PDMS) were determined at 25°C and vapor activity ranging from 0 to 0.7. The polymer and crosslinking agent were supplied by Wacker Silicones Corp. (Adrian, MI) and a film, 251 ± 1 μ m thick, was cast using a procedure described in the literature [207]. We selected this polymer and penetrant as a model system for several reasons. First, the sorption and diffusion characteristics of rubbery PDMS are well known [209-211]. Second, PDMS is a well-behaved polymer in the sense that it does not exhibit any penetrant induced hysteresis or other time-dependent changes in penetrant solubility or diffusion coefficients. Third, it has very high diffusion coefficients so that, even for relatively large penetrants, such as toluene, the experiments are rapid. Finally, toluene is

sufficiently volatile (vapor pressure = 28.8 mmHg at 25°C [212]) to permit this study using conventional methods (*i.e.*, without resorting to the gas/vapor generation system), and it is sufficiently condensable (*i.e.*, it is a liquid at ambient conditions) that it is amenable to study using the gas/vapor generation system. Thus, PDMS and toluene represent a good polymer/penetrant combination for testing the method being developed in this study.

Table 4.2 presents a compilation of carrier gas flow rates, total pressures, and corresponding toluene vapor phase mole fractions in mixtures with nitrogen at 25°C. These vapor/gas mixtures were used in the sorption experiments described below. The volume of liquid toluene in the washing bottle at the beginning of the sorption experiment is given as percentage of the total volume of the washing bottle (500 cm³) in Table 4.2. For similar values of mass flow rates and total pressures, the vapor mole fraction increases with increasing liquid volume in the washing bottle because the contact time of the carrier gas with toluene increases as the liquid volume increases, so the carrier gas absorbs more toluene vapor as the liquid volume increases.

Figure 4.3 presents experimental sorption data as a function of gas phase penetrant activity calculated using Equation 4.1. The figure presents data obtained from three independent sets of experiments. The mixed vapor data were obtained using two different carrier gases (nitrogen and helium) and the experimental set-up and procedure described in the previous section. These data are compared with pure vapor sorption data obtained using the spring balance and the more traditional procedure, which does not involve the use of a carrier gas [8]. The mixed vapor data in Figure 4.3 were fit using the

Flory-Huggins equation, which is commonly used to describe penetrant sorption in rubbery polymers such as PDMS [15]:

$$\ln a = \ln \phi + (1 - \phi) + \chi(1 - \phi)^2 \quad (4.3)$$

where a is penetrant activity, ϕ is penetrant volume fraction in the polymer, and χ is Flory-Huggins interaction parameter. The penetrant volume fraction is related to mass uptake (the ordinate in Figure 4.3) as follows:

$$\phi = \frac{\left(\frac{M_{\infty} \times \rho \times \vartheta}{100 \times MW} \right)}{1 + \left(\frac{M_{\infty} \times \rho \times \vartheta}{100 \times MW} \right)} \quad (4.4)$$

where M_{∞} is the equilibrium uptake (g toluene sorbed/100g polymer), ρ is polymer density (0.98 g/cm³) [207], ϑ is penetrant liquid molar volume at 25°C (106.8 cm³/mol) [213], and MW is toluene molecular weight (92 g/mol). The equilibrium mass uptakes of toluene in PDMS, presented in Figure 4.3, obtained from the mixed vapor sorption experiments are in excellent agreement with the data obtained from pure vapor sorption experiments. Also, the results from mixed vapor sorption experiments are independent of the carrier gas used. Both carrier gases, nitrogen and helium, have extremely low solubility in PDMS relative to toluene. For example, the ratios of solubilities at infinite dilution in PDMS at 25°C are approximately 6,000 and 23,500 for toluene/N₂ and toluene/He, respectively [214]. The Flory-Huggins interaction parameter, χ , resulting from the curve-fit in Figure 4.3 was 1.14 ± 0.05 . It is in good agreement with the values

(ranging from 1.1-0.9 over an activity range of 0.3-0.6) reported in the literature for toluene in PDMS [211].

Figure 4.4a presents a comparison of kinetic sorption results from pure toluene and toluene/N₂ mixture sorption experiments in PDMS at an activity of 0.5. In this figure, the mass uptake at time t , M_t , normalized by the mass uptake at equilibrium, M_∞ , is presented as a function of square root of the time since the sorption experiment began. The data collected during the initial stages of the experiment were not included due to vibration of the spring at the start of the experiment (in response to having the pressure increased from vacuum to the final total pressure of the experiment). These vibrations, which compromise the initial mass uptake data, decay over timescales of the order of one minute or less, and afterwards, the spring displacement accurately reflects mass uptake. The data in Figure 4.4a can be modeled by the following equation, which describes Fickian penetrant diffusion into a semi-infinite plane sheet [25]:

$$\frac{M_t}{M_\infty} = 1 - \frac{8}{\pi^2} \sum_{n=0}^{\infty} \frac{1}{(2n+1)^2} \exp\left(\frac{-\bar{D}(2n+1)^2 \pi^2 t}{\ell^2}\right) \quad (4.5)$$

where \bar{D} is effective, concentration averaged diffusion coefficient and ℓ is sample thickness ($251 \pm 1 \mu\text{m}$). \bar{D} and M_∞ were estimated from a least-squares fit of the experimental data to Equation 4.5. The values of \bar{D} and M_∞ determined from both pure vapor and mixed vapor sorption experiments in Figure 4.4a are in excellent agreement with each other. The diffusion coefficients of toluene from pure and mixed vapor sorption experiments are $1.3 \pm 0.1 \times 10^{-6}$ and $1.1 \pm 0.1 \times 10^{-6} \text{ cm}^2/\text{s}$, respectively. The equilibrium

mass uptakes of toluene are 7.3 ± 0.1 and 7.1 ± 0.2 g toluene/100g PDMS from pure and mixed vapor sorption experiments, respectively.

Figure 4.4b presents a comparison of kinetic sorption results from mixed vapor sorption experiments with two different carrier gases and a toluene vapor activity of 0.35. The estimated diffusion coefficients of toluene are $1.2 \pm 0.2 \times 10^{-6}$ and $1.9 \pm 0.3 \times 10^{-6}$ cm²/s for nitrogen and helium carrier gas, respectively, and equilibrium mass uptake is 4.1 ± 0.1 g toluene/100g PDMS for both carrier gases. Thus, both toluene diffusion coefficients and equilibrium toluene uptake values are independent of the type of carrier gas used, as expected.

Figure 4.5 presents a comparison of toluene diffusion coefficients determined from pure vapor and mixed vapor sorption in PDMS at 25°C. There is excellent agreement between the diffusion coefficients obtained by the two experimental techniques. The diffusion coefficients decrease with increasing penetrant activity or concentration, which is in qualitative agreement with the concentration dependence of diffusion coefficients of ethyl benzene [210], toluene [211], and xylene [211] in PDMS. Sun *et al.* have reported a decrease in toluene diffusion coefficients from 8.2×10^{-7} to 5.5×10^{-7} cm²/s with increasing activity from 0.3 to 0.6 at 25°C [211]. Their values are systematically lower than the diffusion coefficients obtained in this study. This difference might be due to the fact that the PDMS sample used in this study was filler-free whereas the sample used by Sun *et al.* had 32.3 wt% silica resin filler, and such fillers usually reduce penetrant diffusion coefficients [4].

The analysis presented above is valid if the rate-controlling step is Fickian diffusion through the polymer film rather than diffusion of toluene in the gas phase surrounding the film. One concern is the effect of a so-called film or boundary layer resistance near the polymer surface arising from a concentration gradient of sorbing vapor in the gas phase surrounding the polymer. As the polymer film absorbs penetrant, fresh penetrant vapor must be transported *via* diffusion and/or convection to the polymer film surface. If the rate of penetrant transport in the gas phase is slow relative to the rate of penetrant uptake by diffusion into the polymer, the penetrant concentration at the polymer surface could be depleted, which would influence the kinetics of penetrant uptake in the polymer [25]. The relative importance of this effect can be assessed from the mass transfer Biot number (Bi_m), which is the ratio of the mass transfer resistance due to diffusion inside the polymer film to the mass transfer resistance due to transport in the gas phase near the polymer film surface [215]:

$$Bi_m = \frac{k_m \ell}{2\bar{D}} \times \left(\frac{22414}{S P} \right) \quad (4.6)$$

where k_m is the mass transfer coefficient of toluene in a binary mixture with nitrogen or helium ($\text{mol}/\text{cm}^2 \cdot \text{s}$), ℓ is polymer film thickness (cm), \bar{D} is the diffusion coefficient of toluene in the polymer film (cm^2/s), S is the solubility of toluene in the polymer film ($\text{cm}^3(\text{STP})/\text{cm}^3 \cdot \text{cmHg}$), and P is total pressure (cmHg). Conservative values of k_m are estimated from:

$$k_m = \left[\frac{\left(\frac{c}{10^6} \right) P}{RT} \right] \times \frac{D_g}{Z} \quad (4.7)$$

where c is toluene vapor concentration in the bulk gas phase in parts per million (moles/moles), T is the experimental temperature (K), D_g is diffusion coefficient (cm^2/s) of toluene in the carrier gas (nitrogen or helium), which was estimated from available correlations [215], and Z is the distance between the surface of the polymer film and the wall of the sorption chamber (5.1 cm). From a practical viewpoint, if the Biot number is greater than approximately 10, the diffusion of toluene in the polymer film is the rate-controlling step [216]. For mixtures of toluene in nitrogen or helium at the experimental conditions, the calculated values of Bi_m are of the order of 10^3 , suggesting that the impact of the external film resistance is negligible. Therefore, the estimated diffusion coefficients of toluene in the polymer film should not be influenced by the carrier gas used, which is consistent with the experimental result presented in Figure 4.5.

Another concern is the change in concentration of toluene vapor in the gas phase surrounding the polymer film as a result of sorption in the polymer. From toluene solubility values corresponding to the gas phase mole fractions explored in this study (*cf.*, Table 4.2), the change in the gas phase toluene concentration during a sorption experiment is estimated to be approximately 0.1% to 0.14% at most. Thus, the change in toluene concentration as a result of sorption in the polymer is negligibly small. The expression used to evaluate the relative change in gas phase concentration, $\Delta c/c$, during a sorption experiment is:

$$\frac{\Delta c}{c} (\%) = \left(\frac{10^3 \times M_\infty \times M_p \times R \times T}{MW \times c \times P \times V_s} \right) \quad (4.8)$$

where M_p is weight of the polymer film (6.8 mg) and V_s is the volume of the sorption chamber (5300 cm³).

4.5 Discussion

A new experimental technique has been described for performing kinetic gravimetric sorption experiments using low volatility vapors. The sorption and transport properties of toluene in PDMS at 25°C have been provided to illustrate the method. The proposed experimental technique could be useful in applications, such as vapor separation using membranes and food packaging, where it is desirable to know values of penetrant solubility and diffusivity as a function of the partial pressure (or activity) of the vapor in contact with the polymer. Based on the sensitivity of the gas chromatograph (50 ppb for an FID detector) [217] and using Equation 4.1 (penetrant activity, $a = 0.1$ and total pressure, $P = 1$ mmHg), we estimate that penetrants with vapor pressures as low as 10^{-7} mmHg might be studied using this new technique coupled with highly sensitive current generation pressure transducers. The traditional gravimetric sorption method, however, has only been used for studying penetrants with vapor pressures as low as 0.1 mmHg [203]. The spring balance is a well-known but very reliable and robust method for performing such measurements. Because all of the components that contact the vapor being studied are glass, quartz or polymer o-ring seals (which may be selected from very

chemically resistant materials), this method is useful for measuring the uptake of even corrosive or highly condensable vapors in polymers.

4.6 Acknowledgments

The author gratefully acknowledges partial support for this work from Eastman Chemical Co. (Kingsport, TN). The author also thanks Dr. Lora Toy (RTI International, Research Triangle Park, NC) for providing the PDMS film sample and Ms. Anna Iwasinska (University of Texas at Austin, Austin, TX) for helpful discussions regarding gas chromatography.

Table 4.1 Gas chromatograph settings

GC Setting	Value/Type
Injector temperature (°C)	200
Column temperature (°C)	100
Detector temperature (°C)	280
Helium carrier flow rate (cm ³ /min)	10
Elution time (min)	2.1
Detector	FID
Column	SGE [®] BPX-5 capillary column 30 m × 0.53 mm

Table 4.2 Mass flow rates, total pressures, and corresponding toluene vapor mole fractions in mixtures with nitrogen at 25°C

MFC (1) Flow Rate (cm ³ /min)	MFC (2) Flow Rate (cm ³ /min)	Toluene Liquid Volume in Gas Bubbler (%)	Total Pressure (cmHg)	Toluene Mole Fraction
1000	100	65	5.4	0.047
1000	100	65	7.1	0.048
1000	100	15	9.3	0.052
1000	100	65	8.9	0.077
1000	100	15	11.1	0.061
1000	100	15	13.3	0.065
1000	0	15	13.1	0.073
1000	100	65	13.1	0.078
1000	100	65	15.1	0.076
1000	0	35	17.6	0.072
1000	100	65	17.6	0.079
1000	0	65	17.3	0.089

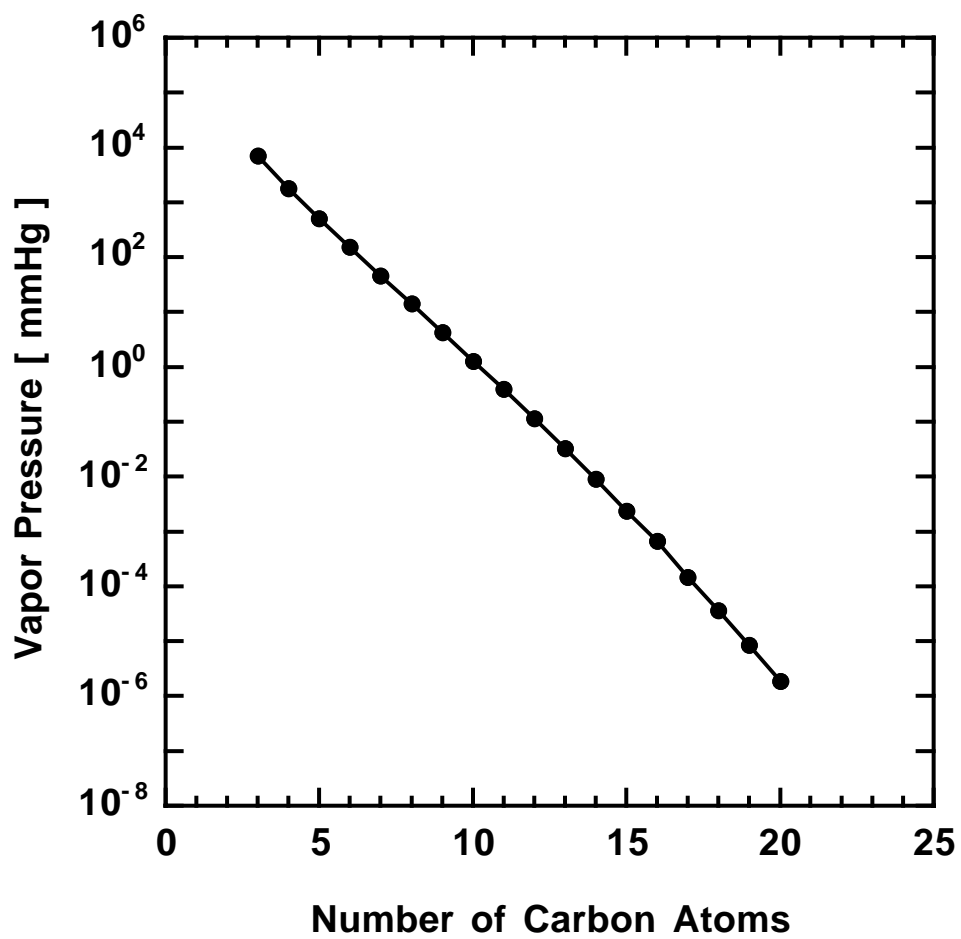


Figure 4.1 Vapor pressures of linear alkanes at 25°C as a function of number of carbon atoms [218].

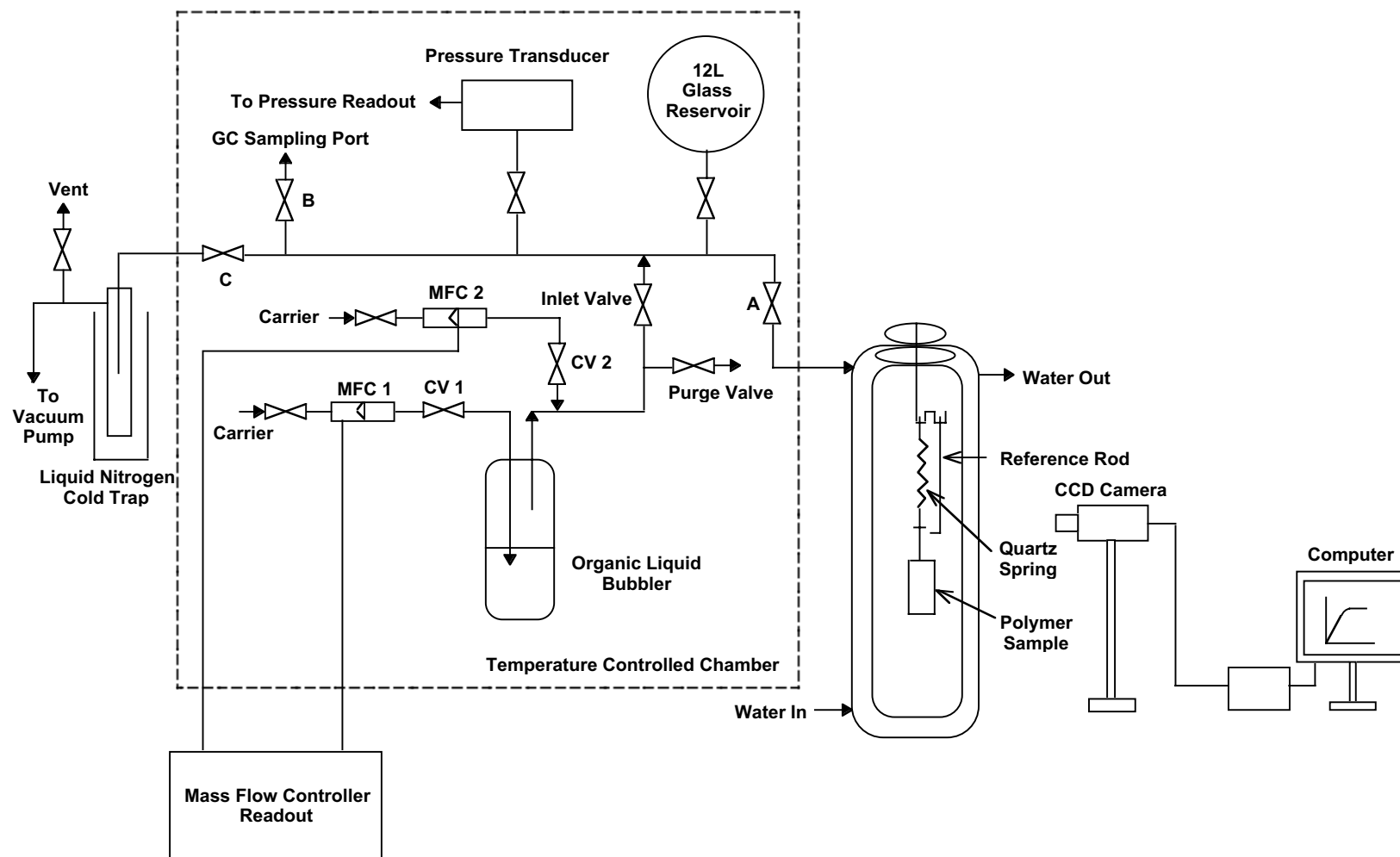


Figure 4.2 Schematic diagram of modified spring balance system.

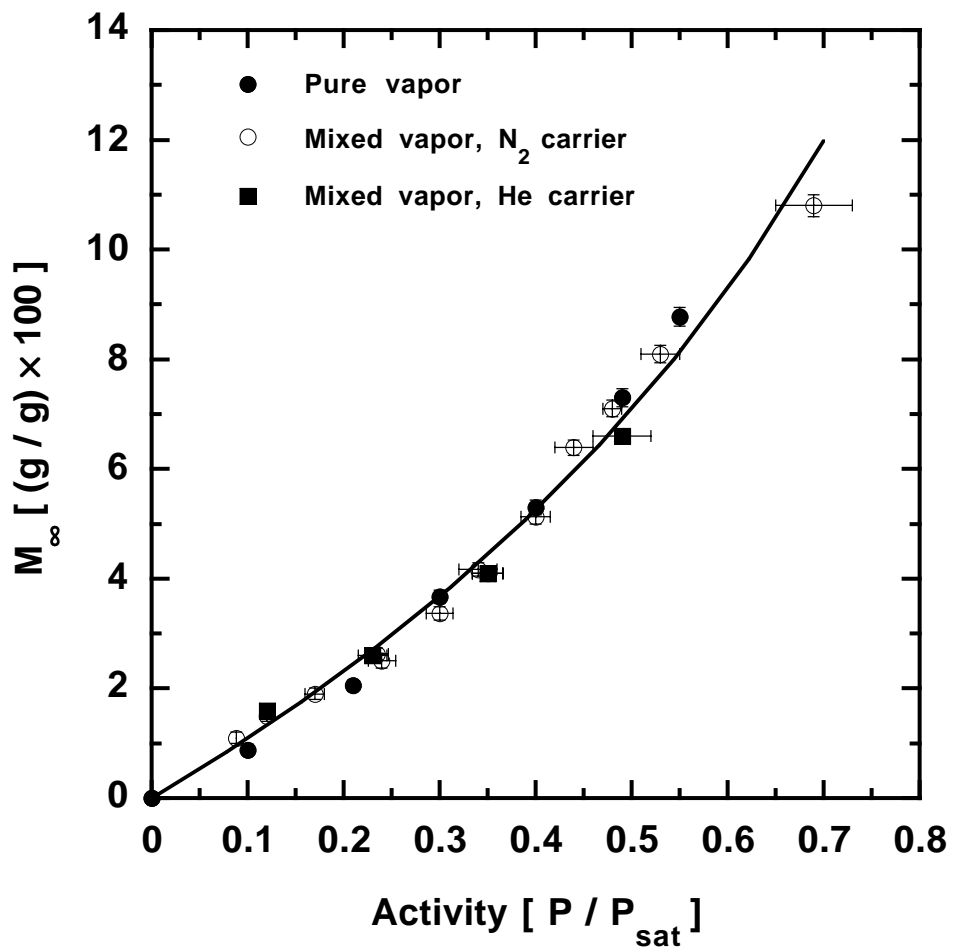


Figure 4.3 Sorption isotherms of toluene in poly(dimethyl siloxane) at 25°C determined from pure and mixed vapor sorption experiments. The saturation vapor pressure of toluene at 25°C is 2.9 cmHg [212]. The experimental data were fit using the Flory-Huggins sorption model ($\chi = 1.14 \pm 0.05$).

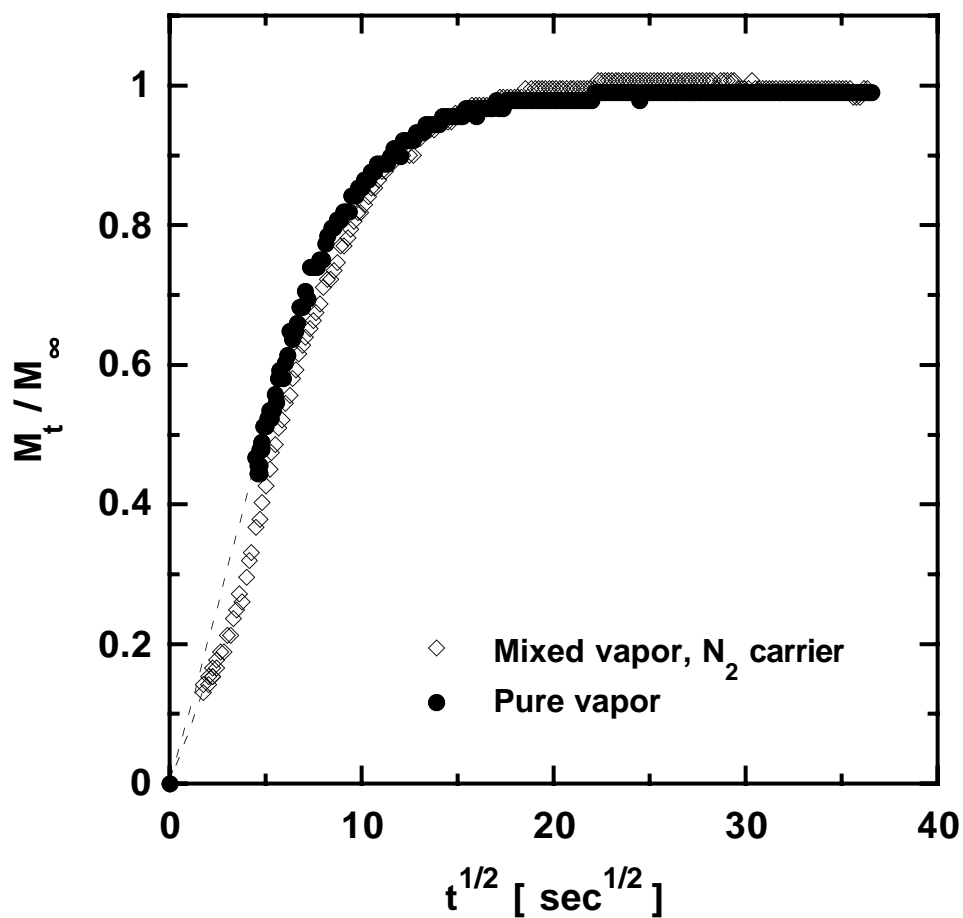


Figure 4.4a Comparison of kinetic sorption data from pure and mixed vapor sorption experiments at 25°C and vapor activity increasing from 0 to 0.5 (● pure vapor: $M_\infty = 7.3 \pm 0.1$ g toluene/100g PDMS and $\bar{D} = 1.3 \pm 0.1 \times 10^{-6}$ cm²/s; ◇ mixed vapor: $M_\infty = 7.1 \pm 0.2$ g toluene/100g PDMS and $\bar{D} = 1.1 \pm 0.1 \times 10^{-6}$ cm²/s). The initial data were not included due to spring vibrations and have been replaced by dotted lines.

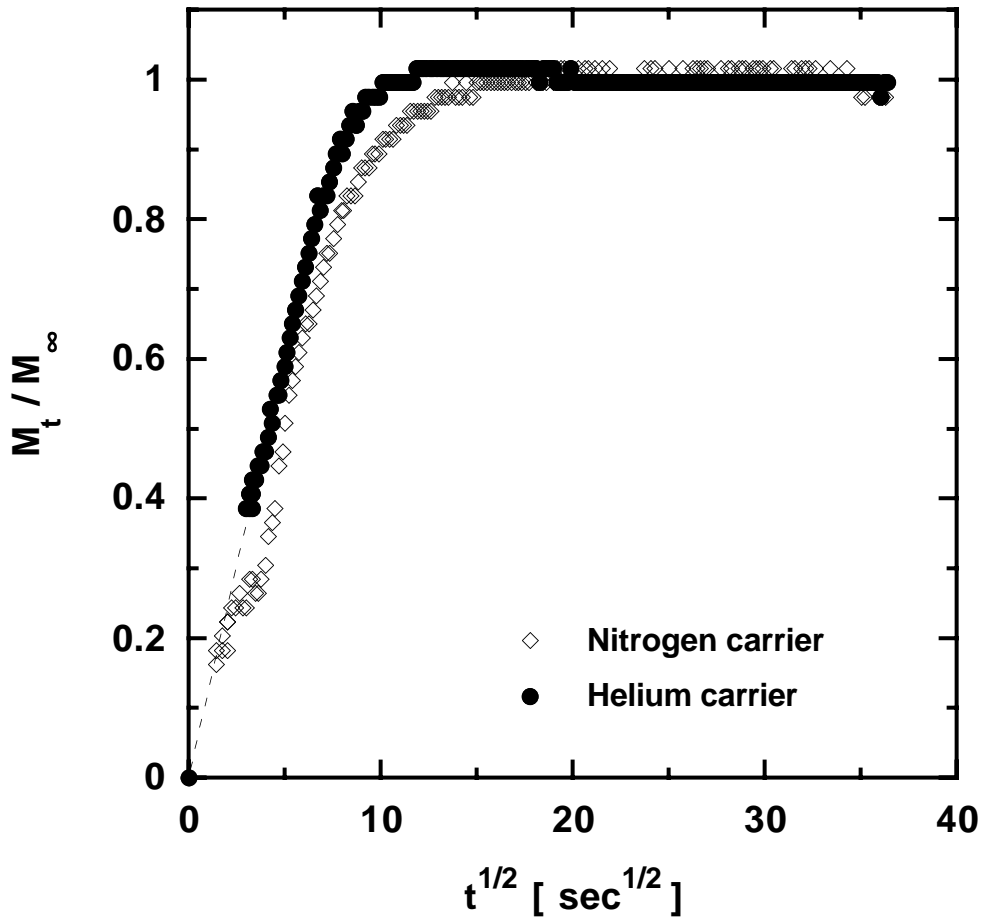


Figure 4.4b Comparison of kinetic sorption data from mixed vapor sorption experiments at 25°C using nitrogen and helium carrier gases and vapor activity increasing from 0 to 0.35 (● helium: $M_\infty = 4.1 \pm 0.1$ g toluene/100g PDMS and $\bar{D} = 1.9 \pm 0.3 \times 10^{-6}$ cm²/s; ◇ nitrogen: $M_\infty = 4.1 \pm 0.1$ g toluene/100g PDMS and $\bar{D} = 1.2 \pm 0.2 \times 10^{-6}$ cm²/s). The initial data were not included due to spring vibrations and have been replaced by dotted line.

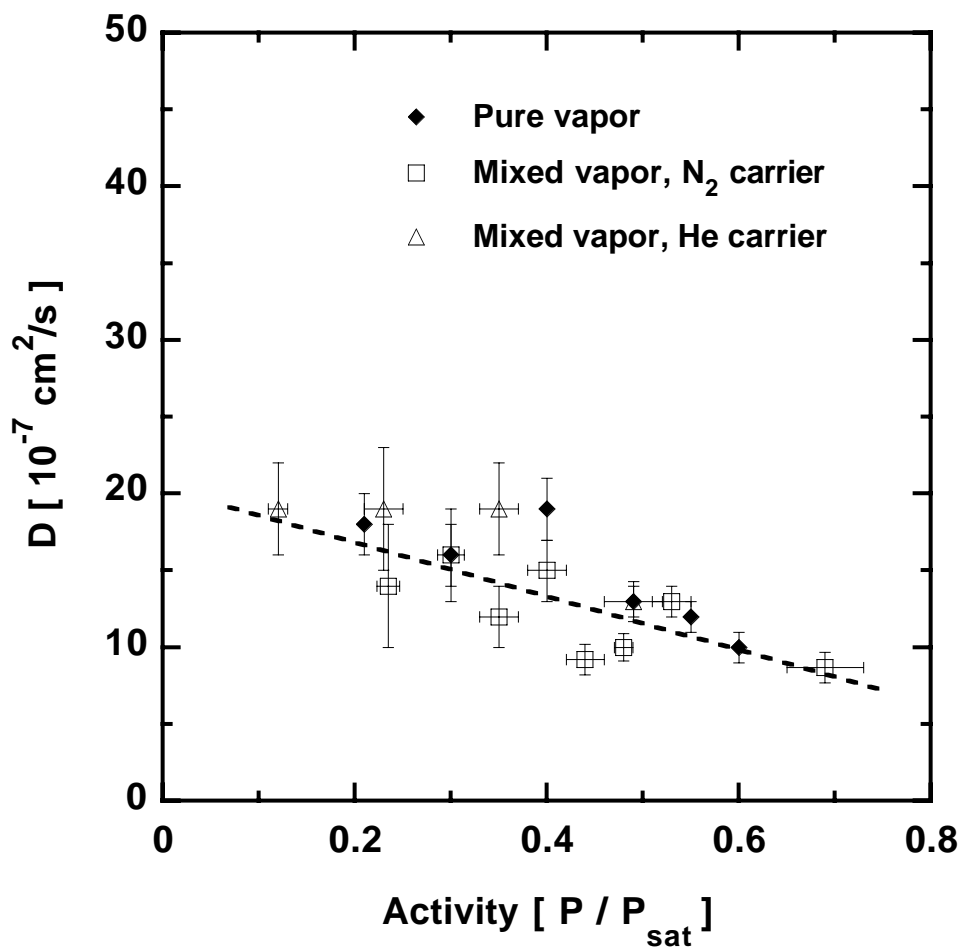


Figure 4.5 Comparison of diffusion coefficients of toluene in poly(dimethyl siloxane) at 25°C from pure and mixed vapor sorption experiments.

CHAPTER 5

Sorption and Transport of Linear Alkane Hydrocarbons in Biaxially Oriented Poly(ethylene terephthalate)

This chapter has been adapted with permission from an article published under the same title in *Journal of Polymer Science (Physics)*, 39 (11), pp. 1160-1172, 2001.

Copyright© 2001 John Wiley & Sons.

5.1 Summary

Equilibrium sorption and kinetics of *n*-butane and *n*-pentane uptake in uniform, biaxially oriented, semicrystalline poly(ethylene terephthalate) (BPET) films are reported at 35°C and for pressures ranging from 0 to approximately 76 cmHg. Sorption isotherms are well described by the dual-mode sorption model. Sorption kinetics are described either by Fickian diffusion or a two-stage model incorporating Fickian diffusion at short times and protracted polymer structural relaxation at long times. Diffusion coefficients increase with increasing penetrant concentration. *n*-Butane solubility is lower than that of *n*-pentane, consistent with the more condensable nature of *n*-pentane. However, *n*-butane diffusion coefficients are higher than those of *n*-pentane. Infinite dilution, estimated amorphous phase diffusion coefficients are well correlated with penetrant critical volume, and infinite dilution, estimated amorphous phase penetrant solubility, with penetrant critical temperature.

5.2 Experimental

5.2.1 Materials

Biaxially oriented PET films having a nominal thickness of 0.9 μm and purchased from Goodfellow Co. (Berwyn, PA) were used as received. The film density, 1.395 g/cm^3 , was furnished by the supplier. The complete details of sample characterization techniques and corresponding results and discussion were presented earlier in Chapter 3. *n*-Butane (99.5% purity) was purchased from Scott Specialty Gases (Durham, NC). High performance liquid chromatographic (HPLC) grade (99.7% purity) *n*-pentane was

purchased from Fisher Scientific International (Fair Lawn, NJ). It was subjected to several freeze-thaw cycles to remove dissolved gases and other impurities before use.

5.2.2 Gravimetric Sorption

Interval kinetic gravimetric sorption experiments were performed using a traditional McBain spring balance system, which was described in Chapter 3. The quartz spring was supplied by Ruska Industries, Inc. (Houston, TX) and had a spring constant of 2.94 mm/mg.

5.3 Results and Discussion

5.3.1 Equilibrium *n*-Butane and *n*-Pentane Uptake

Interval kinetic gravimetric sorption experiments were used to determine sorption isotherms of *n*-butane and *n*-pentane in BPET at 35°C, and the results are presented in Figures 5.1a and 5.1b. Both isotherms are concave to the pressure axis and are well described by the dual-mode sorption model, which is typically used for sorption of gases and vapors in both amorphous and semicrystalline glassy polymers, such as PET [18]. According to this model, penetrants sorb into the equilibrium densified polymer matrix (Henry's Law sites) and into the so-called non-equilibrium excess volume of the glassy polymer (Langmuir sites). The total penetrant concentration is the algebraic sum of the concentration in each mode:

$$C = k_D p + C'_H \left(\frac{bp}{1 + bp} \right) \quad (5.1)$$

where k_D is the Henry's Law coefficient, $C_{H'}$ is the Langmuir capacity parameter, a measure of the sorption capacity in the non-equilibrium excess volume of the glassy polymer, and b is the Langmuir affinity parameter, a measure of the penetrant's affinity for the Langmuir sites. The Langmuir capacity has been associated with frozen microvoids in non-equilibrium glassy polymers [16,17]. Restriction of the backbone chain motions of polymers below the glass transition temperature kinetically limits chain relaxation, presumably resulting in trapped excess free volume or so-called frozen microvoids [16]. While the dual-mode sorption model is the most widely used model for penetrant sorption in glassy polymers, other models, such as the non Equilibrium Lattice Fluid (NELF) model, have also been proposed in the literature [219].

The curves in Figures 5.1a and 5.1b represent least-square fits of the experimental sorption data to Equation 5.1. The dual-mode parameters obtained in this study for BPET are presented in Table 5.2. The dual-mode parameters obtained by Serad *et al.* [9] for *n*-butane sorption in amorphous PET (APET) are also included in Table 5.2. Based on the values in Table 5.2, the infinite dilution, estimated amorphous phase solubility coefficient of *n*-butane, $(k_D + C_{H'} b) / \phi_a$, is higher for our semicrystalline BPET sample ($0.126 \text{ cm}^3(\text{STP})/(\text{cm}^3 \cdot \text{cmHg})$) than for APET ($0.052 \text{ cm}^3(\text{STP})/(\text{cm}^3 \cdot \text{cmHg})$), suggesting that the penetrant-accessible amorphous phase in the oriented BPET sample has considerably higher solubility than that in the highly amorphous APET sample. This result is contrary to the conventional notion that crystallinity decreases penetrant solubility [10]. In this regard, the Henry's Law parameter, k_D , is somewhat lower in the crystalline BPET sample than in the largely amorphous APET sample. However, the higher value of $C_{H'}$ in

BPET indicates the presence of higher non-equilibrium excess volume in the oriented, semicrystalline sample. Since most of the penetrant sorption occurs into the non-equilibrium excess volume at infinite dilution, the infinite dilution solubility is particularly sensitive to the distribution of the non-equilibrium excess volume sites in the amorphous phase. The amorphous phase, fractional free volume estimates, based on PALS (*cf.*, Table 5.1), are consistent with the solubility results.

The effect of crystallinity and chain orientation on sorption and diffusion has been studied [76,79,220]. Sekelik *et al.* [76] determined the effect of crystallinity on amorphous phase solubility of oxygen in PET. They reported an increase in oxygen solubility in the amorphous phase of PET as a result of crystallization. This was due to a decrease in density of the amorphous phase with increasing crystallinity, indicating an appearance of additional free volume. As an example, the apparent amorphous phase oxygen solubility increased from approximately $0.02 \text{ cm}^3/(\text{cm}^3 \cdot \text{atm})$ to $0.06 \text{ cm}^3/(\text{cm}^3 \cdot \text{atm})$ as the density of the amorphous phase decreased from 1.37 to 1.35 g/cm^3 . The authors concluded that hole-filling (*i.e.*, sorption in the Langmuir sites) is the major process by which oxygen sorbs into PET. Our results of *n*-butane sorption in PET are in good qualitative agreement with their results. Shastri *et al.* [79] studied the effect of orientation on oxygen permeability in vinylidene chloride/vinyl chloride (VDC) copolymer and in aromatic nylon. They reported an increase in permeability upon biaxial orientation. For example, the VDC copolymer showed oxygen permeability of $0.3 \text{ cm}^3\text{-mil} / (100 \text{ in}^2 \text{ 24 hr. atm})$ upon 2.5X biaxial orientation. The permeability of an unoriented, extrusion cast film was reported to be $0.2 \text{ cm}^3\text{-mil} / (100 \text{ in}^2 \text{ 24 hr. atm})$. They

attributed the permeability increase to microvoid development during orientation of the polymer chains after crystallinity was fully developed. However, cyclohexane sorption studies in PET [220] suggest a linear decrease in Langmuir capacity parameter (from 0.06 to 0.005 cm³(STP)/cm³) with increasing orientation factor (from 0.022 to 0.124). This trend was ascribed to a stronger decrease in amorphous free volume as a result of chain orientation than the increase in free volume due to microvoid formation.

The Langmuir sorption capacity parameter has been related to the amount of non-equilibrium excess volume in a glassy polymer as follows [221]:

$$C'_H = \frac{V_g - V_l}{V_g} \rho^* = \frac{V_{ex}}{V_g} \rho^* \quad (5.2)$$

where V_g is the specific volume of the polymer, V_l is the specific volume of the densified polymer matrix, and ρ^* is the condensed penetrant density, often estimated as the saturated liquid density of the penetrant at the temperature of the experiment. The densities of *n*-butane and *n*-pentane at 35°C were calculated using the Hankinson-Brost-Thomson correlation [222]. The values are 216.3 cm³(STP)/cm³ and 189.6 cm³(STP)/cm³ for *n*-butane and *n*-pentane, respectively. Thus, if the excess free volume characterized by C'_H is equally accessible to both *n*-butane and *n*-pentane, then C'_H should be higher for *n*-pentane than for *n*-butane, since the density of *n*-pentane is higher. In agreement with this prediction, C'_H is 2.53 cm³(STP)/cm³ for *n*-pentane and 2.16 cm³(STP)/cm³ for *n*-butane. Consistent with Equation 5.2, the C'_H / ρ^* values for *n*-butane and *n*-pentane are similar (0.010 and 0.013, respectively).

The logarithm of infinite dilution, amorphous phase penetrant solubility, S_a , in rubbery and glassy polymers increases linearly with critical temperature if dispersion forces are the dominant contribution to the interaction energy between polymer segments and penetrant molecules [97,223]. The mathematical form of this correlation is given by:

$$\ln S_a = N + MT_c \quad (5.3)$$

Figure 5.2 presents the infinite dilution solubility of *n*-butane, *n*-pentane, and other literature data for PET as a function of critical temperature [9]. The infinite dilution solubility values reported in this figure have been adjusted to an amorphous basis using the following relation [9]:

$$S_a = \frac{S}{\phi_a} \quad (5.4)$$

where S is the infinite dilution penetrant solubility, and ϕ_a is the amorphous phase volume fraction. Although it is widely used, this relation should be regarded as a first approximation, because it does not account for effects of crystallinity (and, in turn, the processing protocols used to vary crystallinity) on the non-crystalline phase morphology, which, as discussed above, can influence solubility levels. A more refined adjustment of solubility values to account for variations in morphology would require a better model of such effects and additional information about the PET samples from the literature, neither of which are presently available. Infinite dilution solubility values were obtained by extrapolating the reported solubility values to zero concentration. Solubilities of nonpolar penetrants increase linearly with T_c , as predicted by the model, while the solubilities of polar or quadrupolar penetrants exhibit somewhat greater scatter around the correlation

line. The *n*-butane and *n*-pentane solubility coefficients obtained in this study are in excellent agreement with this model.

5.3.2 *n*-Butane and *n*-Pentane Sorption Kinetics

Figures 5.3(a-d) present results from four representative *n*-butane and *n*-pentane kinetic sorption experiments in BPET at 35°C. Before beginning a kinetic sorption experiment, the polymer sample is equilibrated in an environment where the penetrant pressure surrounding the polymer sample is p_i . At $t = 0$, the penetrant pressure is increased to p_f , and the sorption experiment begins. M_t is the mass of penetrant sorbed by the polymer at time t , and M_∞ is the equilibrium mass uptake. Penetrant concentration in the polymer at equilibrium, C , can be calculated from the equilibrium mass uptake using the following relation:

$$C = \frac{M_\infty \times 22414 \times 100 \times \rho_{polymer}}{MW} \quad (5.5)$$

where M_∞ is equilibrium penetrant uptake (g/100g), $\rho_{polymer}$ is polymer density (g/cm³), and MW is penetrant molecular weight (g/mol).

In each case, the fractional mass uptake M_t / M_∞ increases linearly with $t^{1/2}$ for short times. This behavior is characteristic of sorption kinetics controlled by Fickian diffusion [27] (see, for example, Figures 5.3a, 5.3c and the dotted curves in Figures 5.3b, 5.3d). At longer times, however, the fractional mass uptake may exhibit a protracted, asymptotic approach towards equilibrium [224] (see, for example, the solid curves in Figures 5.3b, 5.3d). This behavior is ascribed to mass uptake kinetics limited by polymer

swelling and structural rearrangement to accommodate the penetrant (rather than Fickian diffusion). Such two-stage kinetics has been observed for organic vapor sorption in glassy polymers such as benzene in PET [225], acetone in PET [27], ethyl benzene in polystyrene [226], and benzene in polystyrene [227]. These sorption kinetics are often described using the following empirical model [27]:

$$\frac{M_t}{M_\infty} = 1 - (1 - \alpha_R) \left\{ \frac{8}{\pi^2} \sum_{n=0}^{\infty} \frac{1}{(2n+1)^2} \exp\left(\frac{-\bar{D}(2n+1)^2 \pi^2 t}{l^2}\right) \right\} + \alpha_R \times \exp\left(\frac{-(t-t_D)}{\tau_R}\right) \times H(t_D) \quad (5.6)$$

where \bar{D} is the average diffusion coefficient (as defined below), l is polymer film thickness, α_R is the fraction of weight uptake occurring during the protracted, non-Fickian approach to equilibrium, τ_R is the time constant associated with the long time drift in mass uptake, t_D is a delay factor accounting for a delay in the beginning of structural relaxation, and $H(t_D)$ is the Heaviside unit step function [253]. Typical values of t_D range from zero to l^2/\bar{D} , which corresponds to the end of Fickian diffusion. \bar{D} is approximately equal to the average diffusion coefficient over the concentration interval of the Fickian portion of the uptake curve [25].

Figures 5.3b and 5.3d present least-squares fits of Equation 5.6 to the experimental data for *n*-butane and *n*-pentane sorption in BPET at 35°C over the pressure interval from 11.5 to 59.6 cmHg and from 10.4 to 2.7 cmHg, respectively. The initial mass uptake, which is controlled by Fickian diffusion (dotted curves), can be modeled as follows [27]:

$$\frac{M_t / M_\infty}{(1 - \alpha_R)} = 1 - \frac{8}{\pi^2} \sum_{n=0}^{\infty} \frac{1}{(2n+1)^2} \exp\left(\frac{-\bar{D}(2n+1)^2 \pi^2 t}{l^2}\right) \quad (5.7)$$

The protracted non-Fickian approach to equilibrium (solid curves) can be modeled as [27]:

$$\frac{M_t}{M_\infty} = 1 - \alpha_R \exp\left(-\frac{(t - t_D)}{\tau_R}\right) \quad (5.8)$$

Equation 5.8 and the relaxation contribution to Equation 5.6 are valid only for $t > t_D$. The lines through the experimental data in Figures 5.3b and 5.3d are composite curves based on the best fits of Equation 5.7 and 5.8 to the short and long time data, respectively. The dotted curve indicates the fraction of mass uptake controlled by Fickian diffusion, whereas the solid curve indicates the fraction controlled by polymer chain relaxation. Initially, when the mass uptake is controlled by Fickian diffusion, the time for half of the total mass uptake by Fickian diffusion to occur is given by [9]:

$$t_{1/2} = \frac{l^2}{20\bar{D}} = \frac{\tau_F}{20} \quad (5.9)$$

where τ_F is the characteristic timescale for diffusion, defined as l^2/\bar{D} . The ratio τ_R/τ_F is called as the Deborah number. This dimensionless parameter characterizes the timescale for mass uptake due to structural relaxation relative to the timescale for Fickian diffusion.

The following procedure was adopted for calculating the average diffusion coefficients [9]: For data sets containing significant structural relaxation (*e.g.*, Figures 5.3b and 5.3d), the parameters to be determined are M_∞ , \bar{D} , α_R , τ_R and t_D . M_∞ was determined from the mass uptake at very long times. Once the value of α_R is set (from the

plateaus in Figures 5.3b and 5.3d), \bar{D} (and hence, τ_F) was calculated from the slope of the initial kinetic data, which is linear in $t^{1/2}$, using the following relation:

$$\frac{M_t / M_\infty}{(1 - \alpha_R)} = 4 \left[\frac{\bar{D}t}{\pi l^2} \right]^{1/2} \quad (5.10)$$

The parameters τ_R and t_D were determined by fitting the long time kinetic data to the following form of Equation 5.8:

$$\ln \left(1 - \frac{M_t}{M_\infty} \right) = \left(\ln \alpha_R + \frac{t_D}{\tau_R} \right) - \frac{t}{\tau_R} \quad (5.11)$$

In a previous study of *n*-butane diffusion in PET [9], a distinct plateau in the mass uptake kinetic profile was not clearly seen for all experiments. In this study, distinct plateaus were observed at intermediate times during the mass uptake profiles, and these plateaus served as a clear demarcation of the transition from Fickian diffusion to polymer structural relaxation. Hence, the value of fractional mass uptake at the plateau can be set equal to $(1 - \alpha_R)$.

For the uptake plots similar to Figures 5.3a and 5.3c, no polymer structural relaxation was observed. In these cases, \bar{D} was calculated using Equation 5.7 with $\alpha_R=0$.

Figure 5.4 presents the diffusion coefficients of *n*-butane and *n*-pentane in BPET as a function of average penetrant concentration. The average penetrant concentration was defined as follows:

$$\bar{C} = \frac{C_i + C_f}{2} \quad (5.12)$$

where C_i and C_f are the penetrant concentrations at the beginning of the sorption experiment (*i.e.*, the equilibrium penetrant concentration in the polymer at pressure p_i) and end of the Fickian portion of the uptake curve (*i.e.*, the equilibrium penetrant concentration in the polymer at pressure p_f). The majority of the uncertainty in the diffusion coefficients was due to the uncertainty in film thickness. For both penetrants, the logarithm of diffusion coefficient increases approximately linearly with penetrant concentration, consistent with other reports of the concentration dependence of organic vapor diffusion coefficients in glassy [9,27] and rubbery polymers [228]. The following empirical model was used [9]:

$$\bar{D} = D_\infty \exp(\omega \bar{C}) \quad (5.13)$$

where D_∞ , the infinite dilution diffusion coefficient, is $6.7 \pm 2.2 \times 10^{-13}$ cm²/s and $3.1 \pm 5.6 \times 10^{-14}$ cm²/s for *n*-butane and *n*-pentane in BPET, respectively. The slope, ω , is 0.47 ± 0.22 and 1.32 ± 0.97 cm³(polymer)•s/ (cm³(STP)•cm³) for *n*-butane and *n*-pentane, respectively. Thus, over the penetrant concentration range considered, the dependence of \bar{D} on \bar{C} is approximately three times as strong for *n*-pentane as for *n*-butane. The infinite-dilution diffusion coefficients can be adjusted to an amorphous basis using the following relation [20]:

$$D_a = \frac{D_\infty}{\phi_a} \quad (5.14)$$

This relation has been shown to be valid for light gases and water vapor in semicrystalline PET [20]. Roughly speaking, it seeks to account for the effect of tortuosity (due to the presence of impermeable crystallites in the polymer matrix) on

diffusion coefficients. It does not account for effects of chain immobilization on crystallinity. Such effects are not important for light gas transport in PET, but they cannot be ruled out for larger penetrants. Therefore, this relation is used here as a first approximation. The infinite-dilution, estimated amorphous phase diffusion coefficients of *n*-butane and *n*-pentane are 1.1×10^{-12} and 5.1×10^{-14} cm²/s, respectively.

The infinite dilution, estimated amorphous phase diffusion coefficient for *n*-pentane in BPET is more than an order of magnitude lower than that for *n*-butane, consistent with the larger size of *n*-pentane. Penetrant diffusion coefficients generally decrease with increasing penetrant size. Critical volume is a convenient measure of penetrant size, since it is reported for a wide variety of penetrants. The diffusion coefficients of *n*-butane and *n*-pentane scale with critical volume as shown in Figure 5.5. Since the diffusion coefficient values in this study were obtained at 35°C, they were corrected to 25°C using a procedure described in the literature [9]. The correlation is good for the diffusion coefficient values of *n*-butane and *n*-pentane. As penetrant size increases from helium to benzene, the diffusion coefficients decrease by more than 8 orders of magnitude.

The infinite dilution, amorphous phase diffusion coefficients in PET may be roughly correlated with critical volume using the following simple power law model [9]:

$$D_a = \frac{\tau}{V_c^\eta} \quad (5.15)$$

where τ and η are adjustable parameters. The exponent, η , in Equation 5.15 is a measure of the strength of dependence of diffusion coefficients on penetrant size. Polymers with

larger values of η will have stronger dependence of D on V_c than polymers with low η values. For PET, the value of η obtained from the correlation plot is 9.1 ± 0.9 [9]. Equation 5.15 may be used to predict diffusion coefficients of various other molecules of interest, such as flavor molecules in PET, whose critical volumes are either known or can be estimated.

5.4 Conclusions

Equilibrium sorption and uptake kinetics of *n*-butane and *n*-pentane in semicrystalline, biaxially oriented PET films at 35°C are reported. The sorption isotherms are well described by the dual-mode sorption model. Sorption kinetics are well described by a model incorporating Fickian diffusion with protracted polymer structural relaxation. Diffusion coefficients appear to increase with increasing penetrant concentration. The infinite dilution, estimated amorphous phase diffusion coefficient of *n*-pentane in BPET was observed to be more than an order of magnitude lower than that of *n*-butane at 35°C. The infinite dilution, estimated amorphous phase solubility of *n*-butane in BPET is a factor of two higher than that in APET, due to the presence of higher non-equilibrium excess volume in BPET (as characterized by C_H').

Table 5.1 Positron annihilation lifetime spectroscopy (PALS) parameters for biaxially oriented PET (BPET) and amorphous PET (APET) samples

Sample	$\tau_3 \pm 0.025$ (ns)	$I_3 \pm 0.3$ (%)	$\tau_3^3 I_3$	$\tau_3^3 I_3 / \phi_a$
0.9 μm BPET	1.691	17.9	86	141
APET [9]	1.645	22.1	98	104

Table 5.2 Dual-mode model parameters for *n*-butane and *n*-pentane sorption in BPET and *n*-butane sorption in APET at 35°C

Sample / Penetrant	k_D $\text{cm}^3(\text{STP})/(\text{cm}^3 \cdot \text{cmHg})$	C_H' $\text{cm}^3(\text{STP})/\text{cm}^3$	b cmHg^{-1}	$C_H' b / k_D$
APET / <i>n</i> -butane [9]	0.0162	1.16	0.0291	2.1
BPET / <i>n</i> -butane	0.0143 ± 0.0012	2.16 ± 0.11	0.029 ± 0.006	4.4
BPET / <i>n</i> -pentane	0.0109 ± 0.0043	2.53 ± 0.23	0.135 ± 0.020	31

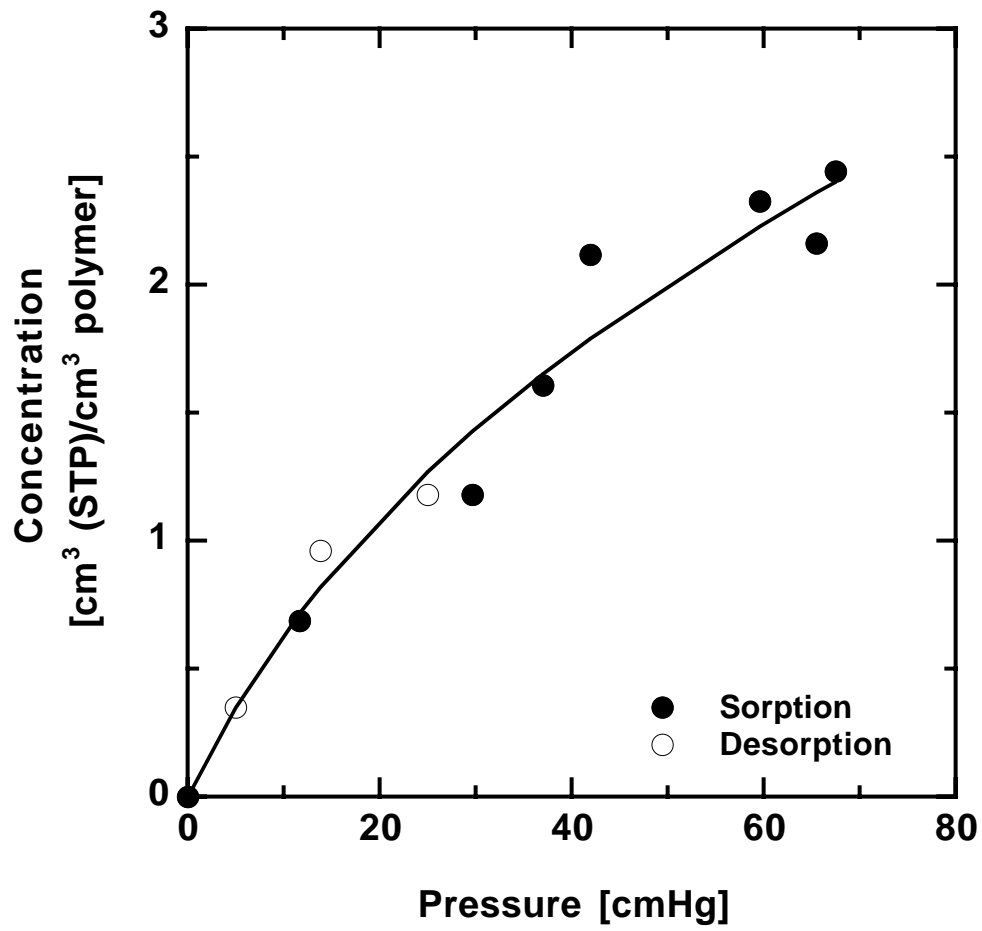


Figure 5.1a Sorption isotherm of *n*-butane in BPET at 35°C. The saturation vapor pressure of *n*-butane at 35°C is 245.8 cmHg [222].

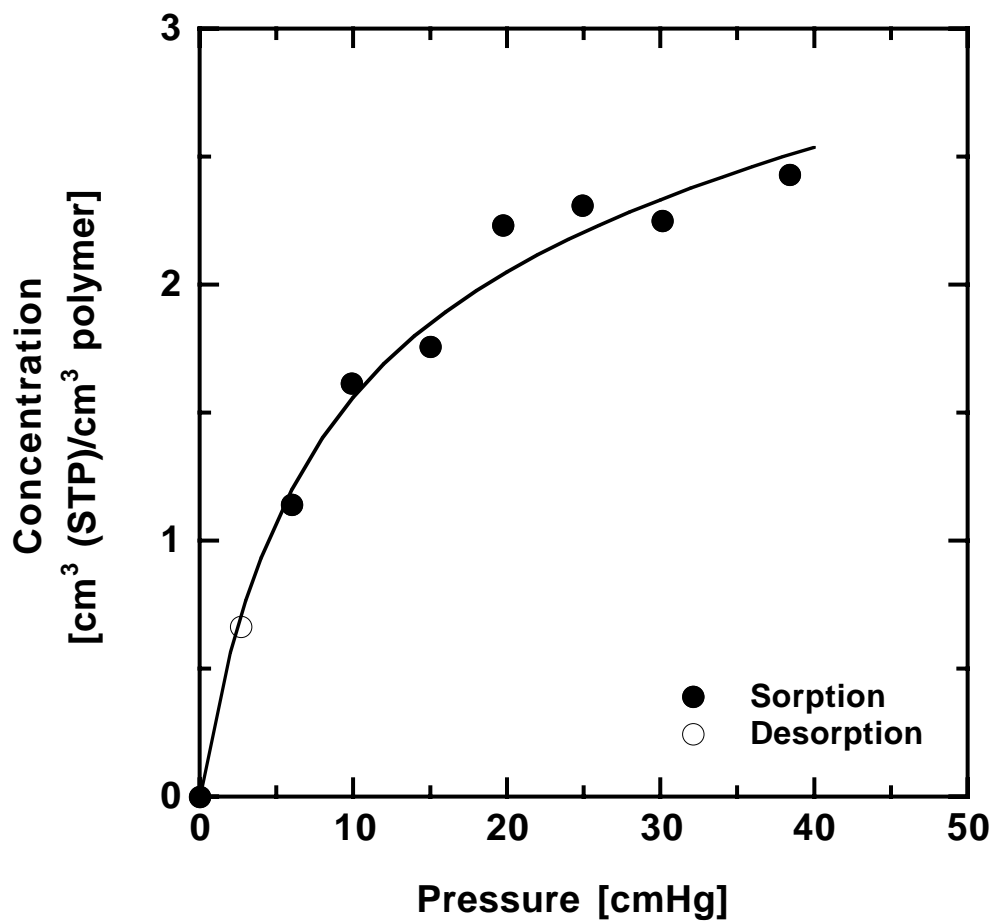


Figure 5.1b Sorption isotherm of *n*-pentane in PET at 35°C. The saturation vapor pressure of *n*-pentane at 35°C is 72.7 cmHg [222].

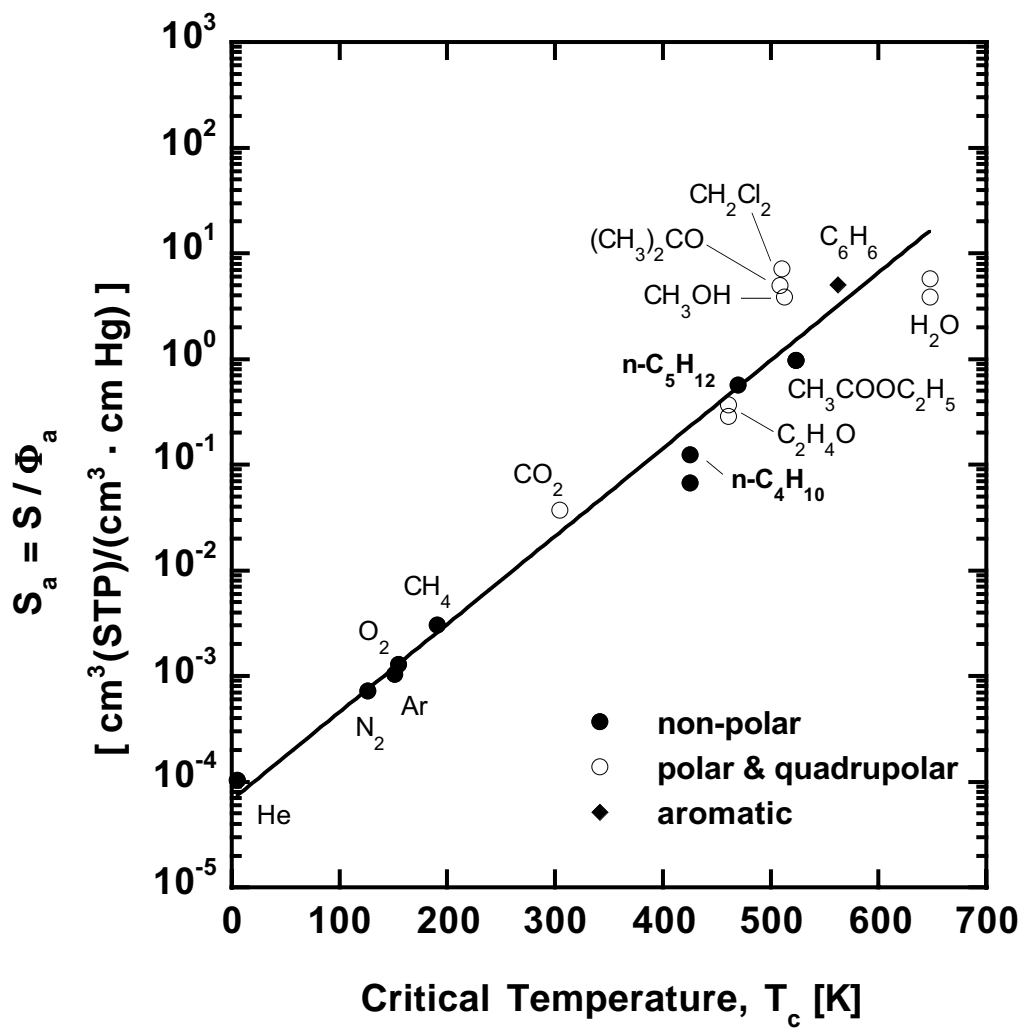


Figure 5.2 Correlation of infinite dilution, amorphous phase solubility coefficients in PET at 25-45°C with penetrant critical temperature [9]. The penetrants from this chapter are highlighted in bold. The slope, M of the least squares line is $0.019 \pm 0.001 \text{ K}^{-1}$ and the intercept, N is -9.6 ± 0.4 .

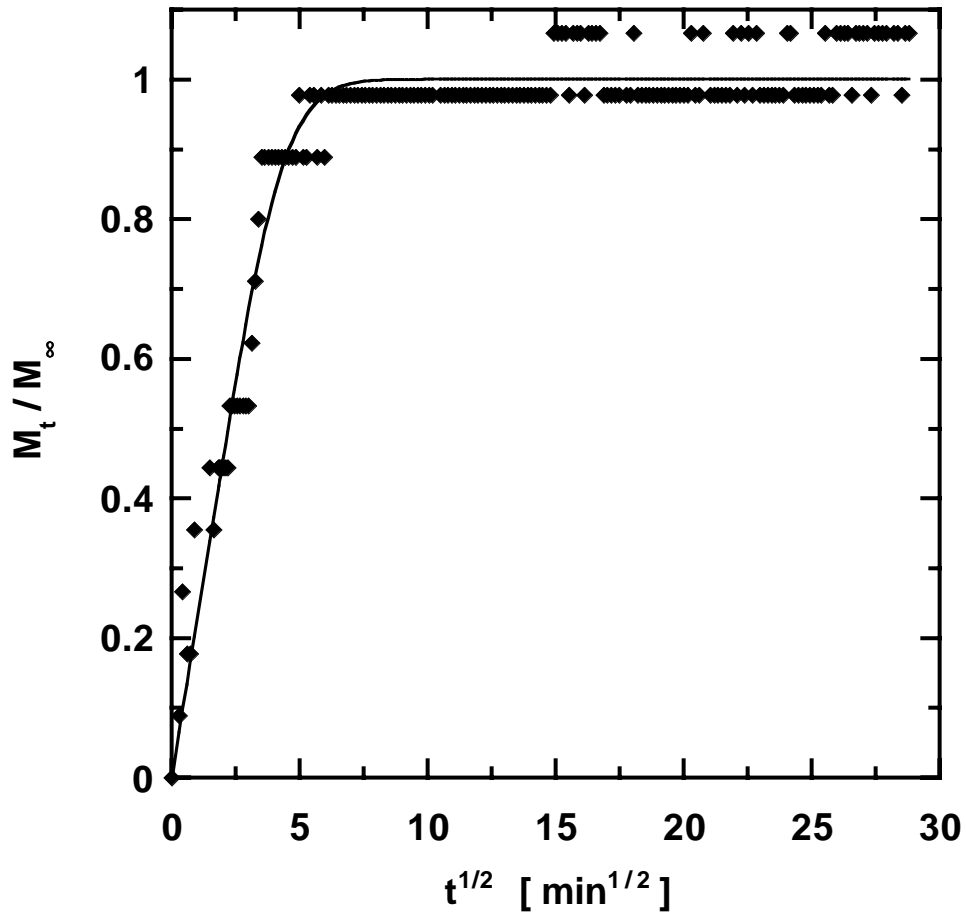


Figure 5.3a Fickian sorption of *n*-butane in BPET at 35°C. $P_{\text{sat}} = 245.8$ cmHg, $p_i = 36.8$ cmHg, $p_f = 67.5$ cmHg, $M_\infty = 0.15 \pm 0.006$ g/100g, $\bar{D} = 1.5 \pm 0.5 \times 10^{-12}$ cm²/s. The sample thickness was 0.95 ± 0.076 μm as determined by profilometry. This thickness value has been used for all calculations.

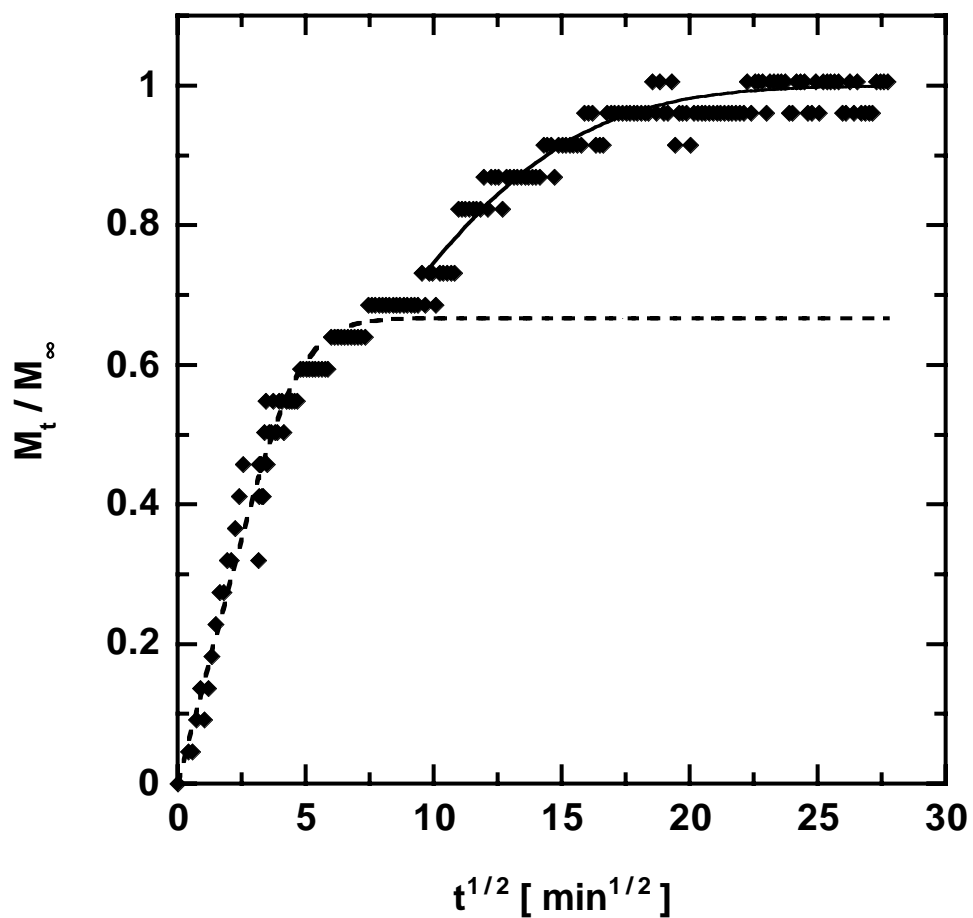


Figure 5.3b Non-Fickian sorption of *n*-butane in BPET at 35°C; $P_{\text{sat}} = 245.8$ cmHg, $p_i = 11.5$ cmHg, $p_f = 59.6$ cmHg, $M_\infty = 0.43 \pm 0.046$ g/100g, $\bar{D} = 1.3 \pm 0.4 \times 10^{-12}$ cm²/s, $\alpha_R = 0.32 \pm 0.04$, $\tau_R = 115 \pm 5$ min., $\tau_F = 115 \pm 41$ min., $t_D = 74 \pm 9$ min.

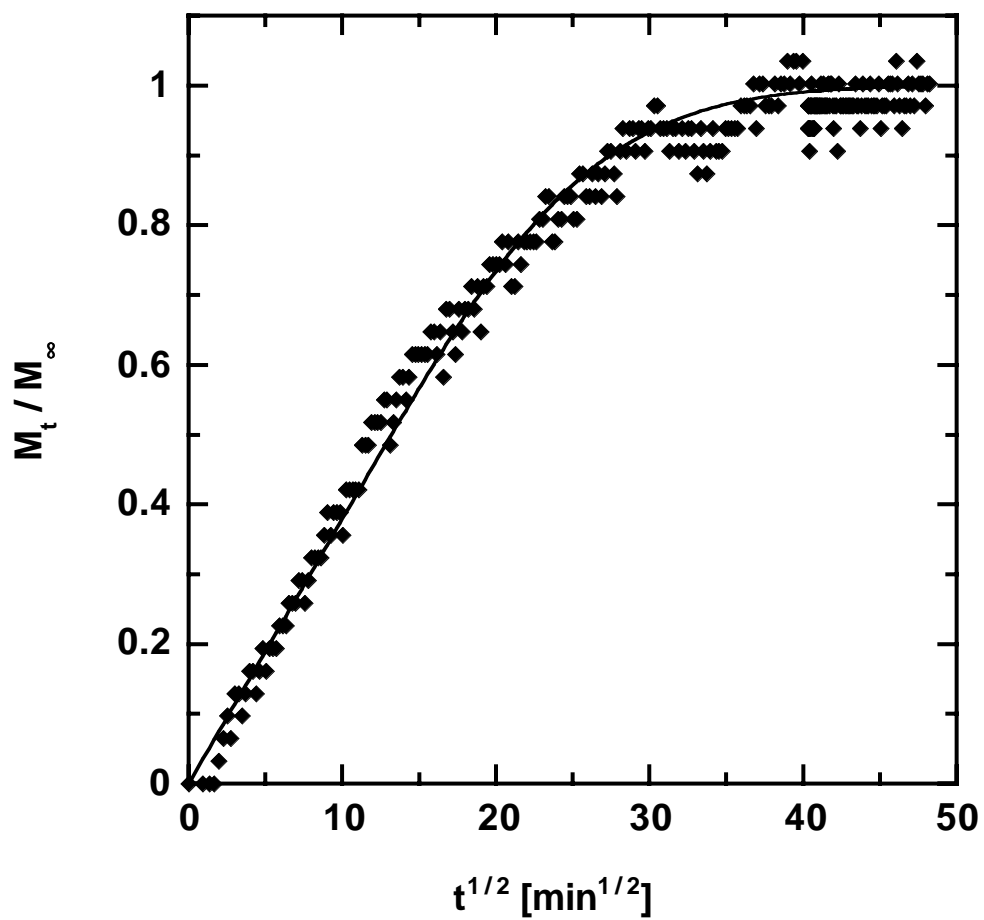


Figure 5.3c Fickian sorption of *n*-pentane in BPET at 35°C. $P_{\text{sat}} = 72.7$ cmHg, $p_i = 0$ cmHg, $p_f = 14.5$ cmHg, $M_\infty = 0.41 \pm 0.007$ g/100g, $\bar{D} = 4.8 \pm 0.8 \times 10^{-14}$ cm²/s.

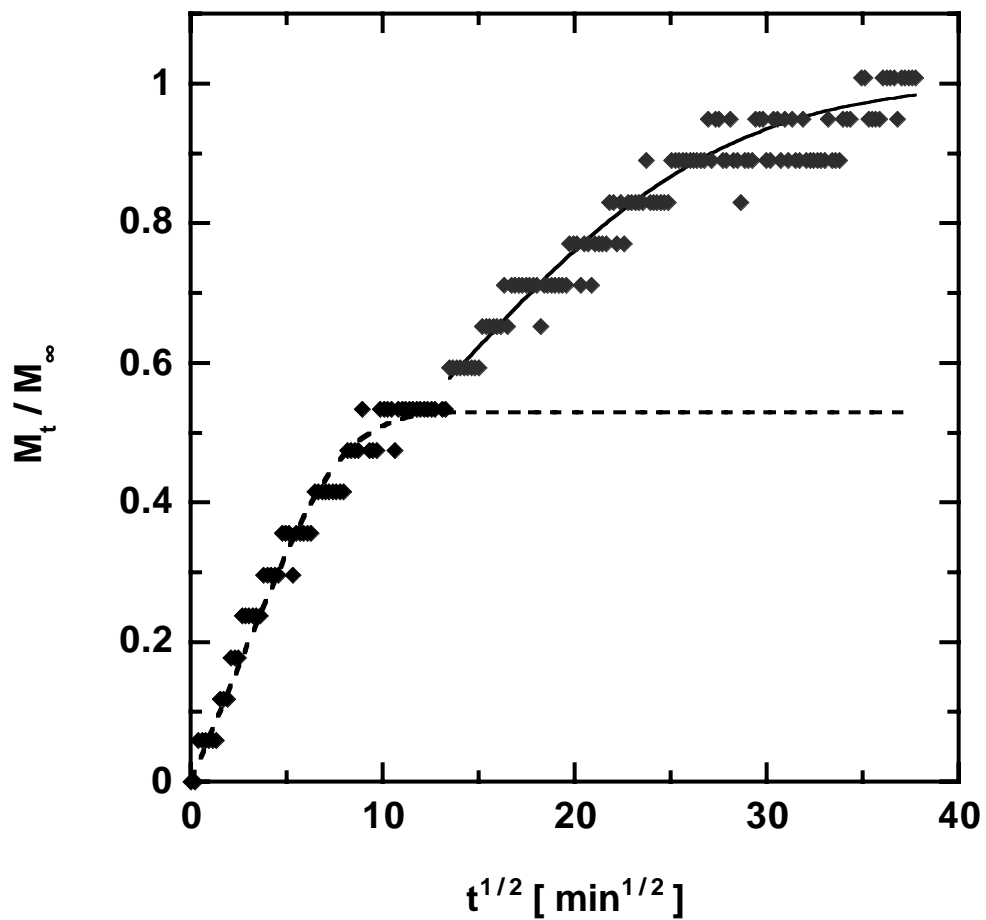


Figure 5.3d Non-Fickian desorption of *n*-pentane in BPET at 35°C. $P_{\text{sat}} = 72.7$ cmHg, $p_i = 10.4$ cmHg, $p_f = 2.7$ cmHg, $M_\infty = 0.22 \pm 0.006$ g/100g, $\bar{D} = 5 \pm 3 \times 10^{-13}$ cm²/s, $\alpha_R = 0.47 \pm 0.06$, $\tau_R = 389 \pm 13$ min., $\tau_F = 330 \pm 220$ min., $t_D = 145 \pm 16$ min.

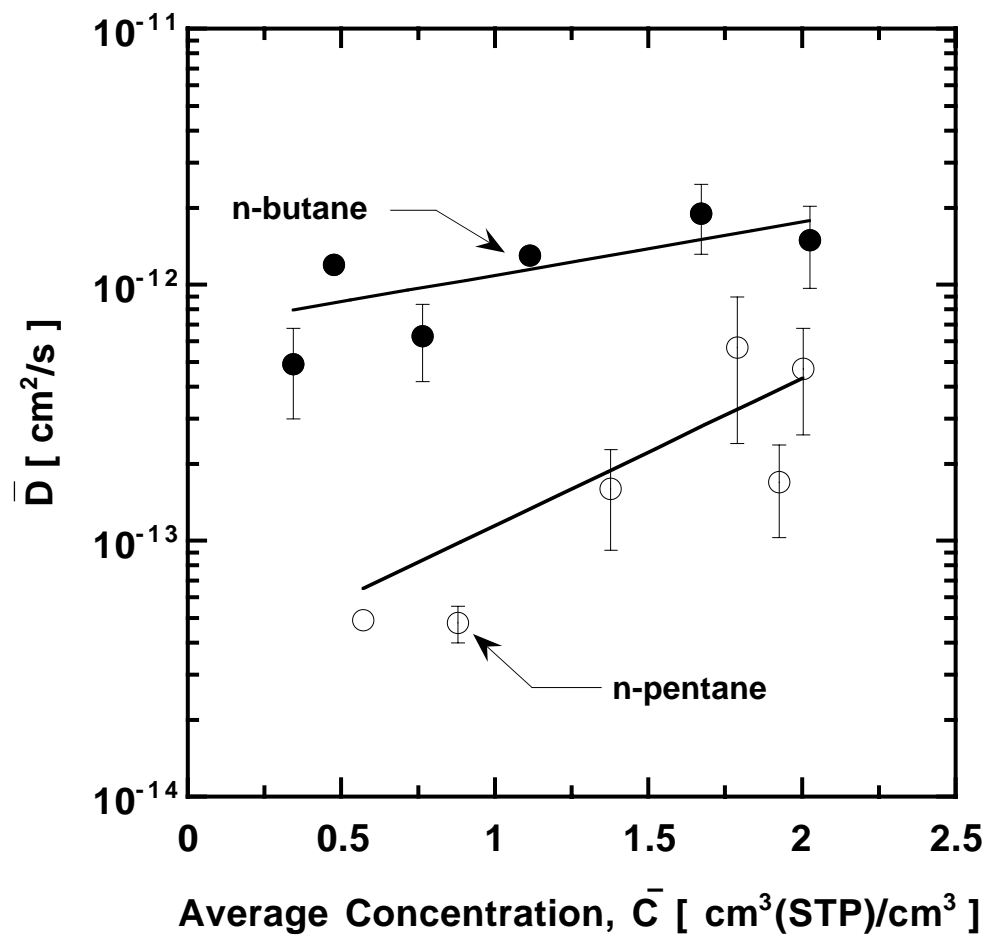


Figure 5.4 Effect of concentration on *n*-butane and *n*-pentane diffusion coefficients in BPET at 35°C.

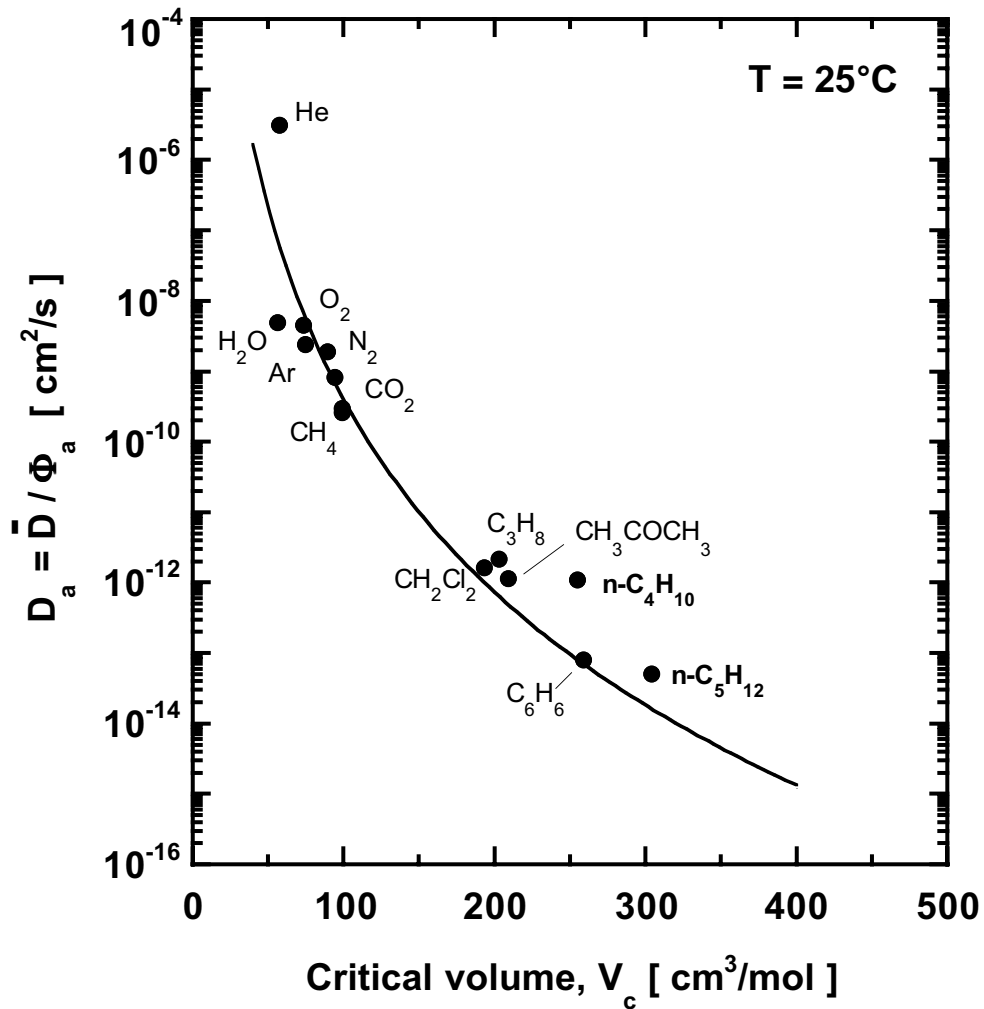


Figure 5.5 Effect of penetrant size on estimated infinite dilution, amorphous phase diffusion coefficients in PET at 25°C [9]. The penetrants from this chapter are highlighted in bold. The best-fit parameters of Equation 5.15 are: $\eta = 9.1 \pm 0.9$, $\tau = 5.7 \pm 1.2 \times 10^8$ (cm²/s (cm³/mol)^{9.1}).

CHAPTER 6

Sorption and Transport of Linear and Branched Ketones in Biaxially Oriented Poly(ethylene terephthalate)

This chapter has been adapted with permission from an article submitted under the same title to *Polymer*.

Unpublished work copyright© 2004 Elsevier.

6.1 Summary

This chapter presents results from a kinetic gravimetric sorption study of four linear and branched ketones, acetone, methyl ethyl ketone (MEK), methyl *n*-propyl ketone (MnPK), and methyl *i*-propyl ketone (MiPK) in uniform, biaxially oriented, semicrystalline poly(ethylene terephthalate) (BPET) films at 35°C and low penetrant activity. Chemical structures and relevant physical properties of these ketones are presented in Table 6.1. This series of penetrants permits a systematic study of the effects of ketone carbon-chain length and branching on solubility and diffusivity. Sorption isotherms for all penetrants are well described by the dual-mode sorption model. Sorption and desorption kinetics are described either by Fickian diffusion or a two-stage model incorporating Fickian diffusion at short times and protracted polymer structural relaxation at long times. Diffusion coefficients and equilibrium solubility at fixed relative pressure decrease in the following order:

acetone > MEK > MnPK > MiPK

Diffusion coefficients for each penetrant increases with increasing penetrant concentration.

6.2 Experimental

6.2.1 Materials

Biaxially oriented PET films having a uniform nominal thickness of 0.9 μm were purchased from the Goodfellow Co. (Berwyn, PA) and used as received. The film density, 1.395 g/cm^3 , was furnished by the supplier. The complete details of sample

characterization techniques and corresponding results and discussion were presented earlier in Chapter 3. High-performance liquid chromatographic (HPLC) grade acetone (99.9% purity), MEK (99.5% purity), MnPK (99.5% purity), and MiPK (99% purity) were purchased from Sigma-Aldrich Corp. (St. Louis, MO). The liquid penetrants were subjected to several freeze-thaw cycles to remove dissolved gases before use.

6.2.2 Gravimetric Sorption

Interval kinetic gravimetric sorption experiments were performed using a traditional McBain spring balance system, as described in Chapter 3 (*cf.* Section 3.2 in Chapter 3). The quartz springs were supplied by Ruska Industries (Houston, TX).

6.3 Results and Discussion

6.3.1 Equilibrium Uptakes of Ketones in PET

Interval kinetic gravimetric sorption experiments were used to determine sorption isotherms of acetone, MEK, MnPK, and MiPK in BPET at 35°C. The results are presented in Figure 6.1 and, at constant pressure, solubility in BPET at 35°C increases in the following order: acetone < MEK \approx MiPK < MnPK. All isotherms are concave to the pressure axis and are well described by the dual-mode sorption model [18]:

$$C = k_D P + C_H' \left(\frac{bp}{1 + bp} \right) \quad (6.1)$$

where k_D is the Henry's Law coefficient, C_H' is the Langmuir capacity parameter, a measure of the sorption capacity in the non-equilibrium excess volume of the glassy

polymer, and b is the Langmuir affinity parameter, a measure of the penetrant's affinity for the Langmuir sites. The curves in Figure 6.1 represent least-square fits of the experimental sorption data to Equation 6.1.

The dual-mode model parameters obtained in this study are recorded in Table 6.2 alongside the dual-mode model parameters obtained by McDowell *et al.* for acetone sorption in semicrystalline, unoriented PET (SPET) [27]. Acetone sorption isotherms in BPET and SPET at 35°C are presented in Figure 6.2. Acetone solubility in SPET is significantly higher than BPET at 35°C even though the crystallinity values of SPET (40 vol. %) and BPET (39 vol. %) are very similar. Assuming that no sorption occurs in the crystalline phase, the differences in acetone uptake should be due to differences in the morphology of the non-crystalline regions of the samples. The BPET sample was produced in a melt phase drawing process that strongly orients the polymer chains whereas SPET was prepared *via* solvent casting, which should introduce little or no orientation. These differences in processing histories likely lead to different morphologies of the non-crystalline phases and these differences are reflected in the density values of oriented BPET (1.395 g/cm³) and unoriented SPET (1.373 g/cm³). The detailed effects of morphology, orientation, and crystallinity on the sorption and transport properties of PET are complex. Such effects have been noted by many investigators, and they have been and continue to be the subject of active research [10,13,16,24,71-73,75,77,187,220,229-235]. Several studies report that the sample processing history affects morphology of *both* the crystalline and non-crystalline phases and that these morphological differences can manifest themselves in the sorption and transport

properties of the sample [10,13,16,24,75,187,220,229-234]. While an investigation of these effects is beyond the scope of this research project, the acetone sorption results in BPET and SPET also suggest that different crystallization techniques and different levels of orientation influence morphologies of the non-crystalline phase and, in turn, penetrant solubilities.

As reported in Chapter 5, the Langmuir capacity parameter can be related to the amount of non-equilibrium excess volume in a glassy polymer as [16]:

$$C_H' = \frac{V_g - V_l}{V_g} \rho^* = \frac{V_{ex}}{V_g} \rho^* \quad (6.2)$$

where V_g is the specific volume of the polymer, V_l is the specific volume of the densified polymer matrix, and ρ^* is the condensed penetrant density, often estimated as the saturated liquid density of the penetrant at the temperature of the experiment. The densities of acetone, MEK, MnPK, and MiPK were estimated at 35°C using the Hankinson-Brost-Thomson correlation [222]. The values are 299.2, 252.8, 217, and 205.2 cm³(STP)/cm³, respectively. If the non-equilibrium excess free volume characterized by C_H' is equally accessible to all penetrants, then the ratio C_H'/ρ^* should be equal. The C_H'/ρ^* values for acetone, MEK, MnPK, and MiPK are similar (0.010, 0.014, 0.009 and 0.009, respectively), and these values are also similar to those of *n*-butane and *n*-pentane (0.010 and 0.013, respectively) in BPET at 35°C (*cf.*, Chapter 5 and [8]).

Figure 6.3 presents the solubility of acetone, MEK, MnPK, MiPK, and other literature data for PET as a function of critical temperature. This solubility correlation plot was previously reported in Chapter 5. The solubility values reported in this figure have been adjusted to an amorphous basis using the following approximate relation [10]:

$$S_a = \frac{S}{\phi_a} \quad (6.3)$$

where S is penetrant solubility and ϕ_a is the amorphous phase volume fraction. This relation should be regarded as a first approximation, as discussed in Chapter 5. In general, for the organic vapor sorption data in Figure 6.3, infinite-dilution solubility values were obtained by extrapolating the reported solubility values to zero concentration [9]. However, because of the scatter in the data at low activity for MEK, MnPK, and MiPK, we did not attempt to compute infinite-dilution solubilities. For these penetrants, the solubility coefficients are reported at an arbitrarily chosen activity (P/P_{sat} , where P_{sat} is the saturation vapor pressure of the penetrant, and P is the penetrant pressure in the gas phase contiguous to the polymer sample) of 0.1 in Figure 6.3. As shown, the logarithm of solubilities increases rather systematically and linearly with T_c . While the general trend is observed, there is noticeable scatter in the data, some of which is likely due to the approximate nature of Equation 6.3. Also, the literature data for some penetrants (methanol, ethyl acetate, and water) were not available at infinite dilution [9], and penetrant solubility is expected to be a function of penetrant activity in PET. While it is difficult to draw definitive conclusions, the solubilities of ketones and many of the other polar penetrants appear to exhibit a positive deviation from the correlation line. This

effect would be even more pronounced if the solubilities of these penetrants were reported at lower activities since solubility increases with decreasing activity (*cf.* Figure 6.4). This trend may reflect favorable interactions between polar penetrants and the polar PET matrix, and this effect will be explored in more detail below.

In order to account for penetrant condensability and to study the effect of penetrant-polymer interactions on solubility, the sorption isotherms are re-plotted as a function of activity or relative pressure, P/P_{sat} . In a previous study with linear alkanes (*cf.*, Chapter 5 and [8]), which are not expected to exhibit any specific interactions with PET, this transformation produced a common isotherm for the two penetrants. As shown in Figure 6.4, in contrast to the behavior of alkanes, this procedure does not collapse the sorption isotherms for the ketones to a single curve. At relative pressure values greater than approximately 0.1 or so, penetrant concentration in BPET increases as follows: $\text{MiPK} < \text{MnPK} < \text{MEK} < \text{acetone}$. This trend, which is almost the opposite of the ranking of isotherms based on pressure (Figure 6.1), is consistent with the difference between the penetrant solubility parameters and the solubility parameter of PET (*cf.* Table 6.1). Typically one would expect the solubility to decrease as the square of the difference between the polymer and penetrant solubility parameters increases [236,237]. Based on this analysis, at constant relative pressure, penetrant solubility should decrease in the observed order. These results are also qualitatively consistent with several literature studies reporting that ketone solubility in polar liquids (*e.g.*, methanol and water) decreases as the ketone chain length increases [238-240].

Sorption isotherms for MEK and *n*-butane and MnPK and *n*-pentane were compared in order to study the effect of the polar carbonyl group on solubility of penetrants with the same number of carbon atoms (C₄ and C₅, respectively) and a similar carbon skeleton. These comparisons are presented in Figures 6.5a and 6.5b, which display uptake as a function of penetrant relative pressure. At constant relative pressure, the solubility coefficients of MEK and MnPK are significantly higher than those of *n*-butane and *n*-pentane, respectively. The solubility parameters of polar MEK and MnPK are more similar to that of PET, which is a polar polymer, than those of the nonpolar alkane analogs, which supports the notion that the polar ketones should be more soluble than their alkane analogs. Similar solubility trends have been observed with ketones and alkanes in polar liquids such as methanol and water [241,242].

6.3.2 Sorption Kinetics of Ketones in PET

Figures 6.6(a-c) present results from three representative kinetic sorption experiments in BPET at 35°C. In each case, the fractional mass uptake M_t / M_∞ increases linearly with $t^{1/2}$ for short times. This behavior is characteristic of sorption kinetics controlled by Fickian diffusion (see, for example, Figures 6.6b, 6.6c and the dotted curve in Figure 6.6a). At longer times, however, the fractional mass uptake may exhibit a protracted, asymptotic approach towards equilibrium [224] (see, for example, the solid curve in Figure 6.6a). This behavior is ascribed to mass uptake kinetics limited by polymer swelling and structural rearrangement to accommodate the penetrant rather than Fickian diffusion, as discussed in Chapter 5.

In this study, similar non-Fickian kinetic behavior was also observed in vapor desorption experiments (see, for example, Figures 6.7(a-c)). Non-Fickian desorption has been reported for a number of glassy polymer/condensable vapor systems [8,225,243-247]. Typical observations include a rapid initial desorption stage, where the mass removal rate is proportional to $t^{1/2}$, consistent with Fickian transport, followed by a protracted second stage. For example, Patton *et al.* reported such behavior for benzene desorption from a thin (2.5 μm) PET film at 50°C [225]. This effect was also reported by Crank and Park for chloroform [246] desorption from polystyrene at 25°C and for methylene chloride [248] desorption from polystyrene. Striking examples of such behavior were observed by Wang *et al.* for benzene and hexane vapor desorption from a very rigid, aromatic polyimide [243]. Drechsel *et al.* reported similar desorption kinetics for acetone removal from cellulose nitrate [247], and Downes and Mackay reported such kinetics for water vapor desorption from wool fibers [249].

The discussion of the cause of non-Fickian desorption behavior focuses on several explanations that are probably not mutually exclusive. Crank [250] proposed a model wherein the diffusion coefficient depended on time in an effort to capture history-dependent phenomena (such as penetrant induced rearrangement of the polymer chain segments or slow molecular relaxation of the polymer (*i.e.*, deswelling) as the penetrant is removed during desorption) that could influence diffusion coefficients. The effect of stresses generated as a result of the concentration profile present during desorption on the rate of mass uptake has also been invoked as a possible contributing factor to observed non-Fickian desorption [248,249,251]. In an extreme example of the impact of stresses

on desorption, Rosen reports actual tensile microfracture (*i.e.*, crazing) upon removal of water from phenol-formaldehyde resins [252]. Perhaps closely related to this line of reasoning is the work by Crank suggesting that the presence of a skin region, where penetrant has been removed and which has a very low diffusion coefficient relative to that in the more swollen, solvent-rich regions of a sample, can lead to the types of desorption kinetics that have been reported [250]. While a detailed molecular explanation of this phenomenon is lacking, it is clear that two stage, non-Fickian desorption is observed in many different polymer/penetrant systems.

In the present study, the non-Fickian sorption and desorption kinetics have been described using the following empirical model [8]:

$$\frac{M_t}{M_\infty} = 1 - (1 - \alpha_R) \left\{ \frac{8}{\pi^2} \sum_{n=0}^{\infty} \frac{1}{(2n+1)^2} \exp\left(\frac{-\bar{D}(2n+1)^2 \pi^2 t}{l^2}\right) \right\} + \alpha_R \times \exp\left(\frac{-(t-t_D)}{\tau_R}\right) \times H(t_D) \quad (6.4)$$

where \bar{D} is the average diffusion coefficient, l is polymer film thickness, α_R is the fraction of weight uptake (or weight desorbed) occurring during the protracted, non-Fickian approach to equilibrium, τ_R is the time constant associated with the long time drift in mass uptake (or mass desorbed), t_D is a delay factor accounting for a delay in the beginning of structural relaxation, and $H(t_D)$ is the Heaviside unit step function [253].

The curves in Figure 6.6a and Figures 6.7(a-c) present least-squares fits of Equation 6.4 to the experimental data for sorption of acetone and desorption of MEK, MiPK, and MnPK in BPET at 35°C, respectively, following the procedure described earlier in Chapter 5 [8]. In Figure 6.6a, the dotted curve indicates the fraction of mass uptake controlled by Fickian diffusion, whereas the solid curve indicates the fraction

controlled by polymer chain relaxation. The time to reach half of the total mass uptake by Fickian diffusion is given by:

$$t_{1/2} = \frac{l^2}{20\bar{D}} = \frac{\tau_F}{20} \quad (6.5)$$

where τ_F is the characteristic timescale for diffusion, defined as l^2/\bar{D} .

Average diffusion coefficients were estimated as described previously [8]. In previous studies of *n*-butane and *n*-pentane [8] as well as acetone diffusion in PET [27], a distinct plateau in the mass uptake kinetic profile was observed in all experiments. In this study, distinct plateaus were observed at intermediate times during the mass uptake profiles of acetone, and these plateaus served as a clear demarcation of the transition from Fickian diffusion to polymer structural relaxation. Hence, the value of fractional mass uptake at the plateau can be set equal to $(1-\alpha_R)$. However, for other penetrants in this study, such plateau regions were not clearly observed for all experiments (see, for example, Figures 6.7(a-c)). In such cases, α_R could not be determined from a qualitative examination of the data. The α_R values were determined by an iterative procedure using an algorithm described in the literature [21].

Figure 6.8 presents the diffusion coefficients of acetone, MEK, MnPK, and MiPK in BPET as a function of average penetrant concentration. The average penetrant concentration was defined as follows:

$$\bar{C} = \frac{C_i + C_f}{2} \quad (6.6)$$

where C_i and C_f are the penetrant concentrations at the beginning and end of the sorption experiment, respectively. For all penetrants, the logarithm of diffusion coefficient increases approximately linearly with penetrant concentration, consistent with earlier studies with *n*-alkanes in BPET (*cf.* Chapter 5). The following empirical model was used to characterize the concentration dependence [8]:

$$\bar{D} = D_\infty \exp(\omega \bar{C}) \quad (6.7)$$

where D_∞ is the infinite-dilution diffusion coefficient and the slope, ω , characterizes the dependence of \bar{D} on \bar{C} . D_∞ and ω values for acetone, MEK, MnPK and MiPK are shown in Table 6.3. On the basis of ω values in Table 6.3, over the penetrant concentration range considered, the dependence of \bar{D} on \bar{C} is similar for all the penetrants studied. The fraction of penetrant sorption due to polymer relaxation, α_R , and chain relaxation constant, τ_R , did not exhibit systematic trends with increasing penetrant concentration.

The infinite-dilution, estimated amorphous phase diffusion coefficient of acetone in BPET is approximately an order of magnitude lower than the corresponding value in SPET, which was 2.3×10^{-11} cm²/s at 35°C [27]. The effects of processing history on morphology and of morphology on diffusion coefficients are complex. In fact, the situation is likely to be more complex for diffusion than for sorption because the kinetics of the diffusion process are expected to be affected by the spatial arrangement of the various domains, while solubility, which is an equilibrium (or in the case of a glassy

polymer a quasi-equilibrium) property is not. For example, it is well known [4] that the orientation and aspect ratios of the impermeable phases affect penetrant flux. Thus, penetrant diffusion coefficients are expected to be affected by not only the amount of crystallinity, but also the morphology of the non-crystalline regions and the larger scale geometry and spatial distribution of these regions. Again, a study of these effects is outside the scope of this work, but the differences between the diffusion coefficients of acetone in BPET and SPET are in qualitative agreement with other studies reporting the effect of orientation on diffusion coefficients of organic vapors and liquids in amorphous and semicrystalline PET [13,20,23,75,230,232,234]. These results suggest that the orientation of PET can lead to more efficient chain packing, thereby reducing the overall free volume and diffusion coefficients.

As demonstrated in Chapter 5, penetrant diffusion coefficients generally decrease with increasing penetrant size. The infinite-dilution, estimated amorphous phase diffusion coefficients of ketones in BPET decrease with increasing penetrant size from acetone to MiPK, as shown in Figure 6.9. The infinite-dilution, estimated amorphous phase diffusion coefficients in PET may be roughly correlated with critical volume using the following empirical power law model [8]:

$$D_a = \frac{\tau}{V_c^\eta} \quad (6.8)$$

where τ and η are adjustable parameters.

Since the diffusion coefficients of the four ketones from the present study were obtained at 35°C, they were adjusted to 25°C using the procedure described in the

literature [9]. The correlation of D with V_c is good for relatively linear penetrants, such as acetone, MEK, and MnPK. However, the diffusion coefficient of MiPK is approximately an order of magnitude lower than the value anticipated by this simple empirical model. This result is not particularly surprising because critical volume cannot accurately capture the effect of penetrant shape on diffusion coefficients and MiPK, being a branched molecule, is expected to present a larger cross-section for diffusion than linear molecules in the same series of penetrants [9].

6.4 Conclusions

Equilibrium sorption and uptake kinetics of acetone, MEK, MnPK, and MiPK in biaxially oriented, semicrystalline PET films at 35°C have been reported. Sorption isotherms for all penetrants are well described by the dual-mode sorption model. At constant relative pressure, penetrant solubility increases in the order: MiPK < MnPK < MEK < acetone. Solubility of polar ketones in BPET is approximately two times higher than that of non-polar alkanes having the same number of carbon atoms and a similar carbon skeleton. These results are consistent with the differences between the solubility parameters of the penetrants and PET. Similar solubility trends have also been observed for ketones and alkanes in polar liquids. Sorption and desorption kinetics in PET are described by a two-stage model incorporating Fickian diffusion at short times and protracted polymer structural relaxation at long times. Diffusion coefficients also increase in the order: MiPK < MnPK < MEK < acetone, and the diffusion coefficients for each penetrant increase with increasing penetrant concentration.

Table 6.1 Chemical structures, critical properties [212], solubility parameters [213], and saturation vapor pressures at 35°C [212] of acetone, MEK, MiPK, and MnPK

Penetrant	Chemical Structure	Critical Temperature (K)	Critical Volume (cm ³ /mol)	Solubility Parameter (MPa) ^{1/2}	Saturation Vapor Pressure (cmHg)
Acetone	$\begin{array}{c} \text{O} \\ \parallel \\ \text{CH}_3-\text{C}-\text{CH}_3 \end{array}$	508.1	209	20.2	34.7
MEK	$\begin{array}{c} \text{O} \\ \parallel \\ \text{CH}_3-\text{C}-\text{CH}_2\text{CH}_3 \end{array}$	536.8	267	19.0	14.2
MiPK	$\begin{array}{c} \text{O} \quad \text{CH}_3 \\ \parallel \quad \\ \text{CH}_3-\text{C}-\text{CH}-\text{CH}_3 \end{array}$	553.4	310	17.4	8.6
MnPK	$\begin{array}{c} \text{O} \\ \parallel \\ \text{CH}_3-\text{C}-\text{CH}_2\text{CH}_2\text{CH}_3 \end{array}$	561.1	301	17.8	5.8

Note: The solubility parameter of PET is 21.5 MPa^{1/2} [254].

Table 6.2 Dual-mode model parameters for acetone, MEK, MiPK, and MnPK sorption in BPET and acetone sorption in solvent-cast PET (SPET) [27] at 35°C

Sample / Penetrant	k_D $\text{cm}^3(\text{STP})/(\text{cm}^3 \cdot \text{cmHg})$	C_H' $\text{cm}^3(\text{STP})/\text{cm}^3$	b cmHg^{-1}	$C_H' b / k_D$
SPET / acetone	0.8	7.2	0.66	5.9
BPET / acetone	0.43 ± 0.01	3.1 ± 0.06	0.6 ± 0.03	4.5
BPET / MEK	0.53 ± 0.02	3.4 ± 0.04	2.2 ± 0.1	14
BPET / MiPK	0.85 ± 0.02	1.8 ± 0.02	16 ± 2	33
BPET / MnPK	1.4 ± 0.07	2.0 ± 0.02	20 ± 1	29

Table 6.3 D_∞ and ω values for acetone, MEK, MnPK, and MiPK at 35°C

Penetrant	D_∞ (cm ² /s)	D_∞ / ϕ_a (cm ² /s)	ω cm ³ (polymer)/cm ³ (STP)
Acetone	$6.7 \pm 1.4 \times 10^{-13}$	1.1×10^{-12}	0.45 ± 0.06
MEK	$1.1 \pm 0.3 \times 10^{-13}$	1.8×10^{-13}	0.47 ± 0.07
MnPK	$3.9 \pm 1.7 \times 10^{-14}$	6.3×10^{-14}	0.46 ± 0.15
MiPK	$4.1 \pm 0.9 \times 10^{-15}$	6.7×10^{-15}	0.48 ± 0.03

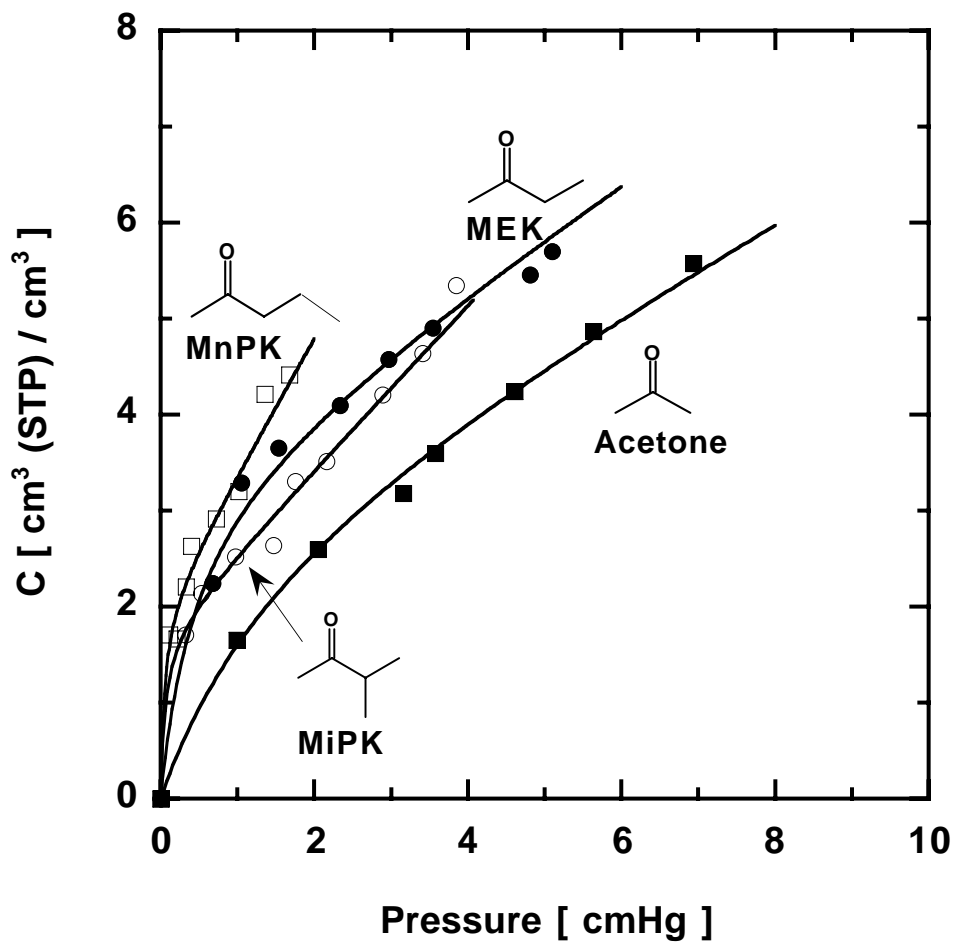


Figure 6.1 Sorption isotherms of acetone (■), MEK (●), MnPK (□), and MiPK (○) in biaxially oriented PET (BPET) at 35°C as a function of pressure.

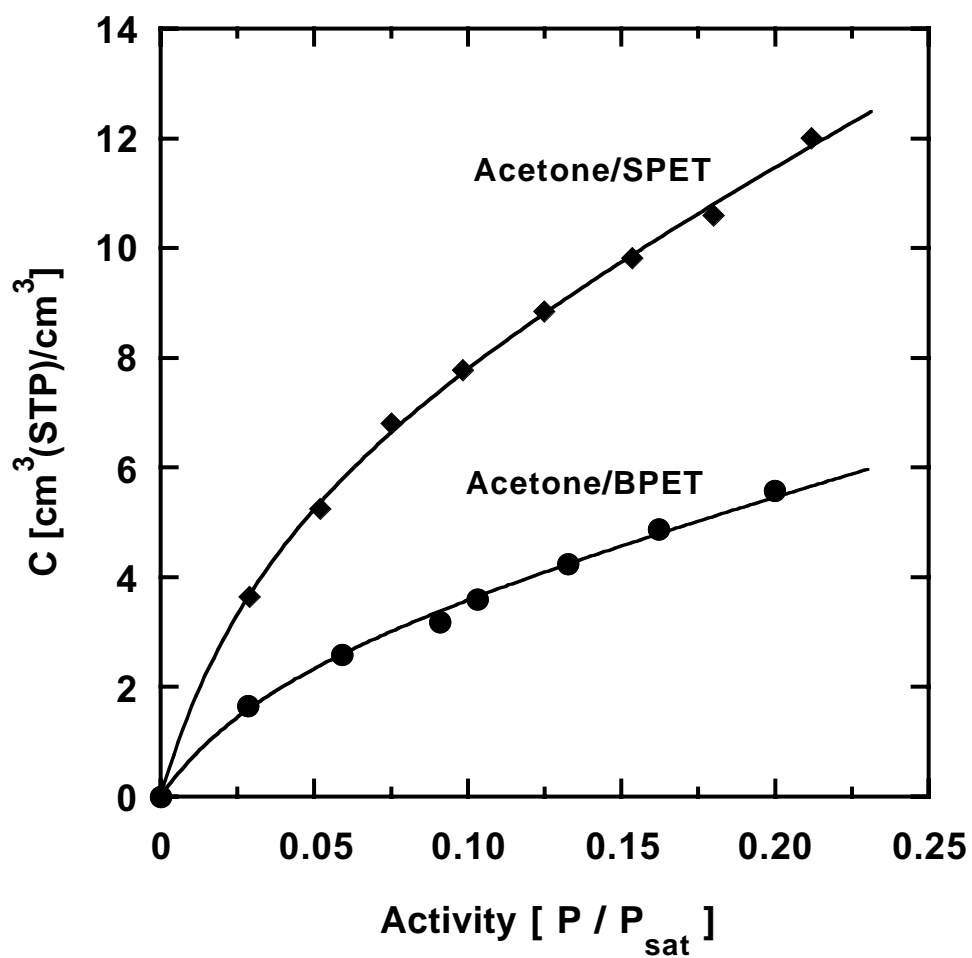


Figure 6.2 Sorption isotherms of acetone in biaxially oriented PET (BPET) and solvent-cast PET (SPET) at 35°C as a function of relative pressure.

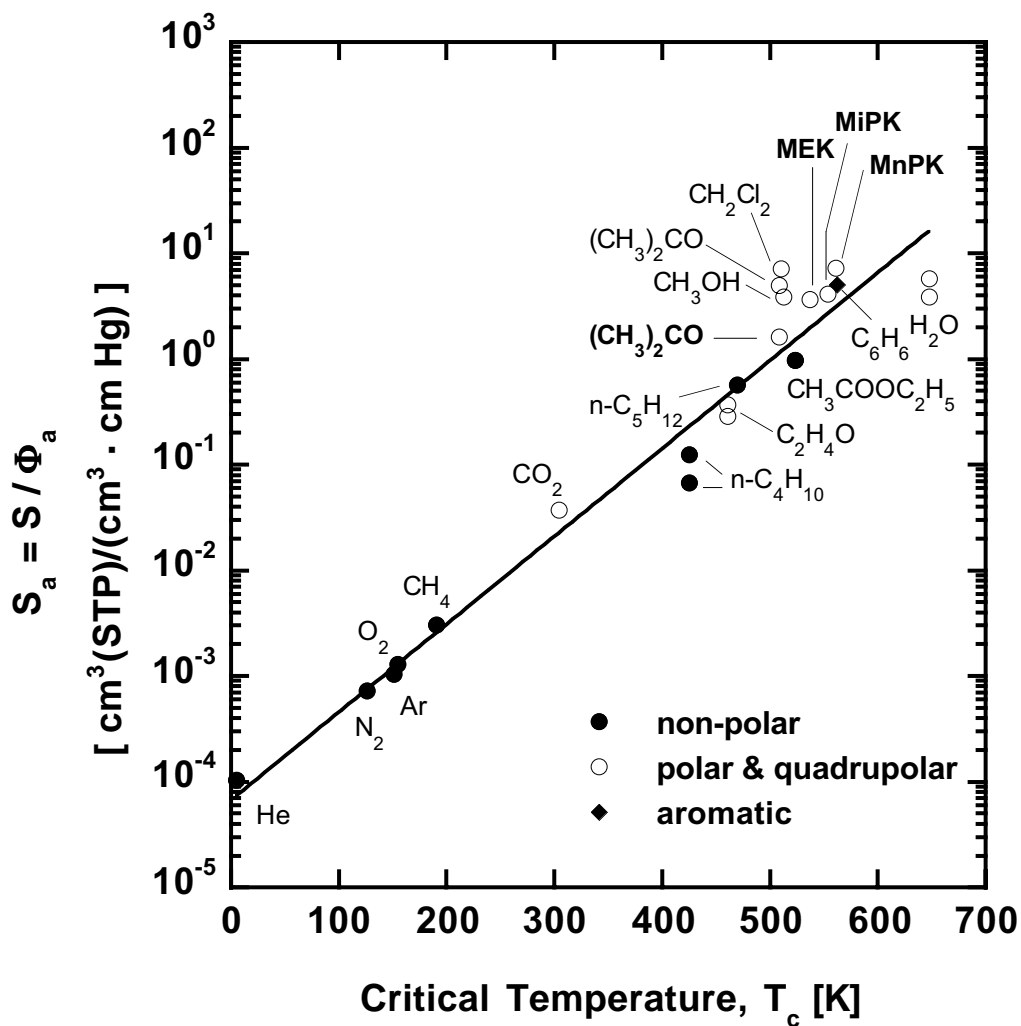


Figure 6.3 Correlation of infinite dilution, estimated amorphous phase solubility coefficients in PET at 25-45°C with penetrant critical temperature [9]. The penetrants from this chapter are highlighted in bold. For most penetrants, the data have been extrapolated to infinite dilution. For MEK, MiPK, and MnPK, the data are reported at a relative pressure of 0.1. The slope, M , of the least squares line is $0.019 \pm 0.001 \text{ K}^{-1}$, and the intercept, N , is -9.6 ± 0.4 .

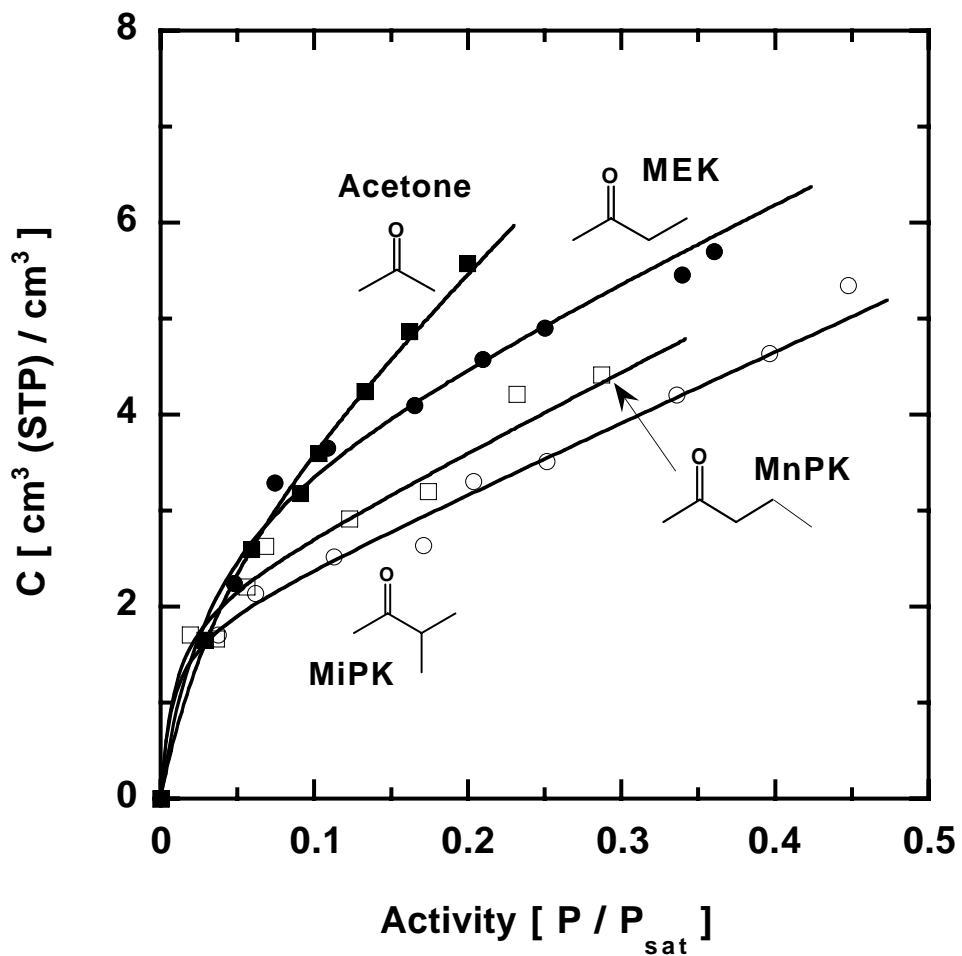


Figure 6.4 Sorption isotherms of acetone (■), MEK (●), MnPK (□), and MiPK (○) in BPET at 35°C as a function of relative pressure.

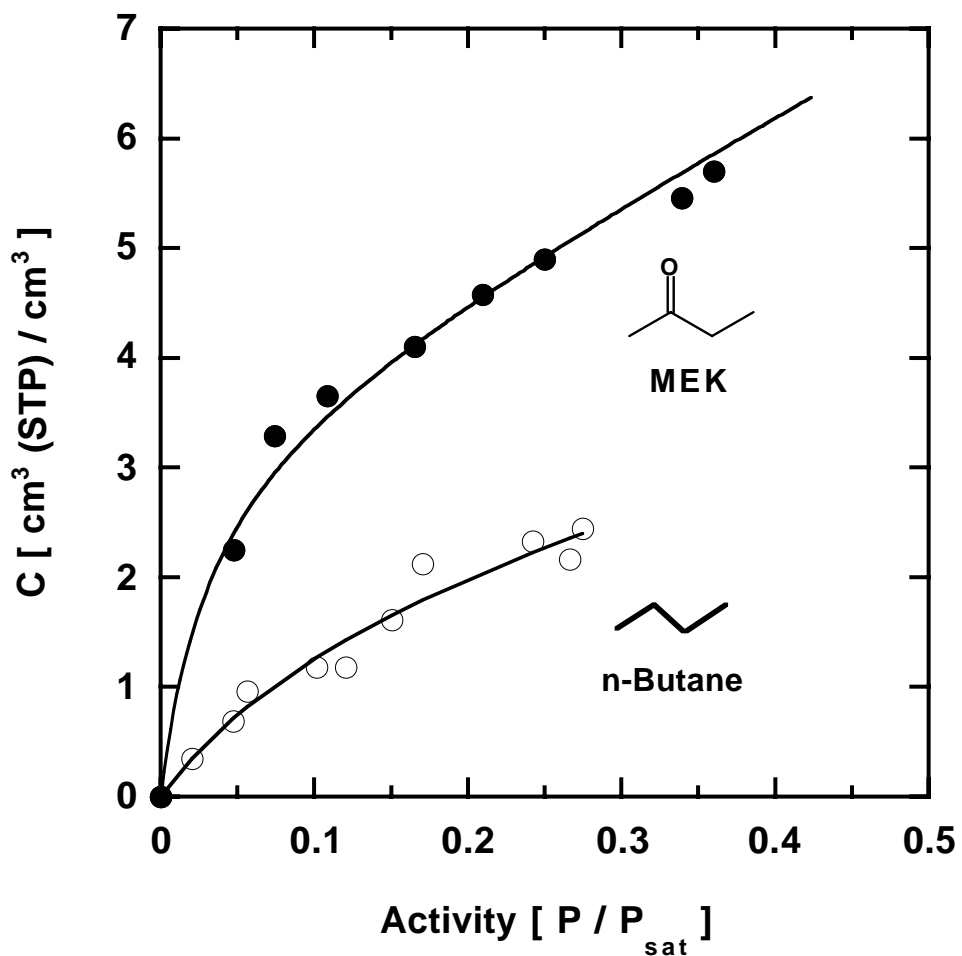


Figure 6.5a Sorption isotherms of MEK and *n*-butane in BPET at 35°C as a function of relative pressure. The saturation vapor pressures, P_{sat} , of MEK and *n*-butane at 35°C are 14.2 cmHg and 245.8 cmHg, respectively [212]. The solubility parameter and molar volume of *n*-butane are 14.1 MPa^{1/2} and 101.4 cm³/mol, respectively [212].

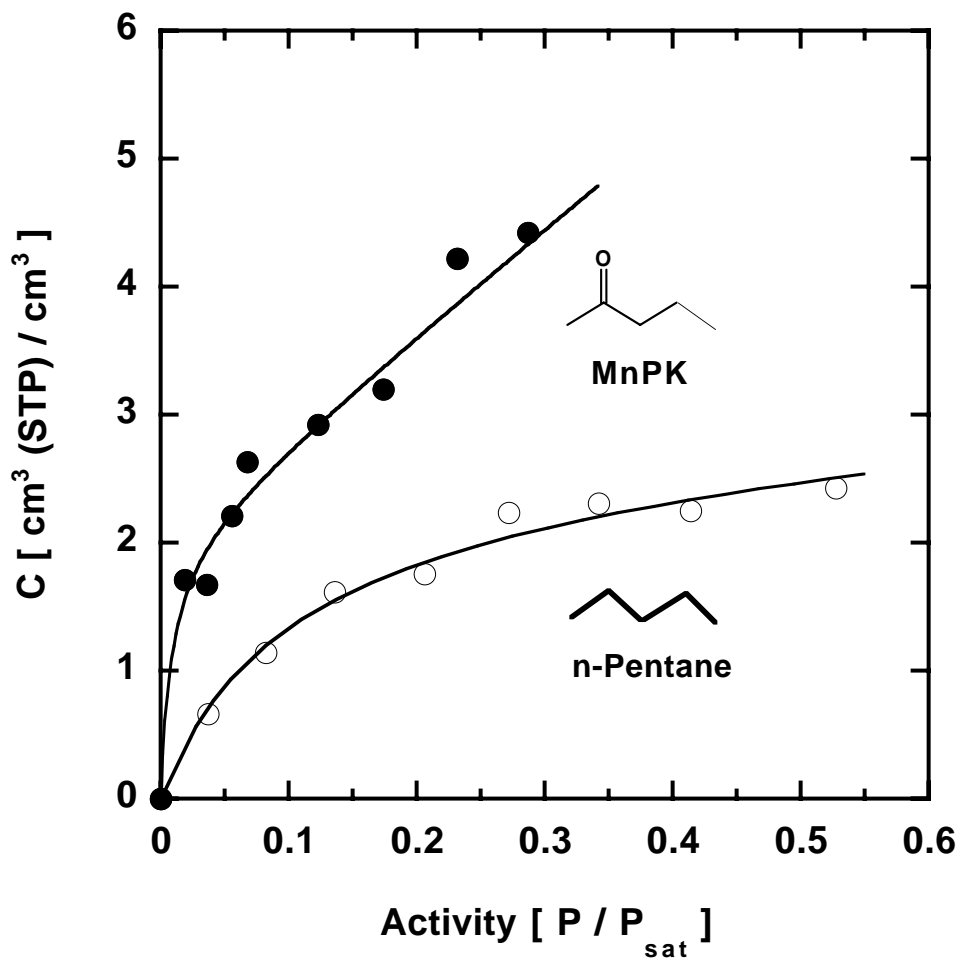


Figure 6.5b Sorption isotherms of MnPK and *n*-pentane in BPET at 35°C as a function of relative pressure. The saturation vapor pressures, P_{sat} , of MnPK and *n*-pentane at 35°C are 5.8 cmHg and 72.7 cmHg, respectively [212]. The solubility parameter and molar volume of *n*-pentane are $14.5 \text{ MPa}^{1/2}$ and $116.2 \text{ cm}^3/\text{mol}$, respectively [212].

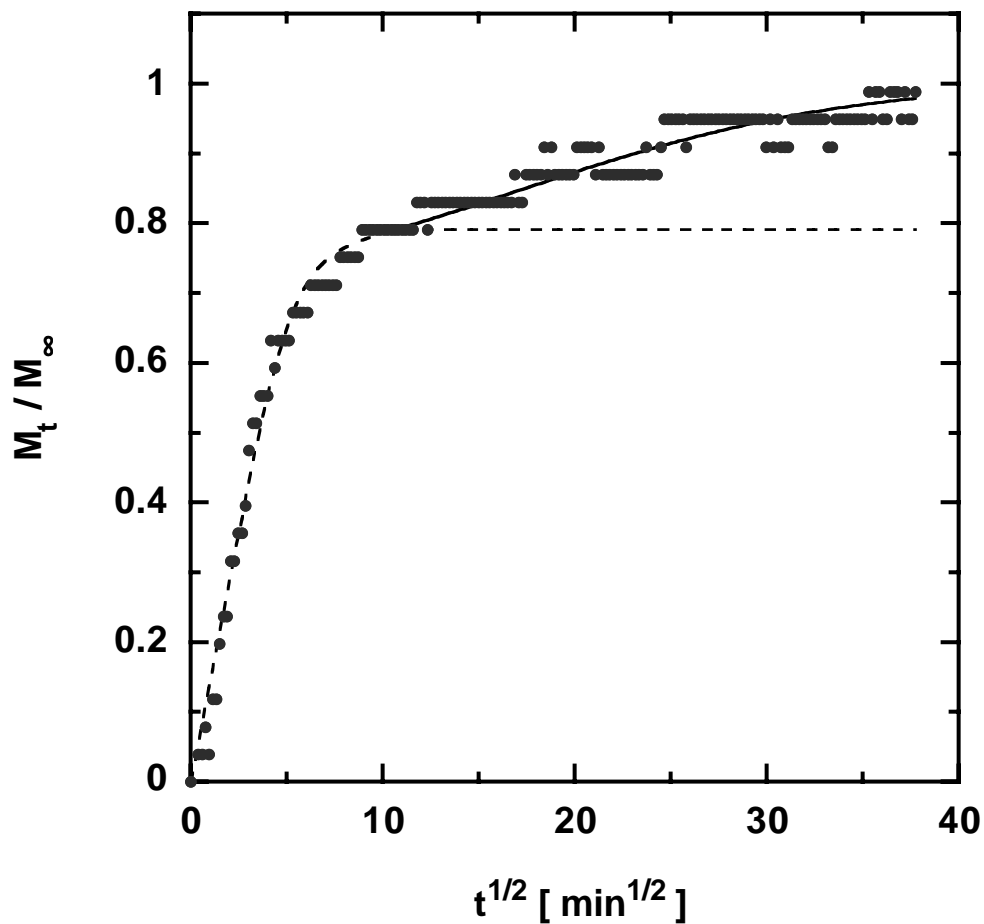


Figure 6.6a Non-Fickian sorption kinetics of acetone in BPET at 35°C.
 $p_i = 0$ cmHg, $p_f = 0.9$ cmHg, $M_\infty = 0.31 \pm 0.02$ g/100g,
 $\bar{D} = 1.1 \pm 0.2 \times 10^{-12}$ cm²/s, $\alpha_R = 0.21 \pm 0.04$, $\tau_R = 340 \pm 20$ min.,
 $\tau_F = 140 \pm 30$ min., $t_D = 0$ min. The dotted line represents a Fickian model
fit to the initial portion of the data.

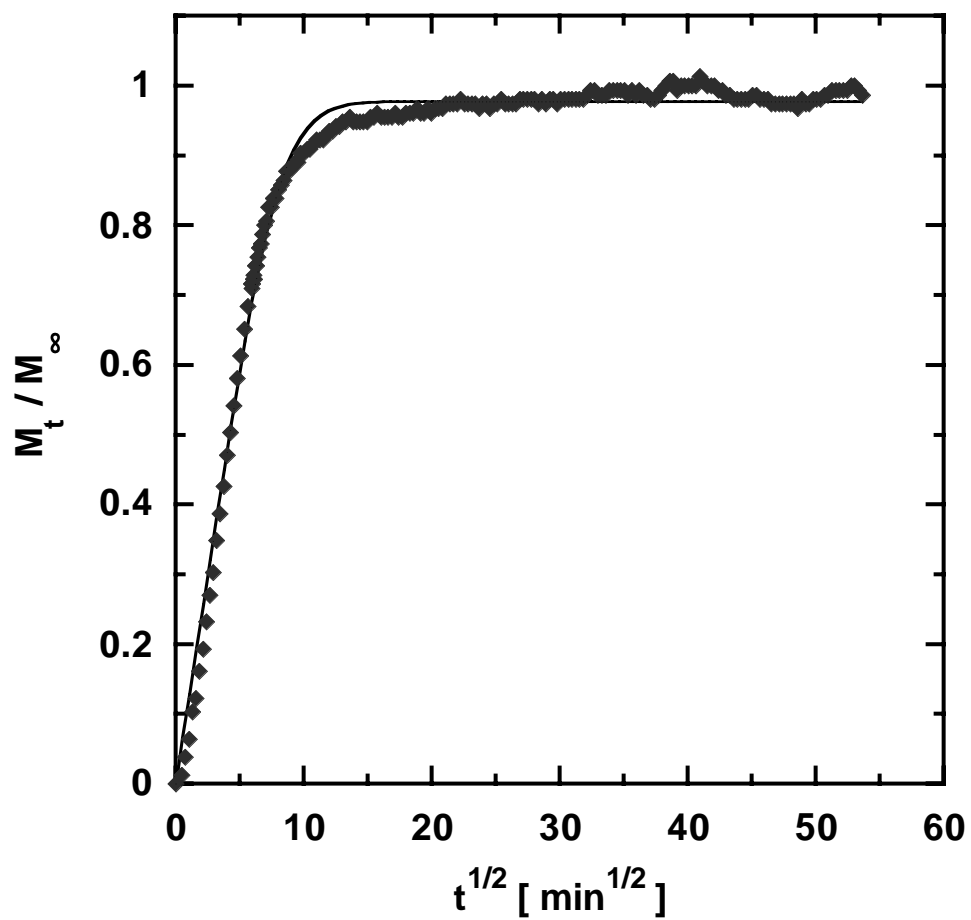


Figure 6.6b Fickian sorption kinetics of MEK in BPET at 35°C.
 $p_i = 0$ cmHg, $p_f = 2.3$ cmHg, $M_\infty = 0.94 \pm 0.003$ g/100g,
 $\bar{D} = 4.4 \pm 1.8 \times 10^{-13}$ cm²/s.

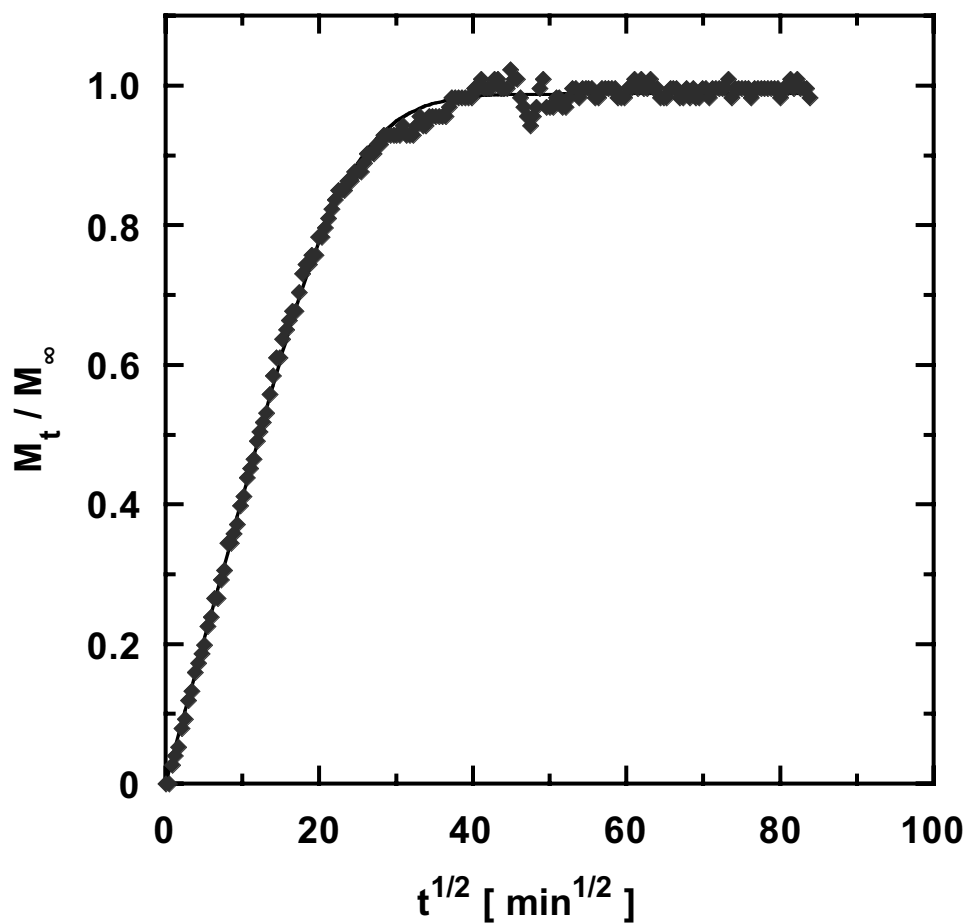


Figure 6.6c Fickian sorption kinetics of MnPK in BPET at 35°C.
 $p_i = 0$ cmHg, $p_f = 0.3$ cmHg, $M_\infty = 0.61 \pm 0.001$ g/100g,
 $\bar{D} = 5.1 \pm 0.7 \times 10^{-14}$ cm²/s.

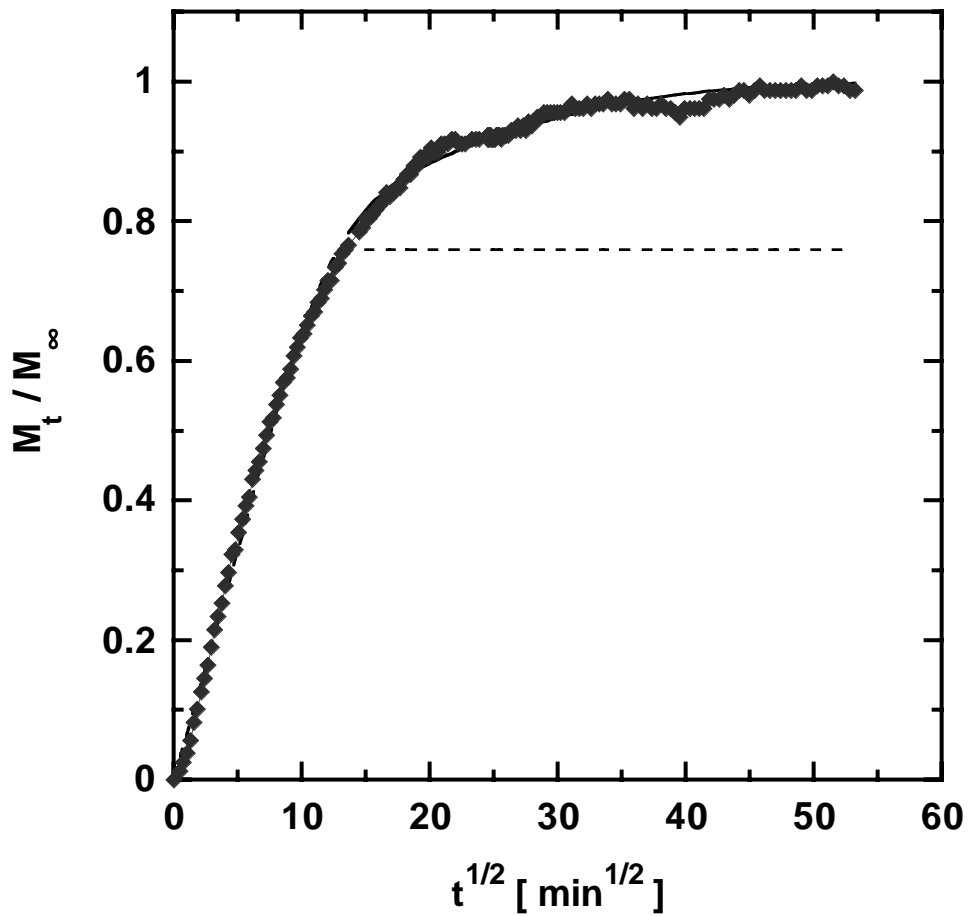


Figure 6.7a Non-Fickian desorption kinetics of MEK from BPET at 35°C.
 $p_i = 1.6$ cmHg, $p_f = 0$ cmHg, $M_\infty = 0.98 \pm 0.03$ g/100g,
 $\bar{D} = 2.3 \pm 0.4 \times 10^{-13}$ cm²/s, $\alpha_R = 0.24 \pm 0.01$, $\tau_R = 1075 \pm 70$ min.,
 $\tau_F = 650 \pm 150$ min., $t_D = 0$ min. The dotted curve represents the Fickian
portion of the desorption data.

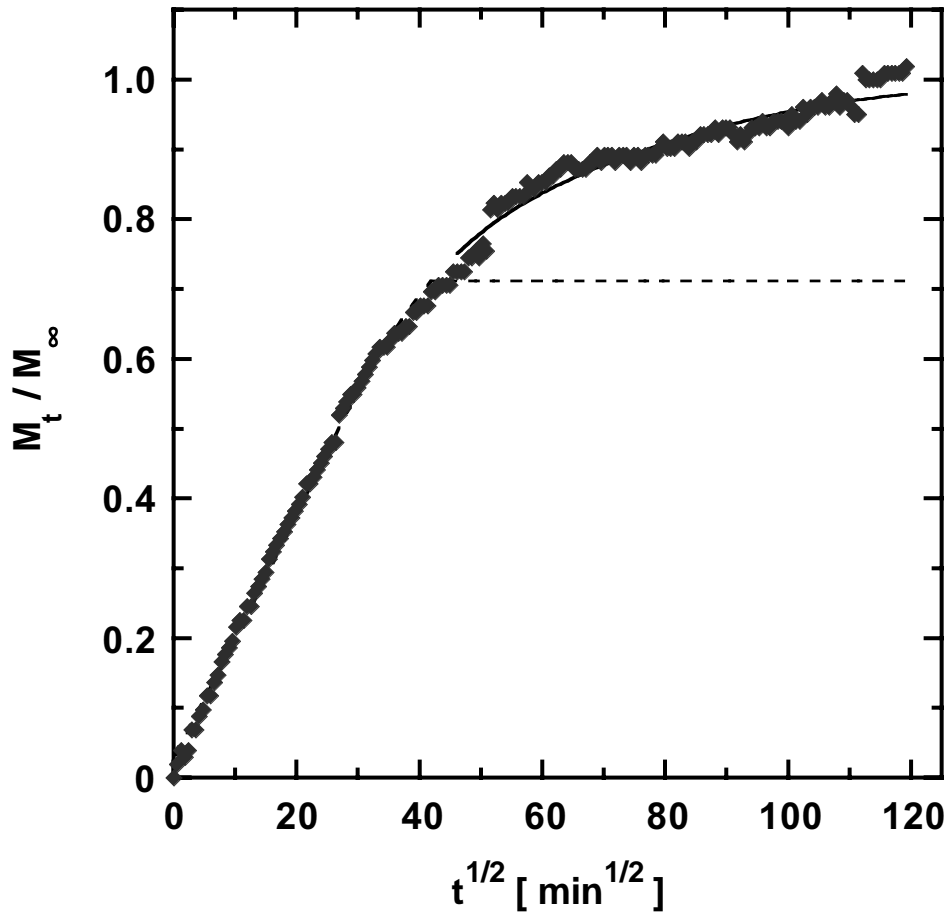


Figure 6.7b Non-Fickian desorption kinetics of MiPK from BPET at 35°C.
 $p_i = 3.3$ cmHg, $p_f = 0.3$ cmHg, $M_\infty = 0.8 \pm 0.04$ g/100g,
 $\bar{D} = 2.5 \pm 0.4 \times 10^{-14}$ cm²/s, $\alpha_R = 0.29 \pm 0.01$, $\tau_R = 5360 \pm 380$ min.,
 $\tau_F = 6020 \pm 1360$ min., $t_D = 0$ min. The dotted curve represents the Fickian
portion of the desorption data.

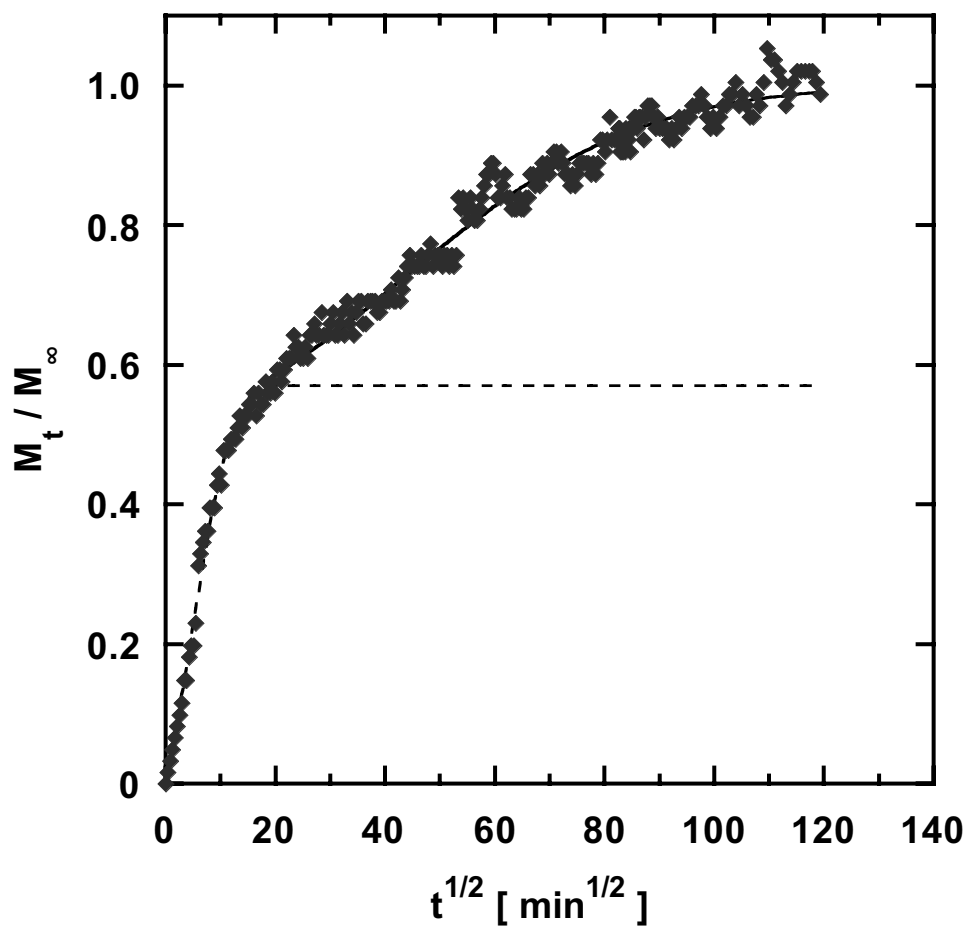


Figure 6.7c Non-Fickian desorption kinetics of MnPK from BPET at 35°C.
 $p_i = 1.7$ cmHg, $p_f = 0.4$ cmHg, $M_\infty = 0.49 \pm 0.004$ g/100g,
 $\bar{D} = 1.9 \pm 0.3 \times 10^{-13}$ cm²/s, $\alpha_R = 0.43 \pm 0.003$, $\tau_R = 3900 \pm 70$ min.,
 $\tau_F = 790 \pm 330$ min., $t_D = 0$ min. The dotted curve represents the Fickian
portion of the desorption data.

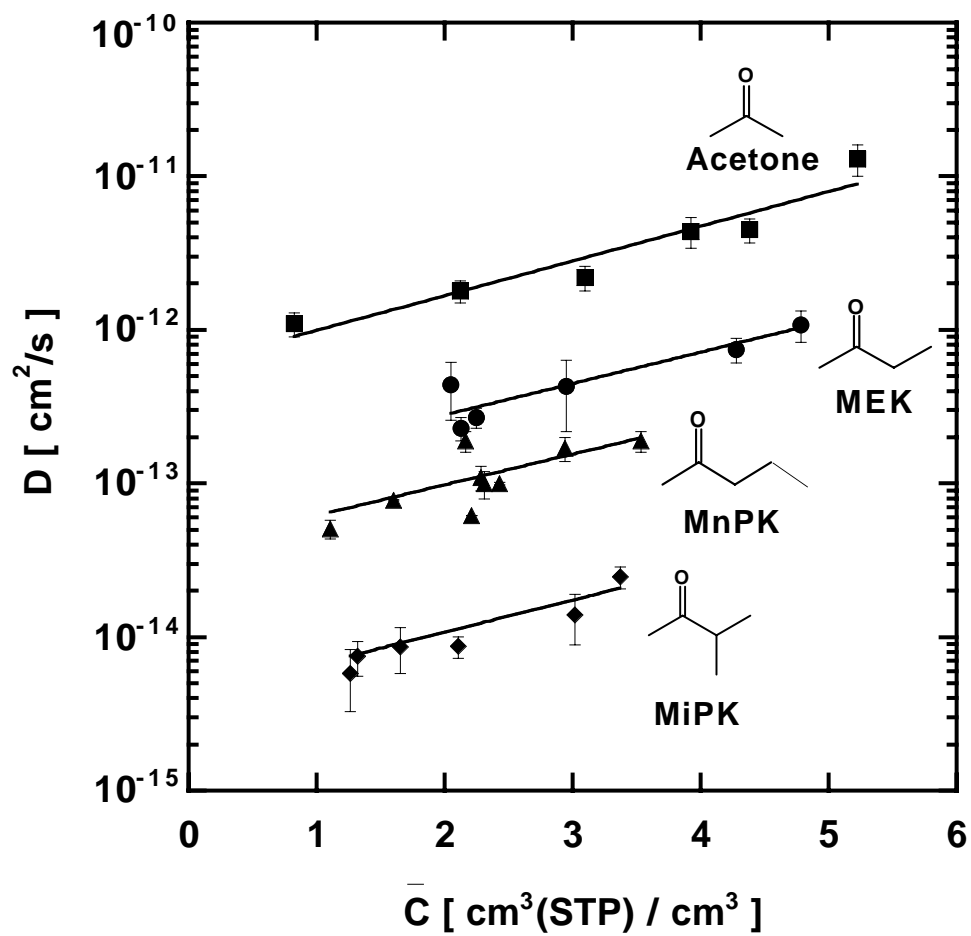


Figure 6.8 Effects of average concentration on apparent diffusion coefficients of acetone, MEK, MnPK, and MiPK in BPET at 35°C.

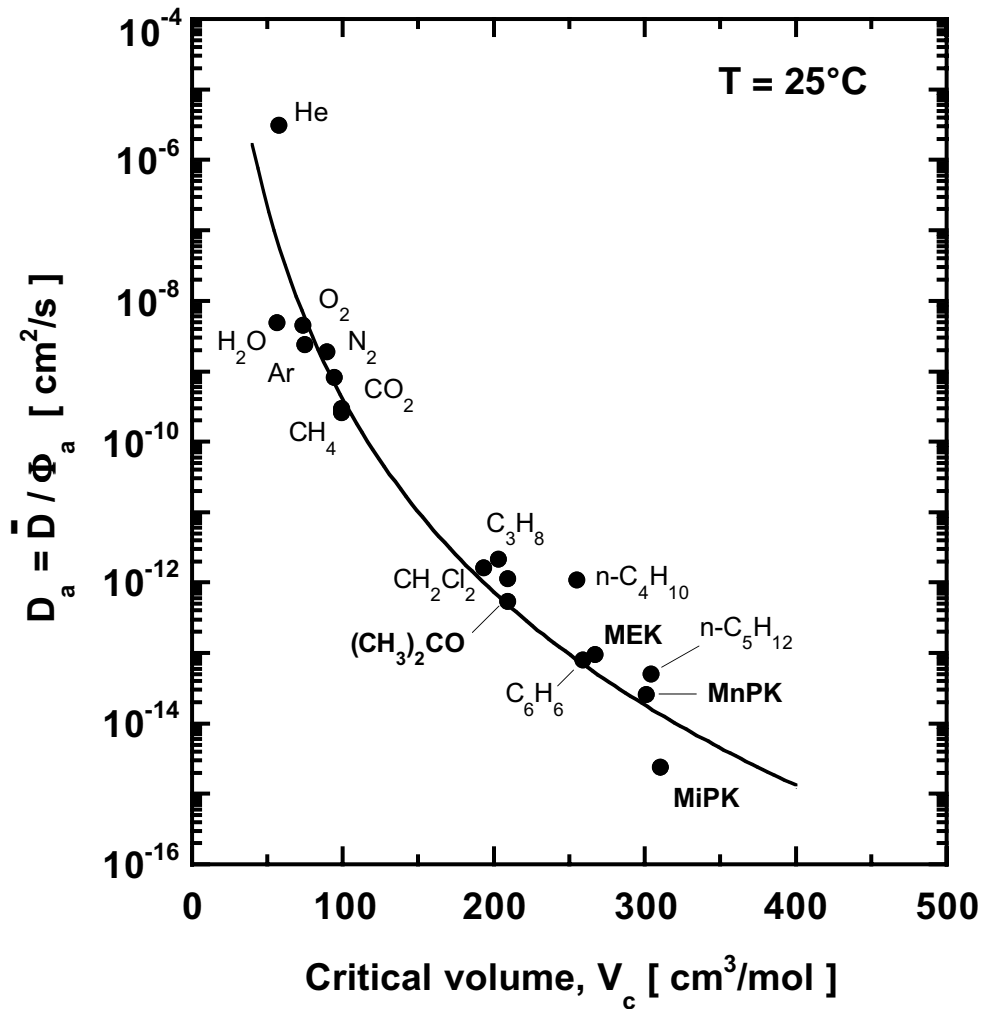


Figure 6.9 Effect of penetrant size on infinite dilution, estimated amorphous phase diffusion coefficients in PET at 25°C [9]. The penetrants from this chapter are highlighted in bold. The best-fit parameters of Equation 6.8 are $\eta = 9.1 \pm 0.9$, $\tau = 5.7 \pm 1.2 \times 10^8 \text{ (cm}^2/\text{s (cm}^3/\text{mol)}^{9.1})$.

CHAPTER 7

Sorption and Transport of Linear Esters and Branched Alkanes in Biaxially Oriented Poly(ethylene terephthalate)

This chapter has been adapted with permission from an article in press under the same title in *Industrial & Engineering Chemistry Research*.

Unpublished work copyright© 2004 American Chemical Society.

7.1 Summary

Equilibrium sorption and uptake kinetics of *i*-butane, *i*-pentane, methyl acetate, and ethyl acetate vapor in uniform, biaxially oriented, semicrystalline poly(ethylene terephthalate) films were determined at 35°C and low penetrant activity (or relative pressure). Chemical structures and relevant physical properties of these penetrants are recorded in Table 7.1. Sorption isotherms of *i*-butane, methyl acetate, and ethyl acetate were well described by the dual-mode sorption model. The sorption isotherm of *i*-pentane was described by the dual-mode model at low activity and the Flory-Huggins model at high activity. At low penetrant activity, the solubility coefficients of *i*-pentane and *i*-butane were 11.5 and 1.3 times lower than those previously reported for their linear analogues, respectively. At constant activity, the solubility coefficients of the two acetates were substantially higher than those of alkanes, and the solubility of methyl acetate was higher than that of ethyl acetate. Sorption kinetics were described either by Fickian diffusion or a two-stage model incorporating Fickian diffusion at short times and protracted polymer structural relaxation at long times. Diffusion coefficients for each penetrant increased with increasing penetrant concentration. The diffusion coefficients of esters (methyl acetate and ethyl acetate) were quite similar to those of ketones (acetone and methyl ethyl ketone) with the same number of carbon atoms.

7.2 Experimental

7.2.1 Materials

Biaxially oriented PET films having a nominal thickness of 0.9 μm and purchased from Goodfellow Co. (Berwyn, PA) were used as received. The film density, 1.395 g/cc, was furnished by the supplier. The complete details of sample characterization techniques and corresponding results and discussion were presented earlier in Chapter 3. *i*-Butane (99.5% purity) was purchased from Scott Specialty Gases (Durham, NC). High-performance liquid chromatographic (HPLC) grade *i*-pentane (99.5% purity), methyl acetate (99.5% purity), and ethyl acetate (99.8% purity) were purchased from Sigma-Aldrich Corp. (St. Louis, MO). The liquid penetrants were subjected to several freeze-thaw cycles to remove dissolved gases before use.

7.2.2 Gravimetric Sorption

Interval kinetic gravimetric sorption experiments were performed using a traditional McBain spring balance system described earlier in Chapter 3. The quartz springs were supplied by Ruska Industries, Inc. (Houston, TX) and had spring constants of 3.03 mm/mg and 3.22 mm/mg.

7.3 Results and Discussion

7.3.1 Equilibrium Uptake of Alkanes in PET

Interval kinetic gravimetric sorption experiments were used to determine sorption isotherms of *i*-butane and *i*-pentane in BPET at 35°C. The results are presented in Figures 7.1a and 7.1b. The sorption isotherms of analogous linear alkane hydrocarbons, *n*-butane and *n*-pentane, in BPET at 35°C [8] (presented previously in Chapter 5) are also included in Figures 7.1a and 7.1b for comparison. The sorption isotherm of *i*-butane is concave to the pressure axis and is well described by the dual-mode sorption model, which is often used to describe sorption of gases and low activity vapors in both amorphous and semicrystalline glassy polymers such as PET [10,16-18,229]. According to this model, the total penetrant concentration is the algebraic sum of the concentration in the equilibrium densified polymer matrix (Henry's Law sites) and the so-called non-equilibrium excess volume of the glassy polymer (Langmuir sites) [16,17]:

$$C = k_D p + C'_H \left(\frac{bp}{1+bp} \right) \quad (7.1)$$

where k_D is the Henry's Law coefficient, C'_H is the Langmuir capacity parameter, a measure of the sorption capacity in the non-equilibrium excess volume of the glassy polymer, and b is the Langmuir affinity parameter, a measure of the penetrant's affinity for the Langmuir sites.

According to the commonly used two-phase model, only the amorphous regions of the polymer are generally regarded to be accessible to penetrant sorption. Hence, the

penetrant concentration in the polymer, C , can be adjusted to an amorphous basis using the following relation:

$$C_a = \frac{C}{\phi_a} \quad (7.2)$$

where C_a is amorphous phase penetrant concentration and ϕ_a is amorphous phase volume fraction. Equations 7.1 and 7.2 can be combined to write the amorphous phase penetrant concentration in terms of the dual-mode model parameters:

$$C_a = \left(\frac{k_D}{\phi_a} \right) P + \left(\frac{C'_H}{\phi_a} \right) \frac{bP}{1 + bP} \quad (7.3)$$

The curve through the *i*-butane data in Figure 1a represents a least-squares fit of the experimental sorption data to Equation 7.3. The sorption isotherm of *i*-pentane (Figure 7.1b) can also be described by the dual-mode model at low penetrant pressure. However, at pressures above ca. 50 cmHg, the isotherm becomes convex to the pressure axis, and the dual-mode model cannot capture this behavior. In this case, we use a combination of the Langmuir sorption term plus the Flory-Huggins model. Such a model is often used to describe sorption isotherms of vapors and high pressure gases in rubbery polymers [255,256] and high activity vapors in glassy polymers [19,40]. The Flory-Huggins sorption model is given by the following equation [15]:

$$\ln a = \ln \phi + (1 - \phi) + \chi(1 - \phi)^2 \quad (7.4)$$

where a is penetrant activity (or relative pressure, p/P_{sat} , where P_{sat} is penetrant saturation vapor pressure), ϕ is penetrant volume fraction in the amorphous region of the polymer, and χ is the Flory-Huggins interaction parameter which characterizes penetrant-polymer

interactions. The concentration dependence of χ is given by the following empirical expression [207]:

$$\chi = \chi_0 + \chi_1\phi \quad (7.5)$$

The curve through the *i*-pentane data in Figure 7.1b represents a least-square fit of the experimental sorption data to Equations 7.3, 7.4, and 7.5, using a procedure described in the literature [126]. The Henry's Law coefficient, k_D , can be related to the Flory-Huggins interaction parameter, χ , at infinite dilution [214]. The dual-mode and Flory-Huggins model parameters for *i*-butane and *i*-pentane obtained in this study are recorded in Table 7.2 along with the dual-mode parameters for *n*-butane and *n*-pentane in BPET [8] (from Chapter 5).

From the data in Figures 7.1a and 7.1b, at constant pressure, *i*-butane and *i*-pentane have lower solubility in BPET than their linear analogues. For example, at 20 cmHg, the solubility ratio for *n*-butane/*i*-butane is 1.3, which is approximately an order of magnitude lower than the value for *n*-pentane/*i*-pentane, which is 11.5. Within the framework of the dual-mode model, penetrant sorption in the non-equilibrium excess volume of glassy polymers is characterized by the Langmuir capacity parameter, which is related to the amount of non-equilibrium excess volume as follows [16]:

$$\frac{C'_H}{\phi_a} = \frac{V_g - V_l}{V_g} \rho^* = \frac{V_{ex}}{V_g} \rho^* \quad (7.6)$$

where V_g is the specific volume of the penetrant-accessible (*i.e.*, amorphous) regions of the polymer, V_l is the specific volume of the hypothetical, densified, equilibrium polymer

matrix, and ρ^* is the condensed penetrant density, which is often estimated as the saturated liquid density of the penetrant at the temperature of the experiment. In this study, the saturation densities were estimated at 35°C using the Hankinson-Brost-Thomson correlation [212]. The values are 207.4 and 188.1 cm³(STP)/cm³, respectively, for *i*-butane and *i*-pentane. If the non-equilibrium excess volume characterized by C_H' is equally accessible to both penetrants, then the ratio C_H'/ρ^* should also be equal. The C_H'/ρ^* values for *i*-butane and *i*-pentane are 0.005 ± 0.001 and 0.001 ± 0.0005 (*cf.* Table 7.2), respectively, suggesting that *i*-butane has far greater access to the non-equilibrium excess volume of PET than *i*-pentane. For comparison, the C_H'/ρ^* values for *n*-butane and *n*-pentane in BPET at 35°C are 0.010 and 0.013, respectively, which are similar [8]. Thus, the lower solubility of the branched alkane hydrocarbons in BPET compared to their linear analogues appears to result in part from restricted access of the branched penetrants to the non-equilibrium excess volume of the polymer, and this seems to have a more pronounced effect on solubility of *i*-pentane in BPET than on *i*-butane.

For comparison, one may consider the effect of chain branching on hydrocarbon solubility in an equilibrium polymer, which would correspond more closely to the sorption in the Henry's law regions of PET. In this regard, experimental sorption isotherms of *n*-butane, *i*-butane, *n*-pentane, and *i*-pentane in low density polyethylene (LDPE) at 25°C are available [214]. Based on the sorption curves presented in Figure 7.2, the infinite dilution solubility ratios for *n*-butane/*i*-butane and *n*-pentane/*i*-pentane in LDPE at 25°C are similar (1.65 and 1.55, respectively). These values are approximately

independent of pressure; for example, at a pressure of 20 cmHg, the solubility ratios are 1.67 and 1.63, respectively. These values are quite similar to the solubility ratios (1.8 for *n*-butane/*i*-butane and 1.7 for *n*-pentane/*i*-pentane) expected based on an analysis using the Flory-Huggins model (see Appendix 7A):

$$\frac{S_{\infty,A}}{S_{\infty,B}} = \frac{P_{sat,B}}{P_{sat,A}} \times \frac{v_B}{v_A} \times \exp(\chi_B - \chi_A) \quad (7.7)$$

where $S_{\infty,A}$ and $S_{\infty,B}$ are the infinite dilution solubility coefficients of penetrant A and B, respectively, $P_{sat,A}$ and $P_{sat,B}$ are the saturation vapor pressures, v_A and v_B are liquid molar volumes, and χ_A and χ_B are the corresponding Flory-Huggins interaction parameters.

This model takes into account differences in infinite dilution solubility due to differences in penetrant vapor pressure, size, and interactions with the polymer matrix. Thus, the effect of chain branching on sorption in rubbery LDPE is consistent with the Flory-Huggins model. This result is in sharp contrast with the sorption results in glassy BPET and, as discussed above, may be linked to the limited accessibility of the branched penetrants to the non-equilibrium excess volume in stiff chain glassy PET, a molecular feature absent in flexible rubbery LDPE and, therefore, in the model just described.

7.3.2 Equilibrium Uptake of Esters in PET

Interval kinetic gravimetric sorption experiments were performed to determine sorption isotherms of methyl acetate and ethyl acetate in BPET at 35°C. The results are presented in Figure 7.3. Both isotherms are well described by the dual-mode sorption model (Equation 7.1), and the model parameters are recorded in Table 7.2. The C_H/ρ^*

values for methyl acetate and ethyl acetate are 0.010 and 0.013, respectively, which are similar to the values reported earlier for linear alkanes [8] (*cf.* Table 7.2) and linear and branched ketones in BPET at 35°C [11] (previously reported in Chapters 5 and 6, respectively). From the data in Figure 7.3, at constant pressure, ethyl acetate solubility is higher than that of methyl acetate, consistent with the higher critical temperature of ethyl acetate (*cf.* Table 7.2).

Figure 7.4 presents the solubility of the branched alkane hydrocarbons and linear esters from this study on the infinite-dilution solubility correlation plot previously presented in Chapters 5 and 6. The solubility values reported in this figure have been adjusted to an amorphous basis as described earlier (*cf.*, Chapter 5) [10]. In general, for the organic vapor sorption data in Figure 7.4, infinite-dilution solubility values were obtained by extrapolating reported solubility values to zero concentration [9]. However, because of the scatter in the data at low pressure for methyl acetate and ethyl acetate, we did not attempt to compute infinite-dilution solubilities. For these penetrants, the solubility coefficients are reported at an activity (or relative pressure) of 0.1 in Figure 7.4. The logarithm of solubility increases rather systematically and linearly with T_c . While the general trend is observed, there is scatter in the data, which may arise from several sources, as discussed in Chapter 6. The solubility of *i*-butane and *i*-pentane is lower than expected, possibly due to the branched structures restricting their access to the non-equilibrium excess volume of PET, as discussed above. While it is difficult to draw firm conclusions, the solubilities of esters from this study and many of the other polar penetrants appear to exhibit a positive deviation from the correlation line. This trend may

reflect favorable interactions between polar penetrants and the polar PET matrix, and this effect is explored further below.

To account for penetrant condensability and to study the effect of penetrant-polymer interactions on solubility, the sorption isotherms of methyl acetate and ethyl acetate were re-plotted as a function of penetrant relative pressure (*i.e.*, activity), following the analysis performed earlier for linear and branched ketones (*cf.*, Chapter 6). As shown in Figure 7.5, this transformation does not collapse the sorption isotherms of the two esters to a single curve, as was the case with an earlier study of linear and branched ketones in PET [11] (*cf.*, Chapter 6). At constant relative pressure, the solubility of methyl acetate is higher than that of ethyl acetate, which is the exact opposite of the ranking based on pressure (*cf.*, Figure 7.3). This is consistent with the difference between the solubility parameters of the esters and PET, which is lower for methyl acetate (*cf.*, Table 7.1). This result is also consistent with other literature studies reporting that ester solubility in polar liquids (*e.g.*, water) decreases as ester chain length increases [257,258]. For example, the solubilities (mole fractions) of methyl acetate and ethyl acetate in water at 25°C are 0.071 and 0.016, respectively [257]. Figure 7.5 also presents the sorption isotherms of the hydrocarbon penetrants in BPET. At constant relative pressure, the esters are significantly more soluble than the alkanes, which is again consistent with the difference between the solubility parameters of the penetrants and that of PET (*cf.*, Table 7.1). This result also supports the notion that polar penetrants have higher solubility in a relatively polar matrix such as PET.

Sorption isotherms of methyl acetate and ethyl acetate were compared to those of acetone [11] and methyl ethyl ketone [11] to study the effect of different polar groups on solubility of penetrants with the same number of carbon atoms (C_3 and C_4 , respectively). These comparisons are presented in Figures 7.6a and 7.6b, respectively. At constant activity, the solubility coefficients of methyl acetate and ethyl acetate are somewhat higher than those of acetone and methyl ethyl ketone, respectively. The 3-component Hansen solubility parameters, which include polar and hydrogen bonding effects, are often used to describe solubility of polar penetrants in polymers [213]. It is useful to compare these parameters for esters and ketones because they have different polar and hydrogen bonding characteristics. Based on the solubility parameter components reported in Table 7.3, the ketones are more polar than the esters, but the esters have stronger hydrogen bonding characteristics. Using literature values for Hansen solubility parameters of the penetrants [213] and PET [254] (*cf.* Table 7.3) and available correlations [213], the estimated χ values for methyl acetate and ethyl acetate are lower than the corresponding values for acetone and methyl ethyl ketone, respectively, which would be consistent with higher solubility of the esters. Similar solubility trends of esters and ketones have also been observed in other polymers [259]. Wibawa *et al.* reported higher solubility coefficients of methyl acetate and propyl acetate relative to that of acetone and methyl ethyl ketone in two polar, rubbery polymers, poly(*n*-butyl methacrylate) and poly(vinyl acetate) [259]. For example, at 313 K and a penetrant activity of 0.19, the solubilities of methyl acetate and acetone in poly(*n*-butyl methacrylate) are 10.8 and 9.3 cm³(STP)/cm³, respectively.

7.3.3 Sorption Kinetics of Alkanes and Esters in PET

Figures 7.7a and 7.7b present results from two representative kinetic sorption experiments of *i*-butane and methyl acetate, respectively, in BPET at 35°C. In each case, the fractional mass uptake, M_t / M_∞ , increases linearly with $t^{1/2}$ at short times. This behavior is characteristic of sorption kinetics controlled by Fickian diffusion (see, for example, Figure 7a and the dotted curve in Figure 7b). In some instances, the fractional mass uptake at longer times exhibits a protracted, asymptotic approach towards equilibrium [224] (see, for example, the solid curve in Figure 7b). As described earlier in Chapters 5 and 6, this behavior is ascribed to mass uptake kinetics limited by polymer swelling and structural rearrangement to accommodate the penetrant rather than Fickian diffusion. These sorption kinetics may be described using the following empirical model [11]:

$$\frac{M_t}{M_\infty} = 1 - (1 - \alpha_R) \left\{ \frac{8}{\pi^2} \sum_{n=0}^{\infty} \frac{1}{(2n+1)^2} \exp\left(\frac{-\bar{D}(2n+1)^2 \pi^2 t}{l^2}\right) \right\} + \alpha_R \times \exp\left(\frac{-(t-t_D)}{\tau_R}\right) \times H(t_D) \quad (7.8)$$

where \bar{D} is the average diffusion coefficient, l is polymer film thickness, α_R is the fraction of weight uptake occurring during the protracted, non-Fickian approach to equilibrium, τ_R is the time constant associated with the long time drift in mass uptake, t_D is a delay factor accounting for a delay in the beginning of structural relaxation, and $H(t_D)$ is the Heaviside unit step function [253].

The curves in Figures 7.7a and 7.7b represent least-squares fits of Equation 7.8 to the experimental data for sorption of *i*-butane and methyl acetate in BPET at 35°C, respectively, following the procedure described in Chapter 5 [8]. In Figure 7.7b, the

dotted curve indicates the fraction of mass uptake controlled by Fickian diffusion and the solid curve indicates the fraction controlled by polymer chain relaxation.

Average diffusion coefficients were estimated using the procedure described in Chapter 5 [8,11]. Figure 7.8 presents the diffusion coefficients of *i*-butane and *i*-pentane, along with previously reported ([8] and Chapter 5) diffusion coefficient values of *n*-butane and *n*-pentane in BPET as a function of average penetrant concentration. For all penetrants, the logarithm of diffusion coefficient increases approximately linearly with penetrant concentration, consistent with earlier reports of the concentration dependence of *n*-alkane and ketone diffusion coefficients in PET (*cf.*, Chapters 5 and 6). The following empirical model was used to describe the data [8]:

$$\bar{D} = D_{\infty} \exp(\omega \bar{C}) \quad (7.9)$$

where D_{∞} is the infinite-dilution (or zero concentration) diffusion coefficient and the slope, ω , characterizes the dependence of \bar{D} on \bar{C} . D_{∞} and ω values for *i*-butane and *i*-pentane are recorded in Table 7.4, along with the values for *n*-butane and *n*-pentane from Chapter 5 [8]. The infinite-dilution diffusion coefficients were adjusted to an amorphous basis using the following relation (*cf.*, Chapter 5):

$$D_a = \frac{D_{\infty}}{\phi_a} \quad (7.10)$$

The infinite-dilution, estimated amorphous phase diffusion coefficient, D_a , of *i*-butane in BPET is two orders of magnitude lower than that of *n*-butane and that of *i*-pentane is an order of magnitude lower than that of *n*-pentane. The diffusion coefficients decrease in the following order:

n -butane > n -pentane > i -butane > i -pentane

suggesting that chain branching has a larger effect on lowering hydrocarbon diffusion coefficients in PET than chain length.

To compare the effect of chain branching versus chain length on hydrocarbon diffusion coefficients in PET, infinite-dilution, estimated amorphous phase diffusion coefficients of linear and branched alkane hydrocarbons in PET from this study and available literature data [9] are presented in Figure 7.9 as a function of number of carbon atoms. Since the diffusion coefficients of penetrants in this study were measured at 35°C, they were adjusted to 25°C using the procedure described in the literature [9]. The logarithm of diffusion coefficients of normal hydrocarbons decreases linearly with increasing chain length (from C₁ to C₅), as shown. To quantify the effect of chain branching on diffusion coefficients, the following procedure was used [102]. An effective chain length was obtained for i -butane and i -pentane based on their diffusion coefficient values and an extrapolated linear curve-fit to the data for the normal C₁ to C₅ hydrocarbons. The effective chain length obtained by this technique was 6.2 for i -butane (C₄) and 7.2 for i -pentane (C₅). Based on this analysis, the effective size contribution to diffusion coefficient of a methyl (CH₃) side-group is 2.2, while that of a CH₃ or CH₂ group in the main chain is unity. Although this method assumes a linear decrease in diffusion coefficients of straight-chain hydrocarbons larger than n -pentane, which may not be accurate, it clearly demonstrates the important effect of chain branching on hydrocarbon diffusion coefficients in PET. This result is consistent with several literature studies reporting the size and shape effects on hydrocarbon diffusion coefficients in

rubbery polymers such as polyisobutylene [260], ethyl cellulose [17], and natural rubber [261], and glassy polymers such as polycarbonate [262].

Figure 7.10 presents the diffusion coefficients of methyl acetate and ethyl acetate as a function of average penetrant concentration. The logarithm of diffusion coefficients increases linearly with penetrant concentration for both penetrants. The data were fit to the model presented in Equation 7.9 and the D_∞ and ω values are recorded in Table 7.4. The dependence of \bar{D} on \bar{C} is similar for methyl acetate and ethyl acetate over the concentration range studied. The diffusion coefficient values of acetone and methyl ethyl ketone in BPET from Chapter 6 [11] are also included in Figure 7.10 for comparison.

Somewhat surprisingly, the diffusion coefficients of methyl acetate and ethyl acetate are quite similar to those of acetone and methyl ethyl ketone, respectively, over the concentration range studied, even though the esters are slightly larger than the ketones with the same number of carbon atoms (*cf.* Table 7.3) [212]. Some literature studies have even reported higher diffusion coefficients of methyl acetate than acetone in rubbery poly(vinyl acetate) [263], and in glassy [264] and rubbery [263] poly(methyl methacrylate). Diffusion coefficients of polar penetrants in polymers can be retarded by specific favorable interactions between the penetrant and polymer matrix [130]. Based on their dipole moments, the ketones are much more polar than esters with the same number of carbon atoms (*cf.* Table 7.3) [212]. The larger sizes of the esters (which would favor lower diffusion coefficients) could be partially offset by their lower polarity (which would favor higher diffusion coefficients), resulting in similar diffusion coefficient values for these two classes of penetrants. Interestingly, the diffusion coefficients of ethyl

acetate and methyl ethyl ketone in a non-polar, rubbery polymer, high-density polyethylene (HDPE), support this notion [265,266]. The diffusion coefficient of methyl ethyl ketone ($4.7 \times 10^{-13} \text{ cm}^2/\text{s}$) is an order of magnitude larger than that of ethyl acetate ($0.4 \times 10^{-13} \text{ cm}^2/\text{s}$) in HDPE at 30°C and a penetrant activity of 0.1 [265]. This result suggests that penetrant-polymer interactions, which act to decrease the diffusion coefficient of the smaller but more polar ketone relative to that of the larger but less polar ester in BPET, are absent in non-polar HDPE.

As reported earlier in Chapters 5 and 6, the infinite-dilution, estimated amorphous phase diffusion coefficients in PET may be roughly correlated with critical volume using the following empirical power law model [8]:

$$D_a = \frac{\tau}{V_c^\eta} \quad (7.11)$$

where τ and η are adjustable parameters. Figure 7.11 presents the correlation plot along with the data for linear esters and branched alkanes from this study. Since the diffusion coefficients of the penetrants studied in this research project (reported in Chapters 5, 6, and 7) were obtained at 35°C, the diffusion coefficients of several other penetrants in Figure 7.11, originally reported at 25°C (*cf.*, Figure 5.5), were adjusted to 35°C using the procedure described in the literature [9]. The infinite-dilution diffusion coefficient of ethyl acetate is approximately an order of magnitude lower than that of methyl acetate, consistent with its larger size. The correlation of D with V_c is good for relatively linear penetrants, such as methyl acetate and ethyl acetate. The values of τ and η ($4.4 \pm 1.2 \times$

$10^7 \text{ cm}^2/\text{s} (\text{cm}^3/\text{mol})^{8.4}$ and 8.4 ± 1.0 , respectively), which were obtained from a curve-fit of the experimental data for spherical and relatively linear penetrants at 35°C , are somewhat different from the parameter values reported earlier at 25°C (*cf.*, Figure 5.5) [9]. The diffusion coefficients of *i*-butane and *i*-pentane are approximately an order of magnitude lower than the values anticipated by this simple empirical model. As reported in Chapter 6, this is because critical volume does not accurately capture the effect of penetrant shape on diffusion coefficients [9,11].

7.4 Conclusions

Equilibrium sorption and uptake kinetics of *i*-butane, *i*-pentane, methyl acetate, and ethyl acetate in biaxially oriented, semicrystalline PET films at 35°C have been reported. The equilibrium solubility of *i*-butane and *i*-pentane is lower than that of the corresponding linear alkanes, possibly due to restricted access of the branched penetrants to the non-equilibrium excess volume of PET. At constant relative pressure, the solubility of methyl acetate is higher than that of ethyl acetate, consistent with solubility trends of esters in other polymers and polar liquids, and the solubility of esters in PET is higher than that of ketones having the same number of carbon atoms. These results are consistent with the differences between the solubility parameters of the penetrants and PET. Similar solubility trends have also been observed for esters and ketones in other polar and rubbery polymers. Thus, penetrant solubility in PET, which is primarily determined by penetrant condensability, also appears to be strongly dependent on penetrant size and shape (for non-polar penetrants) and specific penetrant-polymer

interactions (for polar penetrants). Sorption kinetics of all penetrants are described either by Fickian diffusion or a two-stage model incorporating Fickian diffusion at short times and protracted polymer structural relaxation at long times. Chain branching appears to have an important effect on hydrocarbon diffusion coefficients in PET, consistent with the results reported for other rubbery and glassy polymers. The infinite-dilution diffusion coefficient of ethyl acetate is an order of magnitude lower than that of methyl acetate, which is consistent with its larger size. The diffusion coefficients for each penetrant increase with increasing penetrant concentration. The diffusion coefficients of esters (methyl acetate and ethyl acetate) are quite similar to those of ketones (acetone and methyl ethyl ketone) with the same number of carbon atoms despite the esters being slightly larger than the ketones. Thus, penetrant diffusion coefficients in PET, which are primarily dependent on penetrant size and shape, appear to be influenced by polarity effects as well.

Appendix 7A

The Flory-Huggins model for solubility of penetrants in equilibrium matrices, such as rubbery polymers, is given by:

$$\ln\left(\frac{P}{P_{sat}}\right) = \ln\phi + (1-\phi) + \chi(1-\phi)^2 \quad (\text{A1})$$

where P_{sat} is penetrant saturation vapor pressure, ϕ is penetrant volume fraction, and χ is the Flory-Huggins interaction parameter. The penetrant volume fraction, ϕ , can be written as:

$$\phi = \frac{\frac{Cv}{22414}}{1 + \frac{Cv}{22414}} \quad (\text{A2})$$

where C is penetrant concentration (cm^3 (STP)/ cm^3 polymer) and v is penetrant molar volume (cm^3/mol). The Flory-Huggins interaction parameter can be estimated from the solubility parameters of the penetrant and polymer as [267]:

$$\chi = 0.34 + \frac{v}{RT}(\Delta\delta)^2 \quad (\text{A3})$$

where $\Delta\delta$ is the difference between the solubility parameters of the penetrant and polymer. In the limit of low pressures (*i.e.*, $p \rightarrow 0$ or $C \rightarrow 0$), ϕ is:

$$\phi = \frac{Cv}{22414} \quad (\text{A4})$$

Also, when $\phi \ll 1$, Equation A1 reduces to:

$$\ln\left(\frac{p}{P_{sat}}\right) = \ln\phi + 1 + \chi \quad (\text{A5})$$

Substituting Equation A4 into A5:

$$\ln\left(\frac{p}{P_{sat}}\right) = \ln\left(\frac{Cv}{22414}\right) + (1 + \chi) \quad (\text{A6})$$

Equation A6 can be rearranged to obtain an expression for penetrant solubility at low pressure, S_∞ :

$$S_\infty = \frac{C}{p} = \frac{22414}{v \times \exp(1 + \chi) \times P_{sat}} \quad (\text{A7})$$

Hence, the ratio of infinite-dilution solubilities of two penetrants A and B can be written as:

$$\frac{S_{\infty,A}}{S_{\infty,B}} = \left(\frac{P_{sat,B}}{P_{sat,A}}\right) \times \left(\frac{v_B}{v_A}\right) \times \exp(\chi_B - \chi_A) \quad (\text{A8})$$

where $S_{\infty,A}$ and $S_{\infty,B}$ are infinite dilution solubility coefficients of penetrant A and B, respectively, $P_{sat,A}$ and $P_{sat,B}$ are their saturation vapor pressures, v_A and v_B are penetrant molar volumes, and χ_A and χ_B are the Flory-Huggins interaction parameters.

Table 7.1 Chemical structure, critical properties [212], solubility parameters [213], and saturation vapor pressures at 35°C [212] of linear and branched alkane hydrocarbons and esters

Penetrant	Chemical Structure	Critical Temperature (K)	Critical Volume (cm ³ /mol)	Solubility Parameter (MPa) ^{1/2}	Saturation Vapor Pressures (cmHg)
<i>n</i> -Butane	CH ₃ CH ₂ CH ₂ CH ₃	425.2	255	13.9	245.9
<i>i</i> -Butane	$\begin{array}{c} \text{CH}_3\text{CHCH}_3 \\ \\ \text{CH}_3 \end{array}$	408.2	263	12.6	345.1
<i>n</i> -Pentane	CH ₃ CH ₂ CH ₂ CH ₂ CH ₃	469.7	304	14.3	72.7
<i>i</i> -Pentane	$\begin{array}{c} \text{CH}_3\text{CHCH}_2\text{CH}_3 \\ \\ \text{CH}_3 \end{array}$	460.4	306	13.7	96.3
Methyl Acetate	$\begin{array}{c} \text{O} \\ \\ \text{H}_3\text{C}-\text{C}-\text{OCH}_3 \end{array}$	506.8	228	18.7	32.9
Ethyl Acetate	$\begin{array}{c} \text{O} \\ \\ \text{H}_3\text{C}-\text{C}-\text{OCH}_2\text{CH}_3 \end{array}$	523.2	286	18.1	15.0

Note: The solubility parameter of PET is 21.5 MPa^{1/2} [254].

Table 7.2 Dual-mode and Flory-Huggins model parameters for linear and branched alkane hydrocarbons and esters in BPET at 35°C. The model parameters for *n*-butane and *n*-pentane were obtained from the literature [8]

Penetrant	k_D cm ³ (STP)/(cm ³ .cmHg)	C_H' cm ³ (STP)/cm ³	b cmHg ⁻¹	C_H' / ρ^*
<i>n</i> -Butane	0.0143 ± 0.0012	2.16 ± 0.11	0.029 ± 0.006	0.010
<i>i</i> -Butane	0.009 ± 0.005	1.0 ± 0.3	0.1 ± 0.03	0.005 ± 0.001
<i>n</i> -Pentane	0.011 ± 0.004	2.53 ± 0.23	0.135 ± 0.020	0.013
<i>i</i> -Pentane [†]	0.005 ± 0.001	0.14 ± 0.1	0.08 ± 0.05	0.001 ± 0.0005
Methyl Acetate	0.59 ± 0.02	2.82 ± 0.12	6.4 ± 1.4	0.010 ± 0.0004
Ethyl Acetate	0.76 ± 0.03	2.88 ± 0.13	7.5 ± 1.6	0.013 ± 0.0006

[†] The best-fit parameters of Equation 7.5 are $\chi_0 = 4.8 \pm 3.8$ and $\chi_1 = -181 \pm 3$

Table 7.3 Hansen solubility parameters, critical volumes, and dipole moments of acetone, methyl ethyl ketone, methyl acetate, and ethyl acetate [212,213]

Penetrant	Hansen Solubility Parameters (MPa ^{1/2})			Critical Volume (cm ³ /mol)	Dipole Moment (Debye)
	δ_d	δ_p	δ_H		
	Acetone	15.5	10.4		
Methyl Acetate	15.5	7.2	7.6	228	1.7
Methyl Ethyl Ketone	16.0	9.0	5.1	267	3.3
Ethyl Acetate	15.8	5.3	7.2	286	1.9

Note: The Hansen solubility parameters (δ_d , δ_p , δ_H) for PET are 19.5, 3.5, and 8.6 MPa^{1/2}, respectively [254].

Table 7.4 D_∞ and ω values for linear and branched alkane hydrocarbons and esters at 35°C. The values for *n*-butane and *n*-pentane were obtained from the literature [8]

Penetrant	D_∞ (cm ² /s)	D_∞ / ϕ_a (cm ² /s)	ω cm ³ (polymer)/cm ³ (STP)
<i>n</i> -Butane	$6.7 \pm 0.3 \times 10^{-13}$	1.1×10^{-12}	0.47 ± 0.05
<i>i</i> -Butane	$7.0 \pm 4 \times 10^{-15}$	1.2×10^{-14}	1.4 ± 0.7
<i>n</i> -Pentane	$3.1 \pm 0.4 \times 10^{-14}$	5.1×10^{-14}	1.32 ± 0.09
<i>i</i> -Pentane	$3.3 \pm 2 \times 10^{-15}$	5.4×10^{-15}	2.3 ± 1.4
Methyl Acetate	$9.1 \pm 2.1 \times 10^{-13}$	1.5×10^{-12}	0.34 ± 0.04
Ethyl Acetate	$1.3 \pm 0.4 \times 10^{-13}$	2.1×10^{-13}	0.39 ± 0.05

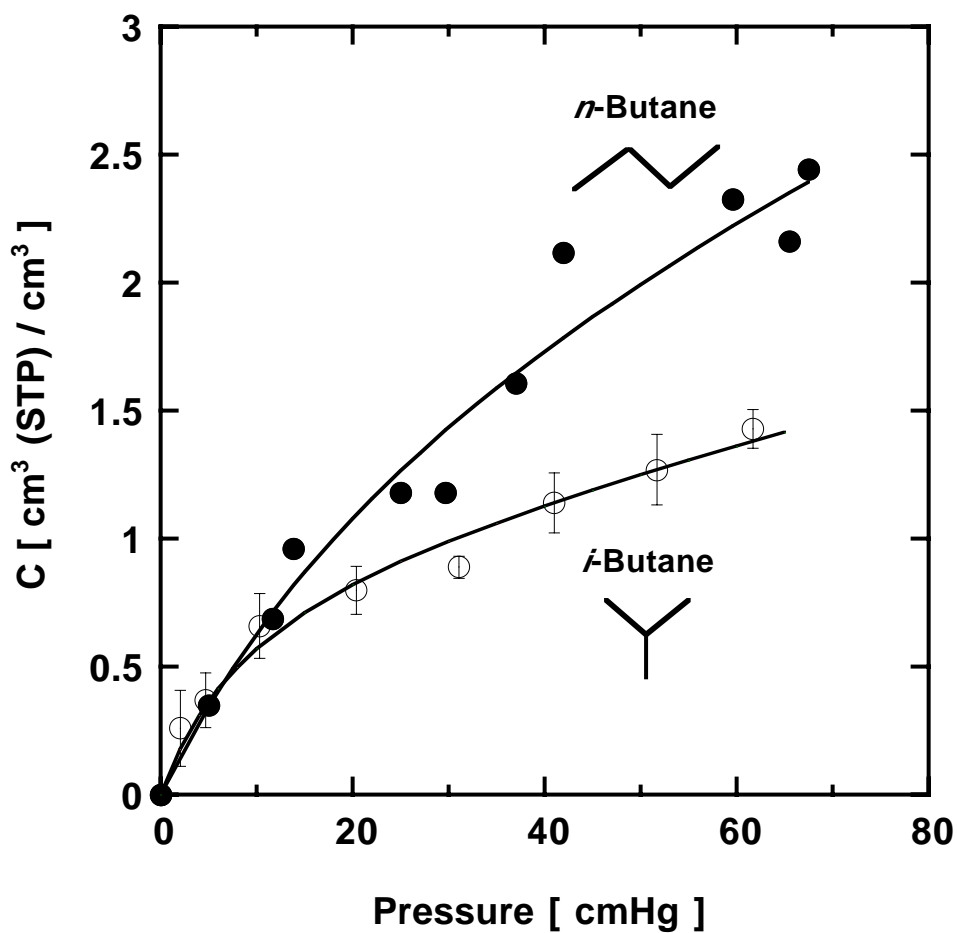


Figure 7.1a Sorption isotherms of *n*-butane [8] and *i*-butane in biaxially oriented PET (BPET) at 35°C as a function of penetrant pressure. The error bars were estimated from the uncertainties in measuring the equilibrium uptake (M_{∞}) values (± 0.01 mg), the penetrant-free polymer sample weight (± 1 mg), and the propagation of errors technique [268].

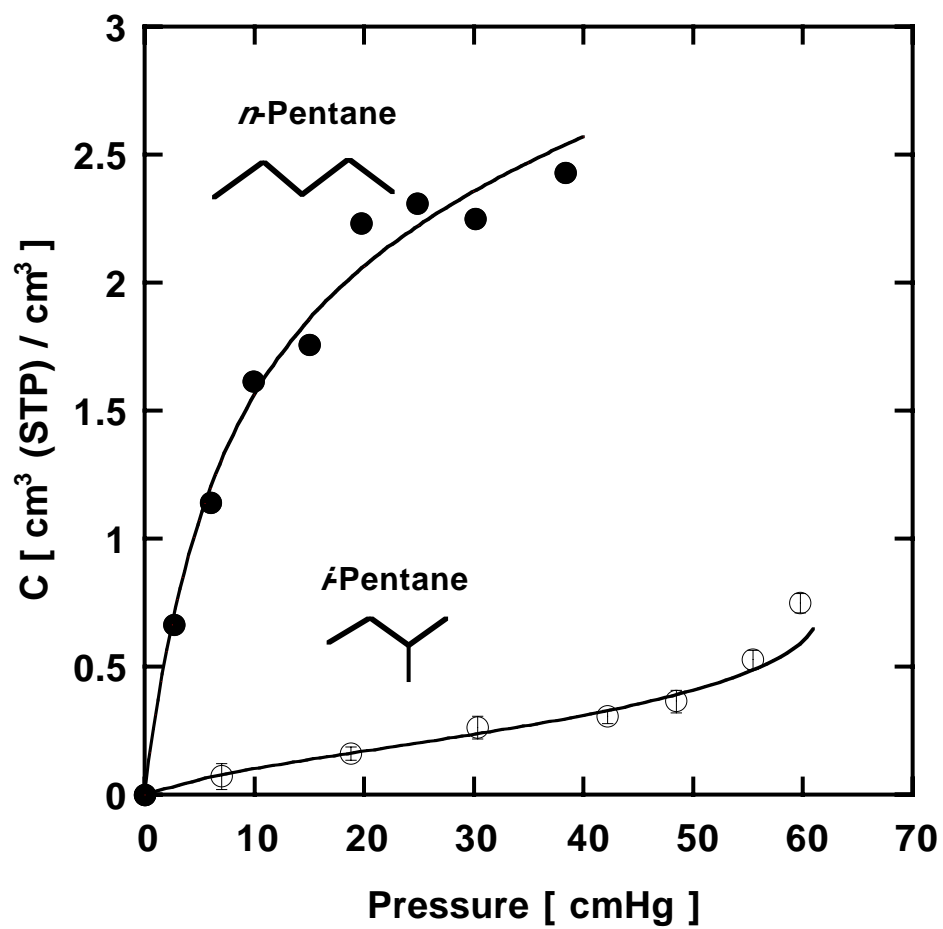


Figure 7.1b Sorption isotherms of *n*-pentane [8] and *i*-pentane in BPET at 35°C as a function of penetrant pressure.

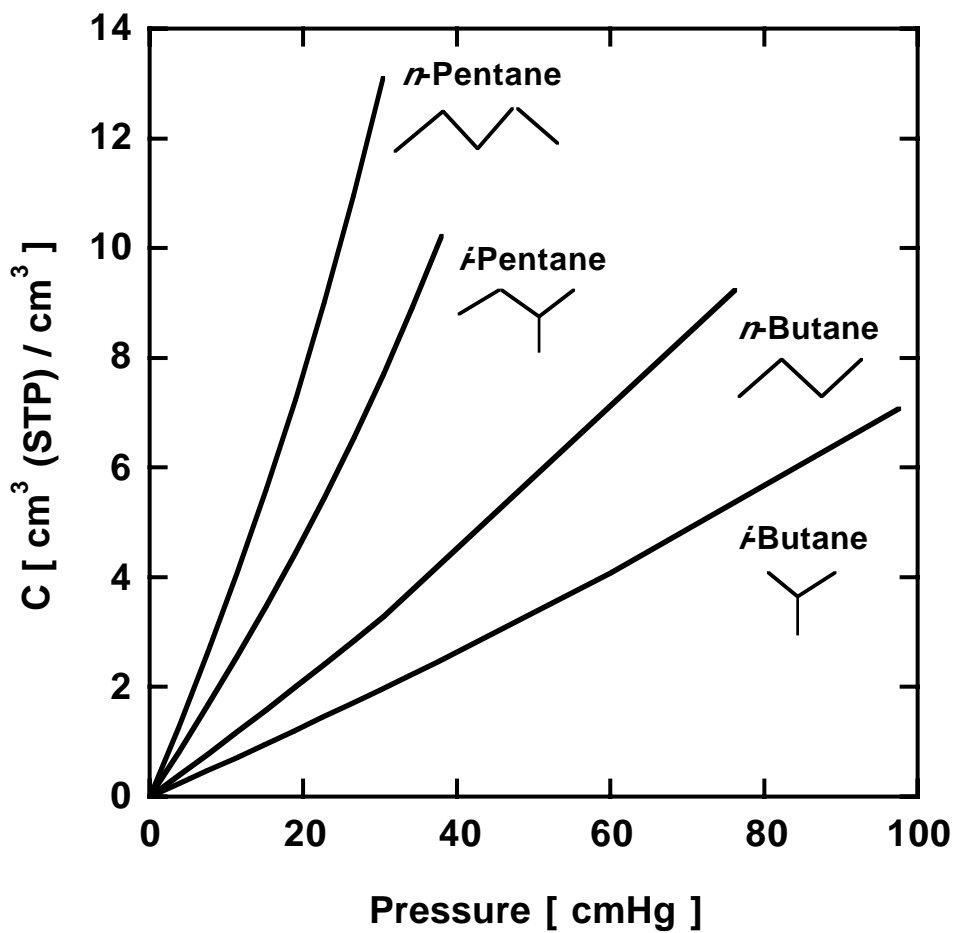


Figure 7.2 Sorption isotherms of *n*-butane, *i*-butane, *n*-pentane, and *i*-pentane in low density polyethylene (LDPE) at 25°C [214].

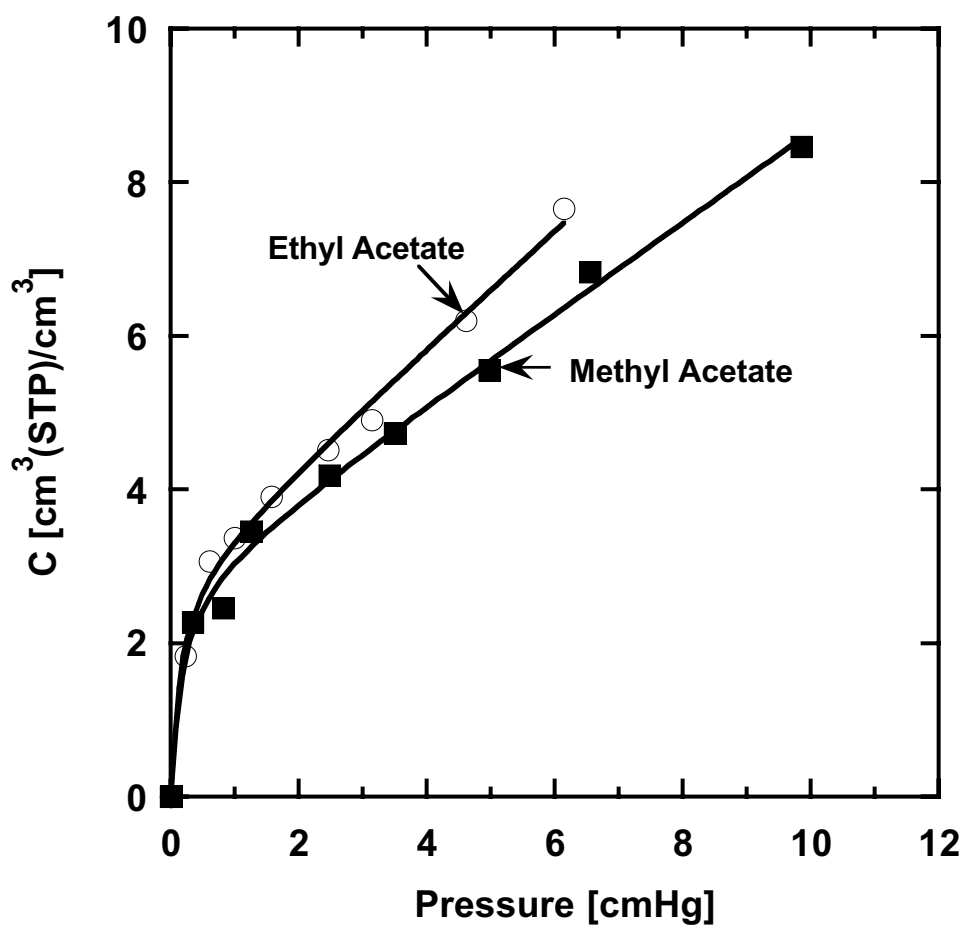


Figure 7.3 Sorption isotherms of methyl acetate and ethyl acetate in BPET at 35°C as a function of penetrant pressure.

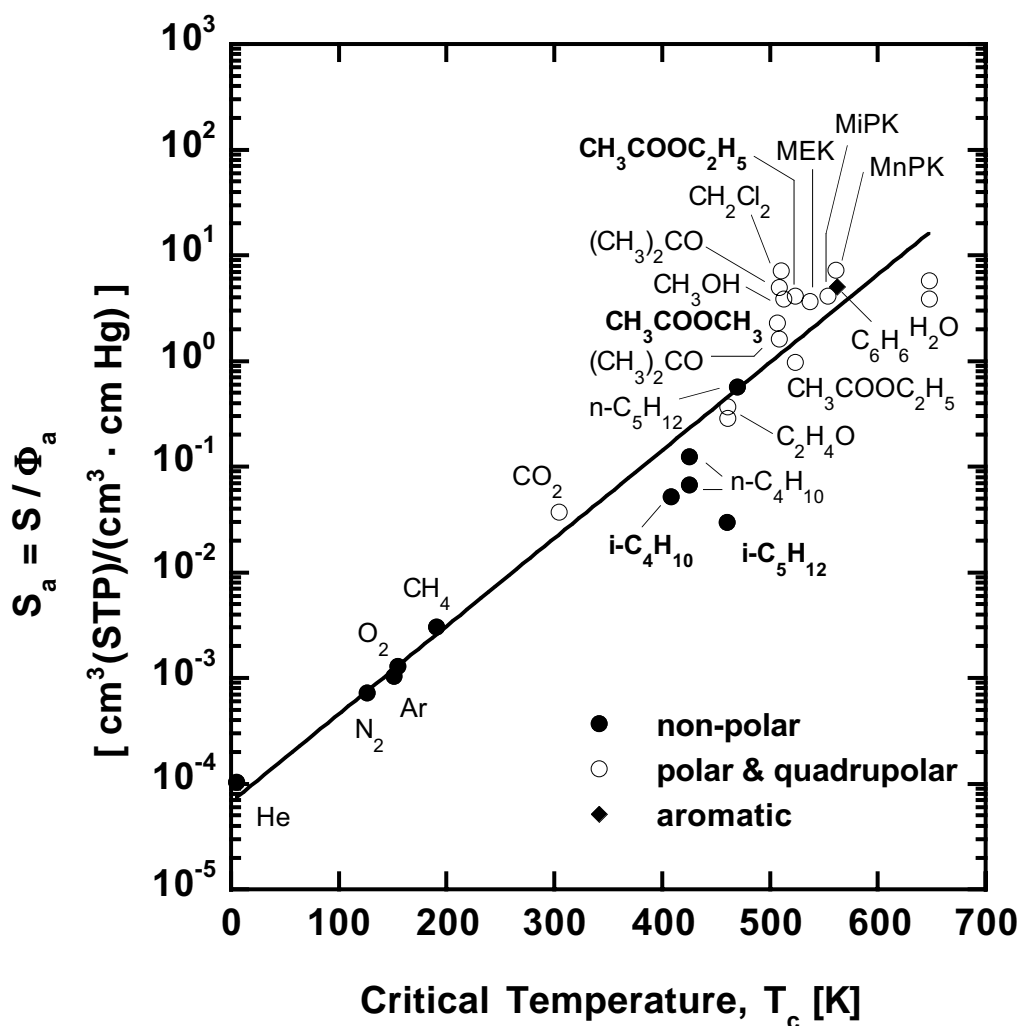


Figure 7.4 Correlation of infinite dilution, estimated amorphous phase solubility coefficients in PET with penetrant critical temperature [9]. The penetrants from this chapter are highlighted in bold. For most penetrants, the data have been extrapolated to infinite dilution. The data for methyl acetate and ethyl acetate from this chapter and for methyl ethyl ketone (MEK), methyl *i*-propyl ketone (MiPK), and methyl *n*-propyl ketone (MnPK) from an earlier chapter [11] are reported at a relative pressure of 0.1. While the data from this study were obtained at 35°C, the temperature range for the data obtained from various literature sources is 25-45°C [9]. The slope, M , of the least squares line is $0.019 \pm 0.001 \text{ K}^{-1}$, and the intercept, N , is -9.6 ± 0.4 .

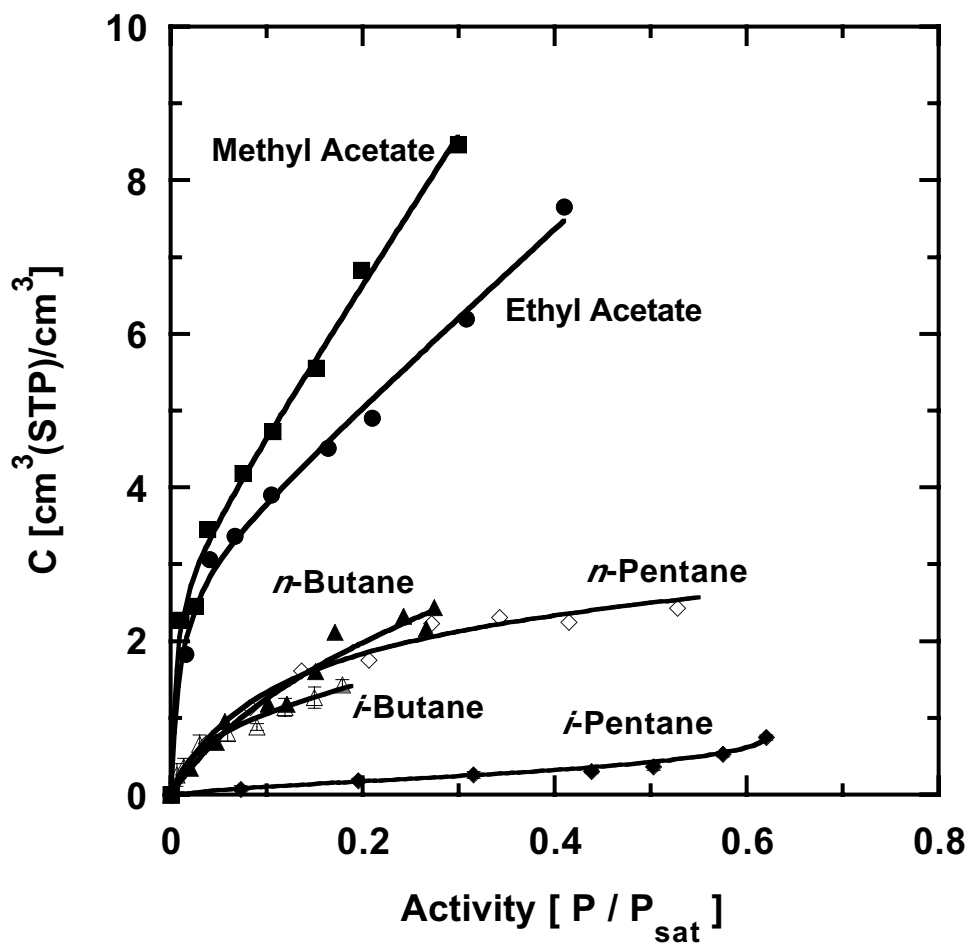


Figure 7.5 Sorption isotherms of methyl acetate (■), ethyl acetate (●), *n*-butane [8] (▲), *n*-pentane [8] (◇), *i*-butane (△), and *i*-pentane (◆) in BPET at 35°C as a function of relative pressure.

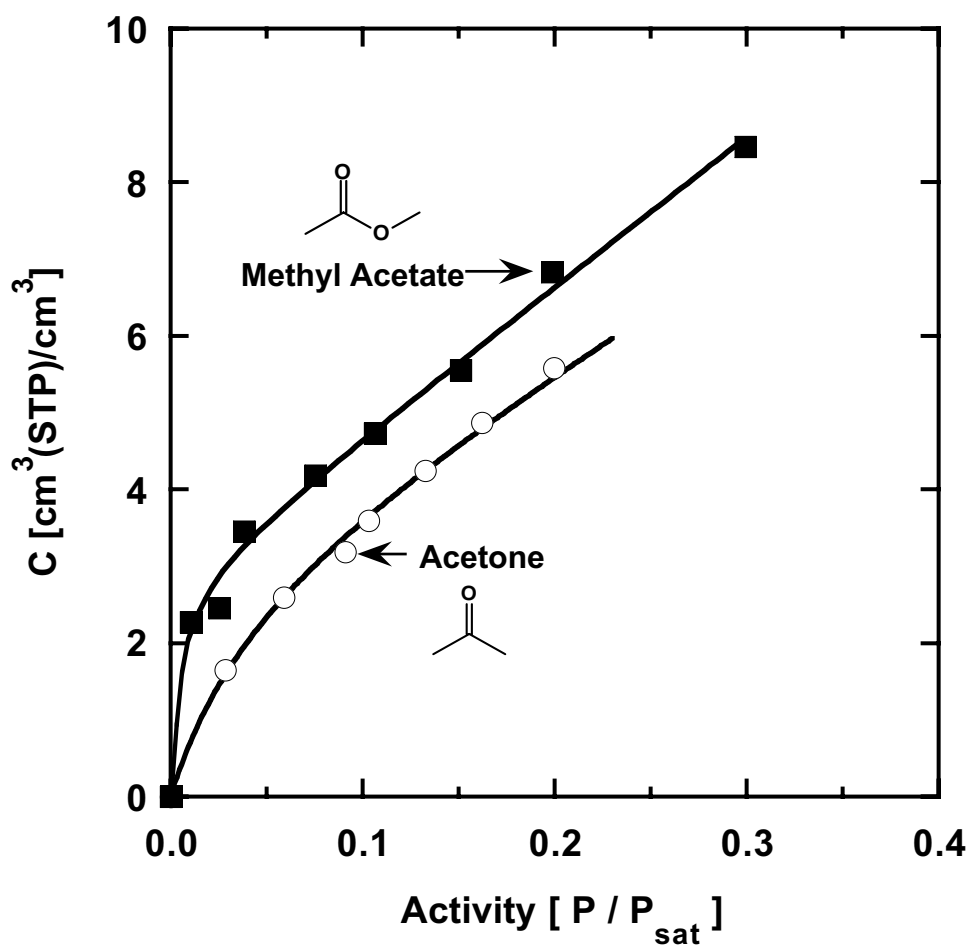


Figure 7.6a Sorption isotherms of methyl acetate and acetone [11] in BPET at 35°C as a function of relative pressure. The saturation vapor pressures of methyl acetate and acetone at 35°C are 32.9 and 34.7 cmHg, respectively [212].

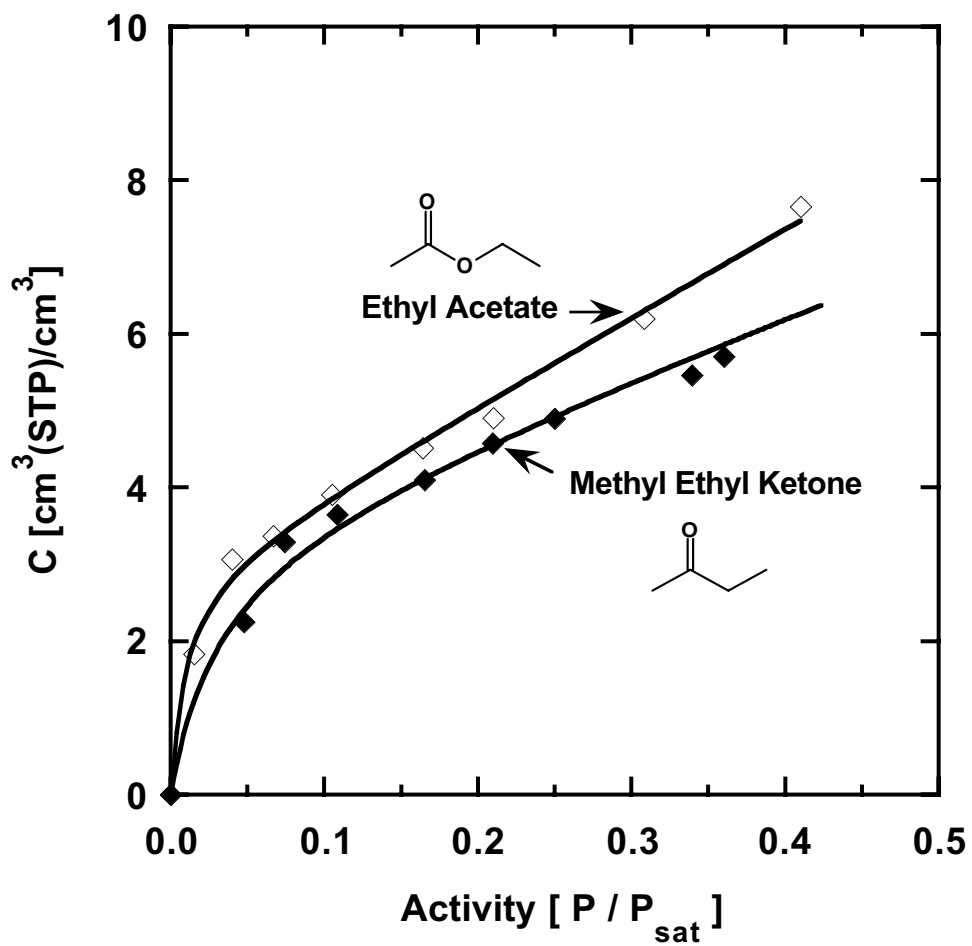


Figure 7.6b Sorption isotherms of ethyl acetate and methyl ethyl ketone (MEK) [11] in BPET at 35°C as a function of relative pressure. The saturation vapor pressures of ethyl acetate and MEK at 35°C are 14.9 and 14.2 cmHg, respectively [212].

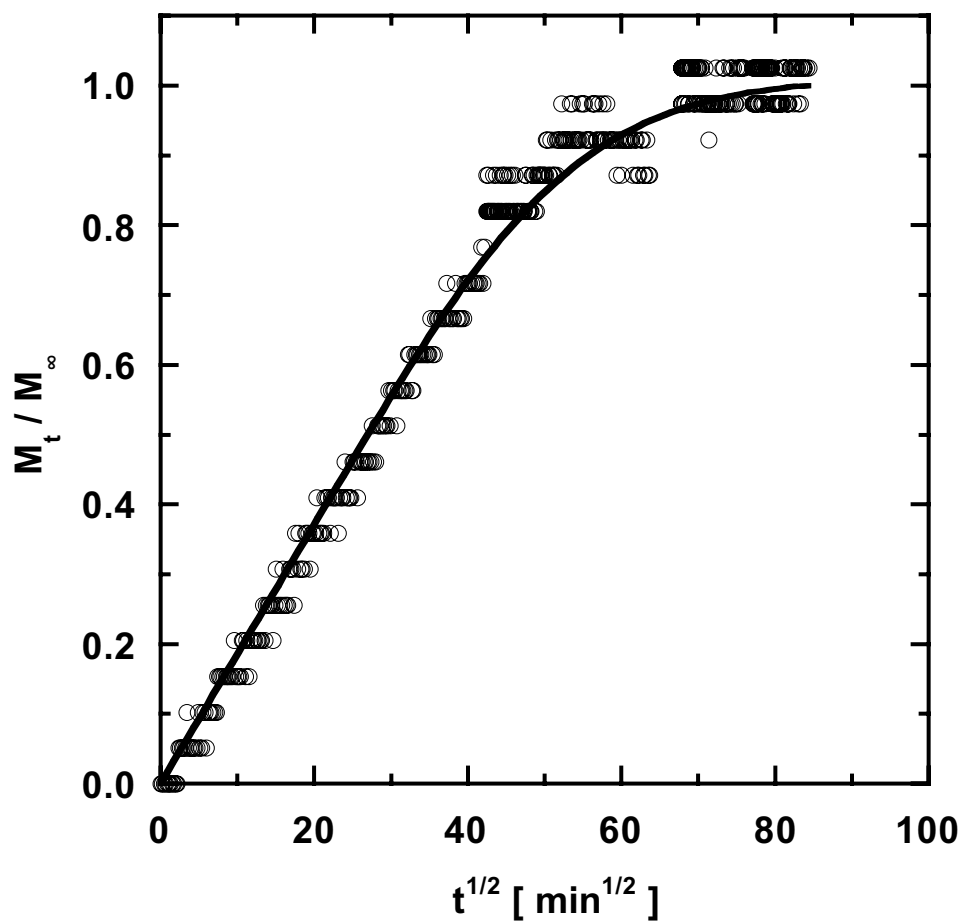


Figure 7.7a Fickian sorption kinetics of *i*-butane in BPET at 35°C. $p_i = 0$ cmHg, $p_f = 31.1$ cmHg, $M_\infty = 0.16 \pm 0.01$ g/100g, $\bar{D} = 1.0 \pm 0.2 \times 10^{-14}$ cm²/s.

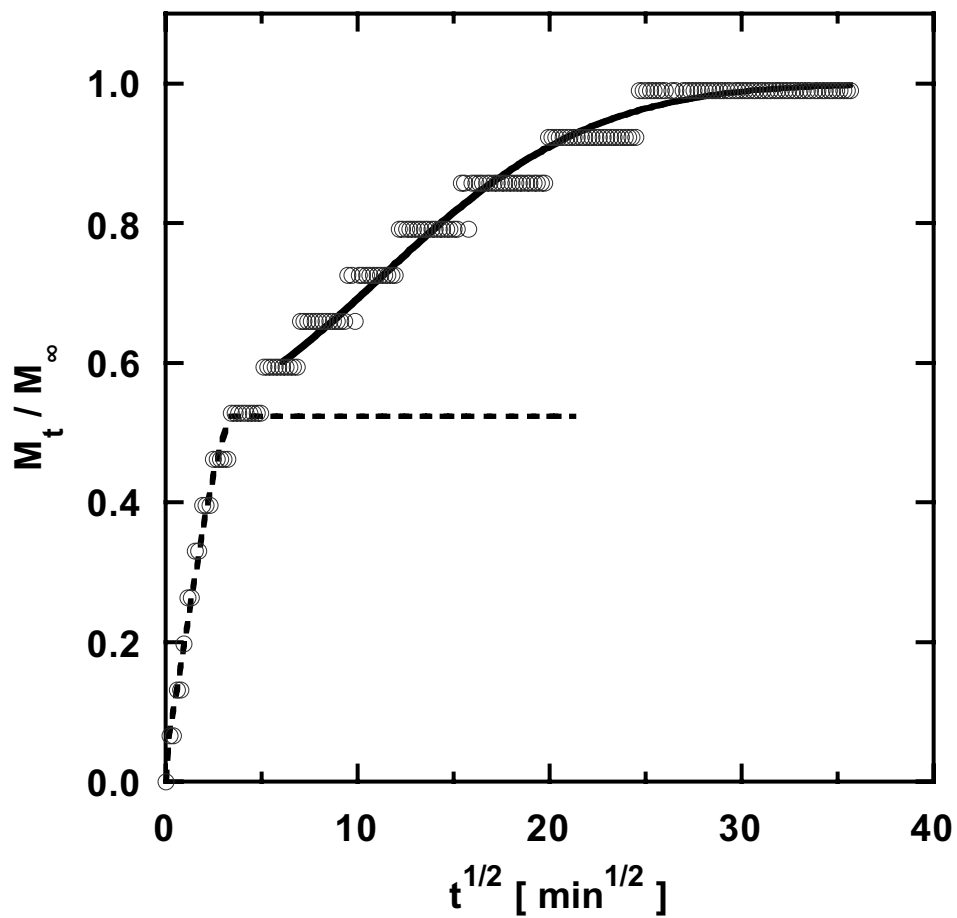


Figure 7.7b Non-Fickian sorption kinetics of methyl acetate in BPET at 35°C.
 $p_i = 2.5$ cmHg, $p_f = 5.0$ cmHg, $M_\infty = 0.32 \pm 0.02$ g/100g,
 $\bar{D} = 6.0 \pm 1.0 \times 10^{-12}$ cm²/s, $\alpha_R = 0.53 \pm 0.06$,
 $\tau_R = 240 \pm 20$ min., $\tau_F = 25 \pm 6$ min., $t_D = 32 \pm 3$ min.

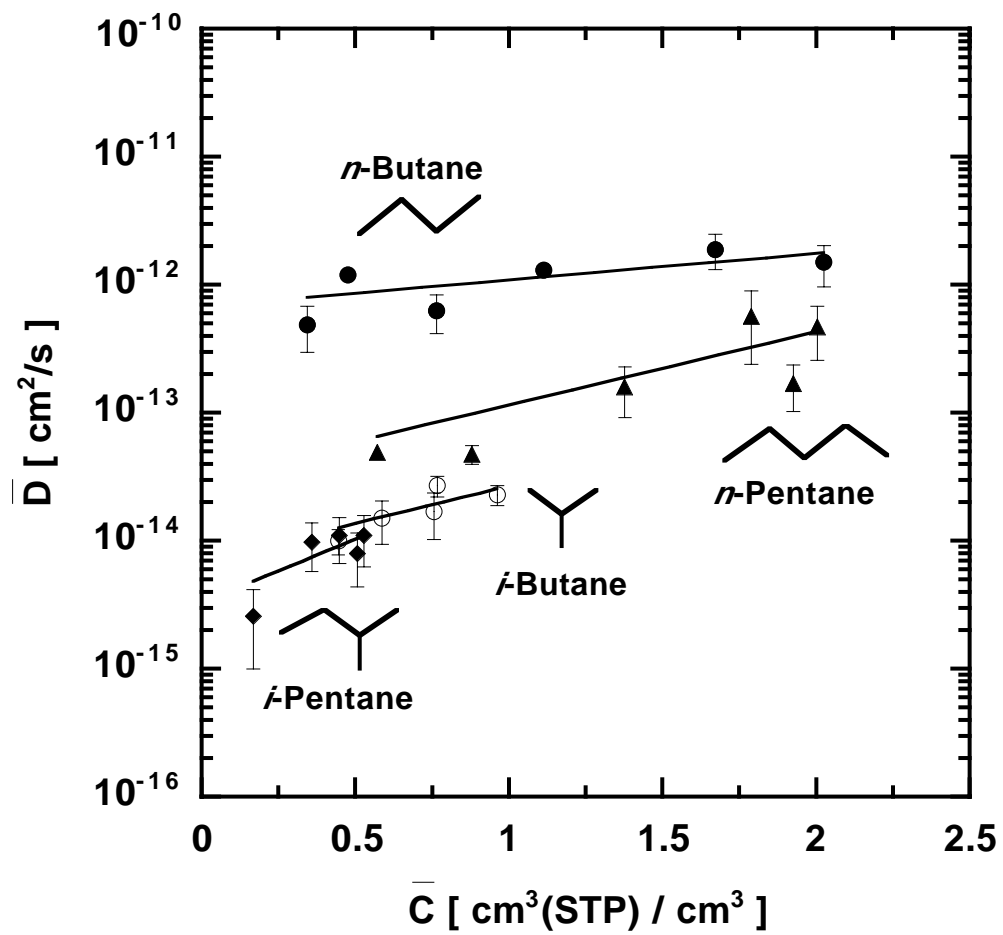


Figure 7.8 Effect of average concentration on apparent diffusion coefficients of linear [8] and branched alkane hydrocarbons in BPET at 35°C.

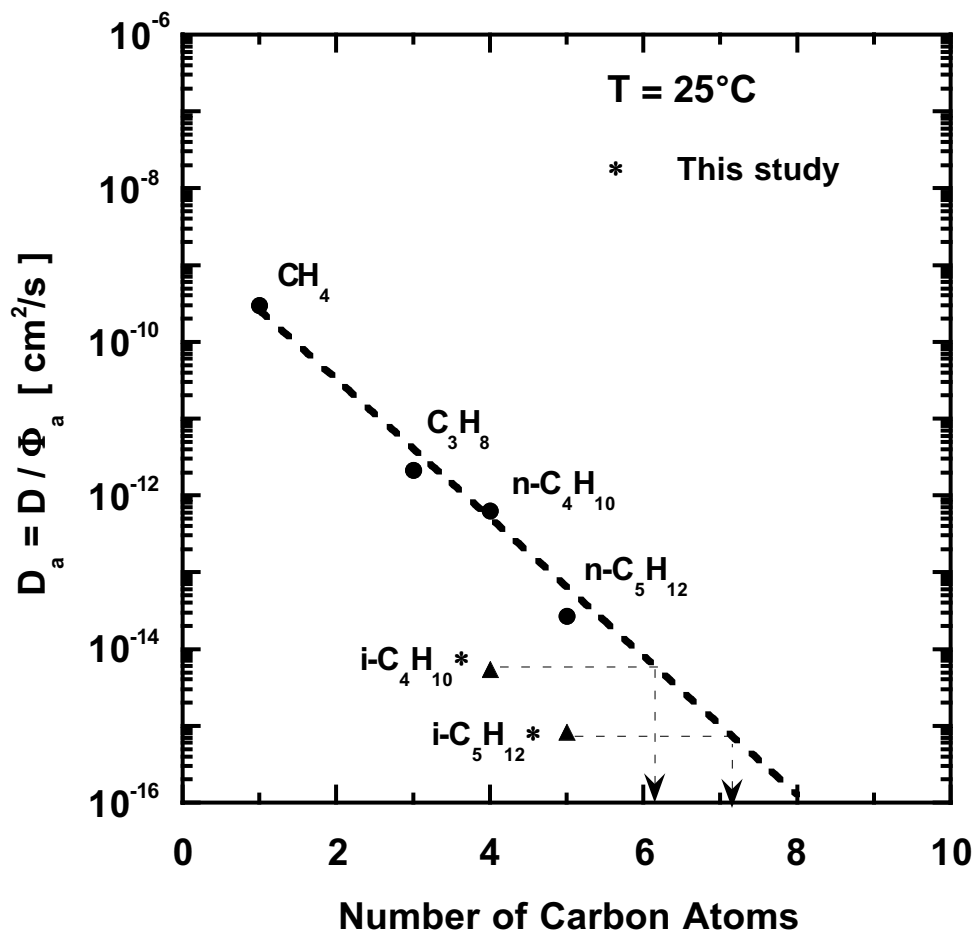


Figure 7.9 Infinite-dilution, estimated amorphous phase diffusion coefficients of linear [8] and branched alkane hydrocarbons in PET as a function of carbon number.

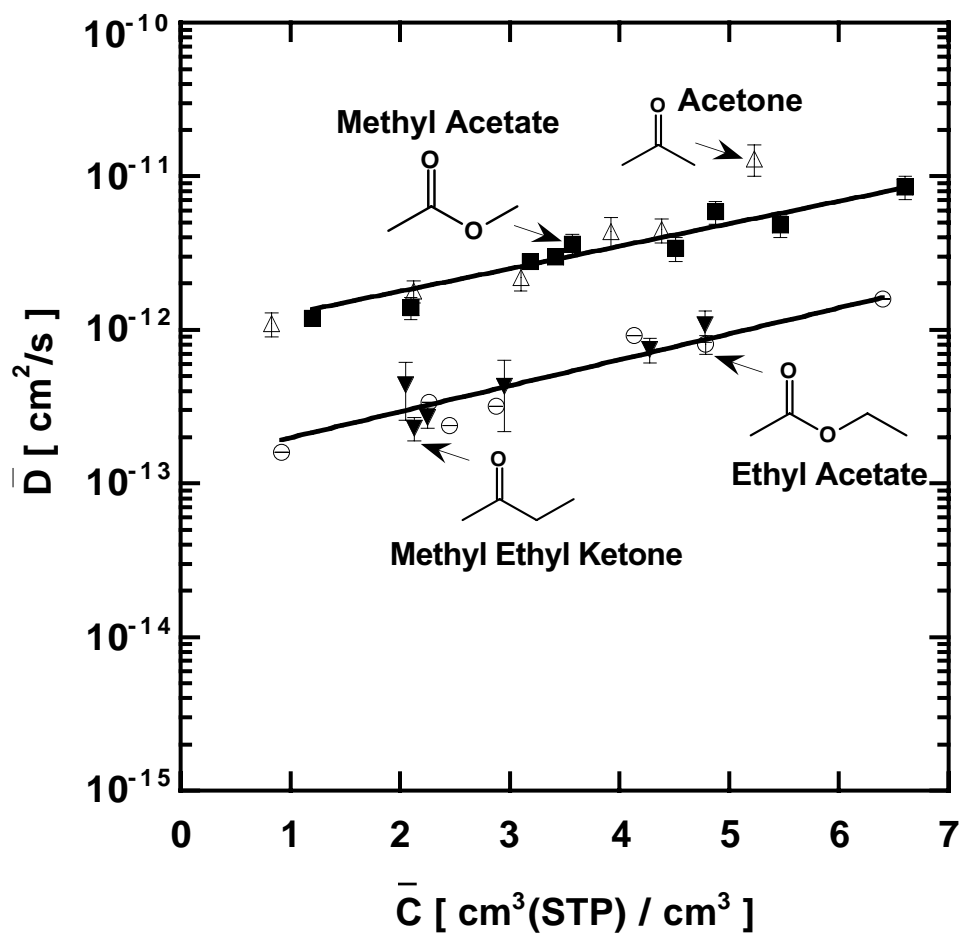


Figure 7.10 Effect of average concentration on apparent diffusion coefficients of methyl acetate (■) and ethyl acetate (○) in BPET at 35°C. The literature data [11] for acetone (△) and MEK (▼) are included for comparison. The critical volumes of acetone and MEK are 209 and 267 cm³/mol, respectively [212].

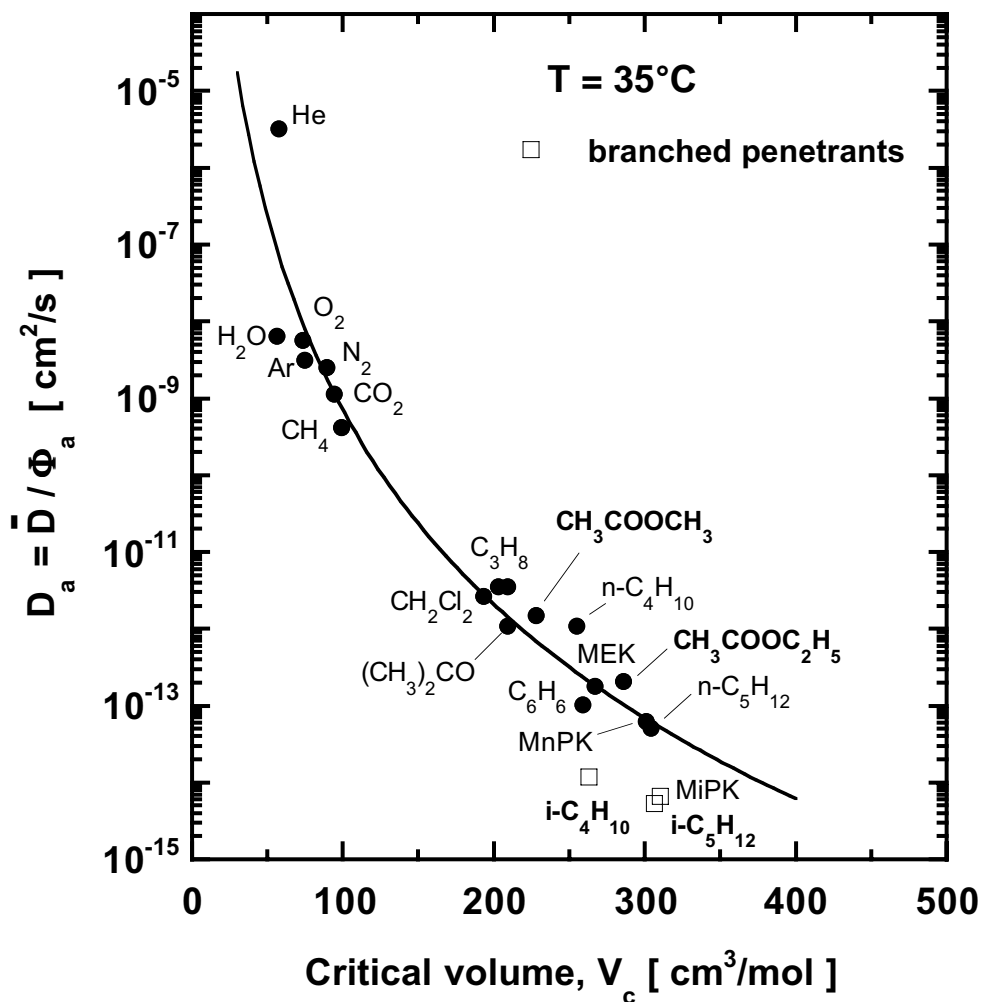


Figure 7.11 Effect of penetrant size on infinite-dilution, estimated amorphous phase diffusion coefficients in PET at 35°C. The penetrants from this chapter are highlighted in bold. The best-fit parameters of Equation 7.11 are $\eta = 8.4 \pm 1.0$, $\tau = 4.4 \pm 1.2 \times 10^7 \text{ (cm}^2\text{/s (cm}^3\text{/mol)}^{8.4}\text{)}$.

CHAPTER 8

Sorption and Diffusion of Toluene and CO₂ in Biaxially Oriented Poly(ethylene terephthalate)

8.1 Summary

This chapter presents results from kinetic gravimetric sorption and dual volume pressure decay sorption studies of toluene and CO₂ in biaxially oriented PET (BPET) films at 35°C and 25°C, respectively. Sorption isotherms of toluene and CO₂ are well described by the dual-mode sorption model. Sorption kinetics of both penetrants are described either by Fickian diffusion or a two-stage model incorporating Fickian diffusion at short times and protracted polymer structural relaxation at long times. Diffusion coefficients of toluene increase with increasing penetrant concentration. Toluene and CO₂ are the largest and smallest penetrant whose sorption and diffusion coefficients were measured in BPET film during this Ph.D. dissertation. Hence, toluene exhibits the highest solubility and one of the lowest diffusion coefficients, whereas CO₂ exhibits the lowest solubility and highest diffusion coefficient among all the penetrants studied. As discussed in the next section, CO₂ was selected in order to compare its sorption and diffusion coefficients in BPET films with available literature values for thicker PET films and understand the extent to which the vapor sorption results from this dissertation are applicable to thicker PET films used in practice.

8.2 Introduction

The primary objective of this research project was to characterize the sorption and transport properties of large organic compounds in PET. The conventional gravimetric sorption techniques are limited to penetrants with high vapor pressures, as discussed in Chapter 4. Therefore, a new experimental technique was developed which extends the

measurement capability of the McBain quartz spring balance and is suitable for penetrants with vapor pressures as low as 10^{-7} mmHg. This technique makes it possible to overcome the limitations of current generation gravimetric sorption techniques and measure the solubility and diffusivity of larger and much more condensable penetrants. To demonstrate the efficacy of this technique, sorption and diffusion coefficients of toluene, the largest and most condensable penetrant selected in this research project, were measured in BPET films.

Sorption and transport properties of glassy polymers, such as PET, depend on the processing history of the sample, as discussed in Chapter 6. Conventional PET films used in practice can be significantly thicker and have a different processing history than the PET films used in this study. To provide a basis for understanding the extent to which the vapor sorption and transport results from this dissertation are applicable to conventional PET films, it is necessary to compare sorption and transport properties of a light gas, such as CO₂, in the thin BPET films with extensive literature data available for thicker films. Therefore, CO₂ permeation experiments were attempted using steady-state permeation equipment (at high upstream pressures (up to 5 atm) and with the downstream at vacuum condition). All samples were masked on both sides along the perimeter using aluminum tape. Also, extreme care was taken while evacuating the permeation cell; the downstream was evacuated first by slowly opening the vacuum valve and a similar procedure was later repeated for the upstream side of the sample. However, several attempts to perform these experiments failed, possibly due to the presence of pinholes in the BPET films (presumably resulting from high orientation). The BPET films were also sent to Ms. Yu

(Ivy) Huang (a member of Dr. Donald Paul's research group), who has considerable experience with permeation measurements of ultra-thin films. She tested several samples after ensuring that they were properly masked and completely flat inside the permeation cell. None of her attempts resulted in successful permeation measurements. The measured flux was too high, suggesting the presence of pinholes in the films. Therefore, CO₂ sorption and diffusion coefficients were determined in separate experiments, and steady state CO₂ flux was not measured directly. The dual volume pressure decay technique (described in Chapter 3) was used to obtain CO₂ solubility coefficients at high pressures, and gravimetric sorption experiments were performed to obtain CO₂ diffusion coefficients at low pressures.

8.3 Experimental

8.3.1 Materials

Biaxially oriented PET films having a uniform nominal thickness of 0.9 μm were purchased from Goodfellow Co. (Berwyn, PA) and used as received. The complete details of sample characterization techniques and corresponding results and discussion have been presented in Chapter 3. High-performance liquid chromatographic (HPLC) grade toluene (99.9% purity) was purchased from Sigma-Aldrich Corp. (St. Louis, MO). It was subjected to several freeze-thaw cycles to remove dissolved gases before use. Alphagaz grade CO₂ gas was purchased from Air Liquide (Houston, TX) and used as received.

8.3.2 Gravimetric Sorption

Integral kinetic gravimetric sorption experiments were performed using the new technique with He carrier gas (described in Chapter 4) for toluene and the traditional McBain spring balance technique (described in Chapter 3) for CO₂. The quartz spring was supplied by Ruska Industries (Houston, TX) and had spring constant of 3.03 mm/mg.

8.3.3 Dual Volume Pressure Decay Sorption

CO₂ sorption experiments were performed at 25°C and pressures in the range of 2 to 11 atm using the dual volume pressure decay sorption technique, as described in Chapter 3.

8.4 Results and Discussion

8.4.1 Equilibrium Sorption and Uptake Kinetics of Toluene in PET

Integral kinetic gravimetric sorption experiments were used to obtain a sorption isotherm of toluene in BPET at 35°C, and this result is presented in Figure 8.1. The isotherm is well described by the dual-mode sorption model [18]:

$$C = k_D p + C_H' \left(\frac{bp}{1 + bp} \right) \quad (8.1)$$

where k_D is the Henry's Law coefficient, C_H' is the Langmuir capacity parameter, and b is the Langmuir affinity parameter. The curve in Figure 8.1 represents a least-squares fit of the experimental sorption data to Equation 8.1. The dual-mode sorption parameters of toluene are reported in Table 8.1. Based on the estimated liquid density of toluene at

35°C [212], the C_H'/ρ^* value for toluene is 0.016 ± 0.005 , which is similar to the C_H'/ρ^* values for the linear alkane hydrocarbons (0.010 – 0.013), ketones (0.009 – 0.014), and esters (0.010 – 0.013) reported earlier in this dissertation (*cf.* Chapters 5, 6, and 7).

Figure 8.2 presents the solubility of toluene along with other literature data for PET on the solubility correlation plot from Chapter 7. In general, for the vapor sorption data in Figure 8.2, infinite-dilution solubility values were obtained by extrapolating the reported solubility values to zero concentration. However, the data for ketones and esters from this dissertation were reported at an activity of 0.1 because of the scatter in the data at low activity (*cf.* Chapters 6 and 7). The solubility coefficient of toluene is also reported at the same activity, and it is in good agreement with the model.

Figures 8.3(a,b) present results from two representative kinetic sorption experiments of toluene in BPET at 35°C. In both cases, the fractional mass uptake M_t/M_∞ increases linearly with $t^{1/2}$ for short times and this behavior is characteristic of sorption kinetics controlled by Fickian diffusion. However, at longer times, the fractional mass uptake may exhibit a protracted, asymptotic approach towards equilibrium, as seen in Figure 8.3b. As discussed previously for alkanes, ketones, and esters, this behavior is ascribed to mass uptake kinetics limited by polymer swelling and structural rearrangement to accommodate the penetrant rather than Fickian diffusion. The sorption kinetics are often described using the following empirical model [8]:

$$\frac{M_t}{M_\infty} = 1 - (1 - \alpha_R) \left\{ \frac{8}{\pi^2} \sum_{n=0}^{\infty} \frac{1}{(2n+1)^2} \exp\left(\frac{-\bar{D}(2n+1)^2 \pi^2 t}{l^2}\right) \right\} + \alpha_R \times \exp\left(\frac{-(t-t_D)}{\tau_R}\right) \times H(t_D) \quad (8.2)$$

where \bar{D} is the average diffusion coefficient, l is polymer film thickness, α_R is the fraction of weight uptake occurring during the protracted, non-Fickian approach to equilibrium, τ_R is the time constant associated with the long time drift in mass uptake, t_D is a delay factor accounting for a delay in the beginning of structural relaxation, and $H(t_D)$ is the Heaviside unit step function [253].

The curves in Figure 8.3(a,b) represent least-squares fits of Equation 8.2 to the experimental data for sorption of toluene in BPET at 35°C following the procedure described in Chapter 5 [8]. In Figure 8.3b, the dotted curve indicates the fraction of mass uptake controlled by Fickian diffusion, whereas the solid curve indicates the fraction controlled by polymer chain relaxation. The relaxation time constant for toluene in BPET (775 min.) is somewhat higher than the available literature value for benzene in PET (413 min.) at 60°C and similar activity [225]. Average diffusion coefficients were estimated using a procedure described previously [8]. In this study, distinct plateaus were observed at intermediate times during the mass uptake profiles of toluene, and these plateaus served as a clear demarcation of the transition from Fickian diffusion to polymer structural relaxation. Hence, the value of fractional mass uptake at the plateau can be set equal to $(1-\alpha_R)$.

Figure 8.4 presents the diffusion coefficients of toluene in BPET as a function of average penetrant concentration. The average penetrant concentration was defined as follows:

$$\bar{C} = \frac{C_i + C_f}{2} \quad (8.3)$$

where C_i and C_f are the penetrant concentrations at the beginning and end of the sorption experiment, respectively. The logarithm of diffusion coefficient increases approximately linearly with penetrant concentration, consistent with earlier studies with alkane hydrocarbons, ketones, and esters in BPET (*cf.* Chapters 5-7). The following empirical model was used [8]:

$$\bar{D} = D_{\infty} \exp(\omega \bar{C}) \quad (8.4)$$

where D_{∞} is the infinite-dilution diffusion coefficient and the slope, ω , characterizes the dependence of \bar{D} on \bar{C} . D_{∞} and ω values for toluene are $3.0 \pm 0.5 \times 10^{-14} \text{ cm}^2/\text{s}$ and 0.69 ± 0.09 , respectively.

Figure 8.5 presents the infinite dilution, estimated amorphous phase diffusion coefficient of toluene at 35°C on the diffusivity correlation plot from Chapter 7. According to this empirical model, diffusion coefficients decrease according to a power law relation with increasing penetrant critical volume, and toluene diffusion coefficient is in excellent agreement with the model.

8.4.2 Equilibrium Sorption and Uptake Kinetics of CO₂ in PET

Dual volume pressure decay sorption experiments were performed to obtain a sorption isotherm of CO₂ in BPET at 25°C and for pressures in the range of 2-11 atm. The sorption isotherm, presented in Figure 8.6, is concave to the pressure axis and can be described by the dual-mode sorption model, as described in the previous section (*cf.* Equation 8.1). The dual-mode sorption model parameters for CO₂ are recorded in Table

8.1. Based on the saturated liquid density of CO₂ (0.85 g/cc) [16], the C_H'/ρ^* value for CO₂ is 0.013 ± 0.001 , which is in good agreement with the corresponding values for the alkane hydrocarbons, ketones, and esters reported earlier in this dissertation. This value is also in reasonable agreement with the C_H'/ρ^* values for CO₂ reported in the literature by Koros and Paul (0.018) [16], Michaels *et al.* (0.012) [10], Veith *et al.* (0.013) [229], and Fenelon (0.014) [269].

The CO₂ sorption isotherm from this study is compared with literature data in Figures 8.7 and 8.8. In Figure 8.7, the comparison is made on a semicrystalline basis (*i.e.*, without any corrections for the effect of crystallinity on CO₂ concentration in the polymer). There are significant differences between the solubility values obtained from various literature sources. Some of the solubility differences could be due to differences in the crystallinities of the PET samples. The effects of morphology, orientation, and crystallinity on the sorption and transport properties of PET are complex, as noted in Chapter 6, and these effects could result in the observed differences in CO₂ solubility values.

In Figure 8.8, the concentrations are adjusted to an amorphous basis using the following relation, which has been used previously for CO₂ in PET [10]:

$$C_a = \frac{C}{\phi_a} \quad (8.5)$$

where C is CO₂ concentration and ϕ_a is amorphous phase volume fraction. For the literature data reported in Figure 8.8, the values of ϕ_c were calculated (and in some cases,

the reported crystallinity values were adjusted) using the reported density values and the following relation:

$$\phi_c = \left(\frac{\rho - \rho_a}{\rho_c - \rho_a} \right) \quad (8.6)$$

where ϕ_c is crystalline phase volume fraction and ρ , ρ_c and ρ_a are densities of the semicrystalline polymer sample, wholly crystalline PET, and wholly amorphous PET, respectively. We used the constant and widely reported amorphous and crystalline density values of 1.335 g/cm³ and 1.515 g/cm³, respectively [8,12,76,195].

As can be seen in Figure 8.8, on an amorphous basis, the data from this study are in good agreement with solubility data reported by Koros and Paul [16] for a 51 μm thick, biaxially oriented, semicrystalline PET film and with those reported by Zhang *et al.* [270] for an 0.5 μm thick, spin-cast, semicrystalline PET film. However, there are significant differences between CO₂ solubility coefficients obtained from various literature sources [10,16,229,234]. This result again highlights the complex effect of morphology, orientation, and crystallinity on the sorption and transport properties of PET, as mentioned above. Such effects have been and continue to be the subject of active research. Several literature studies have reported that sample processing history affects morphology of both the crystalline and non-crystalline phases and that these morphological differences can manifest themselves in the sorption and transport properties of the sample (*cf.* Chapter 6).

Integral kinetic gravimetric sorption experiments of CO₂ in BPET were performed at 25°C and for pressures ranging from 0 to approximately 76 cmHg. The equilibrium

solubility data from these experiments are also presented in Figures 8.7 and 8.8. Average diffusion coefficients were estimated using the procedure described previously [8]. The concentration (or pressure) dependence of diffusion coefficients was described by using the so-called dual mobility model, as discussed below.

Dual Mobility Model

This model of the concentration dependence of diffusivity in glassy polymers is based on the notion that the two populations of penetrant molecules (*i.e.*, Henry's Law and Langmuir) in the dual-mode model have different mobilities [271]. In this so-called dual mobility model, one-dimensional penetrant transport is described by the following form of Fick's law [225]:

$$N = -D_H \frac{dC_H}{dx} - D_D \frac{dC_D}{dx} \quad (8.7)$$

where N is penetrant flux, C_D and D_D are the penetrant concentration and diffusion coefficient in the dense, equilibrium polymer matrix (Henry's law mode), and C_H and D_H are the penetrant concentration and diffusion coefficient in the non-equilibrium excess volume (Langmuir mode). Within the context of the dual mobility model, the average diffusion coefficient determined in integral kinetic gravimetric sorption experiments is [225]:

$$\bar{D} = D_D \left[\frac{1 + FK / (1 + bp)}{1 + K / (1 + bp)} \right] \quad (8.8)$$

where p is penetrant pressure at the end of integral kinetic gravimetric sorption experiments, $K = C_H' b / k_D$ and $F = D_H / D_D$. This model has been used to describe pressure

dependence of diffusion of CO₂, acetone, and benzene in PET [27,225,271]. In the case of acetone, D_D and D_H were taken to be concentration dependent [27]. In this study, D_H and D_D were assumed to be independent of concentration. Figure 8.9 presents the average diffusion coefficients of CO₂ as a function of CO₂ pressure. Due to experimental difficulties, such as fast kinetics and low CO₂ uptake at low pressures, diffusion data could be obtained only in a narrow pressure range. From a non-linear regression analysis method, value of D_D for CO₂ in BPET was estimated to be $3.4 \pm 1.6 \times 10^{-10}$ and $F \ll 1$. The curve-fit in Figure 8.9 is based on Equation 8.8 (in the limit $F \ll 1$) and the value of D_D noted above.

Table 8.2 presents a comparison of D_D value from this study with available literature values [234,271,272]. The D_D values were adjusted to an amorphous basis using the following two-phase model [20]:

$$D_{D,a} = \frac{D_D}{\phi_a} \quad (8.9)$$

where D_{D,a} is amorphous phase diffusion coefficient. The estimated amorphous phase D_D value from this study is approximately a factor of 3 to 8 times lower than the literature values. The literature data were reported for much thicker films and the effects of morphology, crystallinity, and orientation (*i.e.*, processing history) mentioned above (in connection with sorption) are likely to be more complex for diffusion. For example, orientation and aspect ratios of impermeable crystalline phases affect penetrant flux [4]. Thus, penetrant diffusion coefficients are affected by not only the amount of crystallinity, but also by the larger scale geometry and spatial distribution of these regions.

Additionally, the noncrystalline regions of BPET are much more oriented than those in the unoriented PET samples studied by Toi *et al.* and Broly *et al.*, and previous studies (*cf.* Section 6.3.2 in Chapter 6) suggest that orientation in PET leads to more efficient chain packing, thereby reducing the overall free volume and, in turn, diffusion coefficients. Also, the diffusion coefficients in this study were obtained from a non-steady state, kinetic gravimetric sorption technique, while the literature values were estimated from steady state permeability techniques, and the experimental technique used can have an effect on the observed diffusion coefficient values [273]. For example, Barrer *et al.* reported the diffusion coefficient of argon in poly(tetraethyleneglycoldimethacrylate) at 60°C from desorption kinetics and steady state permeation and sorption measurement as 3.2×10^{-9} and 6.3×10^{-9} cm²/s, respectively [273].

CO₂ permeability coefficients can be estimated using the following relation [271]:

$$P = k_D D_D \left[1 + \frac{FK}{(1 + bp_2)} \right] \quad (8.10)$$

where P is CO₂ permeability coefficient, and p₂ is upstream pressure (downstream pressure is assumed to be zero). Using the above equation, at p₂=10 atm, the estimated CO₂ permeability coefficient in BPET is 0.07 Barrer. To compare the CO₂ permeability coefficient in BPET with literature data for various amorphous and semicrystalline PET samples, the permeability values were adjusted to an amorphous basis using the two-phase model [20]:

$$P_a = \frac{P}{\phi_a^2} \quad (8.11)$$

where P_a is amorphous phase permeability. Using the above equation, the P_a value for CO_2 in BPET at 10 atm is 0.18 Barrer.

Table 8.2 presents a comparison of the estimated CO_2 permeability coefficient from this study with literature data [20,54,234,271,272,274]. The estimated amorphous permeability coefficient of CO_2 in BPET from this study is in good agreement with the value reported by McGonigle *et al.* [54] for a 230 μm thick, amorphous PET film. However, the estimated amorphous permeability value from this study is lower than the other literature values reported in Table 8.2; the largest difference can be seen between the permeability value in the BPET film and the value reported by Koros and Paul [271] for a 51 μm thick, biaxially oriented, semicrystalline PET film. As discussed before, sample processing history (*i.e.*, morphology, crystallinity, orientation) influences transport properties of CO_2 in PET. As can be seen in Table 8.2, most of the available CO_2 permeability values are for unoriented PET films (except for the sample used by Koros and Paul), and orientation has been reported to reduce permeability of small molecules in PET. For example, 4×4 biaxial orientation reduced O_2 permeability in PET by a factor of two [24]. So, while the sample crystallinity differences were accounted for crudely by adjusting the permeability values to an amorphous basis (using Equation 8.11), differences in sample orientation can lead to differences in CO_2 permeability values, and these differences are not accounted for in adjustments to the permeability values. Also, CO_2 permeability typically decreases with increasing upstream pressure

[271], and most of the available literature data (reported in Table 8.2) are for pressures less than 1 atm (*cf.* Table 8.2). For example, Koros and Paul reported a decrease in experimentally determined CO₂ permeability (P_a) at 25°C from 0.81 to 0.62 Barrer as upstream pressure increased from 1 to 10 atm [271]. In this study, based on the dual-mode sorption parameters and Equation 8.10, the estimated CO₂ permeability (with $F \ll 1$) is independent of upstream pressure.

8.5 Conclusions

Sorption isotherms of toluene at 35°C and CO₂ at 25°C in BPET are well described by the dual-mode sorption model. Sorption kinetics of both penetrants are described either by Fickian diffusion or a two-stage model incorporating Fickian diffusion at short times and protracted polymer structural relaxation at long times. Diffusion coefficients of toluene increase with increasing penetrant concentration. There are significant differences between CO₂ solubility and diffusion coefficients in PET obtained from various literature sources. These differences are probably related, in part, to the effects of morphology, orientation, and crystallinity on the sorption and transport properties of PET. Considering such effects, the estimated amorphous phase permeability coefficient of CO₂ in the thin BPET sample is in somewhat good agreement with literature data for much thicker samples.

8.6 Acknowledgment

The author wishes to thank Ms. Yu (Ivy) Huang (University of Texas at Austin, Austin, TX) for attempting CO₂ permeation experiments with the thin BPET films from this study.

Table 8.1 Dual-mode model parameters for toluene at 35°C and CO₂ at 25°C in PET

Penetrant	k_D cm ³ (STP)/cm ³ .cmHg	C_H' cm ³ (STP)/cm ³	b cmHg ⁻¹
Toluene	3.0 ± 0.1	3.4 ± 0.1	18 ± 1.2
CO ₂	0.02 ± 0.001	5.8 ± 0.5	0.005 ± 0.0004

Table 8.2 Comparison of estimated amorphous phase CO₂ permeability (P_a) and Henry's Law mode diffusion coefficients (D_{D,a}) at 25°C in a thin BPET film from this study with literature data for much thicker films

Source	Sample Thickness (μm)	Orientation/ Crystallinity (vol%)	D _{D,a} (10 ⁻⁹ cm ² /s)	P _a (Barrer) ^{a, b}	Upstream Pressure
This study	0.9	Biaxial/39%	0.6 ± 0.3	0.18	10 atm
McGonigle <i>et al.</i> [54]	230	Unoriented/ amorphous	NA	0.14	4 atm
Koros <i>et al.</i> [271]	51	Biaxial/60%	5.0	0.62	10 atm
Toi <i>et al.</i> [272]	50-100	Unoriented/ 37.5%	4.0	0.31	< 1 atm ^c
Michaels <i>et al.</i> [20]	75	Unoriented/ amorphous	NA	0.30	< 0.13 atm ^c
Lewis <i>et al.</i> [274]	204	Unoriented/ amorphous	NA	0.36	< 1 atm ^c
Brolly <i>et al.</i> [234]	35	Unoriented/ amorphous	1.5	0.53	Infinite dilution

^a 1 Barrer = 10⁻¹⁰ cm³(STP).cm/cm².s.cmHg

^b Literature permeability values were determined using constant volume, variable pressure permeation techniques (negligible downstream pressure). In this study, the permeability value was estimated from experimentally determined solubility and diffusion coefficients and by using the dual mobility model.

^c Exact upstream pressure not reported

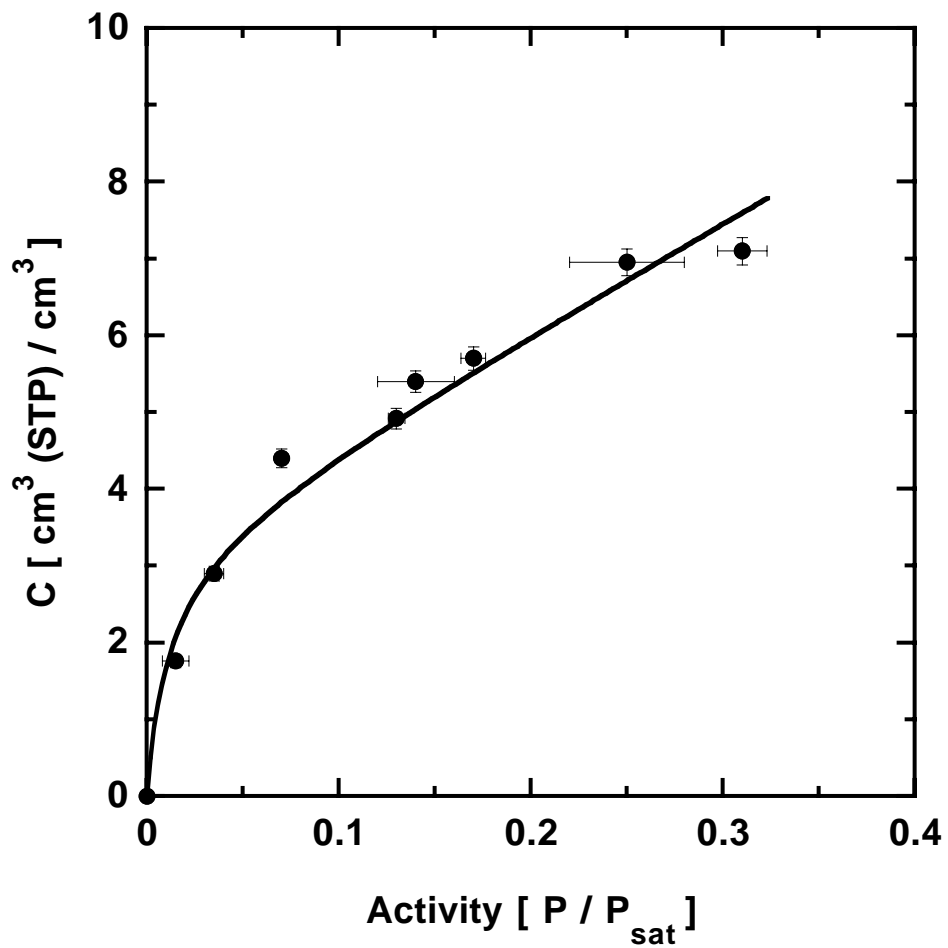


Figure 8.1 Sorption isotherm of toluene in PET at 35°C. The saturation vapor pressure of toluene at 35°C is 4.7 cmHg [204].

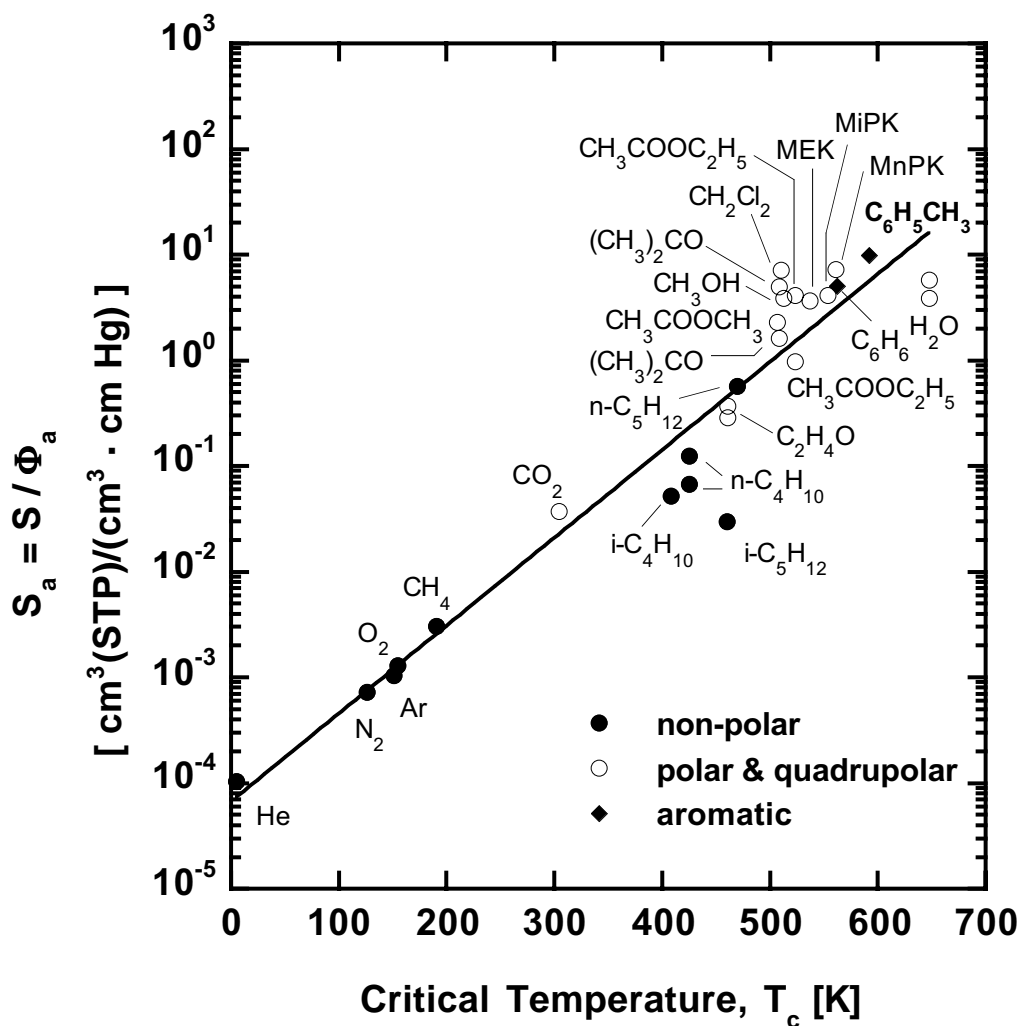


Figure 8.2 Correlation of infinite-dilution, estimated amorphous phase solubility coefficients in PET at 25-45°C with penetrant critical temperature. The data for methyl acetate, ethyl acetate, methyl ethyl ketone (MEK), methyl *n*-propyl ketone (MnPK), methyl *i*-propyl ketone (MiPK), and toluene (highlighted) are reported at an activity of 0.1.

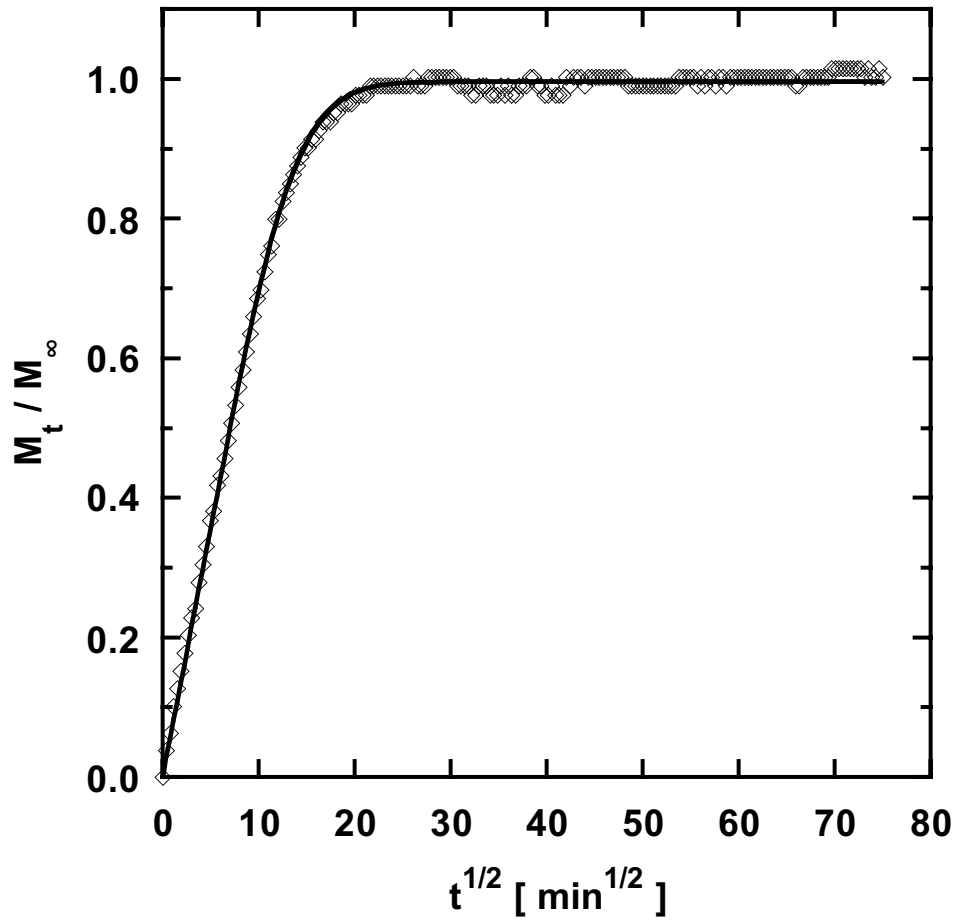


Figure 8.3a Fickian sorption kinetics of toluene in BPET at 35°C.
 $p_i = 0$ cmHg, $p_f = 0.8$ cmHg, $M_\infty = 1.7 \pm 0.02$ g/100g,
 $\bar{D} = 1.3 \pm 0.2 \times 10^{-13}$ cm²/s.
 The saturation vapor pressure of toluene at 35°C is 4.7 cmHg [204].

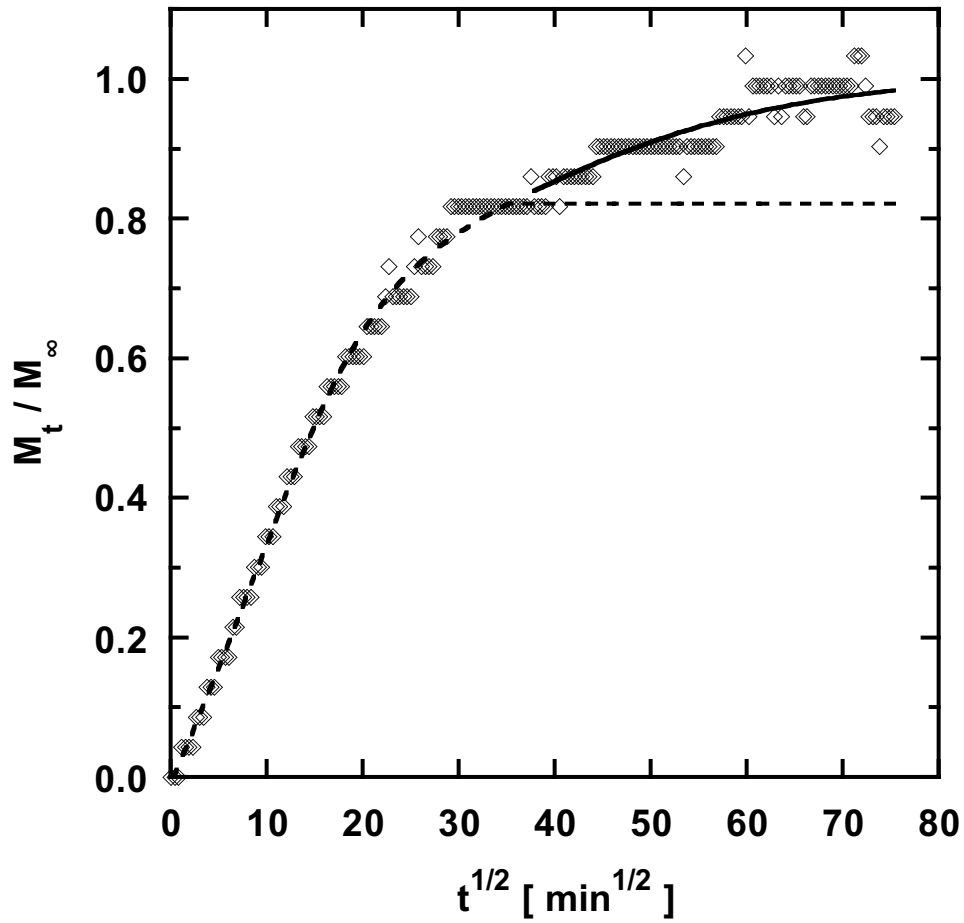


Figure 8.3b Non-Fickian sorption kinetics of toluene in BPET at 35°C.
 $p_i = 0$ cmHg, $p_f = 0.07$ cmHg, $M_\infty = 0.52 \pm 0.04$ g/100g,
 $\bar{D} = 4.8 \pm 0.8 \times 10^{-14}$ cm²/s, $\alpha_R = 0.18 \pm 0.01$, $\tau_R = 775 \pm 33$ min.,
 $t_D = 980 \pm 42$ min.
 The saturation vapor pressure of toluene at 35°C is 4.7 cmHg [204].

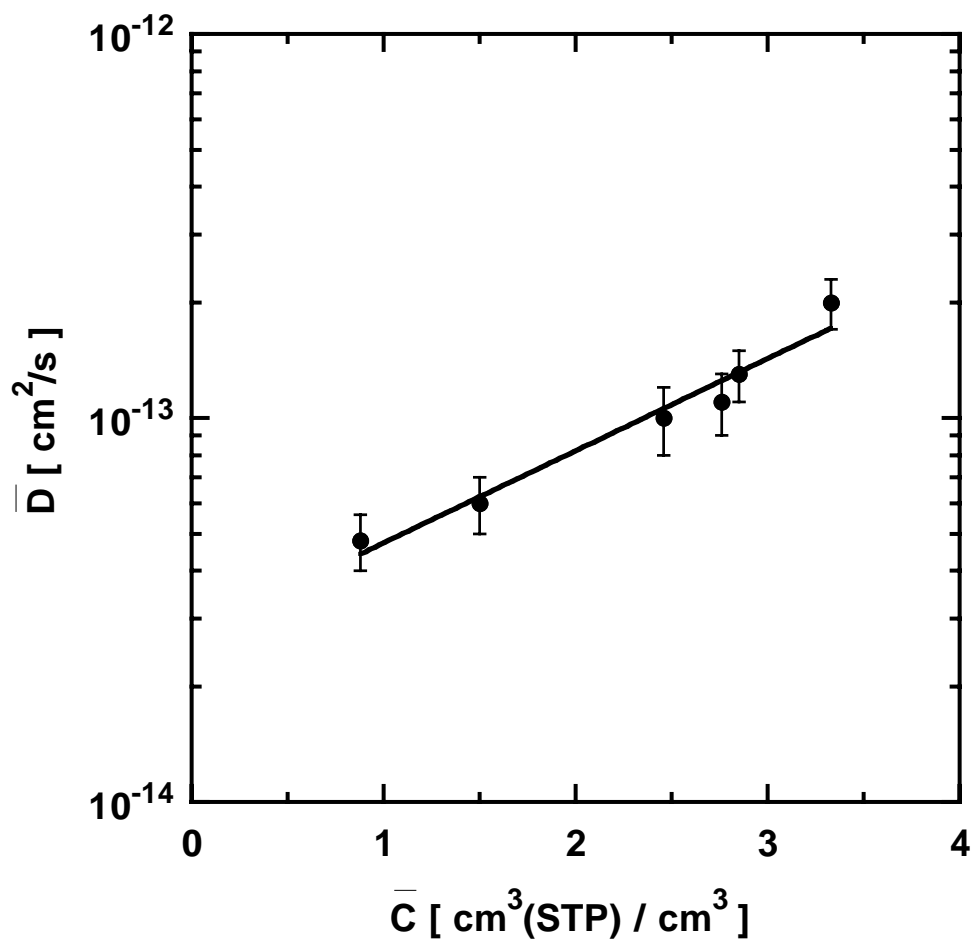


Figure 8.4 Diffusion coefficients of toluene in PET at 35°C as a function of average penetrant concentration.

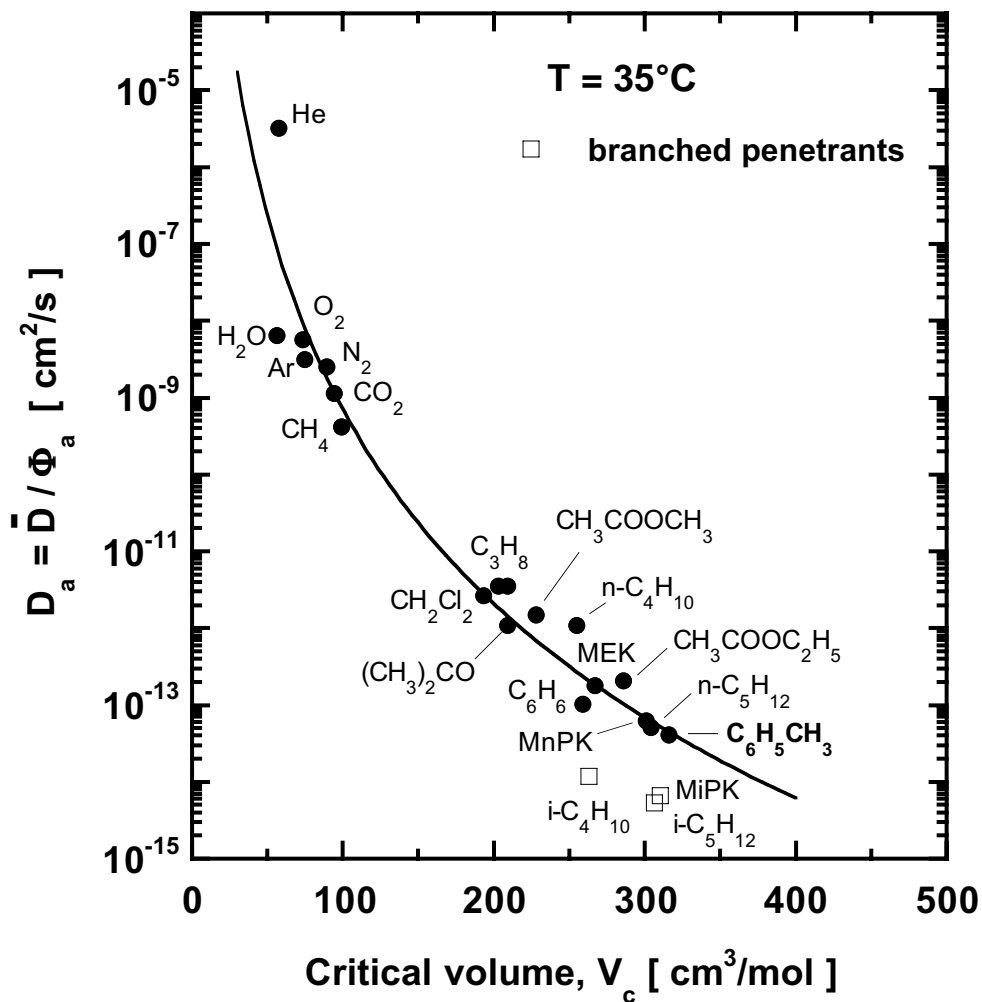


Figure 8.5 Correlation of infinite-dilution, estimated amorphous phase diffusion coefficients in PET with penetrant critical volume. The penetrant from this chapter (toluene) is highlighted in bold.

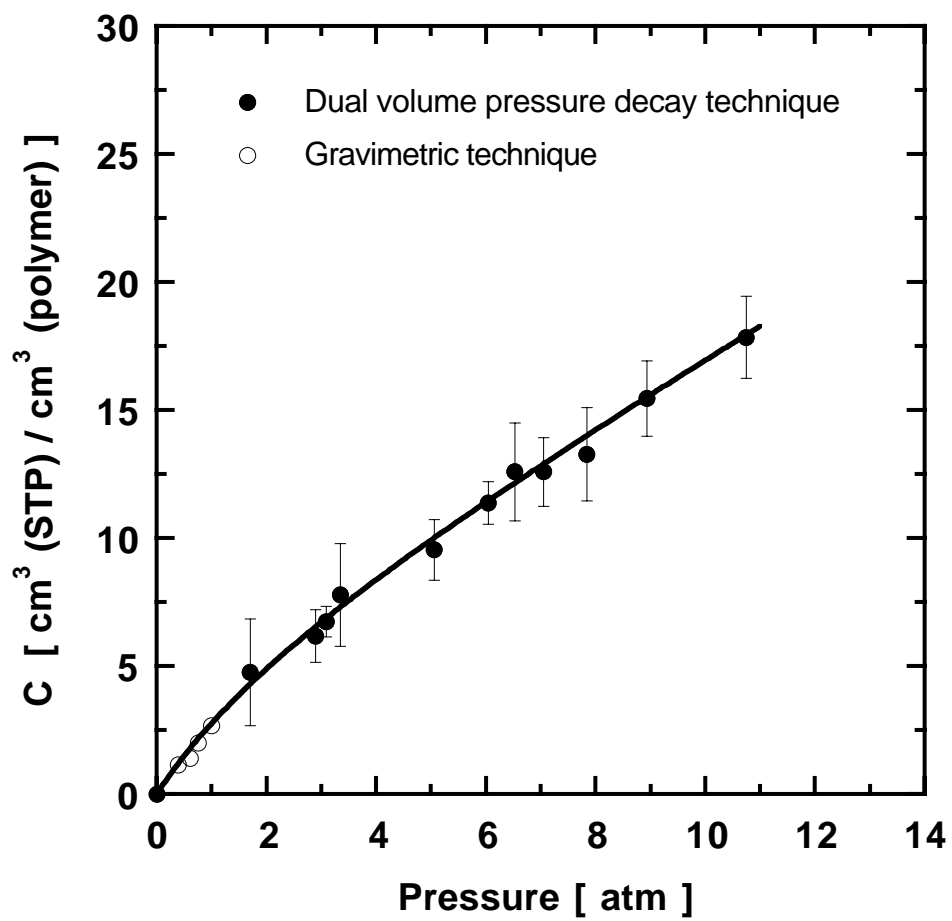


Figure 8.6 Sorption isotherm of CO₂ in BPET at 25°C.

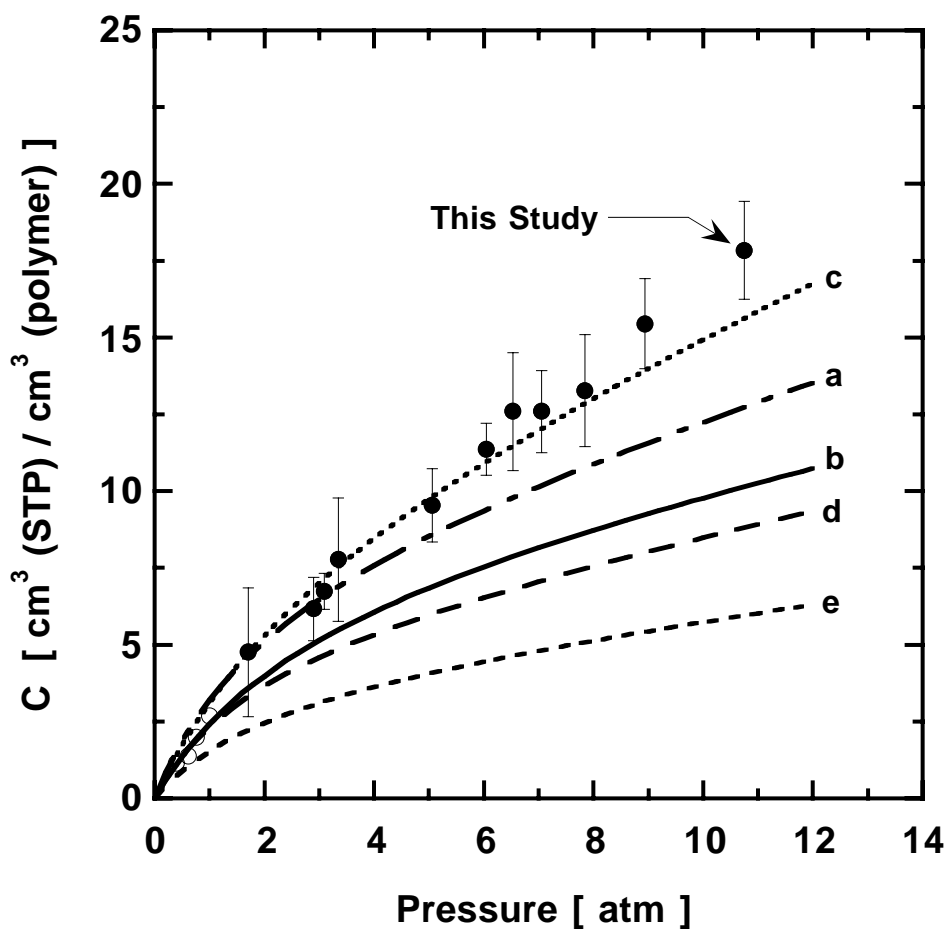


Figure 8.7 Comparison of CO₂ sorption isotherms in PET at 25°C. (●) This study (dual volume pressure decay sorption experiments), (○) This study (gravimetric sorption experiments). a = Zhang *et al.* [270] (46 vol% crystallinity, 0.5 μm thick); b = Koros and Paul [16] (Biaxially oriented, 60 vol% crystallinity, 51 μm thick); c = Brolly *et al.* [234] (Biaxially oriented, 10 vol% crystallinity); d = Vieth *et al.* [229] (Biaxially oriented, 29 vol% crystallinity, 25 μm thick); e = Michaels *et al.* [10] (28 vol% crystallinity, 127 μm thick).

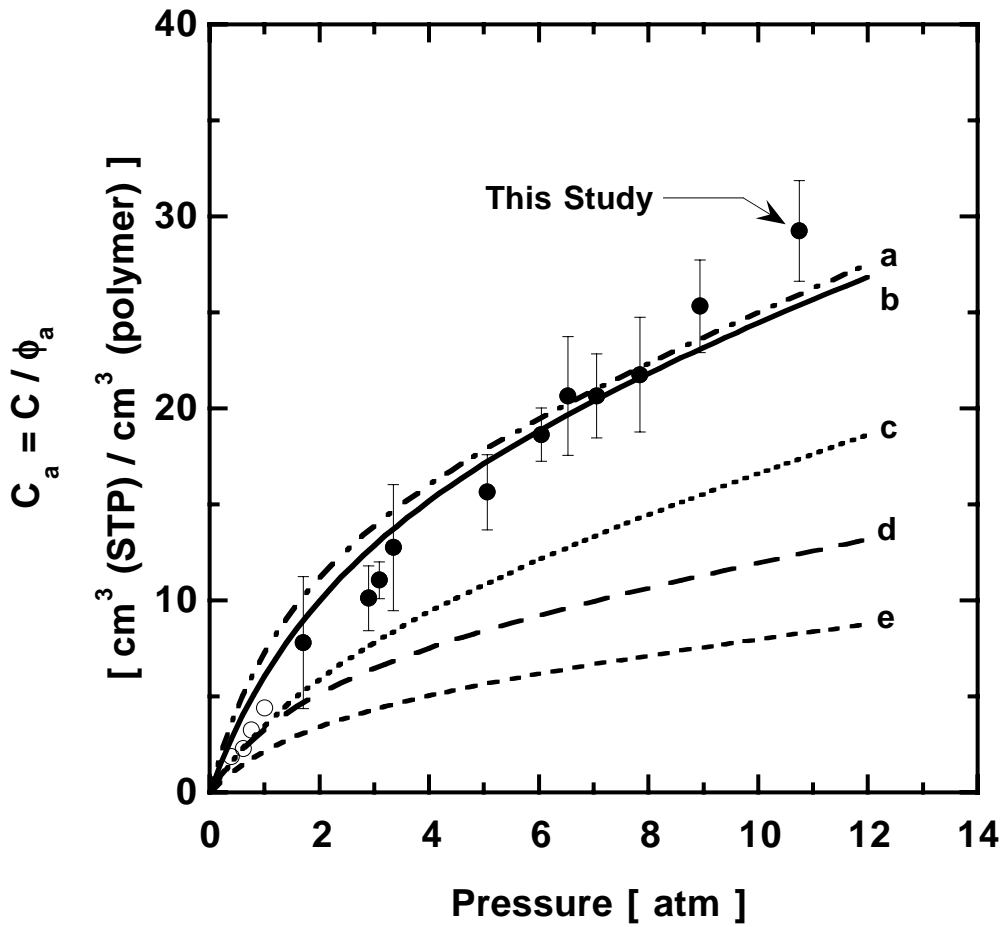


Figure 8.8 Comparison of CO₂ sorption isotherms on an amorphous basis in PET at 25°C. (●) This study (dual volume pressure decay sorption experiments), (○) This study (gravimetric sorption experiments). a = Zhang *et al.* [270] (46 vol% crystallinity, 0.5 μm thick); b = Koros and Paul [16] (Biaxially oriented, 60 vol% crystallinity, 51 μm thick); c = Brolly *et al.* [234] (Biaxially oriented, 10 vol% crystallinity); d = Vieth *et al.* [229] (Biaxially oriented, 29 vol% crystallinity, 25 μm thick); e = Michaels *et al.* [10] (28 vol% crystallinity, 127 μm thick).

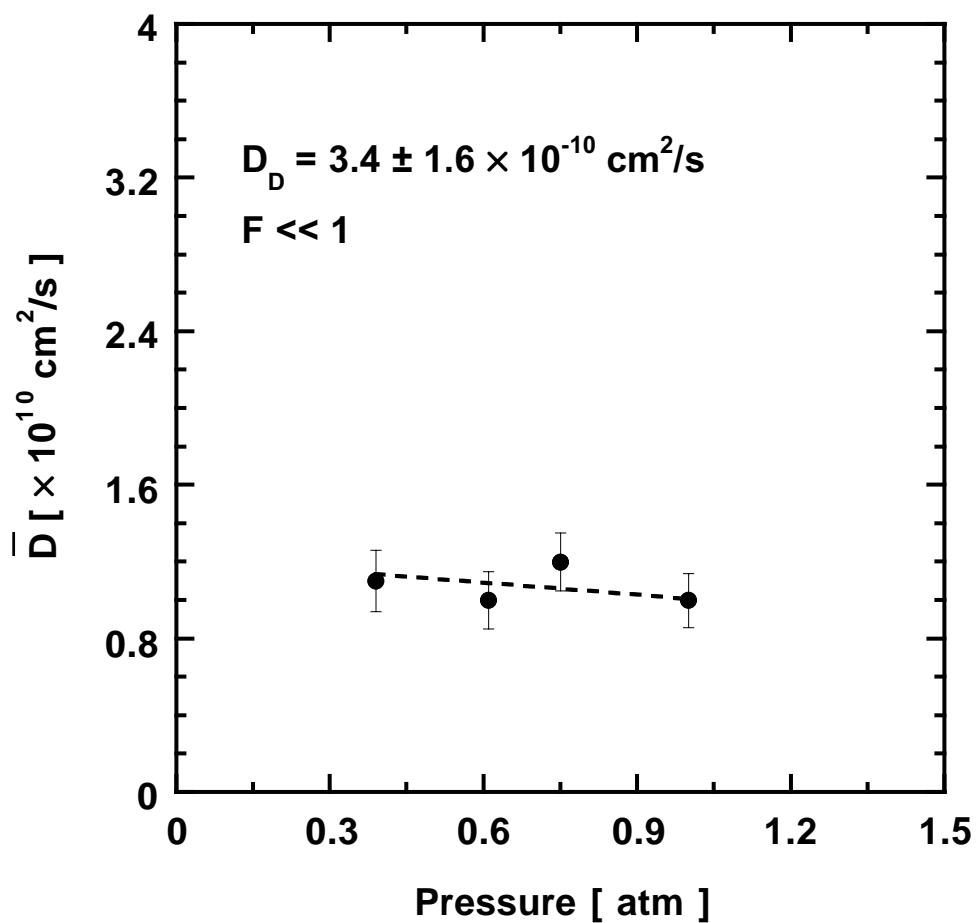


Figure 8.9 Average diffusion coefficients of CO₂ in BPET at 25°C as a function of CO₂ pressure at the end of integral kinetic gravimetric sorption experiments. The beginning pressure for each of these data points was 0 atm. The curve-fit is based on the dual mobility model (Equation 8.8).

CHAPTER 9

Conclusions and Recommendations

9.1 Summary of Conclusions

Equilibrium sorption and uptake kinetics of alkane hydrocarbons (*n*-butane, *i*-butane, *n*-pentane, and *i*-pentane), ketones (acetone, MEK, MnPK, and MiPK), esters (methyl acetate and ethyl acetate), and toluene in thin, biaxially oriented, semicrystalline PET (BPET) films are reported at 35°C and for pressures ranging from 0 to approximately 76 cmHg. Sorption isotherms for all penetrants, with the exception of *i*-pentane, are well described by the dual-mode sorption model. The sorption isotherm for *i*-pentane is described by the dual-mode model at low activity (or relative pressure) and the Flory-Huggins model at high activity. Sorption kinetics of all penetrants are described either by Fickian diffusion or a two-stage model incorporating Fickian diffusion at short times and protracted polymer structural relaxation at long times. Diffusion coefficient for each penetrant increases with increasing penetrant concentration.

To a first approximation, solubility and diffusion coefficients in PET correlate well with penetrant critical temperature and critical volume, respectively (*cf.* Figures 8.2 and 8.5). The logarithm of infinite dilution, estimated amorphous phase solubility coefficient increases linearly with critical temperature, a measure of penetrant condensability. Infinite dilution, estimated amorphous phase diffusion coefficients decrease according to a power law relation with increasing critical volume, a measure of penetrant size.

However, there are a few exceptions. Strictly speaking, the solubility correlation is valid only for equilibrium materials, such as rubbery polymers. Hence, it does not account for sorption effects in the non-equilibrium excess volume of glassy polymers,

such as PET, that may involve different mechanisms, such as hole-filling, than are present in equilibrium materials. For example, the solubility difference between *n*-pentane and *i*-pentane is 10 times larger in glassy PET than rubbery LDPE. The solubility difference between these two penetrants in the equilibrium regions of *both* PET and LDPE appears to be similar. However, PET has an additional mode of sorption, namely the non-equilibrium excess volume. Based on an analysis using the commonly used dual-mode sorption model, linear *n*-pentane appears to fit into (and hence, access) the non-equilibrium excess volume of PET much more easily than branched *i*-pentane. In fact, based on some preliminary experiments, neopentane does not show measurable uptake in PET. The magnitude of such shape effects in glassy polymers cannot be predicted by the solubility correlation.

Also, the solubility correlation is strictly valid only for penetrants that do not have any specific interactions with the polymer matrix. Because PET is polar, the solubility of polar penetrants (*e.g.*, ketones, esters, aldehydes) can be enhanced due to specific, favorable interactions. For example, as discussed in Chapter 6, solubility of polar ketones in PET is approximately two times higher than that of non-polar alkanes having the same number of carbon atoms and a similar carbon skeleton. This effect can also be seen in the solubility correlation plot (*cf.* Figure 8.2). The data for most of the polar penetrants reported in this dissertation show a positive deviation from the correlation line.

The diffusivity correlation is empirical, and is proposed based on analogy with correlations of diffusion coefficients of small molecules in liquids [9]. Critical volume was used as a measure of penetrant size because it is commonly available for a wide

variety of penetrants. However, it cannot capture the effect of penetrant shape on diffusion coefficients, and so the correlation is expected to be less accurate for asymmetric penetrants. As shown in Figure 8.5 (Chapter 8), diffusion coefficients of branched *i*-butane, *i*-pentane, and methyl *i*-propyl ketone are an order of magnitude lower than the predicted values based on a correlation curve drawn using mainly linear and more or less spherical penetrants.

Among the alkane hydrocarbons studied, chain branching is more efficient than chain length in lowering hydrocarbon diffusion coefficients in PET. This effect is demonstrated in Figure 7.9 (Chapter 7). Similar size and shape effects on hydrocarbon diffusion coefficients have been observed in other rubbery (*e.g.*, polyisobutylene, ethyl cellulose, natural rubber) and glassy polymers (*e.g.*, polycarbonate), as reported in Chapter 7.

The interplay of penetrant size and polarity on diffusion coefficients in PET is discussed in Chapter 7. Because PET is polar, diffusion of polar penetrants (*e.g.*, ketones, esters) can be retarded, presumably by specific penetrant-polymer interactions. Smaller, but more polar, ketones have very similar diffusion coefficients to larger, but much less polar, esters. Thus, penetrant diffusion in PET, which is primarily dependent on penetrant size and shape, can also be influenced by polarity effects. Similar effects of penetrant polarity on diffusion coefficients have been previously reported in polysulfones [130]. However, non-polar polymers, such as high-density polyethylene, do not show such effects (*cf.* Chapter 7).

Conventional gravimetric sorption equipment is not suitable for large and highly condensable organic compounds, such as flavor and aroma compounds. The measurement sensitivity of current-generation pressure transducers limits the use of the sorption equipment to penetrants with relatively high vapor pressures. For example, benzyl alcohol, a common flavor compound, has vapor pressure of 0.1 mmHg at 25°C. It would be very difficult to measure its sorption and transport properties over a wide range of activity using conventional gravimetric sorption techniques. This dissertation reports a new technique, which is suitable for such low volatility organic vapors. As discussed in Chapter 4, this technique extends the measurement capability of the widely used McBain quartz spring balance, and is suitable for penetrants with vapor pressures as low as 10^{-7} mmHg.

Chapter 8 reports sorption, diffusion, and estimated permeability coefficients of CO₂ in the thin BPET films used for vapor sorption measurements. As discussed in Chapter 6, sorption and transport properties of PET depend on the processing history of the sample. Conventional PET films used in practice are significantly thicker than the PET films used in this study. To provide a basis for understanding the extent to which the vapor sorption and transport results from this dissertation are applicable to conventional PET films, the sorption and transport properties of CO₂ in the thin BPET films from this study were compared with literature data for thicker PET films. As reported in Chapter 8, the estimated amorphous phase solubility and permeability coefficients of CO₂ in BPET films at 25°C are in good agreement with some literature values for much thicker films. However, there are significant differences between CO₂ solubility and diffusion

coefficients from various literature sources (*cf.* Chapter 8). These results highlight the complex effects of morphology, orientation, and crystallinity on the sorption and transport properties of PET. Such effects have been and continue to be the subject of active research. Several literature studies have reported that sample processing history affects morphology of *both* the crystalline and non-crystalline phases, and these morphological differences can manifest themselves in the sorption and transport properties of the sample.

9.2 Recommendations for Future Work

9.2.1 Solubility and Diffusivity Correlations

This dissertation has focused on systematic characterization of sorption and transport properties of large organic compounds in PET. Several model flavor compounds (*i.e.*, low molecular weight analogs of common flavor compounds) from various classes of non-polar and polar organic compounds were studied. Due to their large sizes and extremely low vapor pressures, it is very difficult to measure sorption and transport properties of flavor and aroma compounds in barrier polymers such as PET. One way of overcoming this drawback is to develop solubility and diffusivity correlations that can be extrapolated to predict sorption and transport properties of flavor and aroma compounds with reasonable accuracy. As discussed in the previous section, the currently available correlations work well only as first approximations because of certain limitations. For example, they do not take into account the effects of penetrant shape and polarity on solubility and diffusivity. The experimental results reported in this

dissertation highlight these limitations. Hence, there is a need to develop better solubility and diffusivity correlations in the future that will take such effects into account and provide more accurate predictions of solubility and diffusivity of flavor and aroma compounds based on their size, shape, and chemical structure.

9.2.2 New Gravimetric Sorption Technique for Low Volatility Organic Vapors

As discussed in Chapter 4, conventional gravimetric sorption techniques are not suitable for low volatility organic compounds, such as flavor and aroma compounds (*e.g.*, vapor pressures of *d*-limonene and benzyl alcohol are 1 and 0.1 mmHg, respectively, at 25°C). To overcome this drawback, a new experimental technique is described in Chapter 4, which might be used for penetrants with vapor pressures as low as 10^{-7} mmHg. This technique was used to measure solubility and diffusivity of toluene vapor in BPET at 35°C (*cf.* Chapter 8). In the future, it can be used to study more condensable organic compounds, including some flavor and aroma compounds (such as lower alcohols), in barrier polymers, over a wide range of activity. The sorption and diffusion data for such penetrants in the liquid phase (unit activity) are commonly available, but to the best of our knowledge, vapor phase data (low activity) in barrier polymers are very limited. Furthermore, the new technique can also be used in the future to characterize gas/vapor mixture sorption properties of polymer membranes used in gas/vapor separation applications.

9.2.3 Solvent-Induced Crystallization of Amorphous PET

In the presence of certain interacting penetrants, crystallization of amorphous polymers can occur at temperatures well below the glass transition temperature (T_g) of the polymer. The interaction of the polymer with the penetrant lowers the effective T_g of the material. If the depression in T_g is large enough to permit sufficient polymer chain motion to allow crystallization, then the polymer chains may reorganize from the amorphous state to the crystalline state. In addition to crystallization, polymer-solvent interactions have been reported to cause void formation in amorphous and oriented PET [9]. The void structure is one of the major differences between solvent and thermally crystallized PET. It is of particular importance in the case of PET fibers in connection with dyeing behavior [71-73,77,235].

It would be interesting to study the effect of solvent-induced crystallization on amorphous phase morphology and transport properties of PET. Our preliminary experiments with 12.7 μm thick, amorphous, extruded PET films exposed to acetaldehyde confirm the development of crystallinity. For example, exposing the initially amorphous sample to acetaldehyde at 45°C and vapor activity of 0.35 resulted in an increase in crystallinity from 5 wt.% to 37 wt.%, as detected by Wide Angle X-ray Diffraction and Differential Scanning Calorimetry (*cf.* Figures 9.1 and 9.2). In the future, techniques such as Positron Annihilation Lifetime Spectroscopy and Small Angle X-ray Scattering can be used to further probe the amorphous phase morphology of the solvent-crystallized PET samples. Also, series of sorption and permeation measurements with light gases and organic vapors can be performed to investigate the effect of induced

crystallinity and accompanying morphology change on sorption and transport behavior of solvent-crystallized PET samples.

9.2.4 Effect of Processing Conditions on Sorption and Transport Properties of PET

As discussed in Chapters 6 and 8, gas and vapor sorption and permeation properties of PET depend on the sample processing history. It would be interesting to study the effect of various processing conditions (thermal annealing, uniaxial and biaxial orientation, *etc.*) and film thickness on sorption and transport properties of PET.

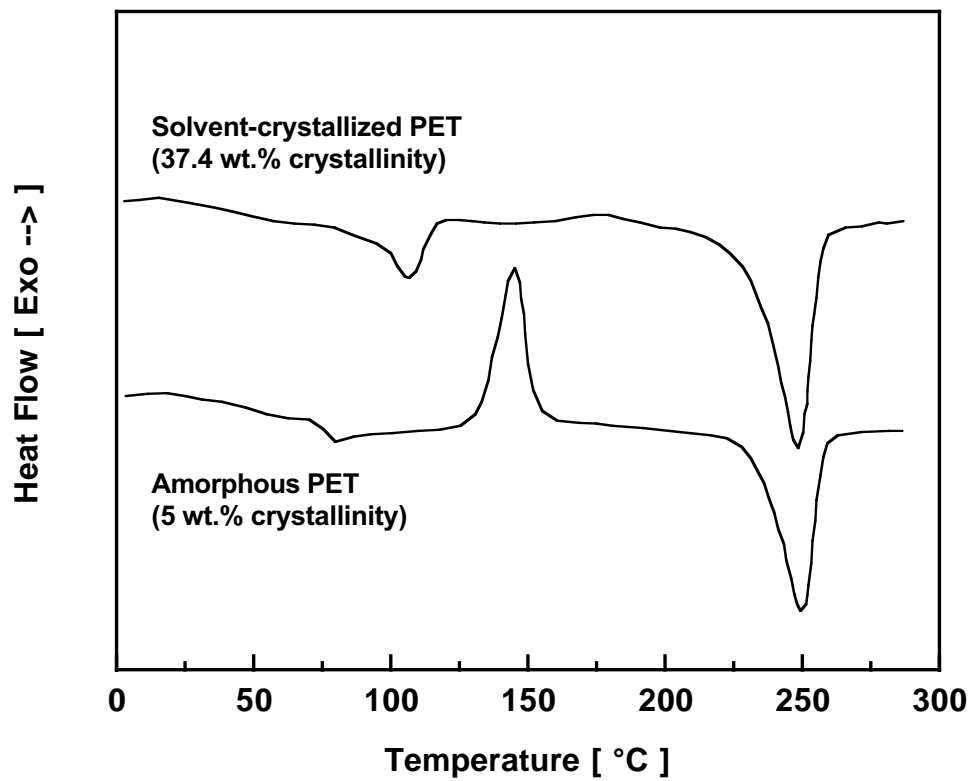


Figure 9.1 Differential Scanning Calorimetry thermograms of amorphous and solvent-crystallized PET films.

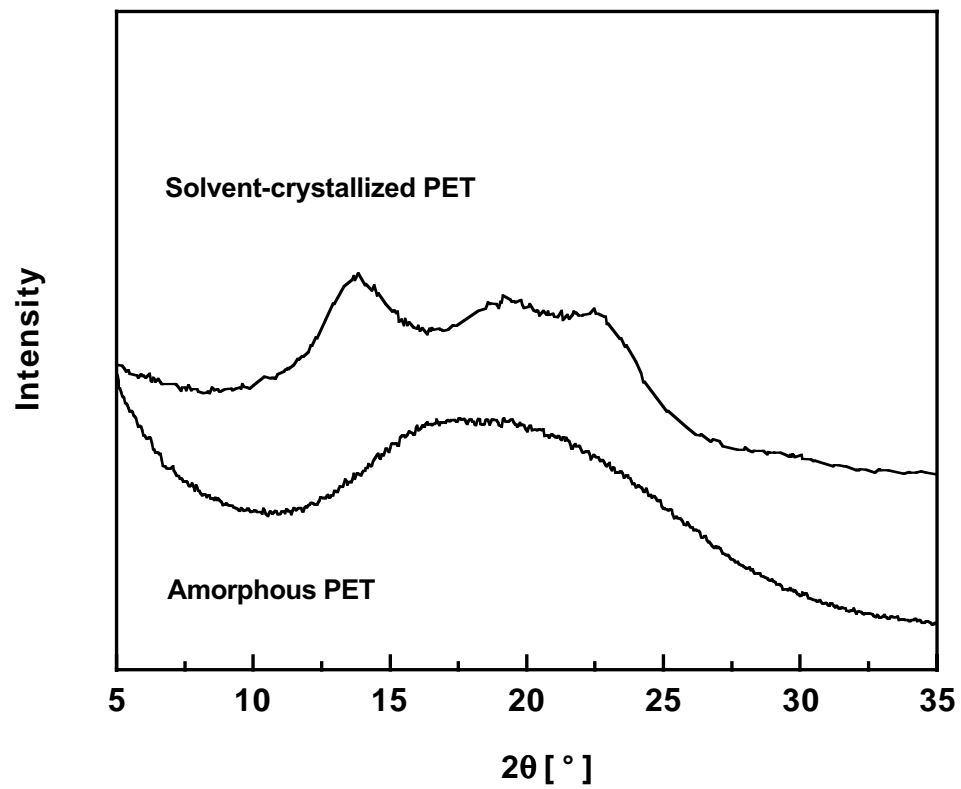


Figure 9.2 Wide Angle X-ray Diffraction spectra of amorphous and solvent-crystallized PET films.

BIBLIOGRAPHY

1. W. E. Brown, Properties of Plastics Used in Food Packaging in *Plastics in Food Packaging*, edited by H. A. Hughes (Marcel Dekker, Inc., New York, 1992), p 103.
2. P. DeLassus, Barrier Polymers in *Encyclopedia of Polymer Science and Engineering*, edited by J. I. Kroschwitz (Wiley-Interscience, New York, 1992), Vol. 3, p 931.
3. A. Tullo, Polymer Makers: New Plastics Packaging Markets Open Up in *Chemical and Engineering News*, May 22, 2000, p 25.
4. S. N. Dhoot, B. D. Freeman, M. E. Stewart, Barrier Polymers in *Encyclopedia of Polymer Science and Technology*, 3rd ed., edited by J. I. Kroschwitz (Wiley-Interscience, New York, 2003), Vol. 5, p 198.
5. A. P. Hansen, D. C. Booker, Flavor Interaction with Casein and Whey Protein in *Flavor-Food Interactions*, edited by R. J. McGorin, J. V. Leland (American Chemical Society, Washington, DC, 1996), Vol. 633, p 75.
6. W. E. Brown, Barrier Design in *Plastics in Food Packaging*, edited by H. A. Hughes (Marcel Dekker, Inc., New York, 1992), p 292.
7. W. J. Koros, Barrier Polymers and Structures: Overview in *Barrier Polymers and Structures*, edited by W. J. Koros (American Chemical Society, Washington, DC, 1990), Vol. 423, p 1.
8. S. N. Dhoot, B. D. Freeman, M. E. Stewart, A. J. Hill, Sorption and Transport of Linear Alkane Hydrocarbons in Biaxially Oriented Poly(ethylene terephthalate) *J. Polym. Sci. : Polym. Phys. Ed.* **39** (11), 1160 (2001).
9. G. E. Serad, B. D. Freeman, M. E. Stewart, A. J. Hill, Gas and Vapor Sorption and Diffusion in Poly(ethylene terephthalate) *Polymer* **42**, 6929 (2001).
10. A. S. Michaels, W. R. Vieth, J. A. Barrie, Solution of Gases in Poly(ethylene terephthalate) *J. Appl. Phys.* **34** (1), 1 (1963).
11. S. N. Dhoot, B. D. Freeman, M. E. Stewart, Sorption and Transport of Linear and Branched Ketones in Biaxially Oriented Poly(ethylene terephthalate) *J. Polym. Sci. : Polym. Phys. Ed.*, submitted (2003).

12. S.-B. Lin, J. L. Koenig, Spectroscopic Characterization of the Rotational Conformations in the Disordered Phase of Poly(ethylene terephthalate) *J. Polym. Sci : Polym. Phys. Ed.* **20**, 2277 (1982).
13. J. A. Slee, G. A. J. Orchard, D. I. Bower, I. M. Ward, The Transport of Oxygen through Oriented Poly(ethylene terephthalate) *J. Polym. Sci : Polym. Phys. Ed.* **27**, 71 (1989).
14. K. Ghosal, B. D. Freeman, Gas Separation Using Polymeric Membranes: An Overview *Polymers for Advanced Technologies* **5**, 673 (1994).
15. P. J. Flory, Statistical Mechanics of Swelling of Network Structures *J. Chem. Phys.* **18**, 108 (1950).
16. W. J. Koros, D. R. Paul, CO₂ Sorption in Poly(ethylene terephthalate) Above and Below the Glass Transition *J. Polym. Sci : Polym. Phys. Ed.* **16** (11), 1947 (1978).
17. R. M. Barrer, J. A. Barrie, J. Slater, Sorption and Diffusion in Ethyl Cellulose. Part III. Comparison Between Ethyl Cellulose and Rubber *J. Polym. Sci.* **27**, 177 (1958).
18. D. R. Paul, Gas Sorption and Transport in Glassy Polymers *Ber. Bunsenges. Phys. Chem.* **83**, 294 (1979).
19. A. R. Berens, Transport of Plasticizing Penetrants in Glassy Polymers in *Barrier Polymers and Structures*, edited by W. J. Koros (American Chemical Society, Washington, DC, 1990), Vol. 423, p 92.
20. A. S. Michaels, W. R. Vieth, J. A. Barrie, Diffusion of Gases in Poly(ethylene terephthalate) *J. Appl. Phys.* **34** (1), 13 (1963).
21. G. E. Serad. Sorption and Diffusion of Small Molecules in Poly(ethylene terephthalate), M.S. Thesis, North Carolina State University, 1999.
22. D. H. Weinkauff, D. R. Paul, Effects of Structural Order on Barrier Properties in *Barrier Polymers and Structures*, edited by W. J. Koros (American Chemical Society, Washington, DC, 1990), Vol. 423, p 60.
23. M. M. Nir, A. Ram, J. Miltz, Sorption and Migration of Organic Liquids in Poly(ethylene terephthalate) *Polym. Eng. Sci.* **36** (6), 862 (1996).
24. M. R. Tant, M. E. Stewart, S. Weinhold, V. K. Long, A. J. Hill, Effects of Processing on the Structure and Properties of Poly(ethylene Terephthalate) and

- Poly(ethylene Naphthalate-2,6-Dicarboxylate) *Polym. Mater. Sci. Eng.* **81**, 374 (1999).
25. J. Crank, *The Mathematics of Diffusion*, 2nd ed. (Clarendon Press, Oxford, 1975).
 26. C. E. Rogers, Permeation of Gases and Vapors in Polymers in *Polymer Permeability*, edited by J. Comyn (Elsevier Applied Science, London and New York, 1988), p 11.
 27. C. C. McDowell, B. D. Freeman, G. W. McNeely, Acetone Sorption and Uptake Kinetics in Poly(ethylene terephthalate) *Polymer* **40** (12), 3487 (1999).
 28. M. Moaddeb, W. J. Koros, Effects of Orientation on the Transport of d-Limonene in Polypropylene *J. Appl. Polym. Sci.* **57**, 687 (1995).
 29. A. H. Windle, Case II Sorption in *Polymer Permeability*, edited by J. Comyn (Elsevier Applied Science, London and New York, 1988), p 75.
 30. R. G. Carbonell, G. C. Sarti, Coupled Deformation and Mass-Transport Processes in Solid Polymers *Ind. Eng. Chem. Res.* **29**, 1194 (1990).
 31. P. H. Hermans, *Contribution to the Physics of Cellulose Fibers* (Elsevier, Amsterdam, 1948), p 23.
 32. J. S. Vrentas, J. L. Duda, Diffusion in Polymer-Solvent Systems: III. Construction of Deborah Number Diagrams *J. Polym. Sci. : Polym. Phys. Ed.* **15** (3), 441 (1977).
 33. K. Bauer, D. Garbe, H. Surburg, *Common Fragrance and Flavor Materials: Preparation, Properties and Uses*, 4th ed. (Wiley-VCH, Weinheim, Germany, 2001).
 34. L. N. Britton, R. B. Ashman, T. M. Aminabhavi, P. E. Cassidy, Prediction of Transport Properties of Permeants through Polymer Films *J. Chem. Edu.* **65** (4), 368 (1988).
 35. R. Franz, Permeation of Volatile Organic Compounds Across Polymer Films-Part I: Development of a Sensitive Test Method Suitable for High Barrier Packaging Films at Very Low Permeant Vapor Pressures *Packag. Technol. Sci.* **6**, 91 (1993).
 36. Y. Osajima, T. Matsui, Dynamic Approach to the Sorption of Flavors into a Food Packaging Film *Anal. Sci.* **9**, 753 (1993).

37. P. Hernandez-Munoz, R. Gavara, R. J. Hernandez, Evaluation of Solubility and Diffusion Coefficients in Polymer Film-Vapor Systems by Sorption Experiments *J Membr. Sci.* **154**, 195 (1999).
38. R. C. Reid, J. M. Prausnitz, B. E. Poling, *The Properties of Gases and Liquids* (McGraw Hill, New York, 1988), p 230.
39. J. Crank, *The Mathematics of Diffusion*, Second ed. (Clarendon Press, Oxford, 1975), p 414.
40. A. R. Berens, Sorption of Organic Liquids and Vapors by Rigid PVC *J. Appl. Polym. Sci.* **37**, 901 (1989).
41. F. Muller-Plathe, Mechanism of Penetrant Transport in Polymers *Acta Polym.* **45**, 259 (1994).
42. W. J. Koros, M. W. Hellums, Transport Properties in *Encyclopedia of Polymer Science and Engineering*, edited by J. I. Kroschwitz (John Wiley & Sons, New York, 1990), Supplement, p 724.
43. D. Hofman, J. Ulbrich, D. Fritsch, D. Paul, Molecular Modeling Simulation of Gas Transport in Amorphous Polyimide and Poly(amide imide) Membrane Materials *Polymer* **37**, 4773 (1996).
44. J. R. Fried, Molecular Simulation of Gas Permeability: Poly(2,6-dimethyl-1,4-phenylene oxide) *J Membr. Sci.* **149**, 115 (1998).
45. A. Bondi, van der Waals Volumes and Radii *J. Phys. Chem.* **68** (3), 441 (1964).
46. D. W. van Krevelen, *Properties of Polymers: Their Correlation with Chemical Structure; Their Numerical Estimation and Prediction from Additive Group Contributions*, 3rd ed. (Elsevier, Amsterdam, 1990), p 875.
47. M. H. Cohen, D. Turnbull, Molecular Transport in Liquids and Glasses *J. Chem. Phys.* **31**, 1164 (1959).
48. K. Ghosal, R. T. Chern, B. D. Freeman, The Effect of Aryl Nitration on Gas Sorption and Permeation in Polysulfone *J. Polym. Sci. : Polym. Phys. Ed.* **33**, 657 (1995).
49. D. H. Weinkauff, D. R. Paul, Gas Transport Properties of Thermotropic Liquid Crystalline Copolyesters. II The Effect of Copolymer Composition *J. Polym. Sci. : Polym. Phys. Ed.* **30**, 837 (1992).

50. W. M. Lee, Selection of Barrier Materials from Molecular Structure *Polym. Eng. Sci.* **20**, 65 (1980).
51. A. Singh, W. J. Koros. Permeation Processes in Barriers and Membranes: Differences and Similarities. Polymers, Laminations & Coatings Conference, San Francisco, CA, 1998; p 361.
52. A. J. Hill, S. Weinhold, G. M. Stack, M. R. Tant, Effect of Copolymer Composition on Free Volume and Gas Permeability in Poly(ethylene terephthalate)-Poly(1,4 cyclohexylenedimethylene terephthalate) Copolyesters *Eur. Polym. J.* **32** (7), 843 (1996).
53. B. D. Freeman, A. J. Hill, Free Volume and Transport Properties of Barrier and Membrane Polymers in *Structure and Properties of Glassy Polymers*, edited by M. R. Tant, A. J. Hill (American Chemical Society, Washington, DC, 1997), Vol. 710, p 306.
54. E. A. McGonigle, J. J. Liggat, R. A. Pethrick, S. D. Jenkins, J. H. Daly, D. Hayward, Permeability of N₂, Ar, He, O₂ and CO₂ through Biaxially Oriented Polyester Films - Dependence on Free Volume *Polymer* **42**, 2413 (2001).
55. V. P. Shantarovich, I. B. Kevdina, Y. P. Yampolskii, A. Y. Alentiev, Positron Annihilation Lifetime Study of High and Low Free Volume Glassy Polymers: Effects of Free Volume Sizes on the Permeability and Permselectivity *Macromolecules* **33**, 7453 (2000).
56. J. E. Robertson, T. C. Ward, A. J. Hill, Thermal, Mechanical, Physical, and Transport Properties of Blends of Novel Oligomer and Thermoplastic Polysulfone *Polymer* **41**, 6251 (2000).
57. G. Dlubek, M. Stolp, C. Nagel, H. M. Fretwell, M. A. Alam, H. J. Radusch, Effect of Crystallization and of Water Uptake on the Free Volume Hole Size in Polyamides 6 and 66 *J. Phys.: Condens. Matter* **10**, 10443 (1998).
58. H. Yang, Y. C. Jean, The Industrial Applications of Positron Annihilation Spectroscopy in Performance Polymers *Mater. Sci. Forum* **255-257**, 40 (1997).
59. R. M. Barrer, Transition-State Theory of Diffusion in Crystals *Trans. Faraday Soc.* **38**, 78 (1942).
60. G. J. van Amerongen, Permeability of Different Rubbers to Gases and its Relation to Diffusivity and Solubility *J. Appl. Phys.* **17**, 972 (1946).

61. R. M. Barrer, G. Skirrow, Transport and Equilibrium Phenomena in Gas-Elastomer Systems. I. Kinetic Phenomena *J. Polym. Sci.* **3**, 549 (1948).
62. R. M. Barrer, Viscosity of Pure Liquids: I. Nonpolymerized Fluids *Trans. Faraday Soc.* **39**, 48 (1943).
63. J. E. Leffler, The Enthalpy-Entropy Relationship and its Implications For Organic Chemistry *J. Org. Chem.* **20**, 1202 (1955).
64. P. Meares, The Diffusion of Gases Through Poly(vinyl acetate) *J. Amer. Chem. Soc.* **76**, 3415 (1954).
65. T. K. Kwei, W. Arnheim, Linear Free Energy Relationships in the Diffusion of Gases Through Polymer Films *J. Chem. Phys.* **37**, 1900 (1962).
66. J. Brandrup, E. H. Immergut, E. A. Grulke, *Polymer Handbook*, 4th ed. (Wiley-Interscience, New York, 1999), p VI/198.
67. M. Salame, The Use of Barrier Polymers in Food and Beverage Packaging in *Plastic Film Technology*, edited by K. M. Finlayson (Technomic, 1989), Vol. 1, p 132.
68. R. R. Light, R. W. Seymour, Effect of Sub-T_g Relaxations on the Gas Transport Properties of Polyesters *Polym. Eng. Sci.* **22** (14), 857 (1982).
69. P. M. Subramanian, I. G. Plotzker, Barrier Materials by Blending in *Polymer Blends*, edited by D. R. Paul, C. B. Bucknall (John Wiley & Sons, 2000), Vol. 2, p 359.
70. A. C. Puleo, D. R. Paul, P. K. Wong, Gas Sorption and Transport in Semicrystalline Poly(4-methyl-1-pentene) *Polymer* **30**, 1357 (1989).
71. H. D. Weigmann, M. G. Scott, A. S. Ribnick, L. Rebenfeld, Interactions of Nonaqueous Solvents with Textile Fibers: Part VII *Text. Res. J.* **46**, 574 (1976).
72. H. Jameel, J. Waldman, L. Rebenfeld, The Effects of Orientation and Crystallinity on the Solvent-Induced Crystallization of Poly(ethylene terephthalate). I Sorption and Diffusion Related Phenomena *J. Appl. Polym. Sci.* **26**, 1795 (1981).
73. H. Jameel, H. D. Noether, L. Rebenfeld, The Effects of Orientation and Crystallinity on the Solvent-Induced Crystallinity of Poly(ethylene terephthalate). II Physical Structure and Morphology *J. Appl. Polym. Sci.* **27**, 773 (1982).

74. A. S. Michaels, R. B. J. Parker, Sorption and Flow of Gases in Polyethylene *J. Polym. Sci.* **61**, 53 (1959).
75. N. Qureshi, E. V. Stepanov, D. Schiraldi, A. Hiltner, E. Baer, Oxygen-Barrier Properties of Oriented and Heat-Set Poly(ethylene terephthalate) *J. Polym. Sci : Polym. Phys. Ed.* **38**, 1679 (2000).
76. D. J. Sekelik, E. V. Stepanov, S. Nazarenko, D. Schiraldi, A. Hiltner, E. Baer, Oxygen Barrier Properties of Crystallized and Talc-Filled Poly(ethylene terephthalate) *J. Polym. Sci : Polym. Phys. Ed.* **37**, 847 (1999).
77. H. D. Weigmann, M. G. Scott, A. S. Ribnick, R. D. Matkowsky, Interactions of Nonaqueous Solvents with Textile Fibers: Part VIII *Text. Res. J.* **47**, 745 (1977).
78. P. H. Hermans, P. Platzek, The Deformation Mechanism and the Fine Structure of Hydrate Cellulose. IX. The Theoretical Relation Between Swelling Anisotropy and the Characteristic Double Refraction of Oriented Filaments *Kolloid Z.* **88**, 68 (1939).
79. R. Shastri, H. C. Roehrs, C. N. Brown, S. E. Dollinger, Permeability of Competitive Oxygen-Barrier Resins in *Barrier Polymers And Structures*, edited by W. J. Koros (American Chemical Society, Washington, DC, 1990), Vol. 423, p 239.
80. R. J. Hernandez, S. E. M. Selke, J. D. Culter, Mass Transfer in Polymeric Packaging Systems in *Plastics Packaging: Properties, Processing, Applications, and Regulations*, (Hanser Gardner Publications, Inc., Cincinnati, OH, 2000), p 313.
81. R. J. Hernandez, Effect of Water Vapor on the Transport Properties of Oxygen Through Polyamide Packaging Materials *J. Food Eng.* **22** (1/4), 495 (1994).
82. G. Strupinsky, A. L. Brody. A Twenty-Year Retrospective on Plastics: Oxygen Barrier Packaging Materials. *Polymers, Laminations & Coatings Conference*, San Francisco, CA, 1998; p 119.
83. W. R. Vieth, *Diffusion In and Through Polymers: Principles and Applications* (Oxford Univ. Press, New York, 1991), p 20.
84. H. L. Frisch, Time Lag in Diffusion. II. *J. Phys. Chem.* **62**, 401 (1958).

85. K. D. Ziegel, H. K. Frensdorff, D. E. Blair, Measurement of Hydrogen Isotope Transport in Poly(vinyl fluoride) Films by the Permeation-Rate Method *J. Polym. Sci.* **7**, 809 (1969).
86. *Annual Book of ASTM Standards; Standard D3985* (American Society for Testing and Materials, West Conshocken, PA, 1994), Vol. 15.09, p 542.
87. *Ox-Tran[®] Oxygen Transmission Rate Measurement System* (MOCON, Inc., Minneapolis, MN, 1998).
88. *Annual Book of ASTM Standards; Standard F1249* (American Society for Testing and Materials, West Conshocken, PA, 1994), Vol. 15.09, p 1051.
89. C. D. Barr, J. R. Giacini, R. J. Hernandez, A Determination of Solubility Coefficient Values by Gravimetric and Isostatic Permeability Techniques *Packag. Technol. Sci.* **13**, 157 (2000).
90. C. C. McDowell, D. T. Coker, B. D. Freeman, An Automated Spring Balance for Kinetic Gravimetric Sorption of Gases and Vapors in Polymers *Rev. Sci. Instrum.* **69** (6), 2510 (1998).
91. B. I. Chaudhary, A. I. Johns, Solubilities of Nitrogen, Isobutane and Carbon Dioxide in Polyethylene *J. Cell. Plast.* **34** (4), 312 (1998).
92. O. Pfannschmidt, W. Michaeli. Determination of the Solubility and Diffusivity of Gases in Polymers by using a High Pressure Magnet-Suspension-Balance. Annual Technical Conference of the Society of Plastics (ANTEC), Atlanta, USA, 1998; p 1918.
93. M. Salame, Prediction of Gas Barrier Properties of High Polymers *Polym. Eng. Sci.* **26** (22), 1543 (1986).
94. J. Y. Park, D. R. Paul, Correlation and Prediction of Gas Permeability in Glassy Polymer Membrane Materials via a Modified Free Volume Based Group Contribution Method *J Membr. Sci.* **125**, 23 (1997).
95. S. C. Fayoux, A. Seuvre, A. J. Voilley, Aroma Transfers in and through Plastic Packagings: Orange Juice and d-Limonene. A Review. Part II: Overall Sorption Mechanisms and Parameters-a Literature Survey *Packag. Technol. Sci.* **10**, 145 (1997).
96. G. Strandburg, P. T. DeLassus, B. A. Howell, Thermodynamics of Permeation of Flavors in Polymers: Prediction of Solubility Coefficients in *Food and Packaging*

- Interactions II*, edited by S. J. Risch, J. H. Hotchkiss (American Chemical Society, Washington, DC, 1991), Vol. 473, p 133.
97. R. M. Barrer, G. J. Skirrow, Transport and Equilibrium Phenomena in Gas-Elastomer Systems. II. Equilibrium Phenomena *J. Polym. Sci.* **3**, 564 (1948).
 98. S. A. Stern, J. T. Mullhaupt, P. J. Gareis, Effect of Pressure on the Permeation of Gases and Vapors Through Polyethylene. Usefulness of the Corresponding States Principle *AIChE J.* **15** (1), 64 (1969).
 99. S. Li, J. S. Paik, Flavor Sorption Estimation by UNIFAC Group Contribution Model *Trans. ASAE* **39** (3), 1013 (1996).
 100. J. S. Paik, M. A. Tigani, Application of Regular Solution Theory in Predicting Equilibrium Sorption of Flavor Compounds by Packaging Polymers *J. Agric. Food Chem.* **41**, 806 (1993).
 101. B. D. Freeman, I. Pinnau, Membrane Materials Design Considerations for Gas Separations in *Polymeric Materials for Gas Separations: Chemistry and Materials Science*, edited by B. D. Freeman, I. Pinnau (American Chemical Society, Washington DC, 1999), p 1.
 102. R. C. Mason, P. T. DeLassus, G. Strandburg, B. A. Howell, Diffusion of Flavors in Polymers: Effect of Permeant Size and Shape *Tappi J.* **75** (6), 163 (1992).
 103. C. S. Coughlin, K. A. Mauritz, R. F. Storey, A General Free Volume Based Theory for the Diffusion of Large Molecules in Amorphous Polymers above T_g, 4. Polymer-Penetrant Interactions *Macromolecules* **24** (7), 1526 (1991).
 104. T. H. Begley, Methods and Approaches Used by FDA to Evaluate the Safety of Food Packaging Materials *Food Addit. Contam.* **14** (6-7), 545 (1997).
 105. O. Piringer, R. Franz, M. Huber, T. H. Begley, T. P. McNeal, Migration From Food Packaging Containing a Functional Barrier: Mathematical and Experimental Evaluation *J. Agric. Food Chem.* **46**, 1532 (1998).
 106. A. O'Brien, A. Goodson, I. Cooper, Polymer Additive Migration to Foods - A Direct Comparison of Experimental Data and Values Calculated From Migration Models for High Density Polyethylene (HDPE) *Food Addit. Contam.* **16** (9), 367 (1999).
 107. W. Limm, H. C. Hollifield, Modeling of Additive Diffusion in Polyolefins *Food Addit. Contam.* **13**, 949 (1996).

108. W. A. Jenkins, J. P. Harrington, The Chemistry and Manufacture of Polymers used in Packaging in *Packaging Foods With Plastics*, edited by W. A. Jenkins, J. P. Harrington (Technomic Publishing Co., Lancaster, PA, 1991), p 46.
109. *Permeability And Other Film Properties of Plastics and Elastomers* (Plastics Design Library, Norwich, NY, 1995), p 706.
110. V. T. Stannett, Barrier Properties and Migration Problems of Plastics *Polym. Eng. Sci.* **18** (15), 1129 (1978).
111. R. J. Ashley, Permeability and Plastics Packaging in *Polymer Permeability*, edited by J. Comyn (Elsevier Applied Science Publishers Ltd., Essex, England, 1985).
112. M. Salame, Barrier Polymers in *The Wiley Encyclopedia of Packaging Technology*, edited by M. Bakker (John Wiley & Sons, New York, 1986), p 48.
113. S. Pauly, Permeability and Diffusion Data in *Polymer Handbook*, 3rd ed., edited by J. Brandrup, E. H. Immergut (Wiley Interscience, New York, 1989), p IV:435.
114. P. T. DeLassus, Interaction of High Barrier Plastics with Food: Permeation and Sorption in *Food Product-Package Compatibility*, edited by J. I. Gray, B. R. Harte, J. Miltz (Technomic Publishing, Lancaster, PA, 1987), p 229.
115. J. Landois-Garza, J. H. Hotchkiss, Permeation of High Barrier Films by Ethyl Esters in *Food and Packaging Interactions*, edited by J. H. Hotchkiss (American Chemical Society, Washington DC, 1988), p 42.
116. M. G. R. Zobel, *Aroma Barrier Properties of Coextruded Films* (Schotland Business Research, Princeton, NJ, 1984), p 75.
117. G. L. Robertson, Structure and Related Properties of Plastic Polymers in *Food Packaging. Principles and Practice*, edited by H. A. Hughes (Marcel Dekker, Inc., New York, 1993), Vol. 6, p 9.
118. R. Catala, R. Gavara, Review: Alternative High Barrier Polymers for Food Packaging *Food Sci. Tech. Int.* **2**, 281 (1996).
119. W. E. Brown, Properties of Plastics used in Food Packaging in *Plastics in Food Packaging*, edited by W. E. Brown (Marcel Dekker, Inc., New York, 1992), p 132.
120. R. J. Hernandez, S. E. M. Selke, J. D. Culter, Major Plastics in Packaging in *Plastics Packaging: Properties, Processing, Applications, and Regulations*, (Hanser Gardner Publications, Inc., Cincinnati, OH, 2000), p 89.

121. *Selar PA Processing Guide* (E.I. du Pont de Nemours & Co., Wilmington, DE, 2001).
122. P. M. Morse, PEN: The New Polyester in *Chemical & Engineering News*, November 10, 1997, p 8.
123. T. M. McGee, A. S. Jones. The Effect of Processing Parameters on Physical Properties of PET/PEN Blends for Bottle Applications. 11th Annual High Performance Blow Molding Conference: Technical Innovations in Blow Molding, Cleveland, OH, 1995; p 89.
124. C. C. McDowell, B. D. Freeman, G. W. McNeely, M. I. Haider, A. J. Hill, Synthesis, Physical Characterization, and Acetone Sorption Kinetics in Random Copolymers of Poly(ethylene terephthalate) and Poly(ethylene 2,6-naphthalate) *J. Polym. Sci : Polym. Phys. Ed.* **36**, 2981 (1998).
125. G. R. Cantrell, B. D. Freeman, H. B. Hopfenberg, S. Makhija, I. Haider, M. Jaffe, The Influence of Thermal Annealing on Organic Vapor Sorption and Transport in a Nematogenic Copolyester in *Liquid Crystalline Polymers*, edited by C. Carfagna (Pergamon Press, Oxford, 1994), p 233.
126. N. R. Miranda, J. T. Willits, B. D. Freeman, H. B. Hopfenberg, Organic Vapor Sorption and Transport in a Thermotropic Liquid Crystalline Polyester *J. Membr. Sci.* **94**, 67 (1994).
127. R. Lusignea, High-Barrier Packaging with Liquid Crystal Polymers *Tappi J.* **80** (6), 205 (1997).
128. R. Lusignea. Flexible Multilayer Packaging with Oriented LCP Barrier Layer. Polymers, Laminations & Coatings Conference, San Francisco, CA, 1998; p 889.
129. D. J. Brennan, J. E. White, A. P. Haag, S. L. Kram, M. N. Mang, S. Pikulin, C. N. Brown, Poly(hydroxy amide ethers): New High-Barrier Thermoplastics *Macromolecules* **29**, 3707 (1996).
130. K. Ghosal, R. T. Chern, B. D. Freeman, W. H. Daly, I. I. Negulescu, Effect of Basic Substituents on Gas Sorption and Permeation in Polysulfone *Macromolecules* **29** (12), 4360 (1996).
131. M. R. Pixton, D. R. Paul, Relationship between Structure and Transport Properties for Polymers with Aromatic Backbones in *Polymeric Gas Separation*

- Membranes*, edited by D. R. Paul, Y. P. Yampolskii (CRC Press, Boca Raton, FL, 1994), p 83.
132. C. H. Silvis, Recent Advances in Polymers for Barrier Applications *Trends Polym. Sci.* **5** (3), 75 (1997).
 133. *BLOX™ Adhesion and Barrier Resins: Product Information* (The Dow Chemical Company, May 2001).
 134. T. Glass, H. Pham, M. Winkler. New Thermoplastic Adhesive and Barrier Resins. ANTEC 2000: Plastics, The Magical Solution, Orlando, FL, 2000.
 135. W. Erickson. New Coextruded PCTFE-Based Moisture Barrier Films for High Performance Packaging. Polymers, Laminations & Coatings Conference, San Francisco, CA, 1998; p 355.
 136. *Aclar Fluoropolymer films: Product Information* (Honeywell International, 2001).
 137. P. T. DeLassus, D. L. Clarke, T. Cosse, Barrier Coating Cuts CO₂ Loss in Small PET Bottles *Mod. Plast.*, 86 (January 1983).
 138. W. E. Brown, Properties of Plastics used in Food Packaging in *Plastics in Food Packaging*, edited by W. E. Brown (Marcel Dekker, Inc., New York, 1992), p 125.
 139. E. Werner, S. Janocha, M. Hopper, K. Mackenzie, Polyester Films in *Encyclopedia of Polymer Science and Technology*, edited by J. I. Kroschwitz (Wiley-Interscience, New York, 1992), Vol. 12, p 193.
 140. N. Whiteman, P. T. DeLassus, J. Gunderson, in *TAPPI Proceedings of PLC Conference*, 2001.
 141. W. E. Brown, Properties of Plastics used in Food Packaging in *Plastics in Food Packaging*, edited by W. E. Brown (Marcel Dekker, Inc., New York, 1992), p 105.
 142. J. L. Throne, Polymer Properties in *The Wiley Encyclopedia of Packaging Technology*, edited by M. Bakker (John Wiley & Sons, New York, 1986), p 529.
 143. A. R. Berens, Penetrant Diffusion in Unplasticized and Plasticized PVC *Makromol. Chem., Macromol. Symp.* **29**, 95 (1989).

144. J. H. Levy. Nylon 6 Barrier Coextrusions: A Cost-effective Packaging Route. *Polymers, Laminations & Coatings Conference*, San Francisco, CA, 1998; p 163.
145. W. A. Jenkins, J. P. Harrington, *Plastics and their Fabrication in Packaging Foods With Plastics*, edited by W. A. Jenkins, J. P. Harrington (Technomic Publishing Co., Lancaster, PA, 1991), p 11.
146. *MXD-6 Nylon Polyamide Property Brochure* (Mitsubishi Gas Chemical Company, Inc., 2001), p 30.
147. D. A. Abramowicz, P. J. Heyes. Comparing the Performance of Barrier-Coated versus Multilayer PET Containers for Oxygen Sensitive Products. *Nova-Pack Americas 2000*, Orlando, FL, 2000.
148. T. Hart. New Effective Barrier Coating for Plastic Containers. *Bev-Pak Americas '97*, Directions 21, Inc., 1997.
149. D. S. Finch, J. Franks, N. X. Randall, A. Barnetson, J. Crouch, A. C. Evans, B. Ralph, Diamond-like Carbon, a Barrier Coating for Polymers used in Packaging Applications *Packag. Technol. Sci.* **9**, 73 (1996).
150. N. Inagaki, Oxygen Gas Barrier PET Films Formed by Deposition of Plasma-Polymerized SiO_x Films in *Silicones and Silicone-Modified Materials*, edited by S. J. Clarson, J. J. Fitzgerald, M. J. Owen, S. D. Smith (Oxford University Press, Washington, DC, 2000), Vol. 729, p 544.
151. R. J. Hernandez, S. E. M. Selke, J. D. Culter, *Converting, Lamination and Coating in Plastics Packaging: Properties, Processing, Applications, and Regulations*, (Hanser Gardner Publications, Inc., Cincinnati, OH, 2000), p 217.
152. G. L. Robertson, Processing and Converting of Thermoplastic Polymers in *Food Packaging. Principles and Practice*, edited by H. A. Hughes (Marcel Dekker, Inc., New York, 1993), Vol. 6, p 111.
153. W. A. Jenkins, J. P. Harrington, *Snack Foods in Packaging Foods With Plastics*, edited by W. A. Jenkins, J. P. Harrington (Technomic Publishing Co., Lancaster, PA, 1991), p 195.
154. A. S. Da Silva Sobrinho, G. Czeremuskin, M. Latreche, M. R. Wertheimer, Study of Defect Numbers and Distributions in PECVD SiO₂ Transparent Barrier Coatings on PET in *Plasma Deposition and Treatment of Polymers*, edited by W. W. Lee, R. d'Agostino, M. R. Wertheimer (Materials Research Society, Boston, MA, 1998), Vol. 544, p 245.

155. K. H. Haas, S. Amberg-Schwab, K. Rose, G. Schottner, Functionalized Coatings Based on Inorganic-Organic Polymers (ORMOCERs) and Their Combination with Vapor Deposited Inorganic Thin Films *Surf. Coat. Tech.* **111**, 72 (1999).
156. M. Hoffmann, S. Amberg-Schwab, H. Bader, M. Gessler, Inorganic-Organic Polymers with Barrier Properties for Water Vapor, Oxygen and Flavors *J. Sol Gel Sci. Tech.* **1/2**, 141 (1998).
157. H. Langowski, Plastics Packaging in the 21st Century *Kunststoffe* **90** (6), 88 (2000).
158. German Brewer Second To Launch In 'Glaskin' in *Packaging World*, May 2000, p 2.
159. I. Bucklow, P. Butler, Plastic Proves It Can Hold Its Beer in *Materials World*, August 2000, p 14.
160. French Brewer Pioneers New Barrier Technology in *Packaging World*, June 1999, p 2.
161. R. M. Barrer, Diffusion and Permeation in Heterogeneous Media in *Diffusion in Polymers*, edited by J. Crank, G. S. Park (Academic Press, New York, 1968), p 165.
162. K. M. Kit, J. M. Schultz, R. Gohil, Morphology and Barrier Properties of Oriented Blends of Poly(ethylene terephthalate) and Poly(ethylene 2,6-naphthalate) with Poly(ethylene-co-vinyl alcohol) *Polym. Eng. Sci.* **35** (8), 680 (1995).
163. O. Motta, L. Di Maio, L. Incarnato, D. Acierno, Transport and Mechanical Properties of PET/Rodrun 3000 Blown Films *Polymer* **37** (12), 2373 (1996).
164. E. Petrovicova, R. Knight, L. S. Schadler, T. E. Twardowski, Nylon 11/Silica Nanocomposite Coatings Applied by the HVOF Process. II: Mechanical and Barrier Properties *J. Appl. Polym. Sci.* **78**, 2272 (2000).
165. S. Brauer, *P 234: Polymer Nanocomposites* (Business Communications Co., Inc., April 2000), p XIII.
166. Honeywell's Polymerized Nanocomposite Nylon Resin in *Packaging World*, November 6, 2000, Web exclusive.

167. K. Kamena. Emerging Nanocomposite Technologies for Barrier and Thermal Improvements in PET Containers. Nova-Pack Americas '99, Orlando, FL, 1999; p 1.
168. L. Vermeiren, F. Devlieghere, M. van Beest, N. Kruijf, J. Debevere, Developments in the Active Packaging of Foods *Trends Food Sci. Tech.* **10**, 77 (1999).
169. W. Scholl. Active Barrier Packaging: A Technology for the 21st Century. Polymers, Laminations & Coatings Conference, Atlanta, GA, 1999; p 671.
170. M. L. Rooney, Active Packaging in Polymer Films in *Active Food Packaging*, 1st ed., edited by M. L. Rooney (Blackie Academic & Professional, Glasgow, UK, 1995), p 74.
171. S. Lambert. New EVOH-Based Oxygen Scavenging Resins for Use in Co-Injected PET Bottles. Nova-Pack Europe 2000, Neuss, Germany, 2000; p 163.
172. E. P. Socci, M. K. Akkapeddi, D. C. Worley. New High Barrier, Oxygen Scavenging Polyamides for Packaging Applications. ANTEC, 2001.
173. B. D. Rodgers. New High Capacity Oxygen Scavenging Polymer For Use in Flexible Packaging. Flex-Pak Europe 2000, Amsterdam, Nov. 2000; p 61.
174. M. A. Cochran, R. Folland, J. W. Nicholas, E. R. Robinson. U.S. Patent 5,639,815, 1997.
175. F. N. Teumac, B. A. Ross, M. R. Rassouli, Oxygen Scavengers Inside Liners of Bottle Closures *MBAA Technical Quarterly* **27**, 122 (1990).
176. C. Yang, E. Nuxoll, E. Cussler, Reactive Barrier Films *AIChE J.* **47** (2), 295 (2001).
177. *Permeability And Other Film Properties of Plastics and Elastomers* (Plastics Design Library, Norwich, NY, 1995), p 143.
178. A. B. Robertson, K. R. Habermann, Fluoropolymer Film in *The Wiley Encyclopedia of Packaging Technology*, edited by M. Bakker (John Wiley & Sons, New York, 1986), p 311.
179. J. Quezada-Gallo, F. Debeaufort, A. Voilley, Mechanism of Aroma Transfer Through Edible and Plastic Packagings in *Food Packaging: Testing Methods and*

- Applications*, edited by S. J. Risch (American Chemical Society, Washington, DC, 1999), Vol. 753, p 130.
180. J. W. McBain, A. M. Bakr, A New Sorption Balance *J. Am. Chem. Soc.* **48**, 690 (1926).
 181. W. J. Koros, D. R. Paul, Design Considerations for Measurement of Gas Sorption in Polymers by Pressure Decay *J. Polym. Sci : Polym. Phys. Ed.* **14**, 1903 (1976).
 182. W. Puff, PFPOSFIT: A New Version of a Program For Analyzing Positron Lifetime Spectra with Non-Gaussian Prompt Curve *Comput. Phys. Commun.* **30** (4), 359 (1983).
 183. S. Fakirov, E. W. Fischer, R. Hoffmann, G. F. Schmidt, Structure and Properties of PET Crystallized by Annealing in the Highly Oriented State: 2. Melting Behavior and the Mosaic Block Structure of the Crystalline Layers *Polymer* **18**, 1121 (1977).
 184. H.-G. Elias, *An Introduction to Polymer Science*, 1st ed. (VCH, Weinheim, 1997), p 287.
 185. K. H. Illers, Melting Behavior of Drawn Polyethylene *Angew. Makromol. Chem.* **12**, 89 (1970).
 186. E. W. Fischer, S. Fakirov, Structure and Properties of PET Crystallized by Annealing in the Highly Oriented State: Part 1. Morphological Structure as Revealed by Small Angle X-ray Scattering *J. Mater. Sci.* **11**, 1041 (1976).
 187. R. M. Gohil, Morphology-Permeability Relationships in Biaxially Oriented PET Films: A Relationship between Oxygen Permeability and PROF *J. Appl. Polym. Sci.* **48**, 1649 (1993).
 188. P. H. Hermans, *Contribution to the Physics of Cellulose Fibers* (Elsevier, Amsterdam, 1946), Appendix 3.
 189. Z. W. Wilchinsky, *Advances in X-ray Analysis* (Plenum Press, New York, 1963), Vol. 6, p 231.
 190. G. R. Cantrell, C. C. McDowell, B. D. Freeman, C. Noel, The Influence of Annealing on Thermal Transitions in a Nematic Copolyester *J. Polym. Sci : Polym. Phys. Ed.* **37**, 505 (1999).

191. G. Farrow, I. M. Ward, Crystallinity of Poly(ethylene terephthalate): A Comparison of X-ray, Infra-red and Density measurements *Polymer* **1**, 330 (1960).
192. G. VerStrate, Z. W. Wilchinsky, Ethylene-Propylene Copolymers: Degree of Crystallinity and Composition *J. Polym. Sci.: Part A-2* **9**, 127 (1971).
193. J. L. Koenig, M. J. Hannon, Infrared Studies of Chain Folding in Polymers. II. Poly(ethylene terephthalate) *J. Macromol. Sci.: Part B1* **1** (1), 119 (1967).
194. L. E. Alexander, *X-Ray Diffraction Methods in Polymer Science*, 2nd ed. (R.K. Publishing Company, Malabar, FL, 1985), p 137.
195. Z. Bashir, I. Al-Aloush, I. Al-Raqibah, M. Ibrahim, Evaluation of Three Methods for the Measurement of Crystallinity of PET Resins, Preforms, and Bottles *Polym. Eng. Sci.* **40** (11), 2442 (2000).
196. K. E. Bacon, Differential Thermal Analysis of High Polymers. V. Ethylene Copolymers *J. Polym. Sci.* **61**, 47 (1962).
197. G. Farrow, I. M. Ward, Comparison of X-Ray and Nuclear Magnetic Resonance Measurements of Crystallinity in Poly(ethylene terephthalate) *Brit. J. Appl. Phys.* **11**, 543 (1960).
198. S. Kavesh, J. M. Schultz, Meaning and Measurement of Crystallinity in Polymers: A Review *Polym. Eng. Sci.* **9** (5), 331 (1969).
199. A. J. Hill, Positron Annihilation Lifetime Spectroscopy to Probe Free Volume Effects in Polymers and Composites in *High Temperature Properties and Applications of Polymeric materials*, edited by M. R. Tant, J. W. Connell, H. L. N. McManus (ACS, Washington, 1995), p 63.
200. A. J. Hill, M. R. Tant, Effect of Crystallinity on Amorphous regions of PET/PCT Copolymer *Polym. Mater. Sci. Eng.* **81**, 281 (1999).
201. L. Xie, D. Gidley, H. Hristov, A. Yee, Positronium Formation in Semicrystalline PET *Polymer* **35** (1), 14 (1994).
202. H. Mohamed, Y. Ito, M. Imai, Change of Distribution of Free Volume Holes During Crystallization of PET Revealed by PALS *J. Chem. Phys.* **105** (11), 4841 (1996).
203. A. M. Roland, J. H. Hotchkiss, Determination of Flavor-Polymer Interactions by Vacuum-Microgravimetric Method in *Food and Packaging Interactions II*, edited

- by S. J. Risch, J. H. Hotchkiss (American Chemical Society, Washington, DC, 1991), p 149.
204. R. C. Reid, J. M. Prausnitz, B. E. Poling, *The Properties of Gases and Liquids*, 4th ed. (McGraw-Hill Book Company, New York, 1988).
 205. J. Miltz, A. Ram, M. M. Nir, Prospects for Application of Post-Consumer Used Plastics in Food Packaging *Food Add. Contam.* **14** (6-7), 649 (1997).
 206. C. K. Yeom, S. H. Lee, H. Y. Song, J. M. Lee, Vapor Permeations of a Series of VOCs/N₂ Mixtures Through PDMS Membrane *J. Membr. Sci.* **198**, 129 (2002).
 207. A. Singh, B. D. Freeman, I. Pinnau, Pure and Mixed Gas Acetone/Nitrogen Permeation Properties of Polydimethylsiloxane [PDMS] *J. Polym. Sci : Polym. Phys. Ed.* **36**, 289 (1998).
 208. H. M. McNair, J. M. Miller, Qualitative and Quantitative Analysis in *Basic Gas Chromatography*, (Wiley-Interscience, New York, 1998), p 126.
 209. T. C. Merkel, V. I. Bondar, K. Nagai, B. D. Freeman, I. Pinnau, Gas Sorption, Diffusion, and Permeation in Poly(dimethylsiloxane) *J. Polym. Sci : Polym. Phys. Ed.* **38**, 415 (2000).
 210. S. V. Dixon-Garrett, K. Nagai, B. D. Freeman, Ethylbenzene Solubility, Diffusivity, and Permeability in Poly(dimethyl siloxane) *J. Polym. Sci : Polym. Phys. Ed.* **38**, 1461 (2000).
 211. Y. Sun, J. Chen, Sorption/Desorption Properties of Ethanol, Toluene, and Xylene in Poly(dimethylsiloxane) Membranes *J. Appl. Polym. Sci.* **51**, 1797 (1994).
 212. R. C. Reid, J. M. Prausnitz, B. E. Poling, *The Properties of Gases and Liquids*, 4th ed. (McGraw-Hill Book Company, New York, 1988), p 656.
 213. C. M. Hansen, *Hansen Solubility Parameters: A User's Handbook* (CRC Press, Boca Raton, 2000), p 168.
 214. Y. Kamiya, Y. Naito, K. Terada, K. Mizoguchi, Volumetric Properties and Interaction Parameters of Dissolved Gases in Poly(dimethylsiloxane) and Polyethylene *Macromolecules* **33** (8), 3111 (2000).
 215. A. F. Mills, *Basic Heat and Mass Transfer* (Irwin, Inc., Boston, MA, 1995), p 677.

216. J. Crank, *The Mathematics of Diffusion*, 2nd ed. (Clarendon Press, Oxford, 1975), p 60.
217. N. H. Snow, G. C. Slack, Gas Chromatography in *Kirk-Othmer Encyclopedia of Chemical Technology*, 4th ed., edited by M. Howe-Grant (Wiley-Interscience, New York, 2002).
218. F. D. Rossini, K. S. Pitzer, R. L. Arnett, R. M. Braun, G. C. Pimentel, *Selected Values of Physical and Thermodynamic Properties of Hydrocarbons and Related Compounds* (Carnegie Press, Pittsburgh, PA, 1953).
219. F. Doghieri, G. C. Sarti, Nonequilibrium Lattice Fluids: A Predictive Model for the Solubility in Glassy Polymers *Macromolecules* **29**, 7885 (1996).
220. W. Czerwinski, The Effect of Molecular Orientation on the Vapor Sorption of Cyclohexane in Amorphous Polyester Fibres *Angew. Makromol. Chem.* **135**, 65 (1985).
221. A. Morisato, B. D. Freeman, I. Pinnau, C. G. Casillas, Pure Hydrocarbon Sorption Properties of Poly(1-trimethylsilyl-1-propyne) (PTMSP), Poly(1-phenyl-1-propyne) (PPP) and PTMSP/PPP Blends *J. Polym. Sci : Polym. Phys. Ed.* **34**, 1925 (1996).
222. R. C. Reid, J. M. Prausnitz, B. E. Poling, *The Properties of Gases and Liquids*, 4th ed. (McGraw-Hill Book Company, New York, 1988), p 55.
223. D. VanKrevelen, *Properties of Polymers: Their Correlation with Chemical Structure; Their Numerical Estimation and Prediction from Additive Group Contributions* (Elsevier Science, Amsterdam, 1990), p 875.
224. A. R. Berens, H. B. Hopfenberg, Diffusion and Relaxation in Glassy Polymer Powders. 2. Separation of Diffusion and Relaxation Parameters *Polymer* **19** (5), 489 (1978).
225. C. J. Patton, R. M. Felder, W. J. Koros, Sorption and Transport of Benzene in Poly(ethylene Terephthalate) *J. Appl. Polym. Sci.* **29**, 1095 (1984).
226. G. F. Billovits, C. J. Durning, Two-stage Weight Gain in the Polystyrene-Ethylbenzene System *Polym. Commun.* **31** (9), 358 (1990).
227. A. Kishimoto, H. Fujita, H. Odani, M. Kurata, M. Tamura, Successive Differential Absorptions of Vapors by Glassy Polymers *J. Phys. Chem.* **64**, 594 (1960).

228. H. Fujita, Organic Vapors Above the Glass Transition Temperature in *Diffusion in Polymers*, edited by J. Crank, G. S. Park (Academic Press, Inc., New York, 1968), p 75.
229. W. R. Vieth, H. H. Alcalay, A. J. Frabetti, Solution of Gases in Oriented Poly(ethylene terephthalate) *J. Appl. Polym. Sci.* **8**, 2125 (1964).
230. G. A. J. Orchard, P. Spiby, I. M. Ward, Oxygen and Water Vapor Diffusion Through Biaxially Oriented Poly(ethylene terephthalate) *J. Polym. Sci. : Polym. Phys. Ed.* **28**, 603 (1990).
231. A. Natu, E. A. Lofgren, W. Kollen, S. A. Jabarin. Effect of Morphology on Barrier Properties of Poly(ethylene terephthalate). 56th Annual Technical Conference - Society of Plastics Engineers, 1998; p 1642.
232. R. Y. F. Liu, D. A. Schiraldi, A. Hiltner, E. Baer, Oxygen Barrier Properties of Cold-Drawn Polyesters *J. Polym. Sci. : Polym. Phys. Ed.* **40**, 862 (2002).
233. J. Lin, S. Shenogin, S. Nazarenko, Oxygen Solubility and Specific Volume of Rigid Amorphous Fraction in Semicrystalline Poly(ethylene terephthalate) *Polymer* **43**, 4733 (2002).
234. J. B. Brolly, D. I. Bower, I. M. Ward, Diffusion and Sorption of CO₂ in Poly(ethylene terephthalate) and Poly(ethylene naphthalate) *J. Polym. Sci. : Polym. Phys. Ed.* **34**, 769 (1996).
235. P. J. Makerewicz, G. L. Wilkes, Diffusion Studies of Poly(ethylene terephthalate) Crystallized by Nonreactive Liquids and Vapors *J. Polym. Sci. : Polym. Phys. Ed.* **16**, 1529 (1978).
236. V. Bellenger, J. Kaltenecker-Commercon, J. Verdu, Interactions of Solvents with Poly(methyl methacrylate) *Polymer* **38** (16), 4175 (1997).
237. G. A. Bernier, R. P. Kambour, The Role of Organic Agents in the Stress Crazing and Cracking of Poly(2,6-dimethyl-1,4-phenylene oxide) *Macromolecules* **1** (5), 393 (1968).
238. V. P. Belousov, M. Y. Panov, *Thermodynamic Properties of Aqueous Solutions of Organic Substances* (CRC Press, Boca Raton, 1994), p 63.
239. A. V. Bailey, D. Mitcham, E. L. Skau, Binary Freezing Point Diagrams for Some Methyl Ketones and Their Complete Solubilities in Acetone, Methanol, Benzene, and Carbon Tetrachloride *J. Chem. Eng. Data* **15** (4), 542 (1970).

240. C. L. Yaws, S. D. Sheth, M. Han, Using Solubility and Henry's Law Constant Data for Ketones in Water *Pollut. Eng.* **30** (2), 44 (1998).
241. W. K. Stephenson, R. Fuchs, Enthalpies of Interaction of Ketones with Organic Solvents *Can. J. Chem.* **63**, 336 (1985).
242. C. L. Yaws, H. C. Yang, Water Solubility Data for Organic Compounds *Pollut. Eng.* **22** (10), 70 (1990).
243. H. Wang, T. Ugomori, K. Tanaka, H. Kita, K. Okamoto, Y. Suma, Sorption and Pervaporation Properties of Sulfonyl-Containing Polyimide Membrane to Aromatic/Non-Aromatic Hydrocarbon Mixtures *J. Polym. Sci. : Polym. Phys. Ed.* **38**, 2954 (2000).
244. H. Odani, M. Uchikura, Y. Ogino, M. Kurata, Diffusion and Solution of Methanol Vapor in Poly(2-vinylpyridine)-block-Polyisoprene and Poly(2-vinylpyridine)-block-Polystyrene *J. Membr. Sci.* **15**, 193 (1983).
245. E. Bagley, F. A. Long, Two-stage Sorption and Desorption of Organic Vapors in Cellulose Acetate *J. Am. Chem. Soc.* **77**, 2172 (1955).
246. J. Crank, G. S. Park, An Evaluation of the Diffusion Coefficient for Chloroform in Polystyrene from Simple Absorption Experiments *Trans. Faraday Soc.* **45**, 240 (1949).
247. P. Drechsel, J. L. Hoard, F. A. Long, *J. Polym. Sci.* **10**, 241 (1953).
248. J. Crank, G. S. Park, Diffusion in High Polymers: Some Anomalies and Their Significance *Trans. Faraday Soc.* **47**, 1072 (1951).
249. J. G. Downes, B. H. Mackey, Sorption Kinetics of Water Vapor in Wool Fibres *J. Polym. Sci.* **28**, 45 (1958).
250. J. Crank, A Theoretical Investigation of the Influence of Molecular Relaxation and Internal Stress on Diffusion in Polymers *J. Polym. Sci.* **11** (2), 151 (1953).
251. G. S. Park, The Glassy State and Slow Process Anomalies in *Diffusion in Polymers*, edited by J. Crank, G. S. Park (Academic Press, New York, 1968), p 141.
252. B. Rosen, Time Dependent Tensile Properties. Part III. Microfracture and Non-Fickian Vapor Diffusion in Organic Glasses *J. Polym. Sci.* **49**, 177 (1961).

253. R. Bracewell, *The Fourier Transform and Its Applications*, 3rd ed. (McGraw-Hill, New York, 1999), p 57.
254. A. F. Barton, *CRC Handbook of Polymer-Liquid Interaction Parameters and Solubility Parameters* (CRC Press, Boca Raton, 1990), p 202.
255. G. K. Fleming, W. J. Koros, Dilation of Polymers by Sorption of Carbon Dioxide at Elevated Pressures *Macromolecules* **19**, 2285 (1986).
256. M. Suwandi, S. Stern, Transport of Heavy Organic Vapors through Silicone Rubbers *J. Polym. Sci. : Polym. Phys. Ed.* **11**, 663 (1973).
257. N. Segatin, C. Klotz, Thermodynamics of Solution of Some Alkyl Acetates in Water *Monatsh. Chem.* **132**, 1451 (2001).
258. D. A. Sullivan, Industrial Solvents in *Kirk-Othmer Encyclopedia of Chemical Technology*, 4th ed., edited by M. Howe-Grant (Wiley-Interscience, New York, 2000).
259. G. Wibawa, R. Hatano, Y. Sato, S. Takishima, H. Masuoka, Solubilities of 11 Polar Organic Solvents in Four Polymers Using the Piezoelectric-Quartz Sorption Method *J. Chem. Eng. Data* **47**, 1022 (2002).
260. S. Prager, F. A. Long, Diffusion of Hydrocarbons in Polyisobutylene *J. Am. Chem. Soc.* **73**, 4072 (1951).
261. A. Aitken, R. M. Barrer, Transport and Solubility of Isomeric Paraffins in Rubber *Trans. Faraday Soc.* **51**, 116 (1955).
262. S. P. Chen, J. A. D. Edin, Fickian Diffusion of Alkanes Through Glassy Polymers: Effects of Temperature, Diffusant Size, and Polymer Structure *Polym. Eng. Sci.* **20** (1), 40 (1980).
263. D. Arnould, R. L. Laurence, Size Effects on Solvent Diffusion in Polymers *Ind. Eng. Chem. Res.* **31**, 218 (1992).
264. A. R. Berens, H. B. Hopfenberg, Diffusion of Organic Vapors at Low Concentrations in Glassy PVC, Polystyrene, and PMMA *J. Membr. Sci.* **10**, 283 (1982).
265. S. J. Huang. Evaluating Isostatic and Quasi-isostatic Procedures for Determining the Organic Vapor Barrier Properties Through Polymer Membranes, M.S. Thesis, Michigan State University, 1996.

266. S. J. Huang, J. R. Giacin, Evaluating the Effect of Temperature and Vapor Concentration on the Organic Vapor Barrier Properties of Polymer Membranes by an Isostatic Procedure *J. Plastic Film Sheeting* **14** (4), 308 (1998).
267. J. Brandrup, E. H. Immergut, E. A. Grulke, *Polymer Handbook*, 4th ed. (Wiley-Interscience, New York, 1999), p VII/685.
268. P. R. Bevington, *Data Reduction and Error Analysis for the Physical Sciences* (McGraw-Hill Book Co., New York, 1969).
269. P. J. Fenelon, in *Permeability of Plastic Films and Coatings to Gases, Vapors, and Liquids*, edited by H. B. Hopfenberg (Plenum, New York, 1974), p 285.
270. C. Zhang, B. P. Cappleman, M. Defibaugh-Chavez, D. H. Weinkauff, Glassy Polymer Sorption Phenomena Measured with a Quartz Crystal Microbalance Technique *J. Polym. Sci : Polym. Phys. Ed.* **41**, 2109 (2003).
271. W. J. Koros, D. R. Paul, Transient and Steady State Permeation in Poly(ethylene terephthalate) Above and Below the Glass Transition *J. Polym. Sci : Polym. Phys. Ed.* **16**, 2171 (1978).
272. K. Toi, Analysis of the Permeation of CO₂ Through Glassy Polymers *J. Membr. Sci.* **41**, 37 (1989).
273. R. M. Barrer, J. A. Barrie, P. S. L. Wong, The Diffusion and Solution of Gases in Highly Crosslinked Copolymers *Polymer* **9** (12), 609 (1968).
274. E. L. V. Lewis, R. A. Duckett, I. M. Ward, J. P. A. Fairclough, A. J. Ryan, The Barrier Properties of Poly(ethylene terephthalate) to Mixtures of Oxygen, Carbon Dioxide and Nitrogen *Polymer* **44**, 1631 (2003).

VITA

Sushil Naresh Dhoot was born on August 6, 1977 in Aurangabad, India, the son of Sudha Dhoot and Naresh Dhoot. After completing his work in St. Xavier's High School and Vivekanand Junior College in Kolhapur, India, he entered Mumbai University Institute of Chemical Technology in May 1994. He graduated with a Bachelor of Science (B.S.) degree in Chemical Engineering from Mumbai University in May 1998. Then, he entered North Carolina State University in Raleigh, NC that same year. He was awarded a Master of Science (M.S.) degree in Chemical Engineering in December 2000. In January 2002, he transferred to The University of Texas at Austin and continued to work with the same supervisor, Professor Benny D. Freeman, in the Chemical Engineering department.

Permanent Address: Rajarampuri 6th Lane, Gayatri Bldg., Kolhapur, 416 008 INDIA.

This dissertation was typed by the author.